Double barrier magnetic tunnel junctions for innovative spintronic devices

Paulo Veloso Coelho

To cite this version:

Paulo Veloso Coelho. Double barrier magnetic tunnel junctions for innovative spintronic devices. Condensed Matter [cond-mat]. Université Grenoble Alpes, 2018. English. NNT : 2018GREAY048 . tel-02046789

HAL Id: tel-02046789

https://theses.hal.science/tel-02046789

Submitted on 22 Feb 2019

Communauté
UNIVERSITÉ Grenoble Alpes

THÈSE

Pour obtenir le grade de

DOCTEUR DE LA COMMUNAUTÉ UNIVERSITÉ GRENOBLE ALPES

Spécialité : PHYSIQUE DES MATERIAUX
Arrêté ministériel : 25 mai 2016

Présentée par

Paulo VELOSO COELHO

Thèse dirigée par **Claire (phys) BARADUC**, CEA
et codirigée par **Mairbek (phys) CHSHIEV**, UGA

préparée au sein du **Laboratoire Spintronique et Technologie des Composants**
dans **l'École Doctorale Physique**

Doubles jonctions tunnel magnétiques pour dispositifs spintroniques innovants

Double barrier magnetic tunnel junctions for innovative spintronic devices

Thèse soutenue publiquement le **30 octobre 2018**,
devant le jury composé de :

Monsieur CORIOLAN VIOREL TIUSAN
PROFESSEUR, UNIV. TECHNIQUE (CLUJ-NAPOCA) - ROUMANIE, Rapporteur
Monsieur MICHEL HEHN
PROFESSEUR, UNIVERSITE DE LORRAINE, Rapporteur
Monsieur JAN VOGEL
DIRECTEUR DE RECHERCHE, CNRS DELEGATION ALPES, Président
Monsieur DAFINE RAVELOSONA
DIRECTEUR DE RECHERCHE, CNRS DELEGATION ILE-DE-FRANCE SUD, Examinateur

I have not failed. I’ve just found 10,000 ways that won’t work.

Thomas Edison

Acknowledgments

The first and main acknowledgments are for my two supervisors Claire Baraduc and Mairbek Chshiev who provided and trusted me with the opportunity of following a PhD at Spintec. First, my deepest thanks to Claire, for always being available for fruitful discussions about our most peculiar results and guiding my work flow. Of course, always in a good mood and with an encouraging sense of humor, even in stressful situations. Thanks to Mair for his incredible knowledge and most helpful insights from his theoretical background. Always providing that unique idea we would take ages to come up with.

To all Spintec staff, from Director to secretaries, to take care of any problem I had with professionalism and for their support. Special acknowledgments to the researchers of the MRAM group for inviting me to their meetings which translated into helpful discussions about some less obvious results and for path to follow. Here, I would like to highlight the help and advice provided by Bernard Dieny, Lucian Prejbeanu and Antoine Chavant. A special thank you to Ricardo Sousa for allowing me to use his automated setup to characterize my wafers and also allowing for the only conversations I had in Portuguese at the lab. Very sincere acknowledgments as well for Andrey Timopheev and Nikita Strelkov for helping in the macrospin simulations, respectively, for in-plane and out-of-plane double MTJs. Thanks to Clarisse Ducruet (Crocus Technology) and Stéphane Aufret for the deposition of most part my wafers. To Laurent Vila for all the e-beam lithographies of my wafers. To the cleanroom process engineers, Guillaume Lavaitte, Nathalie Lamard and Jude Guelfucci for helping me with the fabrication process whenever needed. To all my fellow PhD and Pos-Doc friends at Spintec, with special focus to those who shared with me room 324: Titiksha Srivastava, Mathieu Fabre and Jyotirmoy Chatterjee. We had some very funny moments in that office, specially after working hours when noise was not a problem. A more professional thank you to Jyotirmoy whose help and dedication was paramount to the development of the patent we share but also to push the development of the double junctions with perpendicular anisotropy. A unique thank you to a very special and fun group of friends that ”spin-off” from Spintec a.k.a ”Les Cosmo”: Dali, Roméo, Jude et Guillaume. I will always happily remember all the ”heures heureuses” we had in the city center with good beer and very funny conversations about the most ”sensitive” subjects (ahahah).

A kind word as well for my flatmates from ”ColocAbel”: Marion, Patrick, Estelle, Jeanne and Thèo. Thank you for all the very nice coloc dinners and parties we have made at the apartment. It was a really nice to have shared almost 3 years with you guys in Grenoble.

Although 3 years were spent in France, I must not forget that the majority of the manuscript writing was done in Braga while working at the International Iberian Nanotechnology Laboratory (INL). For that, I have to thank as well my current supervisor Ricardo Ferreira for allowing me to work on the manuscript during the ”not so busy” times. Of course, my current working fellows Cosimo and Mohamed. As well as my new spintronics group friends, Lara, Alex, Tim, Elvira, Leandro and Luana.

Cannot forget my friends ”for life” from my hometown who contributed to keep me connected to my country and made all the comebacks so worthwhile.

Finally, I have to dedicate this ultimate accomplishment of becoming a Dr. to my parents, Lurdes and Paulo. I know it was a dream of yours that required so much sacrifice from you. I will be forever grateful to you. To my little sister Sónia who I love so much. As well, in memory of my grandfather José and my grandmother Ana, I am sure you would be very proud of me and I would love to have you around to celebrate.

Abstract

One of the dilemmas faced by the present STT-MRAM technology is the reduction of the power consumption and increase of data access speed without jeopardizing the data retention. A possible solution lies on the double barrier magnetic tunnel junction (DBMTJ) where the amplitude of the spin transfer torque (STT) on the storage layer can be tuned through a proper magnetic configuration of the outer electrodes. Thus providing more reliable read/write operation modes for MRAM. Despite the reduction in half of the switching current, previous studies on DBMTJs with in-plane magnetization report undesired switchings in read mode associated with field-like torque ($\mathrm{T}_{\perp}$). In this thesis, we further investigate the complex interplay between damping-like and field-like torques in these double barrier structures. Measurements using DC current and short voltage pulses in DBMTJ with symmetric and asymmetric barriers have revealed a strong presence of the field-like torque both in write and read modes. Moreover, in DBMTJs with symmetric barriers set in read mode, we demonstrate pure field-like torque switching which is proportional to a quadratic voltage and adjusted by a b_2 prefactor: $\mathrm{T}_{\perp} \propto \mathrm{b}_2\mathrm{V}^2$. Furthermore, this torque favors a antiparallel alignment between the storage layer magnetization and the two references' magnetizations. The results obtained experimentally were in agreement with macrospin simulation performed with a proper tuning of the damping-like and field-like torque prefactors. In order to suppress the field-like torque and aiming for a further reduction of the writing currents and enhanced scalability of MTJs, we developed and realized DBMTJs with perpendicular anisotropy (p-DBMTJs). Novel seedless multilayers with improved perpendicular magnetic anisotropy to be used as top reference were designed and implemented in functional p-DBMTJs. The optimized p-DBMTJs were patterned into sub-300nm nanopillars and the spin transfer torque studied experimentally in write and read modes. The use of W instead of Ta as a spacer in the FeCoB/spacer/FeCoB composite storage layer showed a 3x improvement of STT efficiency. In write mode, p-DBMTJs have also demonstrated a considerable enhancement of STT efficiency when compared to single barrier p-MTJs. In read mode, switching has been prevented at the center of the bistable region but its thermal stability degraded with high voltage. Among several proposed explanations of this phenomenon, the reduction of the saturation magnetization and effective anisotropy with increasing temperature has been supported by macrospin simulations as

the most probable one.

Keywords

Spintronics, Double Barrier Magnetic Tunnel Junction, Spin Transfer Torque, Perpendicular Magnetic Anisotropy, MRAM

Résumé

Un des dilemmes au quel doit faire face la technologie MRAM est la réduction de la consommation énergétique et l'amélioration des vitesses d'accès aux données sans compromettre la rétention des données. Une des solutions possibles passe par les jonctions tunnel magnétiques à double barrière (JTMDB) dont l'amplitude du couple de transfert de spin de la couche de stockage peut être réglée par le choix de la configuration magnétique des électrodes. Cela permet ainsi des modes d'opération lecture/écriture plus fiables pour les MRAM. Malgré la réduction de moité du courant de commutation, une étude précédente sur les JTMDB avec aimantation dans le plan signale des commutations indésirables en mode lecture liées au couple de transfert de spin perpendiculaire ($\mathrm{T}_\perp$). Dans cette thèse, nous étudions plus en détail l'interaction complexe entre les couples de transfert de spin planaire et perpendiculaire dans ces structures à double barrière. Les mesures effectuées en utilisant courant DC ou des impulsions en tension de courte durée dans des JTMDB avec des barrières symétriques et asymétriques ont montré la présence du couple de transfert de spin perpendiculaire en mode lecture et en mode écriture. De plus, dans les JTMDB avec barrières symétriques en mode lecture, nous démontrons la commutation pure déclenchée par le couple de transfert de spin perpendiculaire qui est proportionnel à la tension quadratique et ajusté par le préfacteur b_2: $\mathrm{T}_\perp \propto \mathrm{b}_2\mathrm{V}^2$. En outre, ce couple de transfert de spin favorise l'alignement antiparallèle entre les aimantations de la couche de stockage et les deux couches de référence. Les résultats obtenus expérimentalement sont en accord avec des simulations macrospin effectuée avec un choix adéquat des préfacteurs des couples de transfert de spin planaire et perpendiculaire. Afin de supprimer l'influence du couple de transfert de spin perpendiculaire, réduire encore plus le courant d'écriture et permettre la miniaturisation des JTM, nous avons développé et fabriqué des JTMDB avec anisotropie perpendiculaire (p-JTMDB). Des nouvelles multicouches sans couche de croissance avec une anisotropie magnétique perpendiculaire amélioré ont été conçues et introduites dans p-JTMDB fonctionnelles comme référence du haut. Les p-JTMDB optimisées ont été fabriquées en nanopiliers de diamètre inférieur à 300 nm et le couple de transfert de spin étudié expérimentalement en mode lecture et écriture. L'utilisation du W au lieu de Ta comme couche intercalaire dans la couche de stockage FeCoB/Couche intercalaire/FeCoB a montré une amélioration de l'efficacité du couple de transfert de spin d'un facteur 3. En mode écriture, les p-JTMDB ont aussi démontré un considérable renforcement de l'efficacité du couple de transfert de spin par comparaison aux p-JTM à simple barrière. En mode lecture, la commutation est empêchée au centre de la région bistable mais la stabilité thermique de l'état magnétique se dégrade aux tensions élevées. Parmi plusieurs explications proposées pour ce phénomène, la réduction de la aimantation à saturation et de l'anisotropie effective avec l'augmentation de la température par effet Joule semble la plus probable selon des simulations macrospin.

Mots-clés

Spintronique, Jonctions Tunnel Magnétiques à Double Barrière, Couple de Transfert de Spin, Anisotropie Magnétique Perpendiculaire, MRAM

Contents

Abbreviations

- AFM, Antiferromagnet
- AP, Antiparallel
- CIPT, Current-in-plane-tunneling
- DBMTJ, Double Barrier Magnetic Tunnel Junction
- FM, Ferromagnet
- FL, Free Layer
- GMR, Giant Magnetoresistance
- IP, In-plane
- LLGS, Landau-Lifshitz-Gilbert- Slonczewski
- MR, Magnetoresistance
- MRAM, Magnetoresistive Random-Access Memory
- MTJ, Magnetic Tunnel Junction
- NM, Non-magnetic
- NSML, Novel Seedless Multilayers
- P, Parallel
- p-DBMTJ, perpendicular Double Barrier Magnetic Tunnel Junction
- PMA, Perpendicular Magnetic Anisotropy
- PMMA, Poly(Methyl Methacrylate)
- PPMS, Physical Properties Measurement System
- RA, Resistance-Area product
- RAM, Random Access Memory
- RIE, Reactive Ion Etching
- RKKY, Ruderman-Kittel-Kasuya-Yosida
- SAF, Synthetic Antiferromagnet
- SEM, Scanning Electron Microscope
- STT, Spin Transfer Torque
- TIAR, Thermally Induced Anisotropy Reorientation
- TBL, Texture Breaking Layer
- TMR, Tunnel Magnetoresistance
- VSM, Vibrating Sample Magnetometer
- VCMA, Voltage Controlled Magnetic Anisotropy

List of Symbols

- G, Conductance
- H, Magnetic Field
- $\mathrm{H_c}$, Coercive Field
- $\mathrm{H_d}$, Demagnetizing Field
- $\mathrm{H_k}$, Anisotropy Field
- $\mathrm{H_{off}}$, Offset Field
- $\mathrm{I_{sw}}$, Switching Current
- $\mathrm{J_{sw}}$, Switching Current Density
- $\mathrm{K_{eff}}$, Effective Anisotropy Energy Density
- M, Magnetization
- $\mathrm{M_s}$, Saturation Magnetization
- P, Polarization
- R, Resistance
- s, Spin
- $\mathrm{T_B}$, Blocking Temperature
- $\mathrm{T_c}$, Curie Temperature
- $\mathrm{T_{\parallel}}$, Damping-like Torque
- $\mathrm{T_{\perp}}$, Field-like Torque
- α, Damping constant
- Δ, Thermal Stability Factor
- μ, Magnetic Moment
- μ_B, Bohr magneton
- ϵ, Demagnetization Factor
- ρ, Density of States
- τ, Pulse Width

CGS to SI Conversion Table

Expression	CGS	SI
Zeeman Energy	$E_z = -4\pi V M_s \left(\vec{m} \cdot \vec{H}\right)$	$E_z = -\mu_0 V M_s \left(\vec{m} \cdot \vec{H}\right)$
Demagnetizing Energy from Shape	$E_d = -\frac{1}{2} V M_s^2 4\pi \boldsymbol{N}$	$E_d = -\frac{\mu_0}{2} V M_s^2 \boldsymbol{N}$

Introduction

The conservation and transmission of information is one of the key features which have enabled the human species to thrive throughout millennia. The ability to store the acquired knowledge and the possibility to spread it has transformed us in the most resilient, versatile and dominant species in the world. We currently live in a ”data-driven” era. With the advent of the Internet and a continuously growing automation of all sectors of activity, data treatment and storage are two domains which require more research and development in order to keep up with technology exponential growth.

Throughout the years, man has been developing more reliable, cheaper and denser memories. In fact, the predictions of Moore’s law have been confirmed year after year with the exponential increase of electronic components on a chip. Therefore, it urges the need for developments in downsize scalability of memory devices. In addition, the universal memory demands a low production cost but also for data to be stored and accessed in no time. Non-volatility is also a required criterion which consists in the conservation of the stored data even when the power is off. This perfect memory would eliminate the current drawbacks in nowadays memories which is the slow access to the stored data and its high prices. Thus providing higher speed data manipulation at a low cost. The growing market for memories is of the order 10-100$\times 10^9$€, stimulated by the ascent of the Big Data and the Internet of Things.

In the past few years, the Magnetoresistive Random Access Memory (MRAM) has become a potential candidate and has attracted the attention of the largest companies of the industry of electronics including Samsung, IBM, Toshiba and GlobalFoundries. Everspin Technologies is one of the first companies that has pushed the MRAM production to an industrial scale. Their most recent chips demonstrate access times of 30ns and data retention larger than 20 years. Among the different types of MRAM, the STT-MRAM has shown to be one of the most promising and competitive non-volatile memory technologies. Moreover, it has been appointed as one of the emerging technologies that can scale down to the 16 nm nod by the *International Technology Roadmap for Semiconductors* (ITRS). This device uses a current induced effect, the spin transfer torque (STT), to switch the magnetization of the storage layer of the key element of the MRAM, the magnetic tunnel junction (MTJ).

In this thesis, we further investigate one alternative to the current STT-MRAM based on single MTJ: the double barrier magnetic tunnel junction (DBMTJ). This work carries on the first developments on DBMTJs made during the thesis of P.-Y. Clément [1]. His most important result was the demonstration of the possibility to modulate the STT amplitude in DBMTJs depending on the alignment of the magnetization of the two reference layers. Therefore, it enables a reduction of the power consumption in the writing process and simultaneously allows for higher access speeds in the reading process. The first objective of this thesis is to provide a better and deeper understanding of the damping-like and field-like torques interplay on write and read mode on in-plane magnetized DBMTJs. Finally, we aimed for the materials optimization of a DBMTJ with perpendicular anisotropy, as well as the demonstration and investigation of STT in patterned sub-100nm perpendicular double barrier magnetic tunnel junctions (p-DBMTJs).

This thesis is divided in five main chapters. In chapter 1, we recall the two most important physics concepts behind the STT-MRAM which are the tunnel magnetoresistance and the spin transfer torque. We present also a general overview about MRAM. Chapter 2 describes in more detail the fabrication techniques required for the fabrication of nanometric DBMTJs and a brief description of the electric characterization performed on our samples. In chapter 3 we study the STT in DBMTJs with in-plane anisotropy with measurements performed with DC current and voltage pulse measurements performed. In addition, macrospin simulations help to get a deeper insight on the role of each damping-like and field-like torques' components and comparisons are made with the experimental results. Chapter 4 focuses on the materials development of a new functional top reference compatible with [Co/Pt]-based multilayers as well as an optimization of the stack of DBMTJ with perpendicular anisotropy. Finally, chapter 5 shows the results of STT in patterned sub-300nm perpendicular DBMTJs in write and read modes and the analysis of unexpected phase diagrams obtained for this type of devices.

1

Theoretical Concepts

Contents

1.1 Introduction

In the last decades, the need for even larger storage capacity has constantly driven storage technology towards further miniaturization. Prior to 1990, all hard-disk drives used the same inductive head for reading and writing. Further downscaling the size of stored bits caused signal amplitude reduction, which necessitated more powerful detectors. Solving this problem required a technological disruption. Anisotropic magnetoresistance (AMR) effect proved to be the successful solution. The first magnetoresistive read-head was implemented in 1990 by IBM. This new technology used an effect discovered by Thomson in 1857: in ferromagnetic metals, the electrical resistance depends on the direction of the current with respect to the magnetization direction. The magnetoresistance ratio (MR), defined as the normalized resistance contrast between maximum and minimum resistance, varies between 0.1 % to a maximum of 5% [2] at room temperature in usual ferromagnetic metals and alloys.

In that context, the most remarkable event was the discovery of giant magnetoresistance (GMR) in magnetic multilayered structures, simultaneously by the groups of A. Fert [3] and P. Grünberg [4] in 1988. For this great contribution to science, they were awarded the Nobel Prize in Physics, in 2007. It was observed that the resistance of antiferromagnetically coupled Fe/Cr/Fe multilayers dropped by 80 %, at 4.2 K, upon application of an applied magnetic field, an effect attributed to spin-dependent scattering of conduction electrons at the interfaces between the Fe/Cr layer.

The GMR discovery opened a new research domain on spin-dependent transport, called spintronics [5], since it combines both magnetism and electronics. By contrast to common electronics, spintronics uses not only the charge of the electron but its spin to operate the device. The applicative potential of the GMR was so important that less than 10 years elapsed between the discovery of the effect and the first implementattion of GMR read-head in a product. More precisely, it was the invention of the spin valve [6] that ramped up the usage of MR-based devices in industry. In fact, spin valves replaced AMR-based HDD read heads in 1997. However, their low resistance (incompatible with CMOS access transistors) and MR (20 to 30% in optimized CPP[1] geometry spin valves [7]) do not make GMR devices suitable for applications as magnetic memory. The solution would pass by the magnetic tunnel junction (MTJ) which demonstrated much higher MR ratios [8] at room temperature.

1.2 Spin Polarized Tunneling

1.2.1 Spin polarized current

In quantum mechanics, electron has a new property, the spin (s) which corresponds to its intrinsic angular momentum. Whereas the orbital angular momentum is related to the operator $\vec{L}$, the spin is associated to operator $\vec{S}$. The electron spin is characterized by a quantum number $s = \pm 1/2$ with two available states called "spin-up"($s = 1/2$) and "spin-down" ($s = -1/2$). The electron spin gives rise to a magnetic moment $\vec{\mu} = (g\, e/2m_e)\, \vec{S}$ where $g \approx 2$ is the Landé factor, e and m_e are the electron charge and mass, respectively. Thus the electron magnetic moment is close to the Bohr magneton $\mu_B = e\, \hbar/2m_e$.

---

[1] Current Perpendicular to Plane

In most solids, the discrete magnetic moments (on each atom) do not interact with each other (paramagnetism and diamagnetism). However, in some cases, one observes a magnetic order. In ferromagnets, the interaction between magnetic moments, called exchange, stems from the combined effect of Coulomb interaction and Pauli exclusion principle. This exchange results in a parallel alignment of discrete moments, creating a non-null magnetic moment per unit volume (or magnetization M), even in the absence of magnetic field.

A precise description of the electronic properties of ferromagnetic metals (Fe, Co, Ni) must take band theory into consideration. These studies show hybridization between the spin polarized d valence band and s conduction band [9], resulting in a high spin polarization (about 30-40 %) of the conduction electrons. Nevertheless, a simplified model (Stoner Model [10]) is widely used: it considers the interplay between exchange and kinetic energy of free electrons. The exchange energy forces the electrons to have the same spin state, though they need to occupy higher energy states, which increases their kinetic energy. If the gain in kinetic energy does not compensate the reduction of exchange energy U, a ferromagnetic order appears. Ferromagnetism occurs if the Stoner criterion $\rho(E_F)U > 1$ is met, where $\rho(E_F)$ is the density of states (DOS) at Fermi level and U the exchange energy. Within this Stoner model, the electronic properties of the ferromagnet are described by two free electrons bands with exchange splitting (Fig. 1.2): this results in a different DOS for spin up and spin down electrons, the former being called majority and the latter minority spins. Electronic transport in ferromagnets is therefore described within a two currents model taking into account these two populations of electrons. Finally, the electrical current flowing in a ferromagnet turns out to be spin-polarized: this property has been essentially ascribed to different scattering efficiencies for majority and minority electrons [2] [11].

1.2.2 Tunnel Magnetoresistance

The fundamental structure of a MTJ consists of two ferromagnetic layers separated by a thin insulating layer (typically an oxide) as depicted in Fig.1.1(a). In this structure the electrons travel from one ferromagnet to the other across the thin oxide barrier, with a finite probability of crossing, through quantum-mechanical tunneling. Since the adjacent layers to the insulator are ferromagnetic, the tunneling becomes spin dependent [12]. This spin dependent tunneling in MTJs is translated into tunnel magnetoresistance (TMR) which is defined by Eq..(**??**) where R_{Max} and R_{Min} correspond to the resistance for antiparallel (AP) and parallel (P) magnetization configurations between the two ferromagnets [see Fig.1.1(b)].

The first observation of TMR in a MTJ structure was by Julière [13] in 1975, at very low temperature (4.2 K). Moreover, he proposed the first simple model of TMR in MTJ, based on the spin polarizations of the ferromagnets. Julière's model lies on two postulates: i) the electron spin is conserved during the tunneling process and ii) the conductance for a determined spin orientation can be calculated using the Fermi golden rule i.e. is proportional to the product between the DOS at Fermi level of the two ferromagnets. Figure 1.1(b) shows a representation of the transport of electrons across a MTJ, based on the spin dependent tunneling of electron waves through the insulating barrier. Depending on the

---

[2] minority electrons are more scattered because of the larger number of available localized d-states.

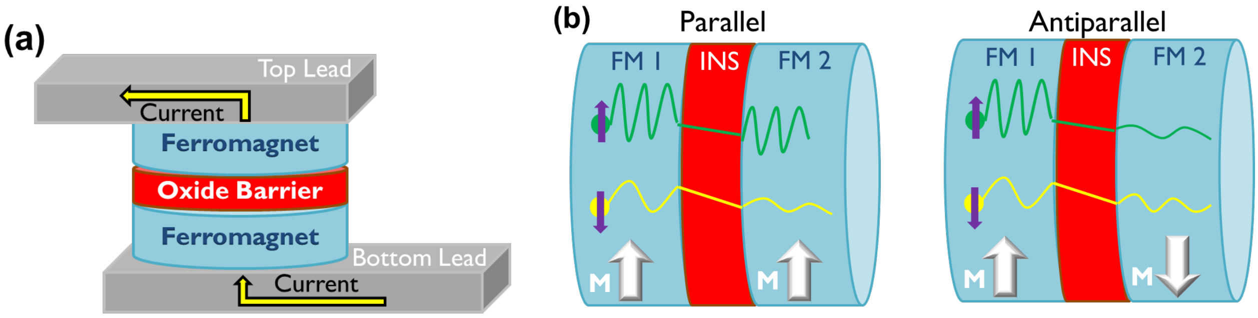

Figure 1.1: (a) Scheme of a MTJ structure in which the two ferromagnets are separated by an insulating oxide layer. The CPP geometry of the MTJ is also shown as the current travels perpendicularly to the interfaces (b) Spin dependent tunneling for a MTJ in parallel and antiparallel states. The white arrows represent the magnetization (M) direction of each ferromagnet. The green and yellow lines represent the wave function of the spin up and spin down electrons, respectively. FM stands for ferromagnet and INS stands for insulating layer.

relative orientation of the two magnetizations, parallel or antiparallel, the electrons conductivity is high or low, respectively leading to the R_{Min} and R_{Max} resistance states. As mentioned before, the imbalance between spin-up and spin-down electrons responsible for the magnetic moment in ferromagnets is described by the Stoner model. The latter is also used to describe the transport in MTJs where the energy bands of s-like electrons are exchange-split as represented in Fig.1.2.

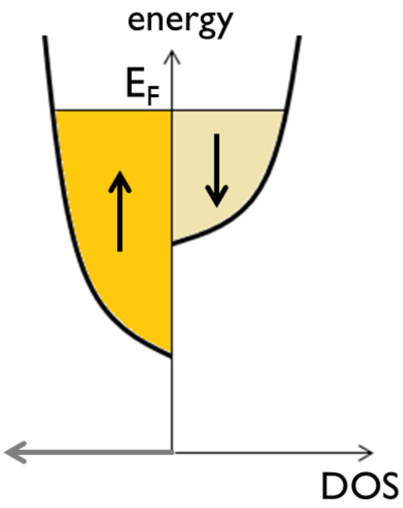

Figure 1.2: Stoner model for conduction (s-like) electrons in a magnetic tunnel junction within Julière's model.

Due to the exchange-splitting, the potential energy becomes spin dependent as well. Assuming Julière's first postulate (see previous paragraph), the system possesses two different electron spin-channels, one for spin-up (in this example majority electrons) and another for spin-down, each one with a corresponding potential energy diagram. When the magnetizations are aligned in parallel, the spin-up electrons tunnel from a majority spin band in one ferromagnet to the majority spin band in the other ferromagnet. Similarly, the spin-down electrons tunnel from a minority to a minority spin band. In this scenario, the number of occupied states at Fermi level in the first electrode perfectly matches the number of vacant states just above Fermi level in the second electrode. Thus the conductance is high corresponding to low resistance R_{Min}. The opposite scenario happens for an antiparallel alignment between magnetizations. The majority band electrons from one ferromagnet tunnel to the minority band of the other ferromagnet and vice versa. The conductance is thus much lower corresponding to the high resistance R_{Max}.

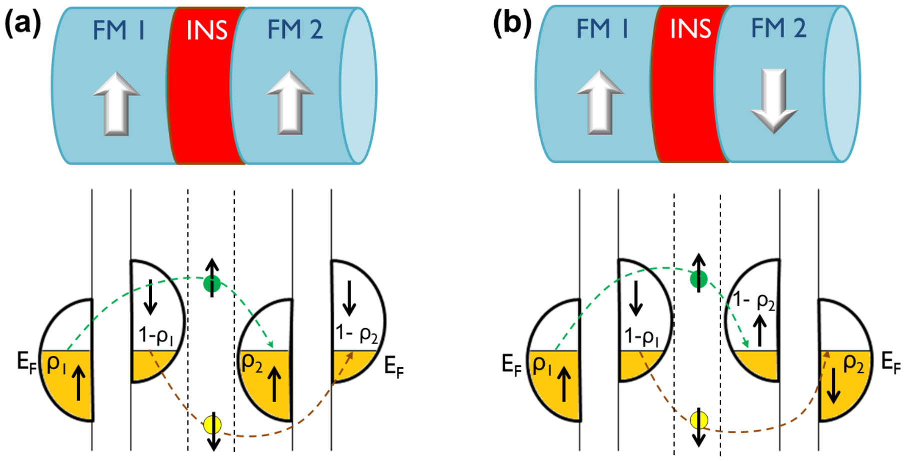

Figure 1.3: Electronic density of states of the ferromagnetic electrodes in a MTJ with magnetizations aligned (a) parallel and (b) antiparallel. E_F is the energy at Fermi level.

The conductance for the parallel (G_P) and antiparallel (G_{AP}) magnetic states can be expressed in terms of the DOS for spin-up (+) and spin-down (-) electrons, for each of the ferromagnets [3] [14]:

$$G_P, G_{AP} \propto \rho_1^+ \rho_2^+ + \rho_1^- \rho_2^- \tag{1.1}$$

By considering Fig.1.3(a), G_P is given by:

$$G_P = \alpha \left[\rho_1 \rho_2 + (1-\rho_1)(1-\rho_2)\right] \tag{1.2}$$

where α is a proportionality constant. In antiparallel alignment of the magnetizations, as shown in Fig.1.3(b), the majority and minority bands interchange spins. Therefore, the conductance for this state is given by:

$$G_{AP} = \alpha \left[\rho_1 (1-\rho_2) + \rho_2 (1-\rho_1)\right] \tag{1.3}$$

The difference in conductance (ΔG) between the parallel and antiparallel magnetic states is thus given by the following:

$$\Delta G = \alpha \left[(2\rho_1 - 1)(2\rho_2 - 1)\right] = \alpha P_1 P_2 \tag{1.4}$$

where P_1 and P_2 are, respectively, the polarizations in FM1 and FM2 as defined below:

$$P_i = \frac{\rho_i^\uparrow - \rho_i^\downarrow}{\rho_i^\uparrow + \rho_i^\downarrow} \tag{1.5}$$

where $i = 1$ or 2.

---

[3] + and - are chosen to code for the spin values whereas ↑ and ↓ code for majority and minority spins.

The combination of equations (**??**),(1.2) and (1.3) results on the Julière's formula for the TMR, which relates the TMR with the effective spin polarization (P_1 and P_2) of the two ferromagnets:

$$TMR = \frac{R_{AP} - R_P}{R_P} = \frac{G_{AP}^{-1} - G_P^{-1}}{G_P^{-1}} = \frac{2P_1P_2}{1 - P_1P_2}. \tag{1.6}$$

The model conceived by Julière was later refined by Slonczewski in 1989 where an angular dependence of TMR was included. This upgraded model was the first to consider the FM/Insulator/FM trilayer as a single quantum mechanical system [15]. The model considers a rectangular barrier of finite height contrary to Jullière's model.The ferromagnets are characterized by parabolic bands of free electrons whose momentum is conserved when flowing across the MTJ. The main change with respect to Jullière's model is a new definition of the spin polarization that takes into account the barrier height. Finally, the MTJ conductance expressed as a function of the angle θ between the magnetizations of each ferromagnetic layer is given by:

$$G(\theta) = \frac{G_P + G_{AP}}{2} + \frac{G_P - G_{AP}}{2} \cos\theta \tag{1.7}$$

1.2.2.A TMR dependence on the ferromagnet spin polarization

The development of magnetic memories and/or sensors encouraged the pursuit for higher TMR values in MTJs. The first generation of MTJs used amorphous barriers of AlO$_x$ which never showed TMR values superior to 70% at room temperature. Equation ((1.6)) has been used to infer the spin polarization of several ferromagnetic alloys, using experimentally acquired TMR as input value. Commonly used 3d ferromagnetic metals and alloys based on Ni, Co or Fe present spin polarization values (at T $<$ 40 K) that range from 0.35 for Ni [16] up to 0.53 for Co$_{72}$Fe$_{20}$B$_8$ [17] and 0.55 for Ni$_{40}$Fe$_{60}$ [18].

Julière's model (Equation (1.6)) suggests that TMR should increase with increasing spin polarization of the ferromagnetic layers. Therefore, the use of more exotic materials, such as half-metals ferromagnets, has been exploited in order to increase TMR. Such materials have only one spin band occupied at Fermi level which results in a spin polarization close to unit [19]. Very low temperatures studies performed by Bowen [20] and Sakuraba [21] have demonstrated record high TMR, respectively, 1800% (at 4 K) in La$_{2/3}$Sr$_{1/3}$MnO$_3$/SrTiO$_3$/La$_{2/3}$Sr$_{1/3}$MnO$_3$ and 570% (at 2 K) in Co$_2$MnSi/AlO/Co$_2$MnSi. Nevertheless, these extremely high TMR values succumbed at room temperature.

1.2.2.B TMR dependence on the tunnel barrier: the Butler's model

A breakthrough was obtained in the pusuit of high TMR at room temperature by using cristalline MgO (001) as a tunnel barrier. At present time, the highest TMR value reported at room temperature is of 500% [22], obtained for MTJs with 3d ferromagnetic alloys based on (Co$_{26}$Fe$_{76}$)$_{80}$B$_{20}$/MgO/(Co$_{26}$Fe$_{76}$)$_{80}$B$_{20}$. The use of MgO crystalline barriers allows a quite efficient spin filtering enabling high TMR, comparable to the use of half-metal as MTJ electrodes. The corresponding tunneling theory was first proposed by Butler *et al.* in 2001 [23], based on the analysis of band diagrams of body-centered cubic (bcc) Fe (001 oriented). This model is based on Bloch waves: the electrons flowing through a crystalline structure are under the effect of a periodic potential whose origin is the electric field generated by the atoms of the matrix. These Bloch waves are deeply dependent of the structure of the material, therefore in a crystal, dependent on its symmetries. In bcc (001 oriented) structures, there are four Bloch states that describe the transport: Δ_1, Δ_2, Δ_2' and Δ_5. Moreover, majority and minority electrons have different Bloch states symmetries. In the case of bcc Fe (001 oriented), for majority electrons, only Δ_1 Bloch state is above E_F associated to a high Fermi velocity. Meanwhile, for minority electrons, Δ_2' and Δ_5 bands intersect the Fermi level energy, though with a much lower Fermi velocity. Another important aspect is the energy gap between the Δ_1 bands for majority and minority electrons: the Δ_1 band for minority electrons is completely below E_F, thus the band diagram is comparable to half-metals. Therefore, a quite efficient spin filtering of Δ_1 Bloch states is expected.

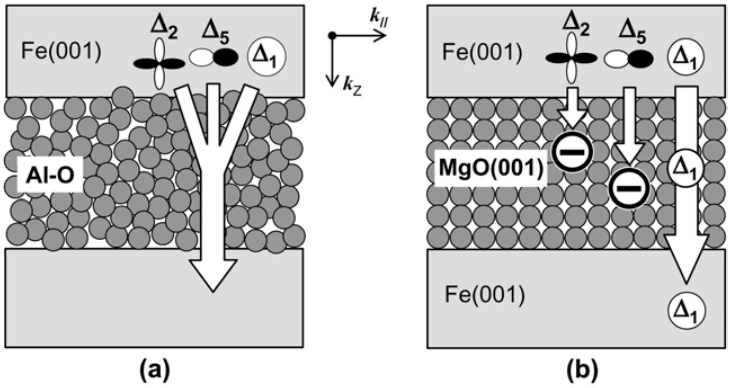

Figure 1.4: Illustration of tunneling through (a) an amorphous barrier (Al_2O_3) and (b) crystalline barrier [MgO (001)]. Image taken from [24].

Therefore the tunneling processes in an amorphous barrier and a crystalline one are quite different, which explains the TMR difference in MTJs using one or the other barrier. The tunneling process in a MTJ with an Al_2O_3 barrier is illustrated in Fig.1.4(a). The top ferromagnet is considered to be Fe (001) which, as mentioned in the previous paragraph, presents Bloch states with different symmetries of wave functions. However, as the oxide barrier is amorphous, no crystallographic symmetry is present, and Bloch states of different symmetries may couple with evanescent states in the amorphous barrier, resulting in finite (yet different) tunneling probabilities, which is usually called incoherent tunneling. In this case, Bloch states with positive (Δ_1) and negative (Δ_2 and Δ_5) spin polarization contribute to the tunneling current, thus the net spin polarization of the electrode is reduced, resulting in low ($<$ 70%) TMR values.

For MTJs with crystalline MgO (001 oriented) barriers, the tunneling is handled by evanescent waves of various well defined symmetries of Bloch states, as represented in Fig.1.4(b). In the typical case of Fe/MgO (001)/Fe, as shown in Fig.1.5, the decay is much slower and the transmission higher for Δ_1 band Bloch state. Since the Δ_1 band is completely spin polarized at Fermi level (P = 1), when the dominant Δ_1 electrons tunnel, high TMR values are expected. Therefore, the role of crystalline MgO is to select the fully spin polarized states of Fe, which is usually called coherent tunneling. The high spin polarization of Δ_1 states is not exclusive of bcc Fe (001), but also exists for other bcc ferromagnetic alloys as bcc CoFe. In the band diagram of CoFe, there are no spin states for minority electrons at

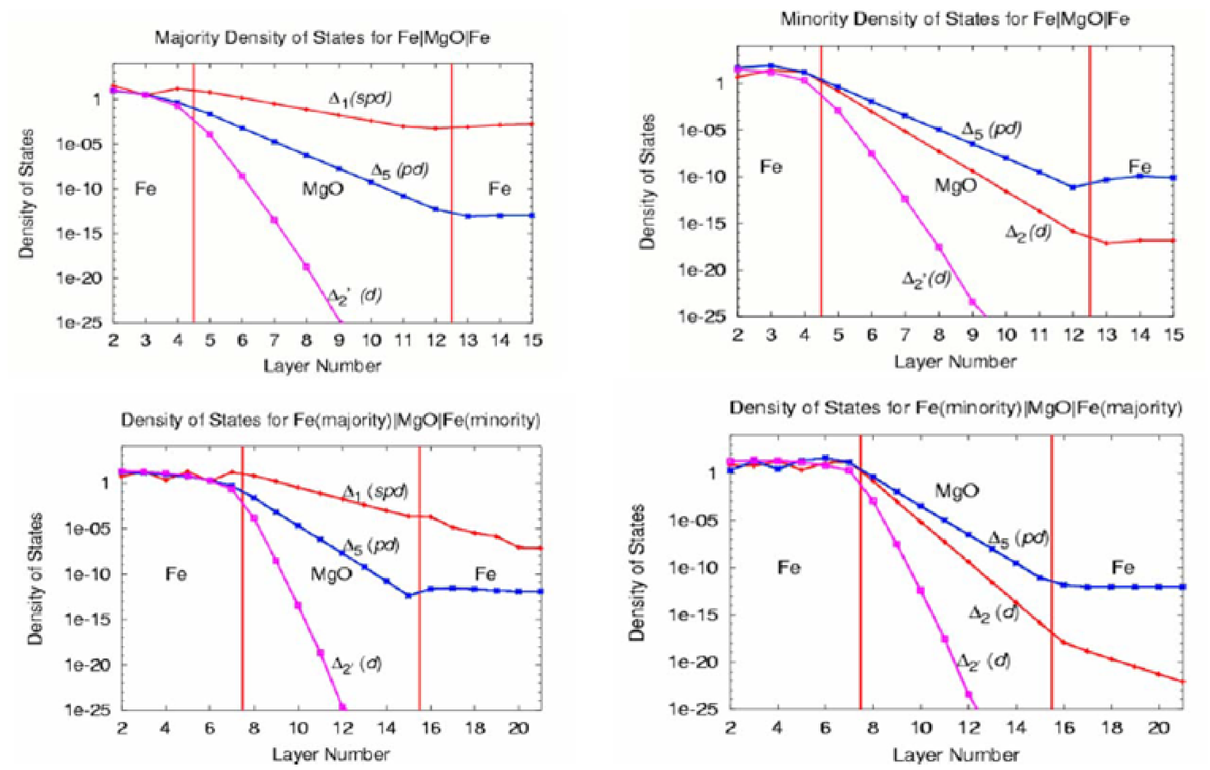

Figure 1.5: Density of Bloch states in Fe/MgO/Fe, for (*Top Left*) majority, (*Top Right*) minority electrons. (*Bottom*) Density of states for an antiparallel alignment between the magnetizations of the Fe electrodes. Image taken from [25]

Fermi level but only one Δ_1 Bloch state for majority electrons [26], which increases the spin filtering effect and consequently TMR. In the case of CoFeB/MgO/CoFeB MTJs (the type of structures used in this thesis), as-grown CoFeB layer is amorphous whereas MgO is polycrystalline. Then annealing induces the migration of B towards its getter (Ta layer) and CoFe crystallizes, starting from the MgO barrier that serves as a crystallization germ.

Comparatively to Al_2O_3, MgO barriers based MTJs present higher TMR values. In 2004, Yuasa *et al.* [27] reported 88% TMR at room temperature for fully epitaxial Fe/MgO/Fe MTJ deposited by molecular beam epitaxy (MBE). The experimental results rapidly improved to ratios up to 200% [28]. Nevertheless, junctions prepared by sputtering techniques have been preferred and developed. Since they present a higher TMR ratio and the sputtering deposition is more convenient for industrial purposes. With a proper tuning of the thickness and compositions of the CoFeB electrodes, TMR as high as 500% was reported [22] at room temperature.

1.2.3 TMR in double barrier MTJ

The first reports of magnetic structures using two or more barriers date from early 1990's with a theoretical study on spin polarized tunneling and MR on double barrier tunnel junctions [29] and experimental results with nonmagnetic triple barrier junctions [30] to explore resonant tunneling. Due to the challenging deposition and fabrication processes involved, the first experimental results on planar double barrier MTJ were only published in 1998 by F. Montaigne *et al.* [31] for Co/Al_2O_3/Co/Al_2O_3/NiFe.

They demonstrated that the decay of MR with bias voltage is lower for a double barrier MTJ than for a similar single barrier one. In fact, TMR would drop from maximum (at zero bias) to half, for a voltage 4x lower in a double barrier structure than in a single barrier. This result was one of the first hints, suggesting that a more complex behavior than sequential tunneling was involved and/or coupled to some coherent/resonant tunneling.

The structures of the form FM/Oxide/NM or FM/Oxide/FM were also very attractive due to the possibility of formation of well defined quantum well states in the middle metal layer sandwiched between the two oxide layers. The first theoretical studies on the coherent tunneling regime of this type of structures with symmetric barriers showed that spin polarized resonant tunneling leads to improved TMR values [32]. However, when the properties of one barrier are different of the other, not only TMR was enhanced but also a new concept of spin diode has been theoretically proposed [33] where the current-voltage (I-V) diode features depend on the magnetic configuration of the ferromagnetic layers which compose the double MTJ. The concept would be later validated experimentally by A. Iovan *et al.* [34]. Unfortunately, the observation of direct spin-dependent resonant tunneling is rather challenging since the appearance of quantum well states is dependent on the thickness of the middle electrode, as shown in Fig.1.6: it thus requires perfectly smooth interfaces.

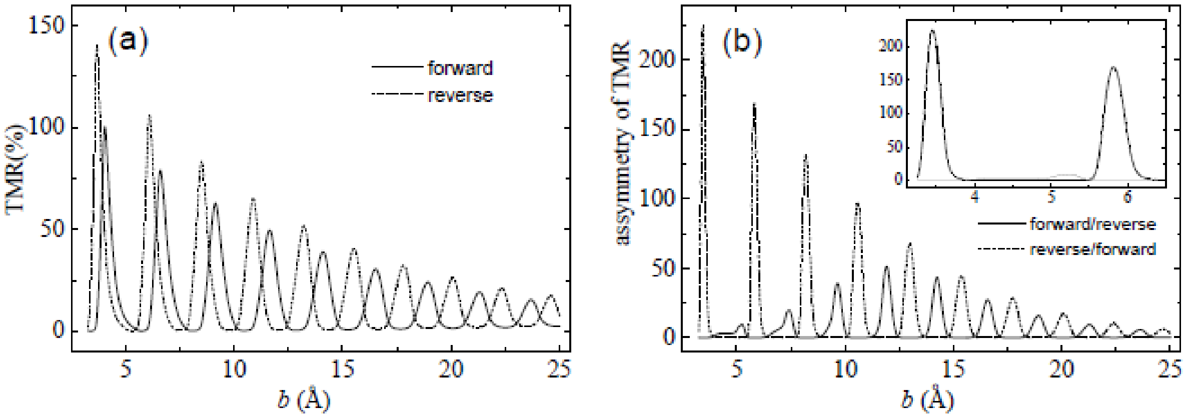

Figure 1.6: Dependence of (a) the TMR and (b) respective asymmetry on the thickness of the middle ferromagnet (*b*) from both forward and backward current through an asymmetric barriers double MTJ. Image taken from [33]

Due to recurring difficulties in growing multilayers with perfect interfaces, the first breakthrough experiment only came with the use of fully epitaxial structures when T. Nozaki *et al.* [35] reported the observation of oscillations of the tunneling conductance, consequence of the quantum well states created in the central Fe layer in Fe/MgO/Fe/MgO/Fe double barrier MTJ. These resonant tunneling effects have always been confined to very limited thicknesses (1-2 nm) of the middle layer under which electron phase coherence is conserved. More recently, though, B.S. Tao *et al.* [36] showed evidence of quantum well states (at room temperature) in thick 12 nm Fe central layer of epitaxially grown double MgAlO$_x$ barrier MTJ.

Despite all the interesting phenomena and potential applications of double barrier tunnel junctions in resonant tunneling regime,in the present thesis, we chose to explore spin transfer torque in this type of structures, envisaging its application as STT-MRAM. The first ever double MTJ STT-MRAM was demonstrated by Z. Diao *et al.* [37] in 2007 for double MgO barriers exhibiting 70% maximum TMR values and with in-plane magnetized ferromagnetic layers. Improvements in the sputtering deposition tools allowed an increase in TMR for the double MTJ with values overcoming 200% [38, 39]. The last generation of double MTJ has perpendicular magnetic anisotropy and until the present date, G. Hu *et al.* [40] and Z. Duan *et al.* [41] have demonstrated STT p-DBMTJ, respectively, with 114% and 150% maximum TMR ratios.

1.3 Spin Transfer Torque

As mentioned in the previous section, current is spin polarized when it passes through a ferromagnetic material. Indeed, it can be viewed as an effect of the magnetization of the ferromagnet onto the electrons spin-angular momentum. The spin transfer torque (STT) can be simply understood as the reciprocal action: a spin polarized current passing through a ferromagnet acts on its magnetization.

First, we present the macroscopic picture of the mechanism of STT considering a macrospin behavior of the system. The simplest example is to consider a trilayer structure composed of FM1/NM/FM2 where NM is a thin non-magnetic spacer [4], as shown in Fig.1.7. Considering that electrons first cross through FM1 and flow towards FM2, in the first ferromagnet, these electrons get spin polarized along the direction of the magnetization $\vec{M}_1$. Whereas the only electrons coming out of FM2 are spin polarized along $\vec{M}_2$. If $\vec{M}_1$ is not collinear with $\vec{M}_2$, the latter should necessarily absorb a part of angular moment carried by conduction electrons polarized in FM1. The spin of the electrons traveling through FM2 should align along its magnetization as this one exerts a torque on their magnetic moments. Reciprocally, the conduction electrons must apply an equal, but opposite, torque on $\vec{M}_2$ which induces precession, or if strong enough, reverses FM2 magnetization.

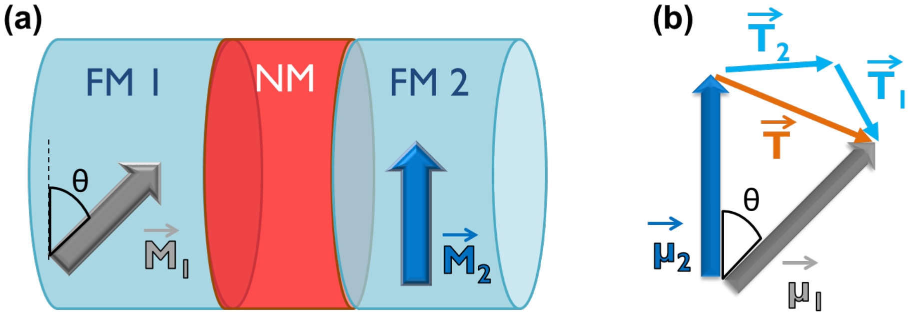

Figure 1.7: a) Schematics of the trilayer structure FM1/NM/FM2 where the corresponding magnetizations $\vec{M}_1$ and $\vec{M}_2$ are misaligned by an angle θ. b) Illustration of the in-plane torques applied on each of the magnetizations. $\vec{\mu}_1$, $\vec{\mu}_2$ and $\vec{T}$ represent, respectively, the ingoing, outgoing and transferred magnetic moments. Adapted from [42].

Still considering the same trilayer structure (Fig.1.7), the incident electrons in FM1 possess a magnetic moment $\vec{\mu}_1 \parallel \vec{M}_1$ and the electrons departing from FM2 a magnetic moment $\vec{\mu}_2 \parallel \vec{M}_2$. The non-collinearity between the two moments implies that some magnetic moment is transferred to the system. However, this transferred moment per time unit (*i.e.* torque) can change the direction of the

---

[4] A metallic layer in the case of a spin-valve or an oxide in the case of a MTJ

magnetization but not its amplitude which is fixed. The torque acting on the magnetization, in analogy with classical mechanics, may be expressed by:

$$\frac{1}{\gamma}\frac{d\vec{M}}{dt} = \vec{T} \tag{1.8}$$

This result suggests that the transferred moment $\vec{T}$ only exists in the orthogonal plane to the magnetization $\vec{M}$ [5]. Thus, $\vec{T}$ is decomposed into two components, $\vec{T_1}$ and $\vec{T_2}$, as represented in Fig.1.7. Each one is exerted, respectively, on $\vec{M_1}$ and $\vec{M_2}$ and both torque components are perpendicular to $\vec{M_1}$ and $\vec{M_2}$, and within the plane $\left(\vec{M_1};\vec{M_2}\right)$.

In summary, the total transferred momentum per time unit is $\vec{T} = \vec{T_1} + \vec{T_2}$ and each term is written as:

$$\vec{T_i} = T_i\vec{m}_i \times (\vec{m}_1 \times \vec{m}_2) \tag{1.9}$$

where $i = 1, 2$ refers to each of the ferromagnets and $\vec{m}_i = \frac{\vec{M_i}}{M_s}$ is the unit vector along $\vec{M_i}$ and M_s is the saturation magnetization of the ferromagnetic layers. This torque was originally named by Slonczewski as "pseudo-torque" [43], currently it is named after its pioneer researcher as Slonczewski torque.

In the particular situation where one the ferromagnetic layers magnetization is fixed and the other is free, the spin transfer torque acting on the latter exists only if there is a misalignment between the two layers magnetizations. The STT is thus given by [44]:

$$\begin{aligned}\vec{T_{\|}} &= -\mu_0 a_{\|}\vec{M} \times \left(\vec{M} \times \vec{p}\right)\\ a_{\|} &= \frac{\hbar\eta}{2e\mu_0}\frac{J}{M_s t}\end{aligned} \tag{1.10}$$

where $\vec{p}$ is the unit vector of the magnetization of the fixed layer, η is the current spin polarization, J is the current density and M_s and t are the saturation magnetization and thickness of the free layer. The subscript || indicates that the torque is parallel to the plane of the two magnetization vectors. Therefore, this torque is also known as *in-plane* torque. Finally, throughout this thesis, this torque is also referred to as *damping-like* torque since it acts similarly to the damping factor in the LLGS dynamics equation (see Eq.(3.12)), either like an extra damping or like an anti-damping term.

1.3.1 STT at electron level

In addition to the intuitive explanation of STT, it is also important to understand the physics of this mechanism at the scale of the electron. For this purpose, let us consider once more the structure with three layers FM1 and FM2, whose magnetizations are misaligned by an angle θ, separated by a non-magnetic spacer NM, as pictured in Fig.1.8. Now, an electron entering FM1 and polarized along the magnetization $\vec{M_1}$ direction (y' axis in Fig.1.8) travels towards NM/FM2 interface. This incident electron can by described a plane wave with wave vector k. As represented in Fig.1.8 while in FM1, the electrons are decomposed in majority and minority, respectively, spin-up (in green) and spin-down (in yellow). As mentioned before, the majority electrons will mostly contribute to the conduction current. With respect

---

[5] Since the magnetization amplitude is constant, $\frac{dM^2}{dt} = \vec{M}\cdot\frac{d\vec{M}}{dt} = 0$; therefore the torque $\vec{T}$ is perpendicular to $\vec{M}$

to the FM2 quantization axis (y), the electron wave function is given by the superposition of the two spin states [42]:

$$\psi_{in} = \frac{e^{ikx}}{\sqrt{\Omega}} \left[\cos(\theta/2)\left|\uparrow\right\rangle + \sin(\theta/2)\left|\downarrow\right\rangle\right] \tag{1.11}$$

The Ω factor has dimensions of a volume which allows the normalization of the wave function. On the other hand, the $\theta/2$ angle dependence is related to the transformation of geometrical angles in angles in spin-space [42].

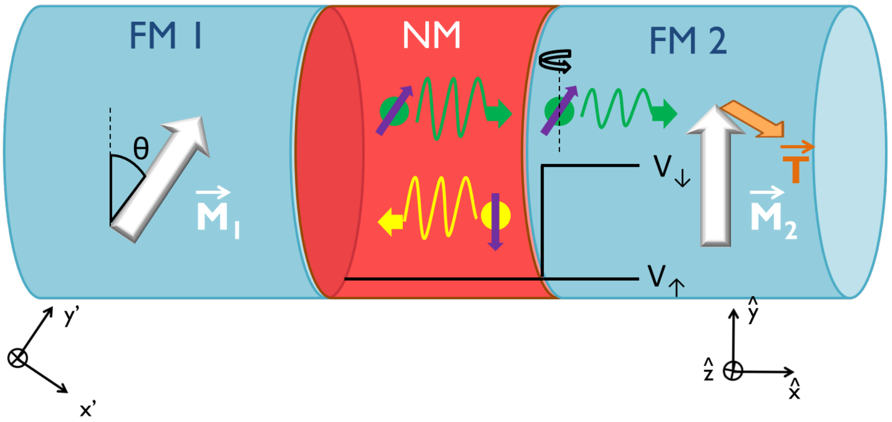

Figure 1.8: Illustration of an incident electron, polarized in FM1 along y', decomposed into majority (or spin-up, represented in green) and minority (spin-down, represented in yellow). If the electron energy is larger than Stoner potential (here $V_\downarrow$), the spin-up part will be fully transmitted, while the spin-down part is partially transmitted (thus leading to spin precession in FM2) and partially reflected. Adapted from [42].

Although majority and minority electrons are considered free electrons, according to the Stoner model, they have distinct energy potentials. Here we assume that majority electrons experience the same zero potential $V_\uparrow = 0$ in FM2 as within the NM. Whereas the minority electrons come across a non zero potential $V_\downarrow = V_\uparrow + \Delta$, where Δ is the exchange energy [45]. Therefore, incoming electrons with spin-up [6] are always transmitted, while electrons with spin-down are either partially or completely reflected depending on their inner energy compared to Δ (see Fig.1.8). The difference in energy of the electron band between spin-up and spin-down (bottom of the band either at $V_\uparrow$ or at $V_\downarrow$) is responsible for the difference in cinetic energy of spin-up and spin-down electrons: therefore they have a different wave vector $(k_\uparrow, k_\downarrow)$. By using the boundary conditions at the interface, the transmitted and reflected wave functions are easily calculated:

$$\begin{cases} \psi_{trans} = \dfrac{e^{ik_\uparrow x}}{\sqrt{\Omega}} \cos(\theta/2)\left|\uparrow\right\rangle + \dfrac{e^{ik_\downarrow x}}{\sqrt{\Omega}} \dfrac{2k}{k+k_\downarrow} \sin(\theta/2)\left|\downarrow\right\rangle \\ \psi_{refl} = \dfrac{e^{-ikx}}{\sqrt{\Omega}} \dfrac{k-k_\downarrow}{k+k_\downarrow} \sin(\theta/2)\left|\downarrow\right\rangle \end{cases} \tag{1.12}$$

The next step is to calculate the total spin flux $\Phi = (\Phi_x, \Phi_y, \Phi_z)$ (proportional to the spin current density) which is given by [42, 44]:

---

[6] with respect to FM2 quantization axis

$$\begin{cases} \Phi_+ = \Phi_x + i\Phi_z = i\dfrac{\hbar^2}{2m}\left(\psi_\downarrow \dfrac{d\psi_\uparrow^*}{dx} - \psi_\uparrow^* \dfrac{d\psi_\downarrow}{dx}\right) \\ \Phi_y = \dfrac{\hbar^2}{2m}\,\mathrm{Im}\left(\psi_\uparrow^* \dfrac{d\psi_\uparrow}{dx} - \psi_\downarrow^* \dfrac{d\psi_\downarrow}{dx}\right) \end{cases} \tag{1.13}$$

By applying Eq.(1.13) onto equations (1.11) and (1.12), the spin flux becomes:

$$\begin{cases} \Phi_{in} = \dfrac{\hbar^2}{2m\Omega}\left(k\sin\theta\hat{x} + k\cos\theta\hat{y}\right) \\ \Phi_{trans} = \dfrac{\hbar^2}{2m\Omega}k\sin\theta\left(\cos\left[\left(k_\uparrow - k_\downarrow\right)x\right]\hat{x} - \sin\left[\left(k_\uparrow - k_\downarrow\right)x\right]\hat{z}\right) \\ + \dfrac{\hbar^2}{2m\Omega}\left[k\cos^2(\theta/2) - k_\downarrow\left(\dfrac{2k}{k+k_\downarrow}\right)^2\sin^2(\theta/2)\right]\hat{y} \\ \Phi_{refl} = \dfrac{\hbar^2}{2m\Omega}k\left(\dfrac{k-k_\downarrow}{k+k_\downarrow}\right)^2\sin^2(\theta/2)\hat{y} \end{cases} \tag{1.14}$$

One of the first conclusions of the analysis of eqs.(1.14) is that if the energy of incoming electrons is larger than Δ, then at the NM/FM2 interface the spin flux is continuous: $\Phi_{in} + \Phi_{refl} = \Phi_{trans}$. Another one concerns the reflected electrons. It is possible to observe that the reflected spin current density is only along $\hat{y}$ which means that transverse [in the $(\hat{x}, \hat{z})$ plane] spin current is zero. This means that these components of the incoming spin flux were fully transmitted in the form of two oscillations with a phase shift of $\frac{\pi}{2}$ and period $\frac{2\pi}{k_\uparrow - k_\downarrow}$. In fact, this result is a direct consequence of the zero potential "felt" by spin-up electrons in the $\hat{y}$ direction. Thus, the real torque exerted on $\vec{M}_2$ only exists on the $(\hat{x}, \hat{z})$ plane which means that the torque deposited is orthogonal to the magnetization. In addition, the reflected spin current (represented in yellow going backwards in Fig.1.8) results from the spin-down electrons which are partly reflected on the potential barrier. When these "recoil" electrons enter FM1 they start to precess along the local field and transfer their moment to $\vec{M}_1$. Therefore, these reflected electrons are responsible for a "back-torque" on FM1 magnetization.

In summary, the torques exerted by incoming electrons in FM2 and the reflected electrons in FM1 have the same direction. Electrons spin polarized along $\vec{M}_1$ try to tilt $\vec{M}_2$ along their direction, while the reflected electrons which are polarized in antiparallel to $\vec{M}_2$ try to tilt $\vec{M}_1$ away from the latter.

1.3.2 Field-like Torque

In 1993, M.D. Stiles [46] explained that the oscillating exchange coupling observed in magnetic heterostructures (with same structure as FM1/NM/FM2) is created by conduction electrons, which are below the Fermi energy level, traveling back and forth across the structure. Therefore, this RKKY coupling would exist, even in the absence of a bias current applied to the system. Although the electrons traveling from both electrodes do not actually create a charge current, whenever a misalignment between the magnetizations of the two ferromagnets exists, a non negligible spin current appears. This spin current acts on the magnetizations in the form of a transverse torque.

Similarly to the case of the damping-like torque, the origin of this torque is better understood if analyzed at electron level. Again, we consider an incident electron traveling towards the NM/FM2 interface. Since the electron is locally affected by the exchange field, it is expected, from the induced precession,

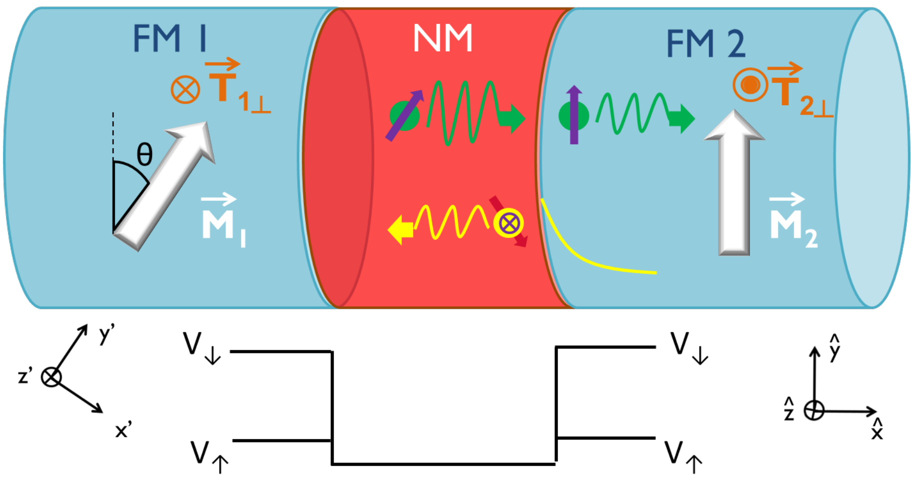

Figure 1.9: Illustration of the FM1/NM/FM2 structure. In this case, the energy of the incident electron lies between $V_\uparrow$ and $V_\downarrow$. Notice that the spin-down part only penetrates FM2 as an evanescent wave (in yellow). $\vec{T}_{1\perp}$ and $\vec{T}_{2\perp}$ represent the applied field-like torques, respectively, on $\vec{M}_1$ and $\vec{M}_2$. The torques have opposite directions. Adapted from [42].

to change the electron angular momentum direction from its initial one. The deposited torque should, not only be planar, but also perpendicular. In this example, let us then consider FM2 with two Stoner potential steps $V_\uparrow$ and $V_\downarrow$ and an incoming electron with an energy comprised between $V_\uparrow$ and $V_\downarrow$ (see Fig.1.9). As mentioned before, the wave function of the incoming spin polarized electron is the superposition of the two (up and down) spin states. In this particular scenario, the spin-up component now faces a slight potential step and it is in part transmitted and partly reflected at the NM/FM2 interface. Meanwhile the spin-down component is completely reflected due to insufficient electron energy to overcome the $V_\downarrow$ step. In fact, the spin-down component does enter FM2 in the form of an evanescent wave. This produces a phase shift between the spin-up and spin-down part of the reflected spin-wave as is the spin had started precessing before being reflected. Thus, the reflected electron gains some moment along $\hat{x}$ which does contribute to a non-zero transverse component Φ_x of the reflected spin flux. As a result, if the non magnetic spacer is seen as a potential well in which the electron is confined, the successive reflections in NM/FM2 and FM1/NM interfaces contribute to a perpendicular torque on both ferromagnetic layers.

From this microscopic picture of the transverse torque, we can jump to a more phenomenological description. As mentioned above, the successive reflections of the electrons at both interfaces give rise to a magnetic coupling between $\vec{M}_1$ and $\vec{M}_2$. Moreover, the exchange coupling energy is given by $E_{ex} = -J\vec{M}_1 \cdot \vec{M}_2$. To this energy, a magnetic field $\vec{H}$ is associated [42]: $\vec{H}_i = \frac{\partial E_{ex}}{\partial \vec{M}_i} \propto \vec{M}_j \; (i \neq j)$. This field exerts a torque $\vec{T}_{i\perp}$ on magnetization $\vec{M}_i$, in each of the two ferromagnets ($i = 1, 2$):

$$\vec{T}_{i\perp} = -\gamma_0 \vec{M}_i \times \vec{H}_i \propto -\vec{M}_i \times \vec{M}_j \tag{1.15}$$

Notice that for this torque the symbol $\perp$ is used in subscript to stress that this torque is perpendicular to the plane of the two magnetizations. Therefore, this torque is called *perpendicular* (or *out-of-plane*) torque. Since this torque acts on the magnetization as a magnetic field would, it is also called (and specially throughout the present thesis) *field-like* torque.

Finally, the perpendicular torque has yet a quite interesting property [47]: $\vec{T}_{1\perp} + \vec{T}_{2\perp} = 0$. Due to the conservation of angular momentum, the two torques are equal but opposite, thus $\vec{T}_{1\perp} = -\vec{T}_{2\perp}$.

1.3.3 STT in Magnetic Tunnel Junctions

We have demonstrated above the general results of both types of torques existing in a magnetic heterostructure when under the effect of spin currents. Although the damping-like torque $\vec{T}_{\parallel} = a_{\parallel}\vec{M} \times \left(\vec{M} \times \vec{p}\right)$ and the field-like torque $\vec{T}_{\perp} = a_{\perp}\vec{M} \times \vec{p}$ formulas remain valid in all systems, the prefactors $a_{\parallel}$ and $a_{\perp}$ are not the same for MTJ as for general metallic systems (*ex.* spin-valve).

The calculation of these prefactors has been studied by various groups, always taking into consideration that spin transfer torque is directly associated with spin current density J_{spin} by $\vec{T} = \vec{\nabla} J_{spin}$ and that it is directly dependent on the characteristics of the ferromagnets composing the MTJ. Several approaches have been used in order to have a reliable description of STT in MTJs: diffusion theory by means of transmission/reflexion matrices at the interfaces [48, 49] or even the use of Green functions within the Keldysh formalism [50, 51]. These studies have allowed the demonstration of the planar and perpendicular torques dependencies with applied voltage:

$$\vec{T}_{\parallel}(V) = \left(a_1 V + a_2 V^2\right) \vec{M} \times \left(\vec{M} \times \vec{p}\right) \tag{1.16}$$

$$\vec{T}_{\perp}(V) = \left(b_0 + b_2 V^2\right) \vec{M} \times \vec{p} \tag{1.17}$$

where the a_i and b_i $(i = 0, 1, 2)$ are parameters which depend on the nature of the ferromagnetic electrodes. In MTJs, the b_0 term does not depend on voltage and it is called *interlayer exchange coupling (IEC)* [15]. The positive or negative sign of the *IEC* is correlated, respectively, to a ferromagnetic or antiferromagnetic coupling between the FM layers adjacent to the tunnel barrier. The IEC value varies with the oxide thickness but also with the technique used to deposit the MTJ, therefore highly correlated with the junction's resistance-area (RA) product [52].

Figure 1.10 shows the results of theoretical investigations of STT in MTJs using the tight-binding model under the non-equilibrium Green functions formalism conducted by M. Chshiev *et al.* [51]. First, the damping-like torque $T_{\parallel}$ follows a linear behavior (a_1) for bias values around zero but, as the applied voltage increases (in absolute value), the quadratic component (a_2) can become preponderant and contribute to reverse the sign of the torque. In Fig.1.10(a), it is also important to remark the higher is the exchange split ($\Delta = \frac{\epsilon^{\downarrow} - \epsilon^{\uparrow}}{2}$), the more pronounced is the curve slope, meaning that the linear contribution (a_1) is substantially higher too. This linear behavior of the torque, associated with a sign change with current polarity, is typical of metallic systems. We see here that it is not necessarily always the case in MTJ. Nevertheless, a change of sign with current polarity is absolutely necessary to obtain an hysteretic behavior of resistance as a function of the applied current, which is crucial for the development of memories.

The field-like torque has a parabolic shape as a function of applied voltage. The V^2 dependence is the most accepted and experimentally observed form of the perpendicular torque [53–55]. Nevertheless,

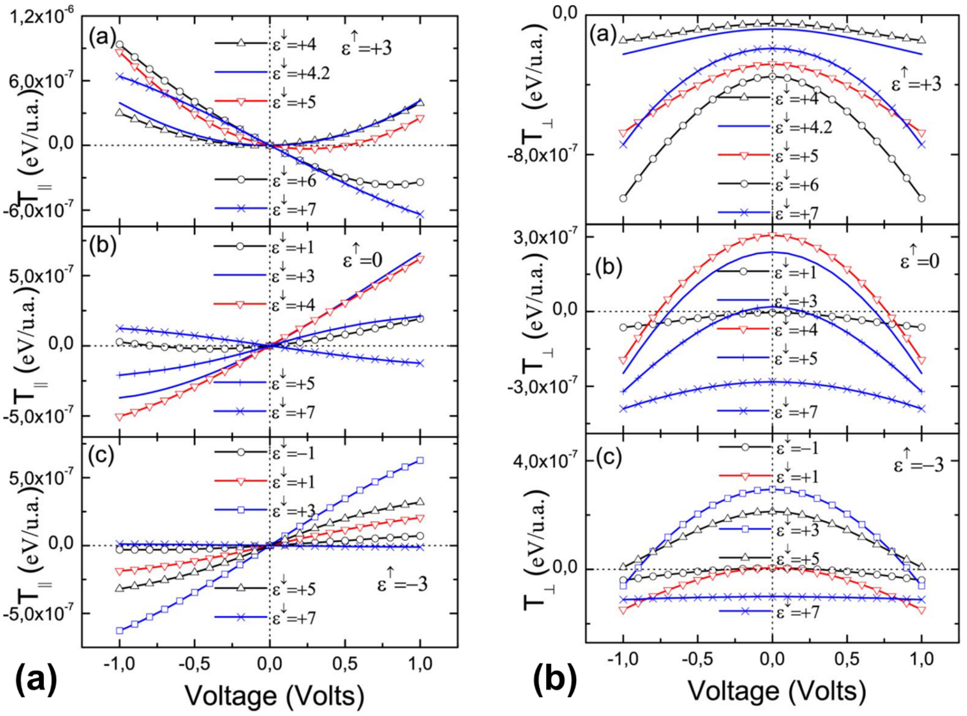

Figure 1.10: Simulations of (a) in-plane $T_{\parallel}$ and (b) perpendicular $T_{\perp}$ torques dependence with applied voltage for different majority ($\epsilon^{\uparrow}$) and minority ($\epsilon^{\downarrow}$) band energies corresponding to different band fillings. Image adapted from [51].

measurements in frequency performed by S. Petit *et al.* [56] have shown hints of a linear component of field-like torque with bias voltage. Later, other experimental works [57] together with some micromagnetic modeling [58] have also supported this claim. By comparing the amplitudes of the two torques in Fig.1.10, $T_{\perp}$ is considerably weaker than $T_{\parallel}$. According to Refs. [53, 59], $T_{\perp}$ in MgO-based MTJs can $10 \sim 30\%$ of $T_{\parallel}$.

1.4 Phase Diagram of Magnetic Tunnel Junctions

1.4.1 Phase diagram boundaries

The Landau-Lifshitz-Gilbert-Slonczewski (LLGS) equation (analyzed in more detail in section 3.4) describes the dynamics of the magnetization. The full equation describes: i) the conservative dynamics through the precession term; ii) the damped dynamics through the precession and damping term and iii) the spin transfer dynamics where the Slonczewski and field-like torque terms are included. For memory applications, the LLG equation (without spin torque terms) is useful to extract the necessary magnetic field to switch the magnetization of a magnetic layer. In fact, the addition of STT terms should reduce the magnitude of this switching field. Therefore, it is very interesting to establish the relationship between the switching field and the STT triggering voltage [7], predicted by the LLGS equation.

The LLGS was solved analytically for a generalized geometry by K. Bernert *et al.* [60]. Using a similar approach as J. Grollier *et al.* [61] for fully metallic devices, they have assumed that the in-plane

---

[7] Although the true source of STT is the current, for this purpose it is more useful to work with voltage.

STT has a linear dependence with voltage while the perpendicular STT has a quadratic one. In addition, they assume that field-like torque always favours a antiparallel state between free and reference layers magnetizations [53,55,59]. Their method is to determine the expression for the unit vector magnetization near equilibrium. The limiting cases where the magnetization vector becomes unstable provides the critical lines of the phase diagram. For a elliptical geometry where the magnetization lies on the plane of the layer, there are four conditions for stability. The parallel (P) state of the magnetizations is stable for voltages larger than,

$$V_P = \frac{a_1}{2\alpha b_2} - \sqrt{\left(\frac{a_1}{2\alpha b_2}\right)^2 + \frac{1}{b_2}\left(-H + H_k - \frac{H_{perp}}{2}\right)}. \tag{1.18}$$

whereas the antiparallel (AP) state is stable for voltages below

$$V_{AP} = \frac{a_1}{2\alpha b_2} - \sqrt{\left(\frac{a_1}{2\alpha b_2}\right)^2 + \frac{1}{b_2}\left(-H - H_k + \frac{H_{perp}}{2}\right)}. \tag{1.19}$$

Other two magnetic field conditions need to be respected. The P state is stable for

$$H_P < H_k - \alpha a_1 V - b_2 V^2 \tag{1.20}$$

while the AP state for magnetic fields following

$$H_{AP} > -H_k - \alpha a_1 V - b_2 V^2. \tag{1.21}$$

In the equations above, a_1 is the linear in-plane STT prefactor, b_2 is the quadratic perpendicular STT prefactor, α is the damping factor, H_k is the in-plane anisotropy field [8] and H_{perp} is the out-of-plane anisotropy field [9]. The critical lines are represented on the phase diagram of Fig.1.11.

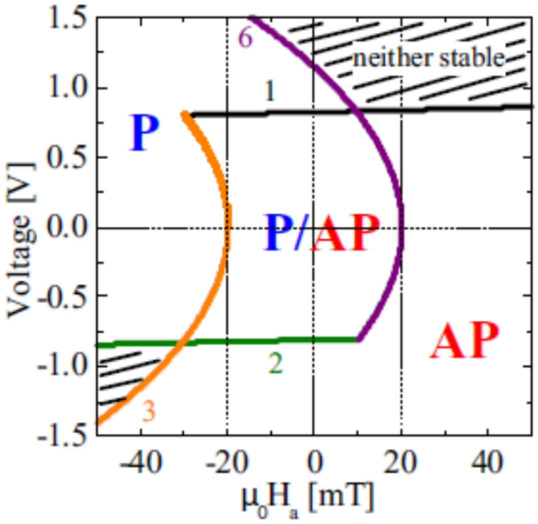

Figure 1.11: Phase diagram with critical stability lines for P and AP states at $T = 0K$. The AP state is stable within the borders defined by lines 1 (Eq.(1.19)) and 3 (Eq.(1.21)). The P state is stable within the other two borders defined by lines 2 (Eq.(1.18)) and 6 (Eq.(1.20)). Image adapted from [60].

---

[8] Experimentally, H_k is the coercive field for $T = 0K$.

[9] Experimentally, H_{perp} is the out-of-plane saturation field.

1.4.2 Critical Switching Current

As we have mentioned before, the LLGS equation [44, 62, 63] has three main terms: damping, precession and STT (including both in-plane and out-of-plane torques). For small-angle excitations and in a simple geometry under a macrospin approximation, it is possible to determine the current value for the spin torque to overcome the damping term, this current is usually called critical switching current (I_{sw0}). In a in-plane (IP) magnetized MTJ (with $T = 0K$), this is the minimum current necessary to switch the magnetization of the free layer and it is given by [64]:

$$I^{IP}_{sw0} = \frac{2e\alpha M_s t_f A(H + H_k + 2\pi M_s)}{\hbar\,\eta} \tag{1.22}$$

where α is the Gilbert damping constant, η is the spin transfer efficiency, H is the applied magnetic field and M_s, t_f, A and H_k are, respectively, the saturation magnetization, thickness, cross-section and in-plane anisotropy field of the free layer. One of the main challenges for the magnetoresistive memories is to have a minimal power consumption, thus it is important to aim for the smallest possible I_{sw0}. The straightforward solutions are: 1) to use materials whose damping constant is as low as possible ($\alpha \approx 0.007$ for CoFeB), 2) reduce the thickness of the free layer and 3) use materials for the free layer with high spin transfer efficiency η. However, one of the most dominant terms in Eq.(1.22) is the $2\pi M_s$ term (typically $2\pi M_s \gg H, H_k$) related to the thin-film demagnetization effect, which favors an in-plane orientation for $\vec{M}$. This term is due to the fact that switching in-plane junctions requires that magnetization becomes out-of-plane during switching, which means overcoming the dipolar energy barrier. Therefore, one strategy to reduce the critical switching current is to suppress the influence of the demagnetizing field. That is possible by using MTJs with perpendicular anisotropy. In that case, magnetization goes through plane during switching, which does not cost any dipolar energy. The critical switching current (at $H = 0$ and $T = 0K$) for an MTJ with out-of-plane magnetization is given by [65]:

$$I^{PP}_{sw0} = \frac{2e}{\hbar}\frac{\alpha M_s t_f A H_k}{\eta} \tag{1.23}$$

1.4.2.A Thermally activated switching

The critical switching currents (or current densities) defined above are also called *intrinsic*, since they are defined for operation, *i.e.* at T = 0K. However, for the vast majority of applications, MTJs work at room temperature (T = 300K). In fact, thermal fluctuations help the magnetization to overcome the energy barrier, thus changing its orientation. For a magnetic moment, this phenomenon is described by the Néel-Brown [66] model (similar to an Arrhenius law). Moreover, the characteristic time τ for the MTJ to pass from one state to the other (*i.e.* for a full reversal of the free layer magnetization) is given by:

$$\tau = \tau_0 \exp\left(\frac{E_b}{k_b T}\right) \tag{1.24}$$

where E_b is the energy barrier to overcome, k_B is the Boltzmann constant and τ_0 is an intrinsic attempt time (typically τ_0 =1 ns).

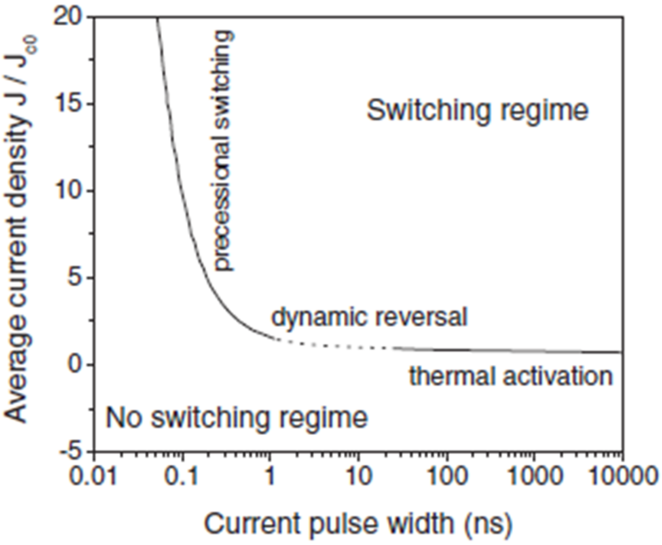

Figure 1.12: Type of current induced magnetization switching regime as a function of the current pulse width. Image taken from [67].

Since T=0K is impossible to achieve for a real device, J_{sw0} (or I_{sw0}) values are obtained by extrapolation of switching current measurements performed at different voltage pulse widths τ_p. For measurements performed at T = 300K, J_{sw0} is close to the average J_{sw} for pulse width $\tau_p \sim 10 - 20ns$ [65]. As represented in Fig.1.12, the switching current density dependence with the bias pulse width shows two main regimes: precession and thermal activation. For very short pulses ($\tau_p < 10ns$), the switching current density is larger than J_{sw0} and details of individual magnetization precession are important. This regime is often called *precessional* (or *ballistic*) and, at T = 0K, the switching current is given by [68]:

$$I_{sw} = I_{sw0}\left(1 + \frac{\tau_r}{\tau_p}\ln\frac{\pi}{2\theta_0}\right) \tag{1.25}$$

where $\tau_r = 1/\left(\alpha\gamma H_k\right)$ is the characteristic relaxation time and θ_0 is the initial angle between the magnetization and the easy axis when the voltage pulse is applied. On the other hand, when the magnetization switching happens for a non-zero temperature, then two effects are to be considered. First the initial angle θ_0 is set according to a Maxwell-Boltzmann distribution [69], thus introducing distribution of I_{sw} for a certain pulse width (typically $\tau_p < 20 - 50ns$). Second, thermal fluctuations will affect the switching process itself. The second switching regime is the *thermally activated* regime for which STT is responsible for increasing the effective temperature of the magnetization and thermal fluctuations activate the magnetization reversal process. The boundary between the two regimes is not rigid and depends on the properties of the MTJ free layer. Based on the thermal activation model, the expression for I_{sw} in the thermally activated regime is given by [68]:

$$I_{sw}(\tau) = I_{sw0}\left[1 - \frac{k_B T}{K_{eff}V}\ln\left(\frac{\tau_p}{\tau_0}\right)\right] \tag{1.26}$$

where $K_eff = \frac{M_s H_k}{2}$ is the effective anisotropy energy density. However, Eq.(1.26) is only applicable for MTJs with in-plane magnetization. For perpendicular anisotropy systems, a slight modification is needed, and I_{sw} becomes $I_{sw} = I_{sw0}\left[1-\sqrt{\frac{k_B T}{K_{eff}V}\ln\left(\frac{\tau_p}{\tau_0}\right)}\right]$. This correction is necessary so the experimental results fit with the analytical perpendicular I_{sw} expression [70].

1.5 Magnetoresistive Random Access Memories (MRAM)

1.5.1 Introduction to Random Access Memories

A computer is a system that processes information. Even before being processed, the data need to be stored. This task is attributed to memories. The memory has four main building blocks:

- Processor registers: the fastest possible access (1 CPU cycle) and small in size (few *kb*);
- Cache: accelerates the data processing by reducing the access time;
- Random access memory (RAM): Contains all the necessary data to run a program. The data is gradually transmitted to the processor according to the program needs. GB in size and best access speed is $\sim$ 10 Gb/s;
- Disk storage: Stores the data provided to the RAM. TB in size. The more mature technology is the Hard Disk Drive (HDD), though being rapidly replaced by Solid State Drive (SSD) since 2017. The latter has a maximum access speed of 2000 MB/s.

Nevertheless, this structure is a requirement of the existing memory technology. The current challenges for the market of memories are: decrease power consumption and device size, increase read/write speed, endurance, data retention and improve non-volatility. This last one separates the memories in two groups: volatile and non-volatile. The volatile memories only keep data stored while power is on. On the other hand, non-volatile memories store data even with power off (for a large but finite number of read/write cycles). Currently, processor registers, cache and some RAM elements (ex. Static RAM and Dynamic RAM) are volatile, while data storage devices (ex. HDD, SSD and flash memory drives) are non-volatile.

Another important aspect that allows to distinguish different types of memories is their core technology, *i.e.* the physical support of the memory data. For one group, the memory feature relies on the atoms displacement in space. This is the case of a simple CD-RW (compact disk-rewritable) but also the phase-change RAM (PCRAM) and the resistive RAM (ReRAM). Another group relies on the displacement of electrical charges. This is the case for the dynamic RAM (DRAM) which stores charges in a separate tiny capacitor within an integrated circuit. With a similar construction as the DRAM but using a ferroelectric layer instead of a dielectric layer, there is also the ferroelectric RAM (FeRAM). The flash memory stores electrons in an array of floating-gate transistors. While the static RAM (SRAM) has two possible circuits for charges. These electric charge based memories are the mainstream technologies used in current personal computers. The last group relies on the orientation of magnetic moments. One of the first memories, using this type of technology, was magnetic-core memory used between 1955 and 1975. Here, the magnetic moments of a small toroidal magnet were read and written by a metallic line capable of generating a magnetic field. Later, this type of memories evolved into magnetic tape based devices such as audio cassettes or VHS, floppy disks, HDD and finally the magnetoresistive random access memory (MRAM).

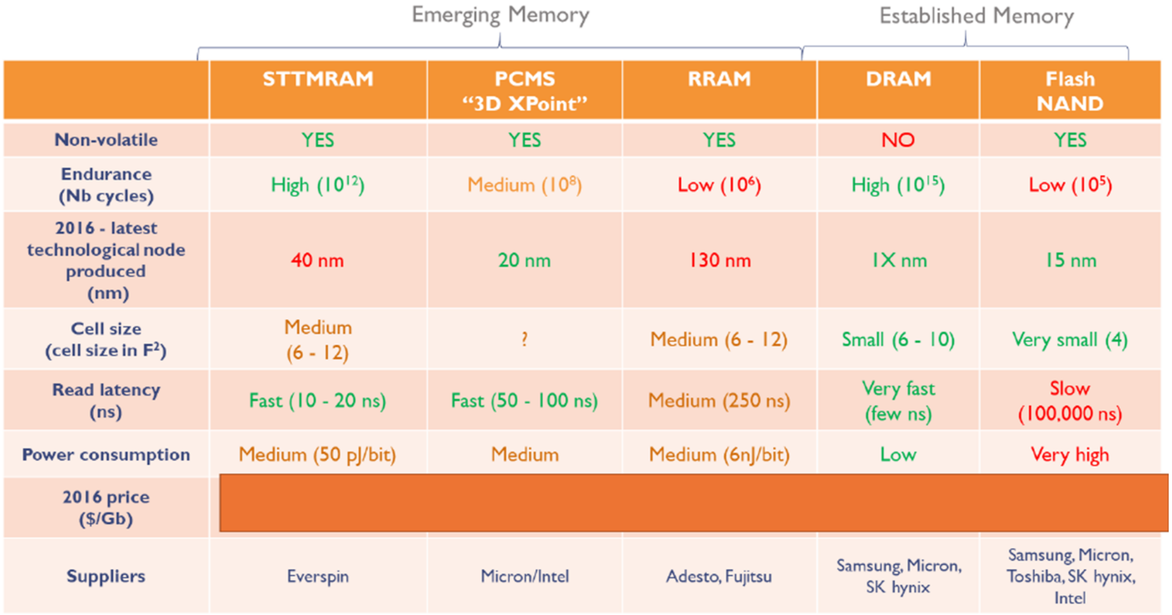

	Emerging Memory			Established Memory	
	STTMRAM	**PCMS "3D XPoint"**	**RRAM**	**DRAM**	**Flash NAND**
Non-volatile	YES	YES	YES	NO	YES
Endurance (Nb cycles)	High (10^{12})	Medium (10^{8})	Low (10^{6})	High (10^{15})	Low (10^{5})
2016 - latest technological node produced (nm)	40 nm	20 nm	130 nm	1X nm	15 nm
Cell size (cell size in F^2)	Medium (6 - 12)	?	Medium (6 - 12)	Small (6 - 10)	Very small (4)
Read latency (ns)	Fast (10 - 20 ns)	Fast (50 - 100 ns)	Medium (250 ns)	Very fast (few ns)	Slow (100,000 ns)
Power consumption	Medium (50 pJ/bit)	Medium	Medium (6nJ/bit)	Low	Very high
2016 price ($/Gb)	[redacted]	[redacted]	[redacted]	[redacted]	[redacted]
Suppliers	Everspin	Micron/Intel	Adesto, Fujitsu	Samsung, Micron, SK hynix	Samsung, Micron, Toshiba, SK hynix, Intel

Figure 1.13: Performance comparison between emerging and well-established RAMs. Source: Yole, InMRAM (2017)

Finally, the table in Fig.1.13 compares the performance between emerging and established RAM memories, focusing on fundamental requirements for memories such as volatility, endurance, device and cell size or power consumption.

1.5.2 Introduction to MRAM

The two main concepts, magnetoresistance and spin transfer torque, presented in sections 1.2.2 and 1.3 are the base technologies for a wide range of devices used for different applications. From data storage to magnetic field sensors, or even microwave oscillators, these two spin current based phenomena are usually present.

Magnetoresistance is the physical property which allows to distinguish the stable magnetic states in a spin-valve or MTJ. For memory applications where high coercivity is essential, only two stable states exist at zero magnetic field. One where the reference and free layer magnetizations are parallel corresponding to a state of minimum MR (in a memory corresponds to a ”0”). And another state where the two magnetizations are antiparallel and MR is now maximum (in a memory corresponds to a ”1”). In general, but specially for memories, the larger the MR, the better. First, there is nearly no readout error since the very large difference in resistance between ”1” and ”0” states enables an easier readout process: the difference between the two states is well above the noise level. Second, a high TMR is favorable to find a suitable reading voltage. Since MR decreases with applied voltage [8,24,27], reading cannot be performed at a high voltage that may compromise the distinction between ”1” and ”0”. On the other hand, readout speed increases with increasing voltages since it is limited to the RC transient time of the access transistor [10]; so a trade-off is necessary. In fact, the MR at zero bias needs to be high enough to enable to obtain the targeted MR at usual reading voltages ($\approx$ 0.2V). One device that mitigates this problem is the double barrier MTJ who has proven to have slower decay rate of MR with applied voltage [31].

The spin transfer torque is the effect that allows high enough applied current to trigger the reversal of the magnetization. STT can be used to switch a MTJ from parallel to antiparallel state,iIn other words, to write the memory bit by switching from ”0” to ”1” and *vice-versa*. The two components of STT are quantities which increase with applied voltage (see eqs.(1.16) and (1.17)). However, along with an increase in the STT amplitude, come two direct consequences: increased power consumption and MTJ breakdown. One of the current challenges in memory development is to reduce power consumption. Therefore, in a device which operates using STT, it is necessary to find a mean for an efficient STT triggered by the smallest current possible. This is, in fact, one of the main goals explored throughout this thesis. The second problem deals with the amplitude of the voltage drop that the oxide barrier can withstand. As any other dielectric, the tunnel barrier can only bear a limited voltage until it breaks down, thus destroying the MTJ. Last but not least, a consequence of using too high voltages is data corruption while reading. Although the applied voltage is only used to access the MTJ resistance during the readout process, it may induce magnetization reversal of the free layer by STT, if it is large enough. On account of this limitation, the reading voltage cannot be increased indiscriminately, which compromises the readout speed. Figure 1.14 summarizes the criteria that should be adopted, in terms of voltage, to read and write with respect to breakdown voltage. This criteria defines that $V_{read} = \frac{1}{4}V_{write}$ in order to avoid data disturbance. Moreover, narrow distributions are critical for error-free operation.

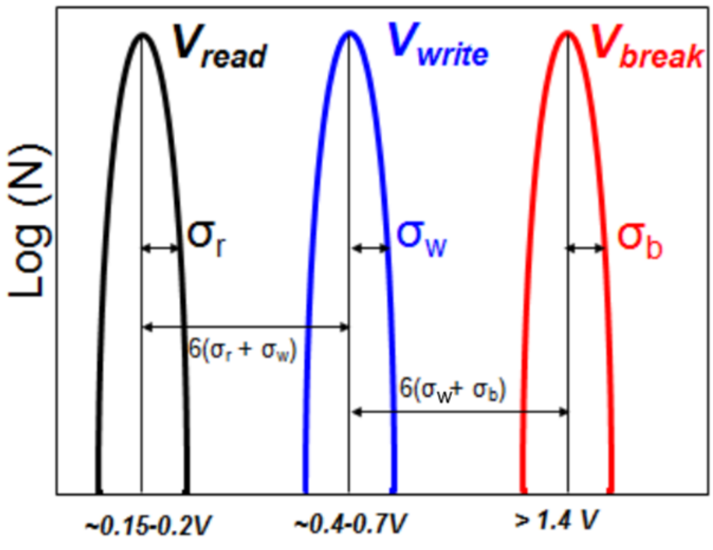

Figure 1.14: Illustration of the distributions of read (V_{read}), write (V_{write}) and breakdown (V_{break}) voltages in STT-MRAM. Adapted from [71].

---

[10] A sufficient voltage difference between ”0” and ”1” states is sooner obtained in transient regime when the asymptotic voltage is higher.

1.5.3 Several families of MRAM

1.5.3.A Field-Written Toggle MRAM

The first generation of MRAM used rows and columns of copper lines, placed on top and bottom of MTJ devices. These lines would create large enough Oersted fields to reverse the free layer magnetization, for devices positioned at the cross point where both a row and column current line were powered, as represented in Fig.1.15(a). This MRAM was called Stoner-Wolfarth MRAM. However, in this type of MRAM, even the non-used bits along the current lines would also ”feel” a magnetic field. Despite the smaller amplitude of this collateral magnetic field, the probability of switching those junctions was non-negligible, causing a problem known as ”half-selection”. In 2003, a solution was proposed by Savtchenko *et al.* [72] by using a synthetic antiferromagnet (SAF) free layer [instead of a single free layer, as present in Fig.1.15(b)] and a programmed write-current pulse sequence [described in Fig.1.15(c)] to toggle the bit from ”0” to ”1” and *vice-versa*. Contrary the Stoner-Wolfarth MRAM where different fields were used to write the high or low states, Savtchenko’s method uses the same field sequence to write both states. The improved MRAMs using the Savtchenko switching are denominated Toggle MRAM. Although these devices present an almost unlimited write endurance and high reliability even at high temperatures, it is of very difficult miniaturization and its main qualities are lost for MTJ diameters below 90 nm.

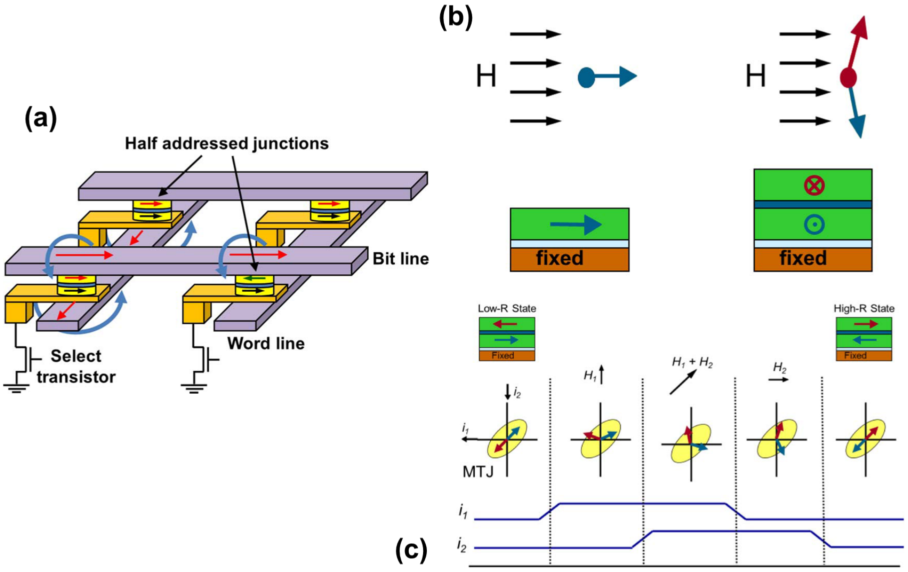

Figure 1.15: (a) Illustration of a Stoner-Wolfarth MRAM for which each cell is composed of a MTJ connected to a select transistor. (b) Response of the magnetizations of a MTJ with single free layer in Stoner-Wolfarth MRAM and of MTJ with a SAF free layer in a Toggle MRAM, to an applied magnetic field. (c) Schematic of the Toggle MRAM write-pulse sequence used to switch the cell from one state to the other. Adapted from [65].

1.5.3.B Thermally Assisted (TAS) MRAM

In this type of MRAM, the MTJ free layer is pinned by exchange with an antiferromagnet. By increasing the temperature (typically via Joule heating caused by applied current), the exchange coupling between the two adjacent layers decreases. When it vanishes, a small magnetic field is applied in the opposite direction of the initial pinning direction, thus allowing to reverse the magnetization of the free layer. The principle of operation is illustrated in Fig.1.16. Unfortunately, these MRAM have never attracted much attention from industry because this operation scheme is difficult to maintain in the whole temperature range necessary for application. Nevertheless, thermally induced writing assisted by spin transfer torque has already demonstrated high quality performances [73].

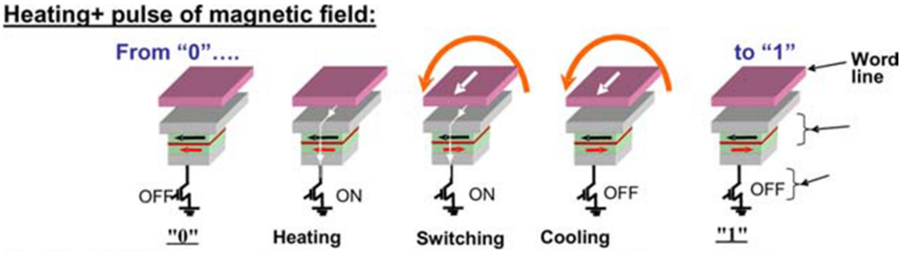

Figure 1.16: Principle of operation the TAS-MRAM where the thermal assistance (Joule heating) is combined with a pulse of magnetic field. Adapted from [74].

1.5.3.C 3-terminal MRAM

The three terminal MRAM can be divided in two important groups. The first type of memories relies on domain wall motion to switch the free layer. Basically the storage layer is composed by a magnetic stripe whose magnetic domains propagate driven by in-plane current thanks to STT, as represented in Fig.1.17(a). This MRAM configurations offers some advantages: improved reliability (less stress on the barrier), low writing currents and multibit architecture. However the three terminal configuration requires large areas and downsizing is difficult.

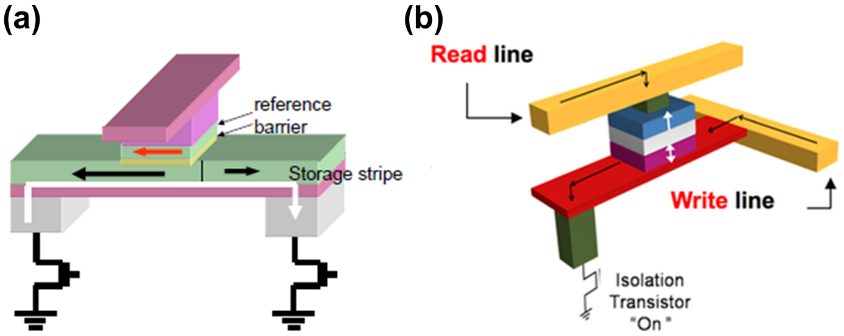

Figure 1.17: (a) Source: B. Dieny InMRAM 2015 (b) Source: http://www.spot-research.eu/The-spOt-project

The other type of three terminal magnetic memories relies on the Rashba effect (or Spin Hall effect) to reverse the magnetization of the storage layer with in-plane current [75]. For this effect to work, it is necessary to have a current line made of an element with high spin-orbit coupling (Pt, Ta, Ag, Bi,..., more details in section 4.2.1). The MTJ is then deposited on top of this line, with the storage layer in direct contact with it, as pictured in Fig.1.17(b). This approach is quite interesting since the electric current used to write the MTJ passes under it, only a small current passes through the MTJ to read its state. Therefore, these Spin-Orbit Torque (SOT) MRAMs have a quite high endurance. Unfortunately, up to now, memory efficiency [11] is 10x lower than a 2-terminal STT-MRAM.

The last family of MRAM uses the spin transfer torque as the main mechanism to switch the storage layer magnetization. In the next subsection, we will describe the different configurations of the STT-MRAM, with a special focus on those that are the subject of the present thesis, the double barrier MTJ STT-MRAM.

1.5.4 STT-MRAM

1.5.4.A Main challenges

As we have mentioned before (in section 1.5.1), the current search for the universal memory is based on five main criteria: size, speed, endurance, power consumption and data retention.

Starting by this last one, industry requires that data should be conserved for a minimum of 10 years. This parameter is directly connected with temperature, since the magnetocrystalline anisotropy energy (which stabilizes a given magnetic state) is in direct competition with thermal energy, thus destabilizing the desired magnetic configuration of the MTJ. However, in a thin film, where the thickness is several times smaller than the layer's lateral dimensions, we need to take into account a magnetostatic energy. Therefore creating an effective anisotropy energy constant given by: $K_{eff} = K_u - 2\pi M_s^2$, where K_u is the uniaxial anisotropy constant and $2\pi M_s^2$ refers to the demagnetizing field with an orthogonal orientation to the layer plane. Considering the thermal effects, the Néel-Brown model [66] allows to determine the probability of reversal of a magnetic particle under non-zero temperature conditions: $p(t) = 1 - e^{-t/\tau}$ where τ is the characteristic reversal time given by Eq.(1.24). This last equation depends on an important parameter called thermal stability factor Δ. Since $E_b = K_{eff}V$, Δ is defined as:

$$\Delta = \frac{K_{eff}V}{k_B T} \tag{1.27}$$

In systems with perpendicular anisotropy, $K_{eff} = \frac{H_k M_s}{2}$, thus Δ is then given by:

$$\Delta = \frac{H_k M_s V}{2k_B T} \tag{1.28}$$

For MRAM to apply as substitutes for Flash type memories, the retention time is τ = 10 years which implies a minimum thermal stability factor of 40, for one isolated bit. For multiple (N) bits, the switching probability becomes:

$$p_N(t, \Delta) = 1 - e^{-\frac{Nt}{\tau_0}\exp(-\Delta)} \tag{1.29}$$

According to this expression, to develop a 1GB memory with a thermal switching probability inferior to 10^{-4}, a thermal stability factor $\Delta > 70$ is necessary.

High data retention is probably the main feature that MRAM must possess in order to directly compete with Flash memories. Although this parameter should be as high as possible, to keep it large is

---

[11] Memory efficiency is defined as (Δ/I_{c0}), where $\Delta = \frac{K_{eff}V}{k_B T}$ is related to the thermal stability of the MRAM state (see next section)

utterly challenging when aiming at downscaling the devices dimensions. Reducing the MTJ size implies a reduction of storage layer volume V. According to eqs.(1.27)-(1.28), the only way to maintain Δ (assuming room temperature operation) is to increase K_{eff}. However, if we admit that saturation magnetization M_s remains constant, K_{eff} only increases through an increase of K_u (and consequently H_k). In the end, size reduction while keeping high data retention, comes with a price to pay which is the increase of the critical switching current density (see Eq.(1.22)). The problem of the enhanced switching current is in itself a disadvantage in terms of power consumption, but also in terms of integration of STT-MRAM device with C-MOS. In fact, the larger I_{sw0}, the larger needs to be the transistor coupled to the MTJ.

So far, three main challenges of the STT-MRAM have been pointed out: increase data retention for a small as possible device without compromising its power consumption. One of the possible solutions to tackle these problems is the STT-MRAM using perpendicularly magnetized MTJs. Comparing the switching current for this type of MTJ (Eq.(1.23)) with the one for in-plane magnetized MTJ (Eq.(1.22)), it is possible to observe that the $2\pi M_s$ term (associated with the demagnetizing fields) vanishes, immediately reducing the critical switching current. In addition, data retention can be maintained high since the materials (Co/Pt and Co/Pd multilayers) used in the perpendicular MTJs (p-MTJs) also have strong perpendicular anisotropies. Unfortunately, along with an higher K_{eff} comes an higher α compromising I_{sw0}, if these materials are used in the free layer. Therefore, the solution found was to add an extra MgO layer on top of CoFeB (common storage layer material with low α) in order to increase anisotropy. Another solution could be to play with the junction shape: for small diameter, in-plane anisotropy decreases thus K_{eff} increases until shape anisotropy favors out-of-plane magnetization for a dot in the shape of a cylinder. Extended explanations about perpendicularly magnetized MTJs can be found in chapter 4.

1.5.4.B Limitation of single barrier MTJ

As we have mentioned in subsection 1.5.2, and specially for certain applications where the memory is much often read than written, increasing the readout speed implies to increase the read voltage as well. A typical MTJ has three different voltage distributions, respectively, to read, write and breakdown. The criteria established by *Everspin® Technologies* is that these voltages should be separated by 6x the sum of the two standard deviations (σ) of the two adjacent distributions, as represented in Fig.1.14. This criterion is crucial to ensure that a read voltage does not disturb the previously written state. With the currently used materials, deposition and nanofabrication techniques, the target writing voltage distribution is centered at ∼0.5 V. This value forces the read voltage to be as low as 0.15 V. In fact, the current used to read the state of the MTJ will also induce STT, which if high enough, may reverse the storage layer magnetization. To ensure $\Delta > 70$ and a maximum switching probability of 10^{-4}, the ratio between the read and write current is $\frac{I_{read}}{I_{write}} \approx 0.28$ [1], which can be rounded down to $\frac{I_{read}}{I_{write}} = \frac{1}{4}$. These read voltage (or current) limitations also condition the readout speed due to the capacitor leakage current of the selection transistors.

In the following subsection, we will see that double barrier tunnel junctions with dual references allow to increase the read voltage without jeopardizing the magnetic state of the storage layer.

1.5.4.C Double Barrier MTJ

The double barrier magnetic tunnel junctions (DBMTJ) is composed by three main magnetic blocks: reference layer, storage layer and control layer (see Fig.1.18). In this structure, the storage layer is sandwiched between two tunnel barriers. The reference and control layers play the role of polarizers whose magnetizations can be set independently of the storage layer. There are two possible magnetic configurations of the DBMTJ depending on the orientation of the magnetizations of reference and control layers. Choosing between these two configurations allows to modulate the amplitude of STT exerted on the storage layer. In consequence, two modes of operation are created, one suited to read and the other to write the memory dot.

(i) Read and Write modes of operation

One of the possible magnetic configurations is the parallel alignment between reference and control layers magnetizations [Fig.1.18(a)]. In this configuration, the torques coming from the reference (T^r) and control (T^c) layers have opposite directions. Therefore, the total torque exerted on the storage layer is expressed as:

$$T^{read} = |T^r| - |T^c| \tag{1.30}$$

The total torque is thus minimum or even cancels out in case of ideal symmetric top and bottom tunnel barriers. This scenario presents the opportunity to apply larger voltages on the DBMTJ without risk of storage layer magnetization reversal. Faster readout speed is then possible in this configuration. This operation mode is called **read mode**.

By constrast, when the reference and control layer magnetizations are in antiparallel alignment [Fig.1.18(b)], the two torques, T^r and T^c, exerted on the storage layer add up. The total torque applied in now given by:

$$T^{write} = |T^r| + |T^c| \tag{1.31}$$

In this situation, the STT is enhanced and writing the storage layer may be performed with lower currents than in the case of a single barrier MTJ. This operation mode is called **write mode**.

The process to set the two different operation modes by switching the direction of the magnetization of the control layer without affecting the one of the reference layer for in-plane anisotropy DBMTJ is explained in more detail in subsection 3.1.2.

The operation modes and their setting have also been demonstrated in DBMTJs with perpendicular magnetization in section 5.1.

(ii) STT in a DBMTJ

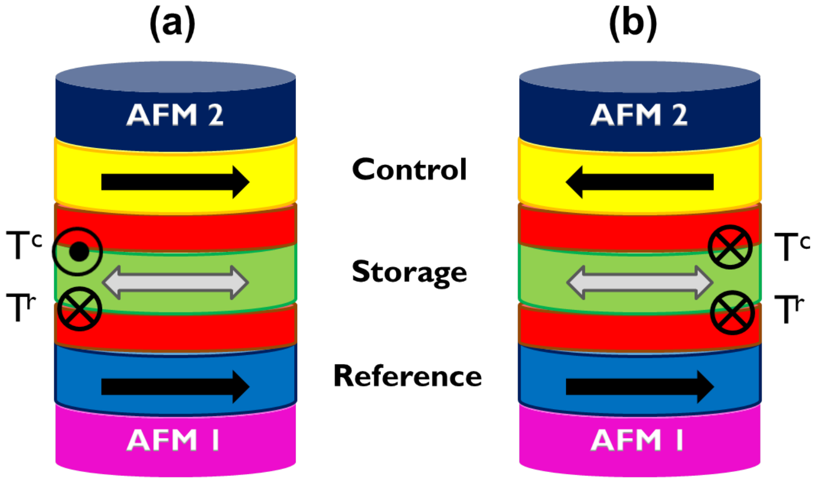

Figure 1.18: (a) Read and (b) write modes of operation in DBMTJ. AFM stands for antiferromagnet. T^r and T^c correspond to the torques exerted on the storage layer coming, respectively, from reference and control layers.

As mentioned above, the most defining feature of the DBMTJ is the modulation of STT acting on the storage layer by manipulation of the magnetic configurations between reference and control layer. Therefore, it is important to discuss in more detail the theory of spin-torque switching of DBMTJs. The most recent study of this theory was performed by D. Worledge [76] in 2017 where he uses the single-domain model to derive the analytical formula for critical switching current I_{sw0} of DBMTJs with perpendicular magnetization (p-DBMTJs).

The study starts by defining the basics of STT for a single barrier MTJ [77]. The torque is defined in function of the angle θ between the free and reference layer magnetizations and an applied voltage V across the MTJ:

$$T(\theta, V) = \frac{\hbar}{2e}\frac{P_R}{R_\perp} V \sin\theta \tag{1.32}$$

where P_R is the spin polarization of the reference layer and $R_\perp$ is the resistance when free and reference layer magnetizations are perpendicular. In addition, the resistance variation with θ in a MTJ is given by [77]:

$$R(\theta) = \frac{R_\perp}{1 + P_F P_R \cos\theta} \tag{1.33}$$

where P_F is the spin polarization of the free layer. The combination of Ohm's law ($V = RI$) and Eq.(1.33), replaced in Eq.(1.32) enables to derive torque as a function of current:

$$T(\theta, I) = \frac{\hbar}{2e}\frac{P_R I}{1 + P_F P_R \cos\theta} \sin\theta \tag{1.34}$$

According to this last equation, torque is larger when $\theta = \pi$ (MTJ in antiparallel AP state) than when $\theta = 0$ (MTJ in parallel P state). Empirically, this is why, for a constant applied voltage, AP→P switching current is smaller than P→AP.

In the case of the double barrier MTJ, apart from the storage layer and reference layer, we need to account for another polarizing layer on top of the top tunnel barrier, the control layer. Therefore, we need to consider the spin polarizations of reference layer P_R, control layer P_C and at the bottom and top interfaces of the storage layer, respectively, P_{Fbot} and P_{Ftop}. Moreover, depending on the magnetic configuration between reference and control layers, the torques, acting on the storage layer, will add up (write mode) or subtract (read mode). For the write mode case where reference and control layers magnetizations are in antiparallel alignment, the total torque is expressed as:

$$T_{write}(\theta) = \frac{\hbar}{2e}\left(\frac{P_C}{R_{c\perp}}V_c(\theta) + \frac{P_R}{R_{r\perp}}V_r(\theta)\right)\sin\theta \tag{1.35}$$

where V_r and V_c are the voltages across the barriers adjacent to the reference and control layers, respectively. Again using Ohms's law [12], these voltages can be written as:

$$\begin{cases} V_r(\theta) = IR_r(\theta) = I\dfrac{R_{r\perp}}{1-(P_{Fbot}P_R\cos\theta)} \\ V_c(\theta) = IR_c(\theta) = I\dfrac{R_{c\perp}}{1+(P_{Ftop}P_C\cos\theta)} \end{cases} \tag{1.36}$$

Notice that the $R_r(\theta)$ and $R_c(\theta)$ have opposite signs in the denominators, representing the opposite directions of the magnetizations in this operation mode. On the other hand, in read mode, the reference and control layers magnetizations have the same direction, resulting in a subtraction between torques:

$$T_{read}(\theta) = \frac{\hbar}{2e}\left(\frac{P_C}{R_{c\perp}}V_c(\theta) - \frac{P_R}{R_{r\perp}}V_r(\theta)\right)\sin\theta \tag{1.37}$$

, in this situation, V_r and V_c have similar expressions since their magnetizations are parallel:

$$\begin{cases} V_r(\theta) = IR_r(\theta) = I\dfrac{R_{r\perp}}{1+(P_{Fbot}P_R\cos\theta)} \\ V_c(\theta) = IR_c(\theta) = I\dfrac{R_{c\perp}}{1+(P_{Ftop}P_C\cos\theta)} \end{cases} \tag{1.38}$$

In order to have a more quantitative perspective of the total torques in both operation modes, we have attributed arbitrary values to current I ($I = 4$) and to the different spin polarizations. For simplicity, we have considered reference, control layers and free layer interface with bottom barrier to have equal spin polarization values, $P_R = P_C = P_{Fbot} = 0.4$. Figure 1.19(a) and (b) describe the variation of torque as a function of the angle θ from the free layer magnetization, respectively, for write and read modes, for different values of P_{Ftop} in an attempt of mimicking a variation of RA symmetry level between the two tunnel barriers [13].

An initial comparison between the torque amplitude between the two modes shows that torque in write mode is, at least, 10x higher than in read mode. In write mode, the variation of RA of the two tunnel barriers does not play a very important role since the torques add up. The only difference among the different curves in Fig.1.19(a) is the angle at which the torque is maximum. The maximum is obtained for $\theta < \frac{\pi}{2}$ when $P_{Ftop} < 0.4$ (bottom barrier thicker), then it is centered on $\theta = \frac{\pi}{2}$ when $P_{Ftop} = 0.4$ (symmetric barriers) and finally is observed for $\theta > \frac{\pi}{2}$ when $P_{Ftop} > 0.4$ (top barrier thicker). In reality, a transition from one state to the other requires less current when the torque is higher. When the bottom barrier is dominant ($P_{Ftop} < 0.4$), the transition from an antiparallel state between reference and free

---

[12] For low RA barriers, the I-V curve is quasi-linear.

[13] This is performed experimentally in chapters 3 and 5, respectively, for in-plane and perpendicular p-DBMTJs

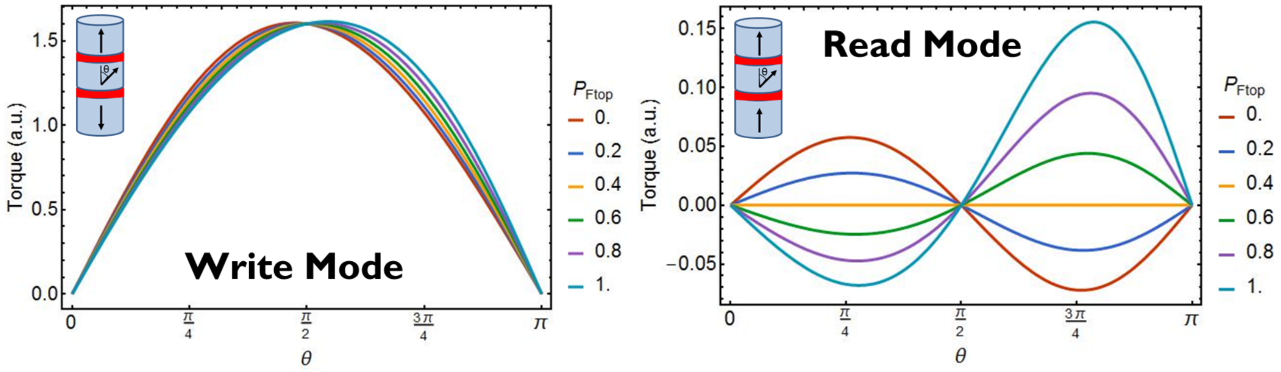

Figure 1.19: Evaluation of STT in (a) write and (b) read modes of operation. The torque was calculated for varying values of P_{Ftop} in an attempt of reproducing the effects of varying the RA of the top barrier relative to bottom one.

layers to a parallel state requires less current than the opposite transition. The same does happen when the top barrier is dominant ($P_{Ftop} > 0.4$) but now from an antiparallel state between control and free layers to a parallel state. The switching current are only equal when the barriers are symmetric ($P_{Ftop} = 0.4$).

In read mode, represented in Fig.1.19(b), the torques subtract thus the total torque is much weaker than in write mode despite the asymmetry between barriers (*i.e.* the value of P_{Ftop}). The full torque cancellation only happens when the barriers are symmetric ($P_{Ftop} = 0.4$), represented by the yellow curve in Fig.1.19(b). It is important to remember that the system only switches for positive torque values. Therefore, in read mode, there are some barrier symmetries that actually favor some specific states. For example, when the bottom barrier is dominant ($P_{Ftop} < 0.4$), the transition towards a full parallel alignment is favored against a transition towards a full antiparallel alignment of the free layer with the reference and control layers. For the case where the top barrier dominates ($P_{Ftop} > 0.4$) , the torque is up to 3x higher (case of $P_{ftop} = 1$) favoring a full antiparallel alignment between the free layer and the two polarizers.

Finally, D. Worledge [76] calculated the I_{sw0} of a DBMTJ, in write mode, by solving the LLG equation including the torque described by Eq.(1.35). For the $\hat{\theta}$ component, and considering for simplicity the case of a symmetric DBMTJ: $P_{Ftop} = P_{Fbot} = P_F$ and $P_R = P_C = P_P$ refers to the spin polarizations of the free layer (P_F) and both top and bottom polarizers (P_P) - the LLGS equation becomes:

$$\frac{1}{\gamma} m \frac{d\theta}{dt} = -\alpha E_b \sin 2\theta + \frac{\hbar}{2e} I \sin\theta \frac{2P_P}{1 - P_F^2 P_P^2 \cos^2\theta} \tag{1.39}$$

where γ is the gyromagnetic ratio, m is the magnetic moment of the free layer, α is the damping constant and E_b is the activation energy. By solving Eq.(1.39), two different switching currents for the p-DBMTJ depend on the product between P_F and P_P. For case where $P_F P_P < 1/\sqrt{3}$, the switching current is given by:

$$I_{sw}^{DBMTJ} = \frac{e}{\hbar} \alpha M_s t_F A H_k \frac{1 - P_F^2 P_P^2}{P_P} \tag{1.40}$$

where M_s, t_F and A are, respectively, the saturation magnetization, thickness and area of the free layer. For the case where $P_F P_P > 1/\sqrt{3}$ (spin torque oscillator state), the switching current becomes:

$$I_{sw}^{DBMTJ} = \frac{e}{\hbar}\alpha M_s t_F A H_k \frac{2}{3\sqrt{3}P_F P_P^2} \tag{1.41}$$

In order to assess the advantage of DBMTJ over single barrier MTJ, D. Worledge compares the switching currents of the two types of devices including the difference in switching current between P→AP and AP→P [14] in a single barrier MTJ. The results are shown in Fig.1.20.

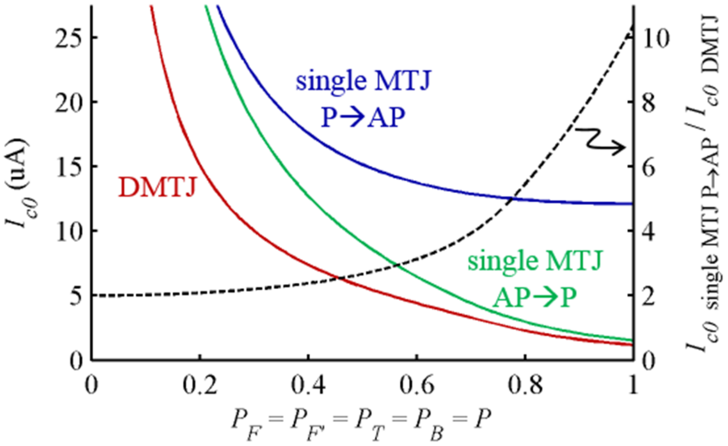

Figure 1.20: Comparison of I_{c0} (left axis) for single barrier MTJ P→AP, single barrier MTJ AP→P, and DMTJ, for E_b = 60 $k_B T$ at T = 300 K and α = 0.004. The blue P→AP curve is the criterion for use of the single barrier MTJ in MRAM, as the transistor must be sized to handle the larger of the two switching currents. The improvement factor (ratio of I_{c0} for the single MTJ to the DMTJ) is shown by the dashed curve (right axis), independent of E_b and α. Re-printed from [76].

Figure 1.20 shows that the DBMTJ provides an improvement factor up to 10 (for perfect polarizations $P = 1$) in reducing the critical switching current. In addition to sum torques coming from reference and control layers, DBMTJ set in write modes present another advantage in comparison to single barrier MTJ. Since the two polarizers have antiparallel magnetizations, one of these is always in the favorable AP configuration with the free layer. So, for whatever transition, the DBMTJ always benefits from the enhanced torque of the AP→P transition while the single barrier MTJ only profits from low switching currents for one transition. In Fig.1.20, it is visible that for very large spin polarizations, the single MTJ AP→P switching current approaches the switching current of the DBMTJ.

Despite the above mentioned study has been made for DBMTJ with perpendicular magnetization, the obtained results can be easily adapted for DBMTJ with in-plane magnetizations. Therefore, the critical switching current density (T = 0K) for this type of DBMTJ may be written as:

$$J_{sw0}^{DBMTJ} = \frac{2e\alpha M_s t_f (H + H_k + 2\pi M_s)}{\hbar} \frac{1 - P_F^2 P_P^2}{P_P} \tag{1.42}$$

In the case of the applied voltage pulses with large pulse width τ ($\tau > 10ns$), the thermal activation regime applies and the switching current density in a planar DBMTJ becomes:

---

[14] As a reminder the switching current in a single barrier MTJ for a P→AP is $I_{sw0}^{P\to AP} = \frac{e}{\hbar}\alpha M_s t_F A H_k \frac{2(1+P_F P_P)}{P_P}$, while the AP→P is given by $I_{sw0}^{AP\to P} = \frac{e}{\hbar}\alpha M_s t_F A H_k \frac{2(1-P_F P_P)}{P_P}$

$$J_{sw}^{DBMTJ}(\tau) = J_{sw0}^{DBMTJ}\left[1 - \frac{k_B T}{K_{eff} V} ln\left(\frac{\tau}{\tau_0}\right)\right] \tag{1.43}$$

In summary, the double barrier tunnel junction presents two major advantages. The write mode allows for a decrease of the writing current, mitigating the energy consumption of the device. While the read mode allows for a readout process performed at higher voltages corresponding to higher speed in accessing information.

The most relevant reports on spin torque in double barrier MTJ with in-plane magnetizations belong to Huai *et al.* [78] and Diao *et al.* [37] focusing mainly on the reduction of the critical switching current with antiparallel polarizers. In 2014 and 2015, Clément *et al.* [79, 80] have studied STT in both read and write operation modes in planar DBMTJs. Cuchet *et al.* [81] have demonstrated the first realization of a DBMTJ with perpendicular magnetization. More recently, IBM (by Hu *et al.* [40]) and Samsung (by Duan *et al.* [41]), have demonstrated STT switching in perpendicularly magnetized DBMTJ (with $TMR > 100\%$) where critical switching currents were found to be 2x lower than in comparable single barrier perpendicular MTJs.

2

Nanofabrication Process

Contents

2.1 Introduction

In this chapter, the fabrication steps necessary to transform a full sheet DBMTJ into patterned devices are described in detail. The DBMTJs used for fabrication were initially deposited by magnetron sputtering using two different physical vapor deposition tools: *Timaris* (in-plane DBMTJs) and *Actemium* (perpendicular DBMTJs). The DBMTJ samples were deposited on 50mm silicon wafers with 500μm of thermal SiO$_2$.

In summary, the main technological steps to fabricate DBMTJ pillars of nanometric size are the following:

- Electron beam lithography to define pillars with diameters below 800nm;
- Optical lithography to design the larger patterns (ex. bottom and top contacts);
- Physical and chemical etching to transfer the designs made by lithography into the thin films;
- Deposition of hard mask, planarization and contact metalization;
- In between steps, the process control inspections are made using optical microscope, scanning electron microscope (SEM) and profilometer to measure the different layers thicknesses;

2.2 Pillar E-Beam Lithography

For the electron beam (e-beam) lithography of the nanometric pillars (circles or ellipses) a positive resist (PMMA) is used, meaning that the exposed resist is removed after development. For this reason, and to act as a protective layer while etching the pillar, an hard mask is deposited after the DBMTJ deposition. This hard mask is defined by a thin Ru layer of 7 nm and thicker layer of 150 nm of Ta. Tantalum was chosen since it is a material easily etched by SF$_6$-based plasma, whereas the Ru acts as a stopping layer.

After the hard mask deposition, the wafer is coated with electron sensitive positive resist - PMMA - with an overall thickness of 80 nm, which is baked at 180°C for 5 minutes. Following the PMMA coating, the sample is placed inside an e-beam tool [Fig.2.1(a)] - *JEOL 6300 FS* - with a field emission source gun, enabling the design of features with lateral resolution inferior to 20 nm. In fact, two sets of pillar sizes were used, respectively, for in-plane and perpendicular DBMTJs. For planar DBMTJs, the devices have two types of cross section geometries - circular and elliptical. The pillars with circular cross sections have nominal diameters of 80 nm, 100 nm, 200 nm and 1 $\mu\mathrm{m}$. While the ellipses have nominal axes dimensions of 40 nm x 140 nm. In the case of perpendicular DBMTJs, shape anisotropy is negligible therefore only pillars with circular cross sections were defined with the following nominal diameters: 40 nm, 50 nm, 80 nm, 100 nm, 200 nm and 300 nm. As represented in Fig.2.1(b), after the exposure and development of the PMMA, 20 nm of Cr are deposited by electron beam physical vapor deposition. This step is completed by a lift-off with acetone [Fig.2.1(c)] which allows for the Cr to remain only on the empty spaces without PMMA and to serve as protective layer of the pillar hard mask.

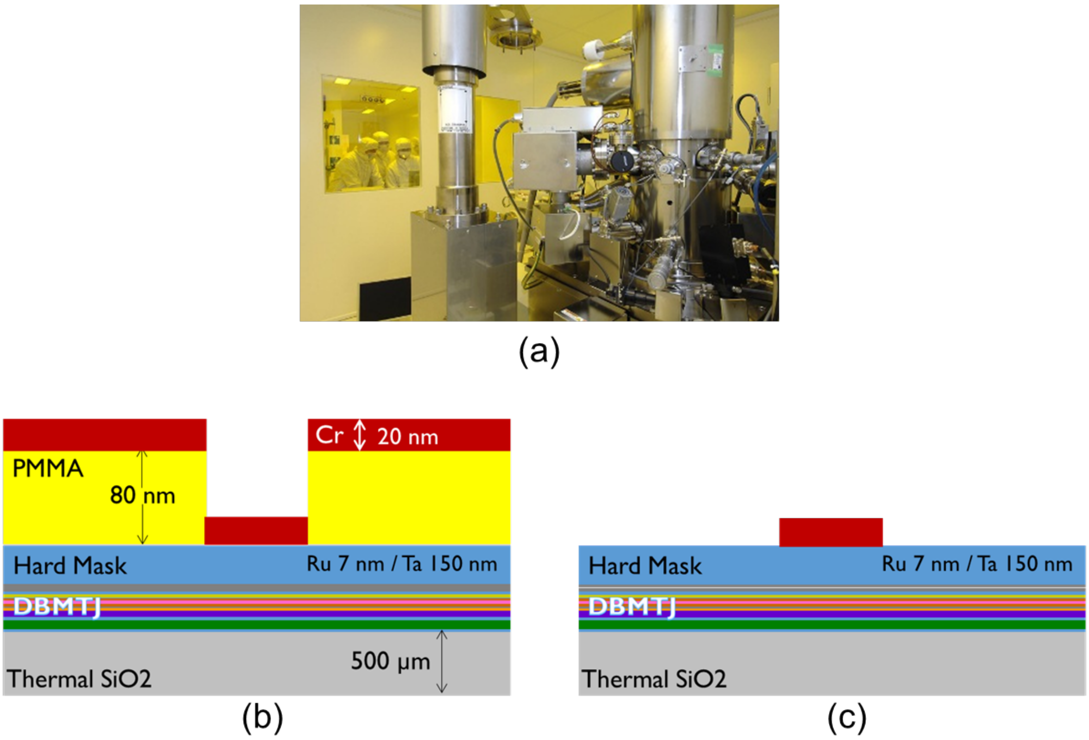
(a)

(b) (c)

Figure 2.1: (a) E-Beam Lithography tool - *JEOL 6300 FS*. (b) Deposition of the 20nm Cr layer after e-beam lithography of the nanopillars. (c) Lift-off.

2.3 Pillar Etch

The first etch step of the process is the hard mask etching using reactive ion etching (RIE). This step is performed in a *ICP STS Multiplex* tool, where a plasma composed of Ar and SF_6 is used to etch selectively the Ta of the hard mask. The evolution of the etched thickness is monitored with an endpoint detection system which tracks the reflectivity of laser signal. The Ru layer serves as stopping point for the RIE. As represented in Fig.2.3(a), the shape of the hard mask will define the structure of the DBMTJ pillar in the following etch step. In this step, the etching time is rather critical since it will define the shape and dimensions of the pillar. Figure 2.2(a) and (b) present SEM pictures of the pillars with an underestimated etching time (under-etch) and overestimated etching time (over-etch), respectively. In the case of the under-etched pillars (residues of Ta still observable at the surface), the pillars have a more conic shape. Although at the top the measured size fits the nominal size, at the base of the pillar the diameter is roughly two times larger and the latter defines the size of the pillar. On the other hand, an over-etched pillar has ”mushroom” shape i.e. is slightly larger at the top than at the bottom, with a diameter at the base inferior to the e-beam lithography nominal value. One of the advantages of over-etching is to reduce the risk of Ta redeposition on the pillar sidewalls. However, and specially for nominal diameters below 30 nm, a too large over-etch may lead the collapse of the pillars. Therefore, a compromise on the RIE time must be found in order to obtain well defined pillars.

After having defined a pillar within the hard mask layer, we proceed to etch the DBMTJ multilayers. Since the DBMTJ is composed of layers of very different materials, the use of a selective etching technique, as RIE, is extremely challenging. Therefore, the etching technique used is Ion Milling, in *IBE*

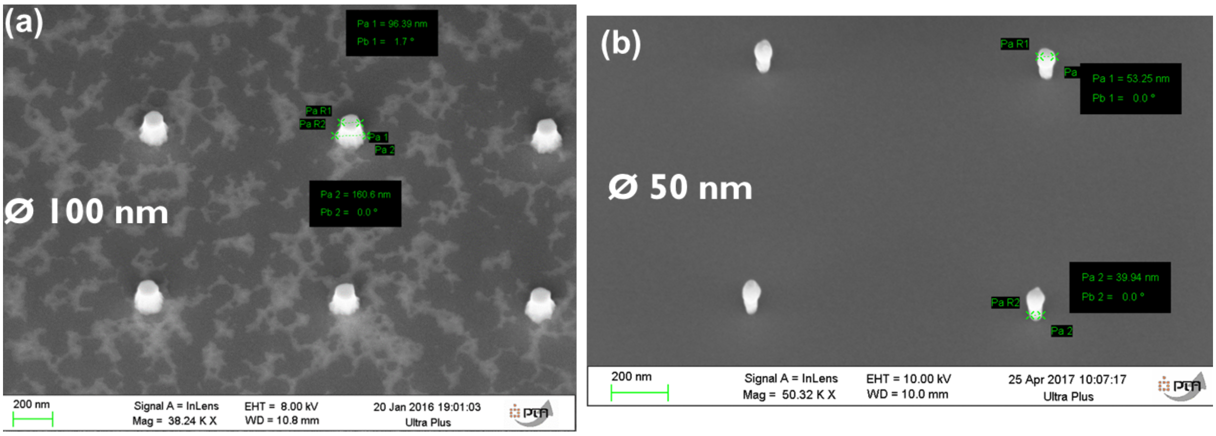

Figure 2.2: SEM images of (a) 100nm nominal diameter pillars with an insufficient etch time and (b) 50nm nominal diameter pillars with over-etch, after hard mask etching by RIE.

Plassys MU400 and *SCIA Mill 150* tools, where Ar ions bombard the junction removing all materials indiscriminately. In this tools, an argon plasma is generated via an RF source and it is accelerated towards the sample with a determined incidence angle. The etching process is controlled through Secondary Ion Mass Spectroscopy (SIMS) to detect the extracted materials. The etching angle and the stopping point can thus be monitored as a function of the etching progress.For the in-plane DBMTJs used in chapter 3, we have chosen a two angles approach for the pillar etch. Following the sketch in Fig.2.3(b), we used an initial high incidence angle (20° from the normal to the film plane) until the first MgO barrier in order to have a straight pillar. Then we increased to a 45° etch angle and stopped around the middle of the PtMn layer (bottom antiferromagnet). At 45°, the etching rate decreases but avoids redeposition of material on the pillar sidewalls which may cause short-circuit of the MgO barriers. The downside is the shape of the pillar that becomes more conic instead of cylindrical.

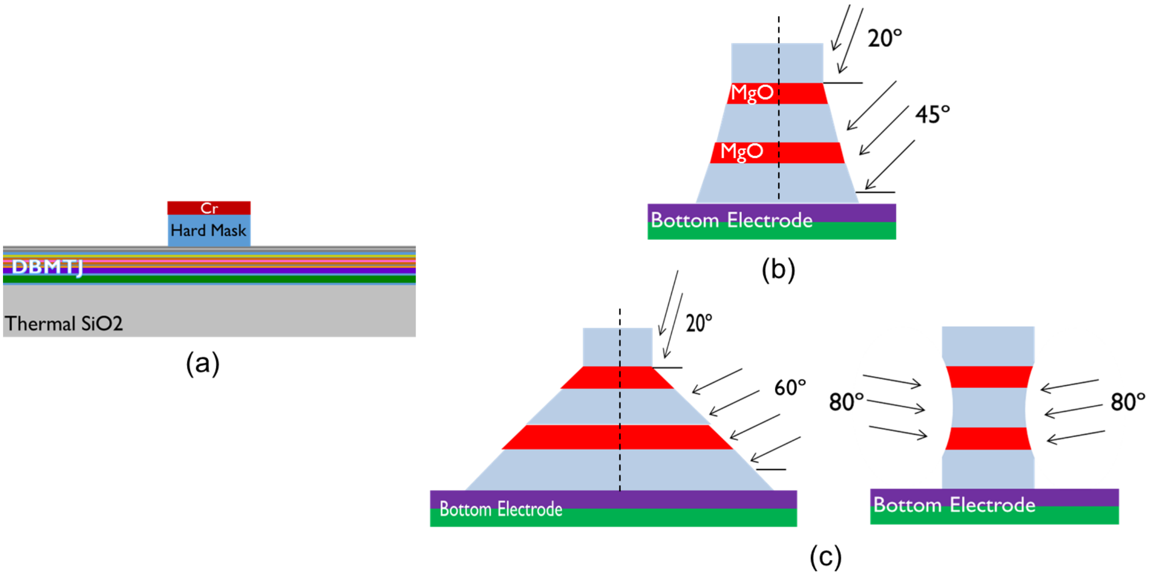

Figure 2.3: (a) Illustration of the hard mask pillar after RIE. Ion Beam Etching of the pillars for (b) an in-plane DBMTJ with two successive incidence angles (20° and 45°) and for (c) perpendicular DBMTJ also with a two angles (20° and 70°) approach followed by a trimming at 80°.

For the perpendicular DBMTJs used in chapter 5, we have improved the etching process with two main goals: reduce sidewall redeposition and minimize the difference between the pillar nominal and real diameter. The initial angle is the same (20°), increasing to 60° before reaching to the first (top) MgO barrier, as showed in Fig.2.3(c). Even though sidewall redeposition is reduced to a minimum, the shape of the pillar becomes conic with a base much larger than the top. In order to mitigate this problem (and also to completely remove any redeposited material), a final etch at an angle almost parallel to the film plane (80°) for about 30s, trims the junction. This trimming technique has already been used before [82] with good results. In fact, depending on the etching time used for the trimming step, the pillar real diameter can be smaller than the nominal diameter, though the shape of the junction becomes similar to an hourglass [right side sketch in Fig.2.3(c)].

2.4 Definition of Bottom Electrode

After having defined the DBMTJ pillars, it is necessary to define their electrodes in order to contact the pillar for posterior electric measurements at a macroscopic scale. In our process, we begin by the definition of the bottom electrode. Since the contacts which enable access to the electrodes are several times larger $(10^2 \mu\mathrm{m})$ than the nanometric size pillars, sub-$\mu\mathrm{m}$ resolution is not needed. For this step, optical lithography replaces the e-beam lithography. The resist used for the optical lithography is a positive resist (*AZ 1512*, 1.3 $\mu\mathrm{m}$). The exposure of the resist is performed in a mask aligner *MJB4* under UV light (λ = 365 nm) for approximately 25s. After exposure, we perform a development that removes the exposed resist, ending up with a pattern similar to Fig.2.4(a).

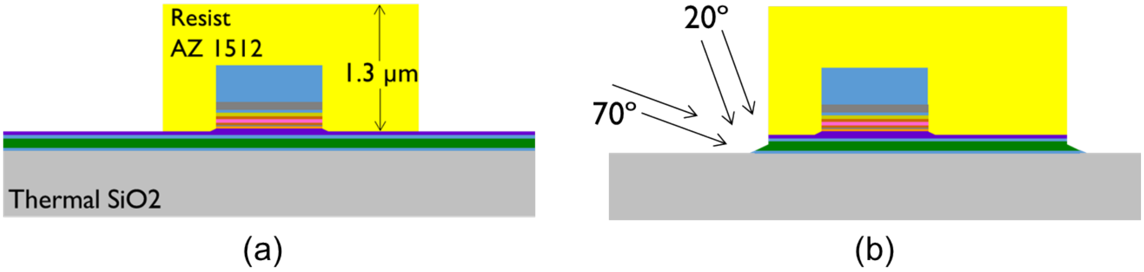

Figure 2.4: (a) Optical lithography of the bottom electrode. (b) Two angle (20° and 70°) approach ion beam etch of the bottom electrode.

Having the pillar protected by the resist, we perform a second etching that removes the remaining material down to the thermal oxide. Here, two different methods were used. For all the in-plane DBMTJs and for some perpendicular DBMTJs, we etched the bottom electrode with Ion Beam Milling, in a two angles approach. As depicted in Fig.2.4(b), a first angle of incidence of 20° was used and finally when already etching the last metallic layer before the thermal SiO_2, the angle is changed to 70° in order to remove redeposited material. An over-etch in the thermal oxide is intended so each DBMTJ device is electrically insulated from the others. An alternative approach was used to etch the bottom electrode of perpendicular DBMTJs. This method used RIE instead of Ion Beam Milling to etch the bottom electrode materials. The recipe, which contains a SF_6 and CHF_3-based plasma, has been optimized by N. Perrissin *et al.* [83] in order to etch Pt along with the other materials from the bottom electrode as Ta or W. This method avoids the problem of redeposition and the lateral features of the bottom electrode are also improved.

2.5 Pillar Passivation

In MTJs, the applied current travels perpendicularly to the films planes. Therefore, electrical contacts are needed on bottom and top electrodes. In order to define the top electrode without causing a short-circuit with the bottom electrode, we need to insulate the DBMTJ pillar. For this purpose, we used a spin-on polymer named *Accuflo*®with a superior thermal stability, reduced viscosity and reduced interfacial surface tension to enhance coating properties. The spin coating of the *Accuflo* on top of the sample is followed by three consecutive baking at different temperatures: 120°C, 180°C and 250°C [1]. The spin coating conditions are optimized so that the *Accuflo* layer thickness (∼400 nm) is much larger than the DBMTJ pillar height. An optical lithography is then performed in order to provide access to the bottom electrode, as represented by the sketch in Fig.2.5(a).

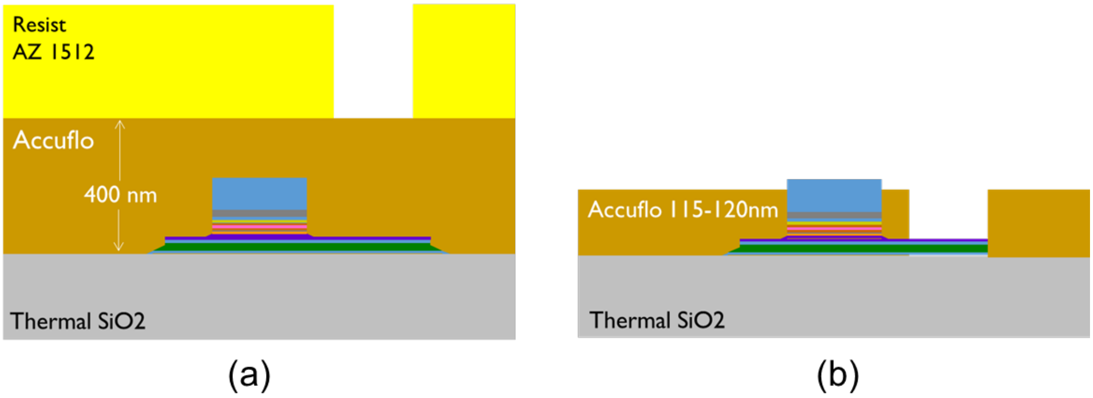

Figure 2.5: (a) Optical lithography after the spin coating of the planarizing polymer *Accuflo*. (b) Etching of the via to the bottom electrode followed by *Accuflo* thinning by RIE.

After lithography, a first reactive ion etching step using an oxygen plasma is performed to remove all the *Accuflo* not protected by the resist. This resist is later removed by acetone. Since the pillar is buried under the *Accuflo* layer, it is necessary to undergo a series of controlled RIE [2] steps carefully interleaved by *Accuflo* thickness measurements on a profilometer. The final *Accuflo* thickness should lay between 115 - 120 nm in order to reveal the top part of the pillar [Fig.2.5(b)] without compromising the encapsulation of the oxide barriers. In general, this step is considered to be very critical, with two undesired possible scenarios. If the final *Accuflo* thickness is larger than 120 nm, the pillar remains buried within the insulating polymer and the electrical test of the device will result in an extremely high resistance (open-circuit). Alternatively, if the final *Accuflo* thickness is much lower than 115 nm, the oxide barriers may be exposed and the electric characterization of the device will result in a very low

---

[1] Notice that, for in-plane DBMTJs, these temperatures are higher than the FeMn blocking temperature. It is necessary to perform additional annealings under magnetic field after device fabrication, in order to set the FeMn exchange.

[2] The RIE does not affect the bottom electrode since the stopping layer after the pillar ion milling is either Pt, PtMn or Ta which are not affected by the oxygen plasma unlike other materials like CuN or Ru.

resistance (short-circuit).

2.6 Definition of Top Electrode and Contacts Metalization

The last steps of the process are needed to define the top electrode and to metallize the electrical contacts (bottom and top). Optical lithography is performed to design the pattern of the top electrode. Then, a bilayer of 10 nm of Cr and 300 nm of Al is deposited using an electron beam evaporator, preceded by a soft etch to clean the surface and improve the adhesion of the metallic layer [Fig.2.6(a)].

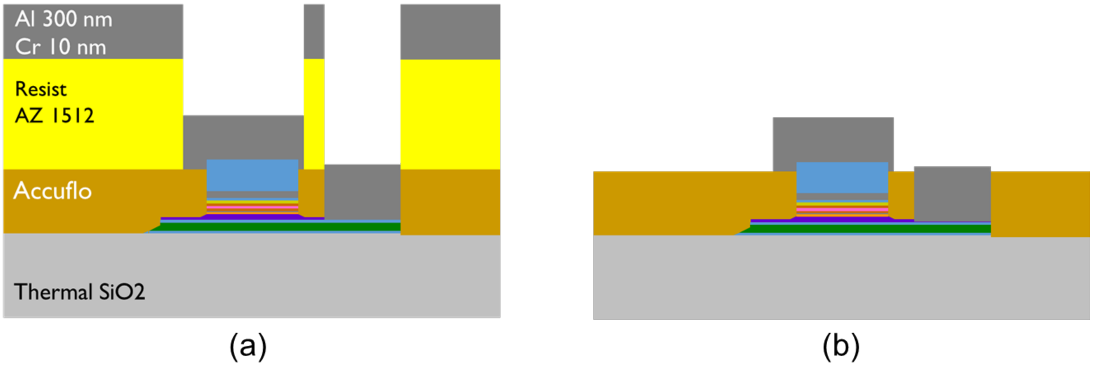

Figure 2.6: (a) Top electrode optical lithography and metallization of the top and bottom contacts. (b) Lift-off.

The device is finalized after lift-off with sample immersed into acetone in an ultrasound bath. The completed device is represented in Fig.2.6(b).

2.7 Electrical Characterization - Wafer Mapping

Once the DBMTJ wafers are processed, they undergo electrical characterization in order to check two of the most important features of MTJs: RA and TMR. Usually samples are characterized in the magnetic configuration that presents higher TMR. Therefore, our DBMTJs [3] are characterized in read mode (parallel alignment of both references). In the case of the in-plane DBMTJs, annealing under applied magnetic field is crucial to set the direction of the top reference (FeMn) which was lost during some high temperature fabrication steps. For the perpendicular DBMTJs, usually a saturation under a very strong magnetic field is also recommended to set well the parallel alignment of the two polarizers magnetizations.

The electrical characterization of the wafers can be performed with two fully automatic measurement wafer probe stations: one with an electromagnet which applies magnetic field parallel to the plane of the wafer (x-y directions) and the other which applies field in a direction perpendicular to the plane of the wafer (z direction). These automatic probe stations allow to measure the resistance as a function of the applied field [R(H)] of each individual device on 50mm and 100mm diameter wafers.

This characterization method enables to map a full wafer and verify swiftly the quality of the fabrication process. Figure 2.7 shows an example of wafer mapping (of a p-DBMTJ) in which the selection

---

[3] The stacks of the in-plane and out-of-plane DBMTJs are described, respectively, in chapters 3 and 5.

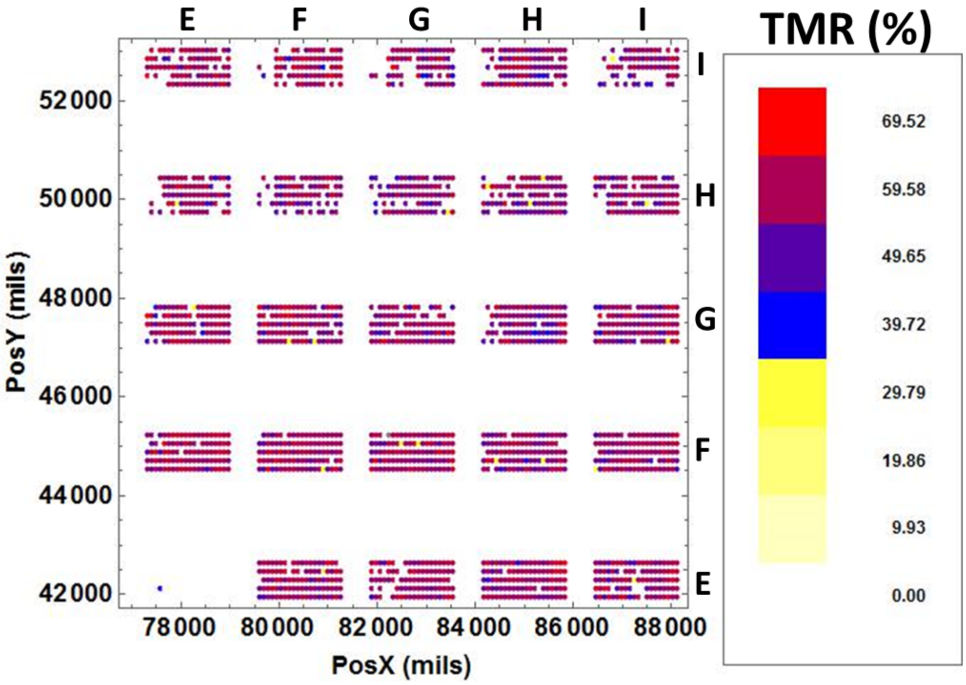

Figure 2.7: Wafer mapping of a p-DBMTJ 50mm wafer. The color scale represents TMR. The yield of the wafer was 80%, considering $25\% \leq \mathrm{TMR} \leq 100\%$.

criterion is TMR. Other type of analysis can also be done based on the results provided by the automatic tester. Figure 2.8 shows the relationship between RA and TMR for devices with different diameters. The example shown corresponds to successfully fabricated wafer where TMR does not change with small variations of RA (mostly due to difference between nominal and real device diameters). A good wafer presents a yield of working junctions of 80%. The data of figs.2.8 and 2.8 was obtained from a wafer whose stack is of a p-DBMTJ with a thicker bottom barrier. For this particular example of a successful wafer, RA (average ± 1σ) is of 59 ± 11 $\Omega.\mu m^2$ and a 19% 1σ uniformity across the wafer. In addition, TMR (average ± 1σ) is 57 ± 5 % with a 9% 1σ uniformity across the wafer.

For information, the typical behaviors of poor quality devices with signs of sidewall redeposition (black dashed line) and parallel resistance (red dashed line) are shown in the same figure. While the first problem is mostly associated with less successful physical etch of the nanopillars, the second behavior is a clear sign of insufficient thinning of the *Accuflo* layer and imperfect connection to the pillar. These fabrication issues were the main reasons the 50% success rate of the wafers fabricated during the thesis.

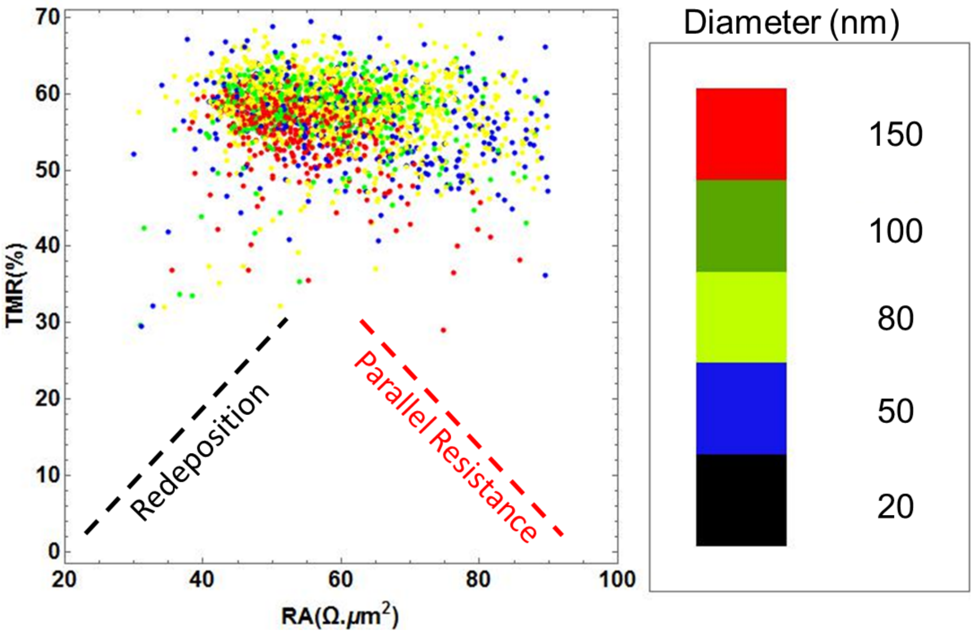

Figure 2.8: TMR vs RA of p-DBMTJ 50mm wafer for various pillar nominal diameters (color scale). Two undesired trends are represented for the case of sidewall redeposition (black dashed line) and parallel resistance, due to incomplete *Accuflo* thinning (red dashed line).

3

Spin transfer torque in double barrier tunnel junctions with in-plane anisotropy

Contents

3.1 Introduction

3.1.1 MTJ Stack

In order to get a better insight on the behavior and interplay of spin transfer torques in double barrier structures, double magnetic tunnel junctions with an identical magnetic stack but different RAs were deposited. The general magnetic stack with the used materials and respective thicknesses are shown in Fig.3.1. The free layer (in green in Fig.3.1), also referred as the storage layer, has its magnetization free to rotate as response to an external magnetic field (or spin transfer torque in our case). It is also the layer responsible for storage of the information in the memory dot. The bottom reference layer (in light blue in Fig.3.1) is part of a SAF whose pinned layer (CoFe) magnetization direction is set by exchange coupling with an antiferromagnet (PtMn) with a high blocking temperature (T_B). PtMn blocking temperature (T_B^{PtMn}) is slightly inferior to 300°C, which means that an annealing at a minimum temperature of 300°C is necessary to break this exchange coupling. The top reference layer (in yellow in Fig.3.1), also referred as control layer, is integrated in a similar SAF as the bottom reference layer, though the anitferromagnet which sets the SAF pinned layer magnetization direction has a low T_B. The chosen antiferromagnet is FeMn which has $T_B^{FeMn} \approx 100°C$ [84]. The T_B difference between the bottom and top antiferromagnets allows to unblock only the exchange bias of the control layer without affecting the reference layer. By performing an annealing at temperatures between 180 - 220°C and then cooling down under a 1T applied magnetic field, it is possible to change the direction of the magnetization of the top reference layer without changing the one of the bottom reference layer. Therefore, the bottom reference layer has the status of primal reference layer since it has a higher exchange bias field and it is thermally more robust. The top reference is the control layer since by annealing under magnetic field is possible to choose the direction of its magnetization. The aforementioned process is the one that allows to change the DBMTJ from read to write mode, and *vice-versa*.

This DBMTJ structure has two oxide barriers whose electrical properties can be individually tuned, namely their *RA* and their magnetoresistance *MR*. In this chapter, DBMTJ structures with symmetric and asymmetric barriers are studied. Symmetric barriers structures have equal nominal RA for bottom and top barriers ($RA_B = RA_T$) and asymmetric barriers structures can be of two types, according to the position of the thicker barrier: top barrier thicker ($RA_B < RA_T$) and bottom barrier thicker ($RA_B > RA_T$). Table 3.1 shows the nominal RA values [1] for the DBMTJs studied in the following sections.

Table 3.1: List of the types of in-plane DBMTJs used in this chapter with nominal RA values for each barrier.

Sample	Type of barriers	RA_T ($\Omega.\mu m^2$)	RA_B ($\Omega.\mu m^2$)
E5541	Symmetric thick barriers 1	45	45
E5545	Asymmetric bottom thick barrier	10	35
E5546	Symmetric thin barriers 2	10	10
E5547	Asymmetric top thick barrier	35	10

---

[1] RA values are always defined for parallel alignment of the magnetization of the electrodes.

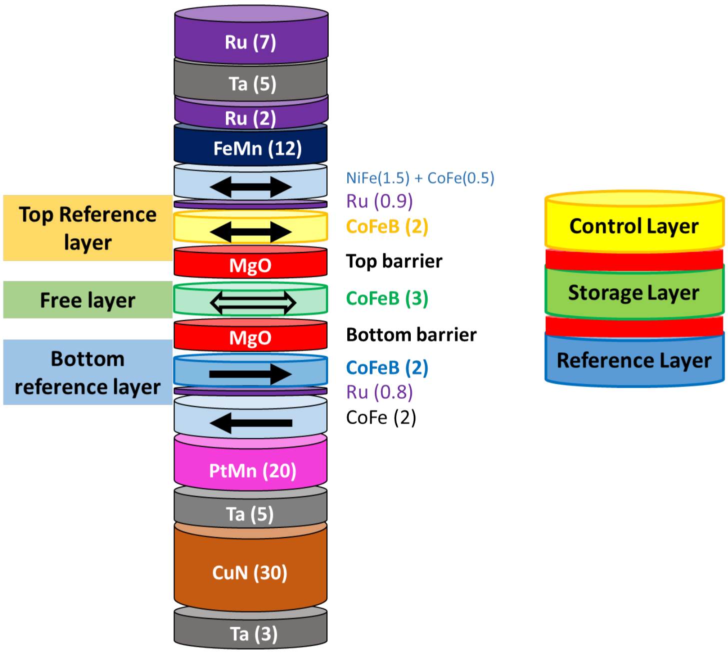

Figure 3.1: Illustration of the general magnetic stack for the in-plane magnetized DBMTJs used in this chapter. The thickness of each layer is given inside ( ) in nm. The standard tri-layer structure of the DBMTJ (Reference layer/Free layer/Control layer) is also highlighted. The MgO barriers are titled as bottom and top with respect to their proximity to the bottom and top references. The nomenclature *top* and *bottom* is the one chosen for the oxide barriers throughout the manuscript, so no confusion may arise.

3.1.2 Setting of two magnetic configurations

As mentioned in section 1.5.4.C, two modes of operation, *write* and *read* [79], are possible in double barrier MTJs. As a matter of fact, a certain sequence of annealings is necessary to attain the desired magnetic configurations of the two references. Upon deposition of the magnetic stack, a first annealing at 300°C is performed to break the exchange coupling of both PtMn and FeMn. The sample is then cooled down under a magnetic field of 10 kOe that will set in the same direction the magnetizations of both ferromagnets at the interface with PtMn and FeMn layers. Therefore, the reference layers (in blue and yellow in Fig.3.1) will have their magnetizations in parallel alignment and in the opposite direction with respect to the pinned layers, due the antiferromagnetic RKKY coupling within the SAF [2]. The unpatterned sample is then set in *read* mode as both reference layers' magnetizations are parallel to each other. As the sample is subjected to temperatures up to 250°C during nanofabrication, T_B^{FeMn} is exceeded, unpinning the top SAF. Thereupon, and as explained in the section above, a second annealing is mandatory to set both references in a parallel (*read* mode) or antiparallel (*write* mode) configuration.

The resistance (R) vs. applied field (H) loop represented in Fig.3.2(a) shows one symmetric barriers DBMTJ in read mode. The hysteresis loop of the free layer is nearly centered around zero field, with a very small offset field (≈ -10 Oe). At much larger positive field ($\approx +500$ Oe), the Zeeman energy overcomes the RKKY coupling energy and the magnetizations of the top SAF are no more in antiparallel alignment: this new configuration of the control layer magnetization induces a decrease of resistance.

---

[2] A Synthetic AntiFerromagnet (SAF) is composed of two ferromagnetic layers separated by a thin metallic layer (often Ru); the coupling between layers is chosen to fix the magnetizations in antiparallel alignment.

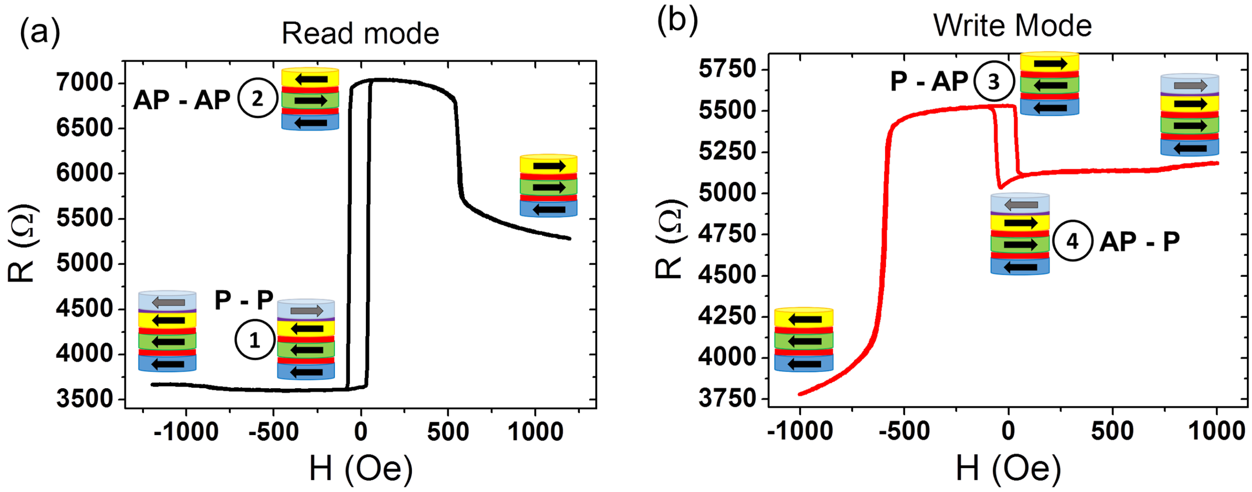

Figure 3.2: Resistance vs. applied field loop for a symmetric barriers double junction, whose nominal dimensions are 40 x 140 nm, set in (a) read mode (parallel references) and (b) write mode (antiparallel references). Acquired at a bias current of $1\mu A$. The inset illustrations show the different configurations of the magnetizations of the tri-layer structure for different values of the applied field. The top pinned layer (in light blue) is added to show the rotation of its magnetization when the Zeeman energy overcomes the exchange coupling energy.

Similarly, at sufficiently large negative applied fields (≈ -1000 Oe), the exchange coupling is broken, allowing the pinned layer to rotate. This transition is associated with a slight increase in resistance. As the DBMTJ is set in write mode [Fig.3.2(b)], free layer offset and transition fields change sign.

Thus, there are a total of four distinct magnetic states (see Fig.3.2): 1) free layer is parallel to both references (P - P), 2) free layer is antiparallel to both references (AP - AP), 3) free layer is parallel to bottom reference and antiparallel to top reference (P - AP) and 4) the opposite state (AP - P). The RA product of these four states can be translated in four equations, which are described by the following system:

$$\begin{cases} RA_1 = RA_B + RA_T \\ RA_2 = RA_B(1+TMR_B) + RA_T(1+TMR_T) \\ RA_3 = RA_B + RA_T(1+TMR_T) \\ RA_4 = RA_B(1+TMR_B) + RA_T \end{cases} \tag{3.1}$$

in which RA_n is the resistance-area product of the DBMTJ in #n magnetic state, TMR_B and TMR_T are the tunnel magnetorestiance of bottom and top barriers, respectively. These equations allow the determination of the RA and TMR of each barrier individually which is important to ensure that the properties of the DBMTJ upon deposition have not significantly changed after patterning. In spite of having four unknowns (RA_B, RA_T, TMR_B and TMR_T) and a system of four equations, one of these parameters needs to be known *a priori* since one of the four equations can be obtained by a linear combination of the others. The margin of error for the parameters extracted by equations 3.1 depends on the accuracy of the pre-determined variable and the estimation of the lateral dimensions of the pillar. These parameters can also be retrieved by fitting the data obtained via current-in-plane-tunneling (CIPT) with a mathematical model developed specifically for double barrier MTJs [85, 86].

3.1.3 Junctions characterization

In this subsection, a characterization of the magneto-transport properties of the symmetric and asymmetric barriers DBMTJs is presented. The objective of this summary is to describe the different types of DBMTJs used for STT studies described in sections 3.2 and 3.3.

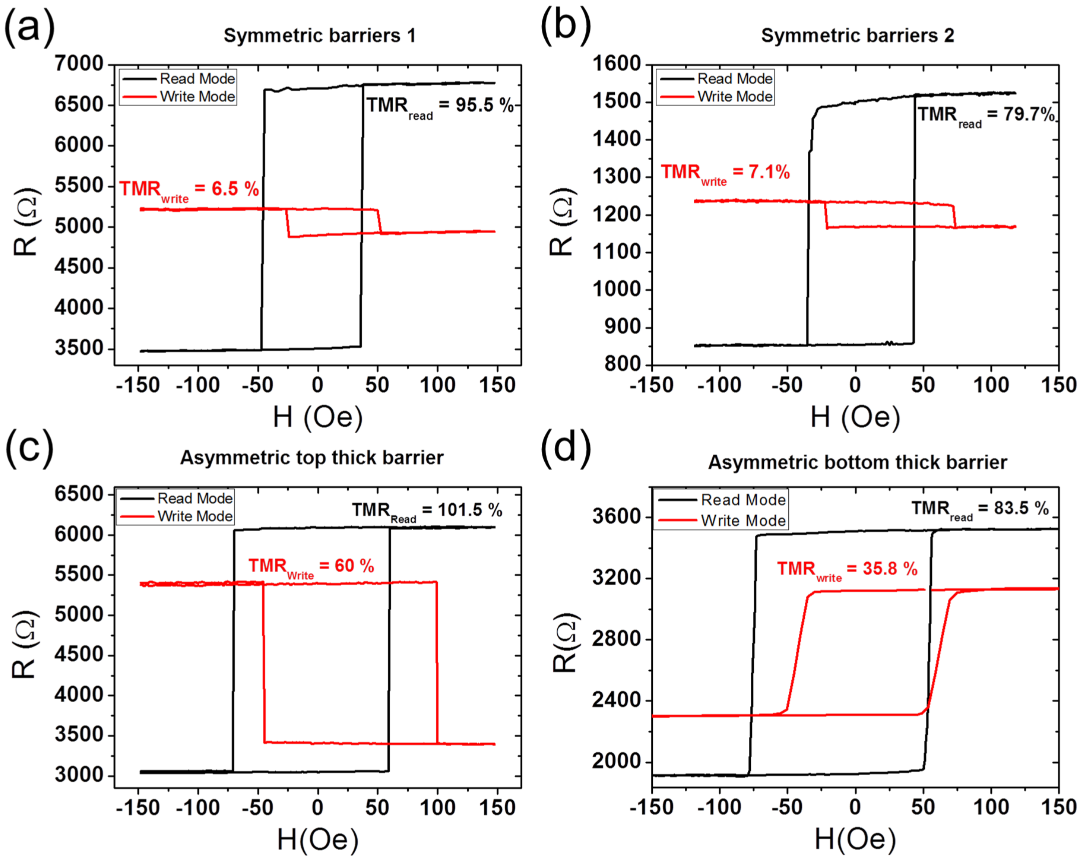

Figure 3.3: Resistance vs applied field loops of typical devices representing the four types of DBMTJs in read (black curve) and write (red curve) modes: a) symmetric thick barriers, b) symmetric thin barriers, c) asymmetric barriers: top thick barrier and d) asymmetric barriers: bottom thick barrier. The RA values can be consulted in table 3.1. All four devices are ellipses with lateral nominal dimensions of 40 × 140 nm. The TMR values are represented in the color associated with the respective mode.

Figure 3.3 shows the R(H) loops for typical devices of the four types of DBMTs studied. As expected for all cases, the TMR in read mode is larger than in write mode since it is the only mode where the free layer is antiparallel to both references. Although the values presented represent one single device, it has been chosen out of a 50mm wafer with more than 4000 working devices. From a complete wafer mapping, we have extracted the average values of TMR in read mode for each type of DMTJ: 95 ± 20 % for symmetric thick barriers, 66 ± 27 % for symmetric thin barriers, 82 ± 29 % for asymmetric top thick barrier and 86 ± 21 % for asymmetric bottom thick barrier. These values are close to those reported for other DBMTJs [39, 87, 88], but still lower than state-of-the-art single barrier MTJs [38]. According to references [39] and [38], the lower TMR is due to a lack of crystallization of the CoFeB free layer between the two MgO barriers. Since there is no boron getter, boron migrates towards both MgO barriers: boron oxide is probably formed at the barrier edge and the presence of boron prevents crystallization in the vicinity of both barriers, thus reducing the TMR. The TMR in write mode is variable since the free layer is on a hybrid state relatively to the two references and thus the situation is very different for symmetric or asymmetric barriers structure. The TMR in write mode is given by the difference in resistance (ΔR) between #3 and #4 states [see Fig.3.2(b)], $\Delta R_{3-4} = R_T TMR_T - R_B TMR_B$, divided by the resistance of the state with lower resistance. In the case of asymmetric barriers DBMTJ [see figs.3.3(c) and (d)] the values of TMR_{write} are large since $RA_T \neq RA_B$. For symmetric DBMTJ, no TMR should be observed in write mode ($\Delta R_{3-4} = 0$), if the barriers were perfectly symmetric ($RA_T = RA_B$ and $TMR_T = TMR_B$). However, a small asymmetry is observed in nominally symmetric barriers that accounts for the small TMR observed (6-7 %). It can be explained by the difference in growth conditions of the top barrier with respect to the bottom one. Therefore, it is of particular importance to calculate the individual RA and TMR of each barrier to ensure the comprehension of the results observed for the current induced spin transfer torque switching in these structures. Table 3.2 presents the calculated parameters of top and bottom barriers for each junction of Fig.3.3, using the system of equations 3.1. Since in the system only 3 equations are independent, one of the parameters needed to be set *a priori*. R_T was the parameter set with its nominal value because, according to [39] and also observed by P.-Y. Clément [1], the top barrier has superior texture quality than the bottom barrier [3]. Despite the general amorphous state of the CoFeB in the free layer, at the interface with the top barrier lattice planes are formed, promoting a better texture and favoring the (001) orientation of the MgO. Consequently, top barrier should have RA values closer to nominal [4] and a better TMR.

In the case of the two symmetric barriers structures, though perfect symmetry was not achieved, the two barriers have very similar RAs (difference below 5 $\Omega.\mu m^2$) which translates in the very low TMR of these DMTJs in write mode. It is also noticible that the top barrier has a slightly higher RA and TMR than the bottom barrier. For the two asymmetric barriers structures, the obtained values for RA are in most agreement with barriers nominal values. However, for the structures with thicker bottom barrier, we observe that $TMR_T > TMR_B$, whereas the thicker barrier was expected to have the larger TMR. If we take into account the above mentioned higher crystalline quality of the top barrier, then the difference in TMR of a barrier with same nominal RA (10 $\Omega.\mu m^2$) above or below the free layer might be explained. While the same barrier has a TMR of 94 $\%$ when grown on top of the free layer, it reduces down to 42$\%$ when grown below it.

Table 3.2: Calculation of RA and TMR for each individual barrier for the devices exhibited in Fig.3.3. RA_T was the parameter chosen to remain fixed. The lateral dimensions taken into account for the calculation were 140 $\times$ 220 nm since the pillar has a conical shape due to the angle used during IBE etch.

Type of barriers	RA_T **($\Omega.\mu m^2$)**	RA_B **($\Omega.\mu m^2$)**	TMR_T **($\%$)**	TMR_B **($\%$)**
Symmetric thick barriers	45	42.3	96.8	90.5
Asymmetric bottom thick barrier	10	36.3	94.5	80.5
Symmetric thin barriers	10	9.4	80.2	75.5
Asymmetric top thick barrier	35	12.8	104.7	42.5

---

[3] This is just an assumption since only TEM analysis of a the DBMTJ vertical cross section would help to support this statement. However, one hypothesis lies on the possibility of better growth of the top barrier since the FL CoFeB layer (3 nm) is thicker than the CoFeB layer (2 nm) of the bottom SAF below the bottom MgO barrier.

[4] Note that this statement cannot be supported by the CIPT measurements for barriers with RA values so close to each other, since the error margin is too large.

3.2 DC current measurements

In this section, a first set of measurements, performed using DC current, were conducted to study the current-induced spin transfer torque in the double barrier MTJs. Here the behavior of STT was analyzed for symmetric and asymmetric barriers structures, focusing on the two different modes of operation: *Write* and *Read*.

The experimental setup was composed of a pair of Helmholtz coils, fed by a Kepco power source, with a maximum applied magnetic field of 200 Oe with a precision of 1 Oe and a Keithley multimeter connected to four probes. The measurements were made using four points: two for applying current and the other two to measure voltage [see Fig.3.4(a)]. Figure3.4(b) presents an illustration of the electron flow direction for each current polarity.

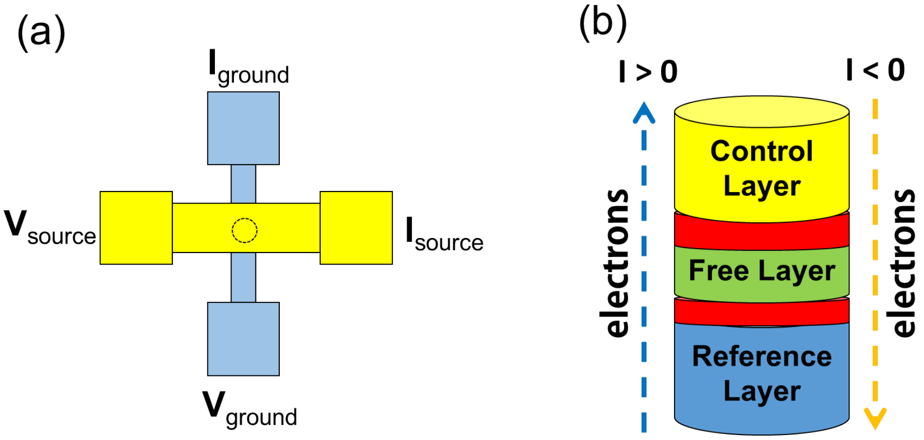

Figure 3.4: (a) Schematic of the four point measurement. (b) Representation of the direction of the electron flow through the tri-layer structure: from reference to control layers for positive current ($I > 0$) and on the opposite direction for negative current ($I < 0$).

The experiments consisted on measuring resistance as a function of dc current for specific values of applied field, since a change in resistance is proof of the current induced switching of the free layer. Therefore, for each value of applied field and initial magnetic state, two different kinds of current sweeps were performed: *decreasing* and *increasing* sweeps. *Decreasing* sweeps are defined by applied current that starts from zero and decreases towards maximum negative current ($0 \rightarrow -I_{max}$), then increases towards maximum positive current ($-I_{max} \rightarrow +I_{max}$) and returns back to maximum negative current ($+I_{max} \rightarrow -I_{max}$). While the *increasing* sweeps are similar but starting from zero towards positive maximum current, described in a nutshell as $0 \rightarrow +I_{max} \rightarrow -I_{max} \rightarrow +I_{max}$.

3.2.1 Write Mode

3.2.1.A Asymmetric barriers: top thick barrier

The asymmetric double barrier junction is set with its polarizers' magnetizations antiparallel to each other. Figures 3.5 and 3.7 present examples of the resistance vs. current $R(I)$ measurements performed in selected devices with elliptical and circular shapes, respectively. The $R(H)$ loops at the center of the images have markers (black and green colors) indicating the applied field and the initial magnetic state state chosen for the realization of the sweeps. By analyzing the two R(I) plots on the bottom of Fig.3.5 represented by the black and green squares, the switching from the AP-P state to P-AP occurs only for positive current. Considering the junction's initial state [state 4 of Fig.3.2(b)] and the electron flow for positive current [see Fig.3.4(b)], the electrons will be initially polarized in the reference layer, carrying the same moment as $\vec{p_r}$. The free layer's magnetic moment, $\vec{m}$, is antiparallel to $\vec{p_r}$, thus the incident electrons arriving at the free layer apply a torque, destabilizing its initial state, *i. e.* favoring the reversal of the free layer's magnetization. Then the transmitted electrons travel from $\vec{m}$ to $\vec{p_c}$ which are parallel at the initial state. Although, the torque exerted by the incident electrons on $\vec{p_c}$ favor its initial configuration, most part of the electrons reflected at the interface between the top barrier and the control layer carry the opposite moment to $\vec{p_c}$ and are thus responsible for a second transfer of angular momentum onto $\vec{m}$, assisting on its reversal. The total torque applied onto the free layer is then the sum of the torques coming from both reference and control layers, $| T_{\|total} |=| T_{\|r} | + | T_{\|c} |$. We conclude that, for an asymmetric DBMTJ with a thicker top barrier, an electron flow from reference to control layer ($I > 0$ in our case) favors the transition from AP-P towards P-AP state. Starting from the same initial state AP-P but applying a negative current, and following a similar interpretation, it is trivial to conclude that the sum of the torques exerted on $\vec{m}$ favor the stabilization of its initial configuration. The decreasing sweep of Fig.3.5(b) demonstrates the conservation of the AP-P state when a negative current is injected into the system. Reversal of the storage layer only happens when the current polarity changes.

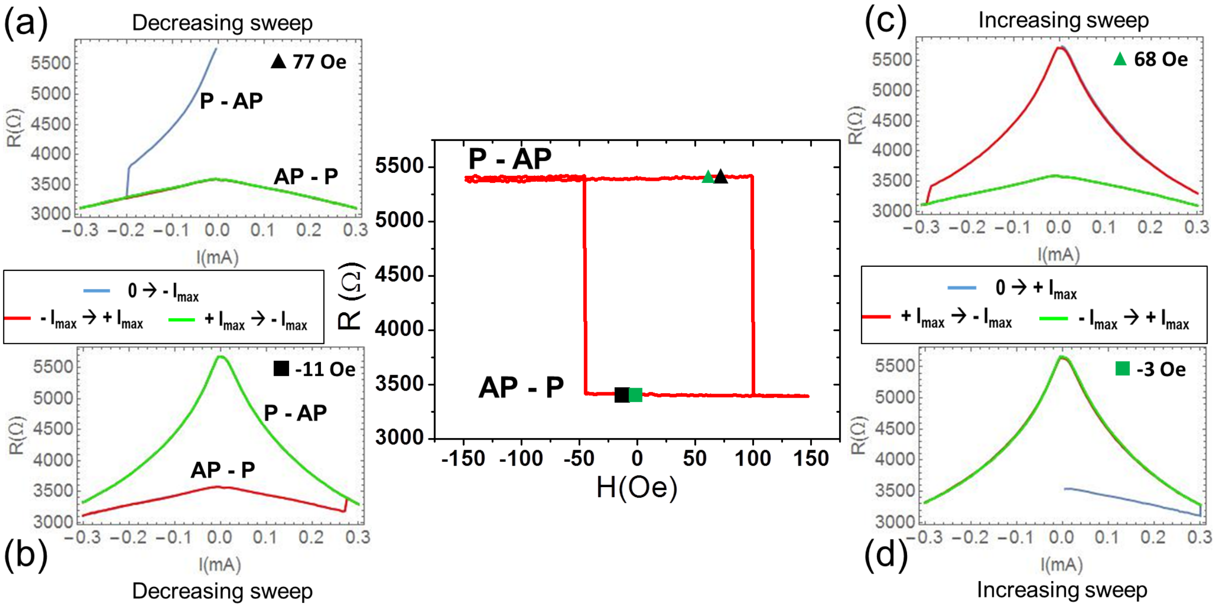

Figure 3.5: Descriptive resistance vs current plots of an elliptical asymmetric top thick barrier junction of nominal dimensions 40×140 nm [same as in Fig.3.3(c)], set in write mode. The R(H) loop at the center shows the bistable region (where switching is possible) of the DBMTJ when the reference layers' magnetization are in antiparallel alignment. DMTJ's coercive field is $H_c = 72Oe$ and offset field is $H_{off} = 27Oe$. (a)-(b) Decreasing and (c)-(d) increasing sweeps are represented by the black and green markers, respectively while their shape refers to the initial magnetic configuration of the DBMTJ: AP-P (square) or P-AP (triangle).

Following the same line of thought and physical interpretation, if the initial configuration is now P-AP, the requirements to reverse or favor the direction of $\vec{m}$ are inverted. Therefore, electron flow from control to reference layers (negative current) induces the reversal of storage layer magnetization direction and transition to AP-P state, while positive current reinforces the P-AP configuration. The results are in agreement with previously reported experiments performed by P.-Y. Clément *et al.* in asymmetric DBMTJs with thicker top barrier. [80]. Figure 3.6 presents an illustration which summarizes the aforementioned relationship between the current polarity and the reversal of the storage layer by STT when the DBMTJ is set in write mode. Notice that the same scheme is valid for the other two types of DBMTJs (asymmetric with thick bottom barrier and symmetric barriers) since the position of the dominant barrier is unimportant due to the adding effect of the torque coming from reference and control layers.

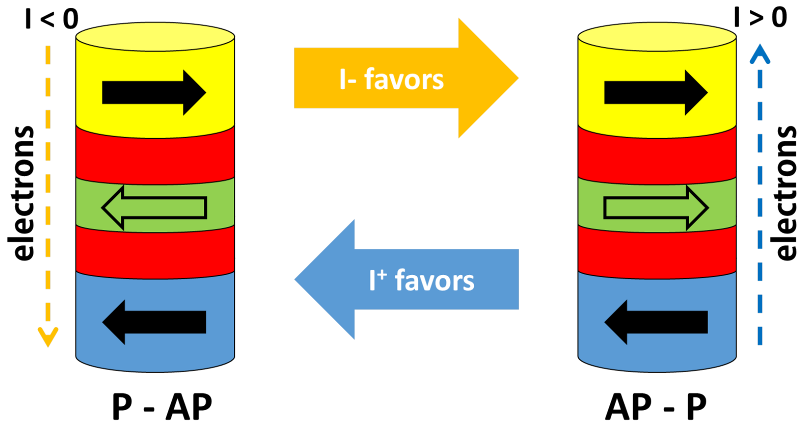

Figure 3.6: Illustration of the current polarity effect on the spin torque switching of the free layer of a DBMTJ set in write mode. This scheme is applicable to the three types of double barrier configuration (symmetric and two types of asymmetric barriers). Since the two torques add up, the position of the dominant barrier does not change current polarity which favors a particular state.

In circular junctions, similar results were found, concerning current polarity and favored magnetic states for DBMTJs in write mode. Figure 3.7 shows the same type of measurements as Fig.3.5 but for a 80 nm diameter (nominal dimensions) circular shape junction. Due to the lower coercive field compared to elliptical double junction, switching from AP-P to P-AP and *vice-versa* (double switching) can be measured for the same magnetic field point within the bistable region. The difference between the elliptical and circular cross section junctions lies in shape anisotropy. For elliptical junctions, the effective anisotropy field has two contributions, uniaxial anisotropy field H_u and shape anisotropy field H_d and is further expressed by [65, 89]

$$H_k = H_u + H_d = H_u + 2\frac{M_s t(AR-1)}{wAR} \tag{3.2}$$

where M_s is the saturation magnetization of the free layer, t is the free layer thickness, w is the short axis dimension of the ellipse and AR is the ellipse aspect ratio (length divided by width); for circular junctions $AR = 1$, thus no shape anisotropy energy is added to the system. For elliptic double junctions, switching was only observed for applied magnetic fields close to $H_c \approx H_k$. When magnetic field is further away from coercive field, the switching current increases and for sufficiently large currents, undesired effects may occur, before storage layer reversal, such as junction breakdown and mode switch (to be discussed later).

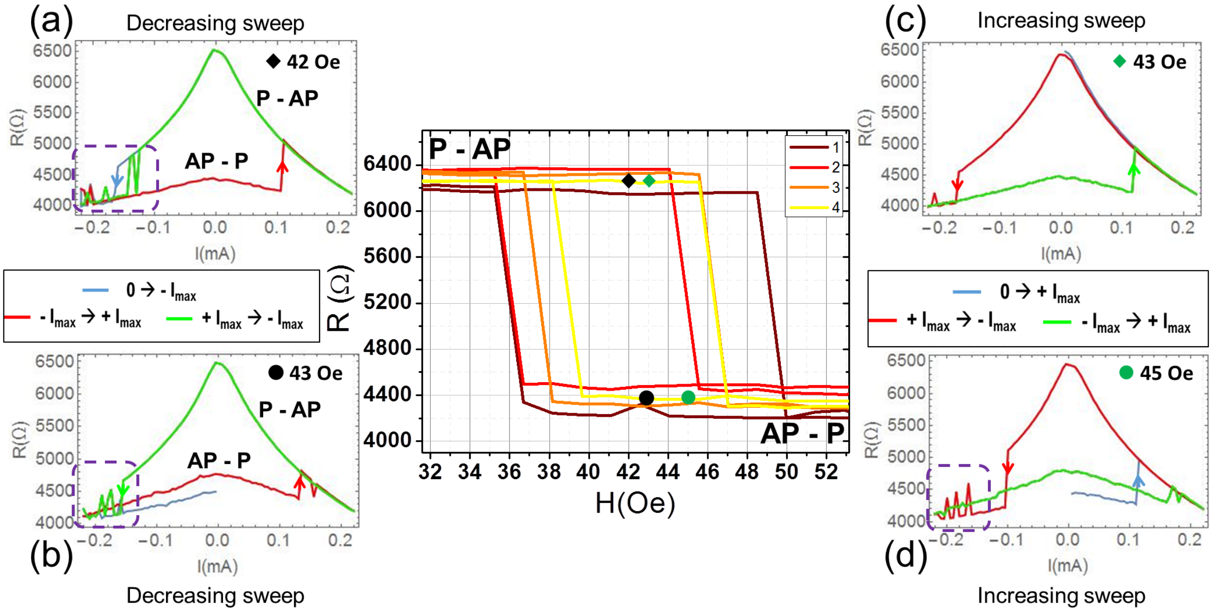

Figure 3.7: Descriptive resistance vs current plots of a circular cross section asymmetric top thick barrier junction with a nominal diameter of 80 nm, set in write mode. The R(H) loops at the center shows the bistable region (where switching is possible) of the DBMTJ when the reference layers' magnetization are in antiparallel alignment. The color gradient from red to yellow represent the sequence of sweeps performed before the re-measurement of the R(H) loop. DMTJ's coercive fields are $H_c \approx 4 - 12Oe$ and offset fields are $H_{off} \approx 40 - 43Oe$. Variation of coercivity may be due to increase of temperature. The (a)-(b) decreasing and (c)-(d) increasing sweeps are represented by the black and green markers, respectively while their shape refers to the initial magnetic configuration of the DBMTJ: AP-P (circle) or P-AP (diamond). The zones enclosed (purple dashed line) are evidence of "backhopping" where the in-plane torque compete with the perpendicular torque.

Telegraphic transitions between the AP-P and P-AP states (surrounded by a purple dashed line rectangle in Fig.3.7) are present in some R(I) plots at absolute current values higher than the switching current. This effect has been observed before and has been reported both for single [90] and double barrier MTJs [80]. In fact, this phenomenon is known as *backhopping* (or *backswitching*), which may have two different origins. The first is a competition between in-plane and perpendicular torques [91,92]. As mentioned before, in our measurement setup, $T_{\parallel}$ induces switching from P-AP to AP-P states for negative current. On the other hand, field-like torque favors the antiparallel state around the dominant barrier, i.e. P-AP state in the case of the asymmetric top thick barrier DBMTJ. The field-like torque has mainly a quadratic dependence with voltage ($T_{\perp} \propto bV^2$), consequently both torques have similar magnitudes at high currents ($I \propto V$) and so backhopping exists for large negative current values (see R(I) loops of Fig.3.5). The other reason for backhopping is due to the low thermal stability of the junction which is directly related to a low anisotropy H_k. In this scenario, the backhopping may occur for both current polarities. When the current pulse amplitude and/or width increases, the junction temperature increases due to Joule effect, thus leading to thermally activated reversals of the free layer [93]. This is the type of backhopping observed on the R(I) loop of Fig.3.8. The oscillatory switching occurs for positive currents. If we consider the two types of torque, at positive currents, both of them should favor the P-AP state and no backhopping should be observed. Moreover, this type of backhopping is only observed for applied fields close to H_c in circular devices with low anisotropy (or low coercivity). As observed in the R(H) loop of Fig.3.7 (same as Fig.3.8), coercivity varies with sequential current sweeps. This variation is caused by high temperatures created by Joule heating when large current is applied. Although the coercivity variation is not dependent of current polarity, thermal backhopping was only observed for positive currents. The black dot present in the R(H) loop of Fig.3.8 shows that the initial state of the junction is AP-P and the applied field is close to H_c, so transition can be achieved with low thermal activation energy. When positive current is injected, the double junction switches to P-AP due to $T_{||}$ but, as the current (and thus temperature) increases, H_c decreases so that the applied field is no longer inside the bistable region: so the storage layer switches back. When negative current is injected, $T_{||}$ favors the original state as well as the variation of H_c that might put the applied field outside the bistable region without changing the free layer's magnetization direction.

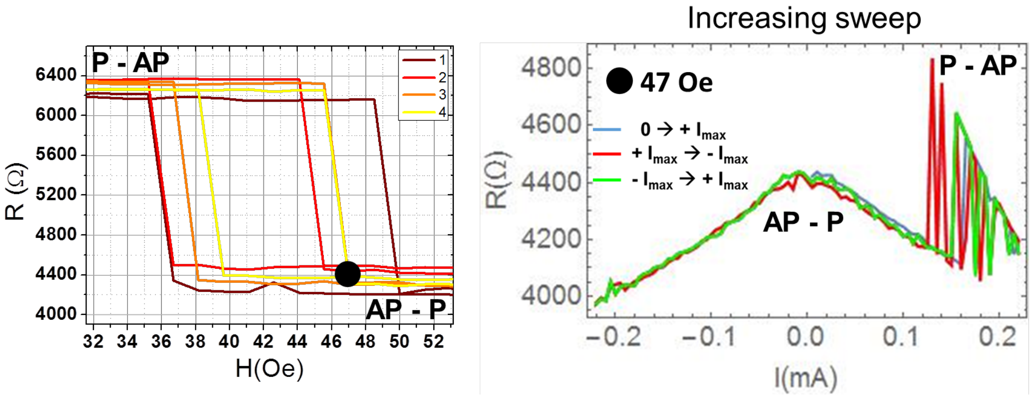

Figure 3.8: (*Right*) R(I) increasing sweep of the circular cross section DBMTJ also on Fig.3.7 with respective R(H) loop (*left*). The black dot points to the initial state of the double junction. Backhopping is observed for positive current polarity.

Backhopping is an undesired effect as it compromises the written information on the memory. Therefore some strategies have been reported to tackle this problem. One lies on increasing the device aspect ratio (AR) to enhance its anisotropy as its raises the threshold current of the backhopping effect [93]. This was also verified by us since no backhopping was observed in DBMTJs with elliptical cross section (see Fig.3.5). Another solution seeks to change the dependence of the perpendicular torque with voltage, increasing its linear component, by playing with different materials on each side of the barrier thus hampering the interplay between torques for even higher voltages [91]. Reducing the RA of the tunnel junction [92] or switch to perpendicular anisotropy devices are other ways to avoid the problem.

The switching currents from all the possible R(I) measurements performed for both elliptical and circular cross sections junctions (same junctions as figs.3.5 and 3.7) are represented under the form of current density (J_{sw}) vs. applied field (H) in figures 3.9(a) and (b), respectively. The calculation of J_{sw} is based on the electric area $A_{elec} = RA_{total}/R_{min}$ where RA_{total} is the sum of the nominal RA of the two barriers and R_{min} corresponds to the resistance of the double junction when the storage layer magnetization is parallel to both references. A_{elec} values correspond to a 100 nm × 190 nm ellipse and 127 nm diameter circle. In figures 3.9(a) and (b), near the free layer switching fields, -42 Oe / 93 Oe (ellipse) and 38 Oe / 46 Oe (circle), transitions from AP-P to P-AP and P-AP to AP-P were observed for both current polarities (yellow colored regions). These transitions are not in agreement with damping-like

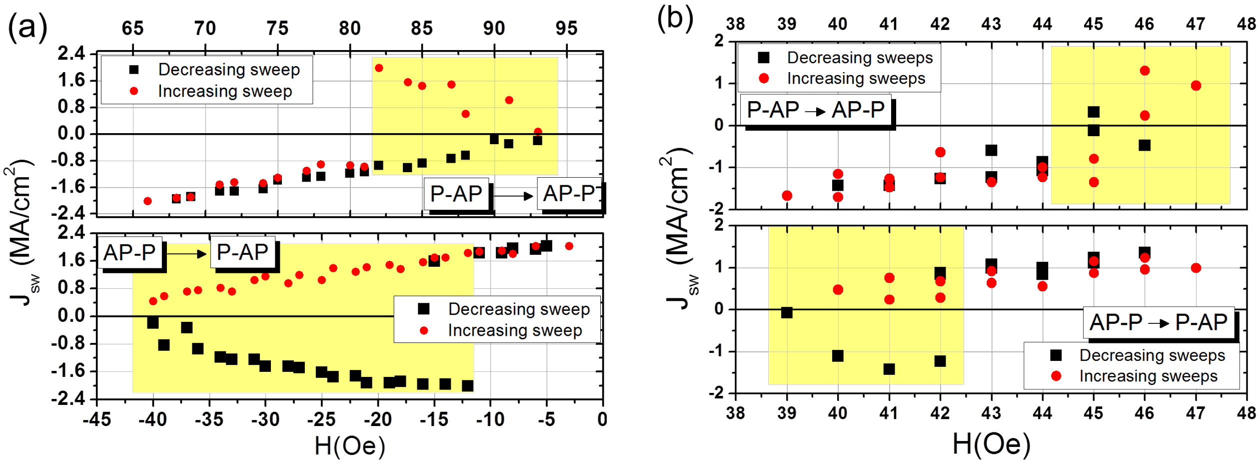

Figure 3.9: Switching current density (J_{sw}) as a function of the applied field (H) for a thick top barrier asymmetric DBMTJ device with (a) elliptical cross section (real dimensions: $80\,nm \times 190\,nm$) and (b) circular cross section (real diameter: 125 nm). Decreasing (black squares) and increasing (red circles) sweeps were performed for both transitions. Yellow colored regions represent the area where switching happen for both current polarities due to thermal fluctuations and low energy barrier near the coercive fields.

torque which has a dominant linear dependence with voltage ($T_{\parallel} \propto a_1 V$). These undesired transitions are due to a reduced energy barrier near the switching fields which is easily overcome by the storage layer's magnetization in the presence of high thermal fluctuations. In figs.3.9(a) and (b), the thermally induced region is larger for the AP-P to P-AP transition than for the inverse one. This difference may be explained by the additional influence of field-like torque which will favor the antiparallel state around the thicker barrier and, like the thermal effects, is mostly independent of the current polarity.

The critical current density is defined as the average switching current density that enables both transitions and is given by:

$$J_c = \frac{|J_{sw}^{AP-P \to P-AP}| + |J_{sw}^{P-AP \to AP-P}|}{2} \tag{3.3}$$

where $J_{sw}^{AP-P \to P-AP}$ (resp. $J_{sw}^{P-AP \to AP-P}$) is the current density required to switch the free layer magnetization from AP-P to P-AP (resp. from P-AP to AP-P) magnetic states. J_c was calculated at the center of the coercive zone, thus at the offset field H_{off}. Both $J_{sw}^{AP-P \to P-AP}$ and $J_{sw}^{P-AP \to AP-P}$ were obtained by extrapolating the switching current density linear dependence on the applied field (as shown in Eq.(3.3)) to H_{off} (only the data points outside of the thermal switching region were considered for the linear fits). For elliptical junction: $J_{sw}^{AP-P \to P-AP}$ = 2.49 MA/cm^2 and $J_{sw}^{P-AP \to AP-P}$ = -3.04 MA/cm^2 - and for the device with circular cross section: $J_{sw}^{AP-P \to P-AP}$ = 0.86 MA/cm^2 and $J_{sw}^{P-AP \to AP-P}$ = -1.04 MA/cm^2. A clear difference between $AP-P \to P-AP$ and $P-AP \to AP-P$ switching current densities is noticeable. It is known for single barrier MTJs that there is an asymmetry between the switching currents: the AP to P transition requires less current. In the case of a double barrier, in write mode, the storage layer magnetization is always antiparallel to one reference and parallel to the other therefore the asymmetry between switching currents should not exist. As the less current demanding transition is that towards the antiparallel state around the top barrier, one may assume that the field-like torque is contributing to the switching in addition to the damping-like torque. Introducing the experimental values into equation 3.3, J_c is 2.76 MA/cm^2 and 0.95 MA/cm^2 for the elliptical and circular devices, respectively. The lower value obtained for the circular DBMTJ comes from the absence of shape anisotropy (AR = 1) in comparison with the elliptical device which has an AR of almost 2. Nevertheless, for a similar type of asymmetric top thick barrier double junction, Clément *et al.* [80] obtained a $J_c =$ 0.69 MA/cm^2 for an elliptical device which is closer to the J_c found for the circular pillar but diverges from the result presented here for a DBMTJ of equal geometry. The disparity between the values found by Clément *et al.* for the elliptical junction can be explained by a larger area of our device which is more likely to excite nonuniform dynamic magnetization modes during switching [94].

3.2.1.B Asymmetric barriers: bottom thick barrier

The same asymmetry between the two barriers is conserved but the position of the thicker barrier is now on the interface between the bottom reference and the storage layer. The double junction is still set in *write mode* with antiparallel alignment between the two references.

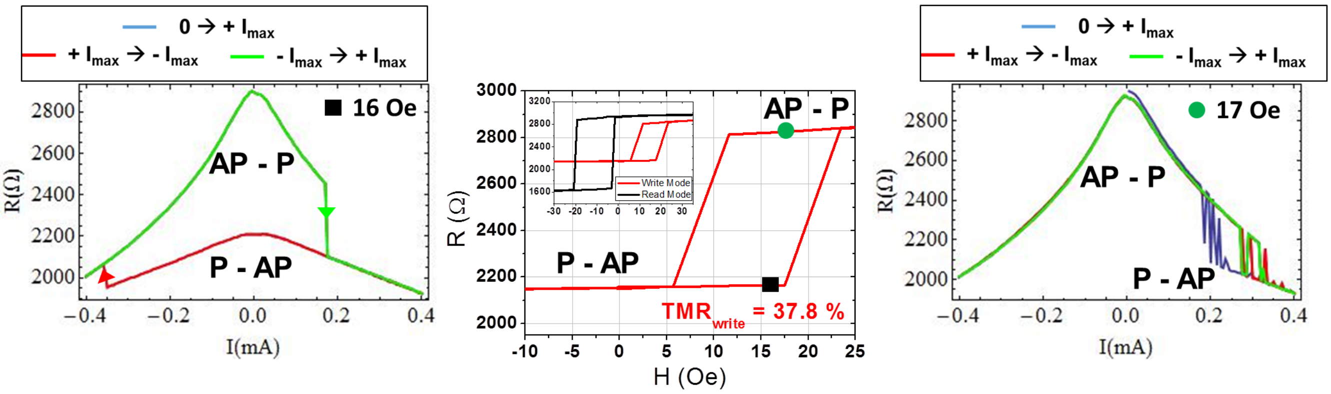

Figure 3.10: (*Center*) R(H) cycle of a circular asymmetric bottom thick barrier junction with 190 nm (real) diameter in write mode. TMR = 37.8 %, $H_c = $ 6 Oe and H_{off} = 14.5 Oe. Read (black line) and write mode (red line) R(H) cycles on the inset. TMR = 87.8 % in read mode. R(I) plots of increasing sweeps performed (*Left*) from an initial P-AP state at H = 16 Oe (black square) and (*Right*) from an initial AP-P state at H = 17 Oe (green circle). Backhopping is observed at positive current in the R(I) plot at the right.

In the center R(H) plot of figure 3.10, we observe that AP-P state corresponds to the high resistance state while P-AP to the low resistance state, contrary to the asymmetric top thick barrier. In the same figure, on the left R(I) plot, the transitions from low to high resistance state (and *vice-versa*) are now performed at inverted current polarities. However, as the magnetic configuration corresponding to the high/low resistance states is also reversed, the P-AP $\longleftrightarrow$ AP-P transitions conserve the same current sign as in the previous case. Therefore, the current induced spin transfer torque switching description of subsection 3.2.1.A is still applicable. Regarding the backhopping effect, and according to R(I) cycle at the right of Fig.3.10, it now occurs at positive current. Following the same explanation as before, field-like torque favors the antiparallel state of reference and free layers around the dominant barrier (currently AP-P state) and has a quadratic dependence with current. Therefore, the competition between damping and field-like torque will, henceforth, happen for the positive polarity of the applied current.

Likewise the asymmetric top thick barrier case, the switching current densities J_{sw} as a function of the applied field H was measured for two different geometries of DBMTJ, circular and elliptical, as presented

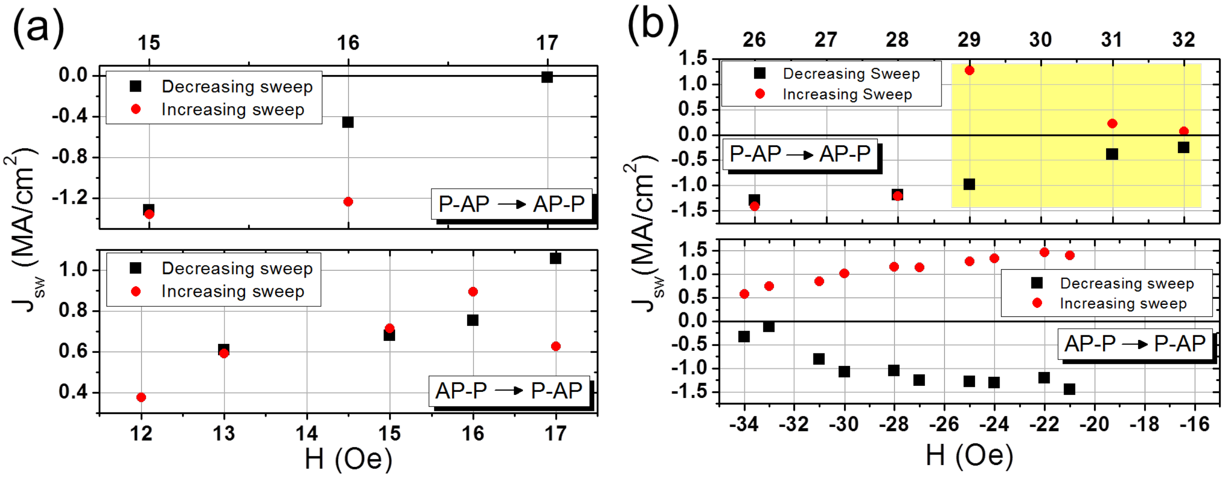

Figure 3.11: Switching current density in function of the applied field for a bottom thick barrier asymmetric DBMTJ device with (a) circular cross section (real diameter = 190 nm) and (b) elliptical cross section (real dimensions 160 nm × 250 nm). Decreasing (black squares) and increasing (red circles) sweeps were performed for both transitions. Yellow colored region represents the area where switching happened for both current polarities due to thermal fluctuations and low energy barrier near the coercive fields.

in figures 3.11(a) and (b), respectively. The yellow region marked in Fig.3.11(b) represents the field zone where thermally induced switching is observed. This region is undoubtedly identified for the P-AP $\to$ AP-P transition since unilateral switching exists from $H = 28Oe$ towards smaller fields. By contrast, for the opposite transition, switching is always observed for both current polarities in the field range studied: it was not possible to measure a single positive current induced switching as expected from STT theory. Therefore, we choose not to tag this region yellow as thermal fluctuations may not be the main reason for this current sign independent switching. In fact, similar observations were made using voltage pulses (section 3.3). The values $J_{sw}^{AP-P\to P-AP}$ and $J_{sw}^{P-AP\to AP-P}$ at $H = H_{off}$ were determined by linear extrapolation of the data points of the J(H) plots in Fig.3.11. For the circular junction, $J_{sw}^{AP-P\to P-AP} =$ 0.69 MA/cm^2 and $J_{sw}^{P-AP\to AP-P} =$ -1.71 MA/cm^2 and for the elliptical junction, $J_{sw}^{AP-P\to P-AP} =$ 2.26 MA/cm^2 and $J_{sw}^{P-AP\to AP-P} =$ -3.24 MA/cm^2. Similarly to the top thick barrier DBMTJ, the AP-P $\to$ P-AP transition requires less current than its opposite, however that does not agree with an addition of field-like torque to the existing damping torque since it should favor the transition towards antiparallel state around the thicker bottom barrier (AP-P state). In addition, opposite results were obtained by P.-Y. Clément [1] in similar type of asymmetric DBMTJs. This issue of favoring the P-AP state in this type of asymmetric barriers is going to be discussed in the next section 3.3. The critical current densities J_c were calculated using Eq.3.3 and results are the following: $J_c^{circle} =$ 1.20 MA/cm^2 and $J_c^{ellipse} =$ 2.75 MA/cm^2.

3.2.1.C Symmetric barriers

The behavior of double barrier tunnel junctions with two nominally symmetric MgO barriers under applied DC current was also studied. Two types of symmetric barriers DBMTJs were measured: thick and thin barriers with nominal RA of 45 $\Omega.\mu m^2$ and 10 $\Omega.\mu m^2$, respectively (see tables 3.1 and 3.2, respectively, for nominal and estimated values of RA and TMR). As described in subsection 3.1.3, RA and TMR are not exactly equal for both barriers. If that was the case, and for the DBMTJ set in write mode, $RA_3 = RA_4$ in Eq.3.1 and knowing that $TMR_{write} = \frac{1}{A}\frac{RA_3 - RA_4}{RA_4}$, then $TMR_{write} = 0$. In fact, the measured TMR_{write} for the fabricated symmetric barriers devices has average values below 15%. For some devices, this value is under 10%, as showed in the R(H) loops of figures 3.3(a) and (b), revealing a quite strong similarity between the two MgO barriers concerning both RA and TMR. Moreover, for the 3 symmetric barrier devices presented [figs.3.3(a)-(b) and 3.12(a)] here, the top barrier is dominant therefore the P-AP state is the one of higher resistance. Two reasons may explain the slightly larger RA and TMR of the top barrier relative to the bottom one: i) the texture quality of the top MgO and its interfaces with CoFeB from top reference and storage layers (as discussed before in subsection 3.1.3) and ii) lower probability of sidewall redeposition, during the etch of the magnetic stack, for the top barrier than for the bottom barrier.

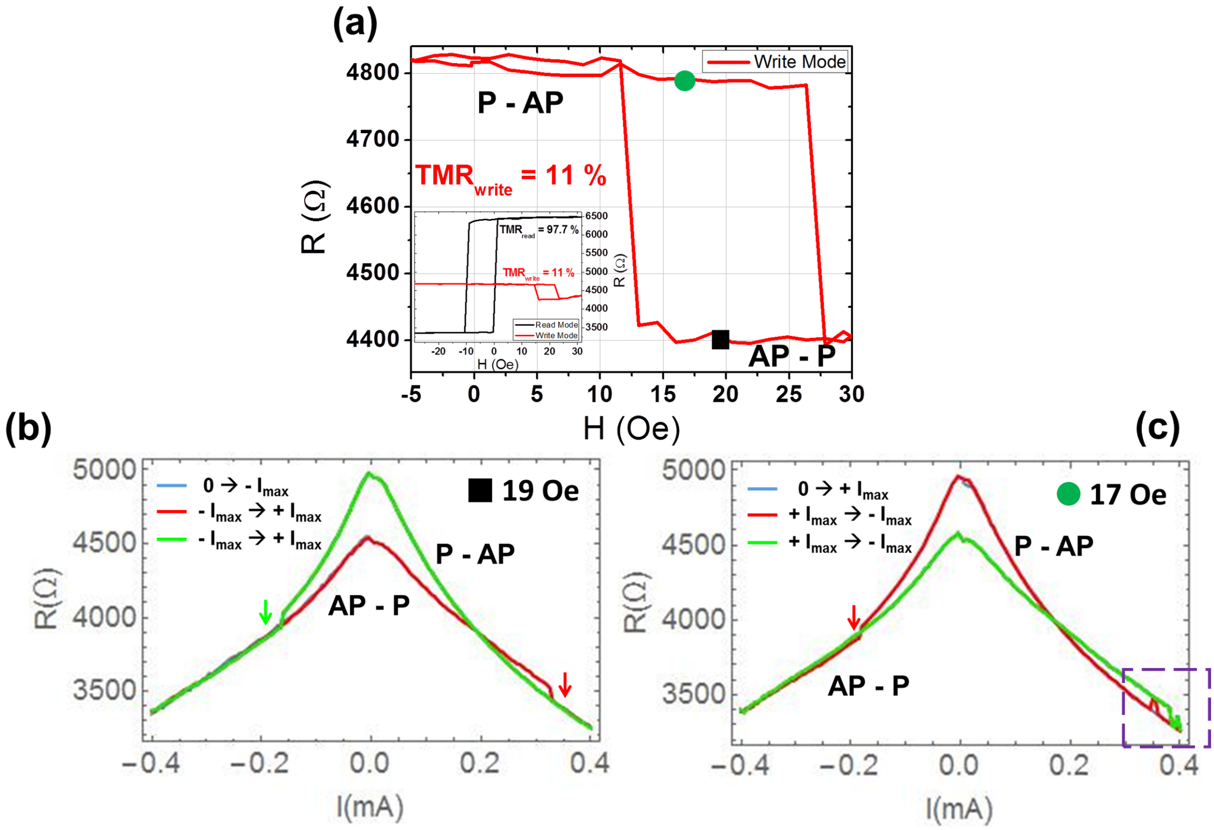

Figure 3.12: (a) R(H) cycle of a circular symmetric junction with thick barriers ($\phi = 186$ nm real diameter) in write mode. TMR=11 %, H_c = 3.5 Oe and H_{off} = 19 Oe. Inset: read and write mode R(H) cycles. (b) R(I) plots of decreasing sweeps performed from an initial AP-P state at H = 19 Oe (black square) and (c) increasing sweeps from an initial P-AP state at H = 17 Oe (green circle). Backhopping is observed at positive current (dashed line rectangle).

Figures 3.12(b) and (c) present the R(I) sweeps performed on a symmetric thick barriers double junction with a circular cross section of 187 nm electrical diameter. $TMR_{write} = 11\%$ which corresponds to a difference in resistance $\Delta R = R^{P-AP} - R^{AP-P} \approx 500\ \Omega$ between the P-AP and AP-P magnetic states for a near-zero bias current. These two plots show that ΔR decreases with applied current, and if no storage layer reversal occurs, a crossover between the two states resistances happen for $I \approx$ 0.15 - 0.2 mA. In an attempt to explain this crossover, one must first realize that while the resistance decreases with applied current for both magnetic states, the decline is more noticeable for the P-AP alignment where storage layer and top reference layers magnetizations are antiparallel around the slightly thicker barrier. In addition, the drop in resistance is stronger for low bias current ($I <$ 0.15 mA). Zhang *et al.* [95] named this last phenomenon as *zero bias anomaly* and proposed an explanation to it, for the case of single barrier junction. They suggest that the sudden resistance reduction is due to ”hot electrons” which are energized above the Fermi level (effect of the applied voltage) and that cause collective excitations of local spins at the interfaces between oxide barrier and ferromagnets. In parallel state, the junction resistance is only determined by the probability of electron transfer through the barrier. By contrast, in antiparallel state, the electron transfer is limited by the density of available states on the receiving electrode. If hot electrons may flip their spin, the junction conductance is no more limited by the low density of states of minority electrons; as a consequence, the junction conductance increases and resistance decreases. This mechanism explains why the AP-state resistance decreases more significantly with increasing bias voltage, as compared to the P-state resistance [5]. Considering now double barrier junctions as two single barrier MTJs in series and in the hypothesis of perfectly identical barriers, one should expect the same resistance for P-AP and AP-P states, with identical decay with voltage/current bias. In our junctions however, the top barrier is slightly dominating, thus the resistance of the P-AP state is a little larger and the resistance decay with applied bias is also slightly more pronounced.

When $I >$ 0.2 mA, $\Delta R < 0$ as well as TMR_{write} since $RA_3 < RA_4$. Negative TMR has already been observed when resonant tunneling occurs [96] as well as the crossover between AP and P resistances in MTJs for large applied voltages ($V > 0.5V$) and for different ferromagnets/oxide interface structures [97]. Nevertheless, the behavior of the DBMTJ, in write mode, cannot be directly compared with the single barrier MTJ since AP and P configurations exist at the same time, one for each barrier. In our case, the crossover represents the point of exact symmetry between the two barriers. Beyond that point, the dominant barrier changes from top to bottom and thereon the state of high resistance is the AP-P state. Indeed, the observation of backhopping when $I > 0$ in Fig.3.12(c) may be related with this inversion of the dominant barrier. When backhopping was observed in both types of asymmetric barriers DBMTJs, its origin was attributed to the interplay between damping and field-like torque. Since the latter torque was said to favor the AP configuration of storage and reference layers around the thicker barrier, the current polarity for which backhopping occurred was the same that favored the opposite transition (P configuration around the thicker barrier), triggered by damping-like torque. Likewise the asymmetric top thick barrier DBMTJ, $I > 0$ favors the transition towards the high resistance P-AP state and $I < 0$ favors the transition towards the low resistance AP-P state therefore backhopping was expected to happen for negative current polarity. However, the magnitude of the field-like torque is only comparable to the damping-like torque for current values larger than the resistances' crossover point in which the bottom barrier starts to be the dominant one. In fact, even in this case, the competition between the two torques still supports the occurrence of backhopping, only the interpretation of the effects of field-like torque changes. From the crossover point thereafter, the thickness disparity between the two barriers does not change but their TMR does. Thence, the field-like torque must favor the AP alignment of the

---

[5] The small resistance decay in P-state as a function of bias voltage is simply related to the usual evolution of tunnel conductance with voltage.

ferromagnetic layers around the barrier with higher TMR and not the thicker one, as mentioned before[6].

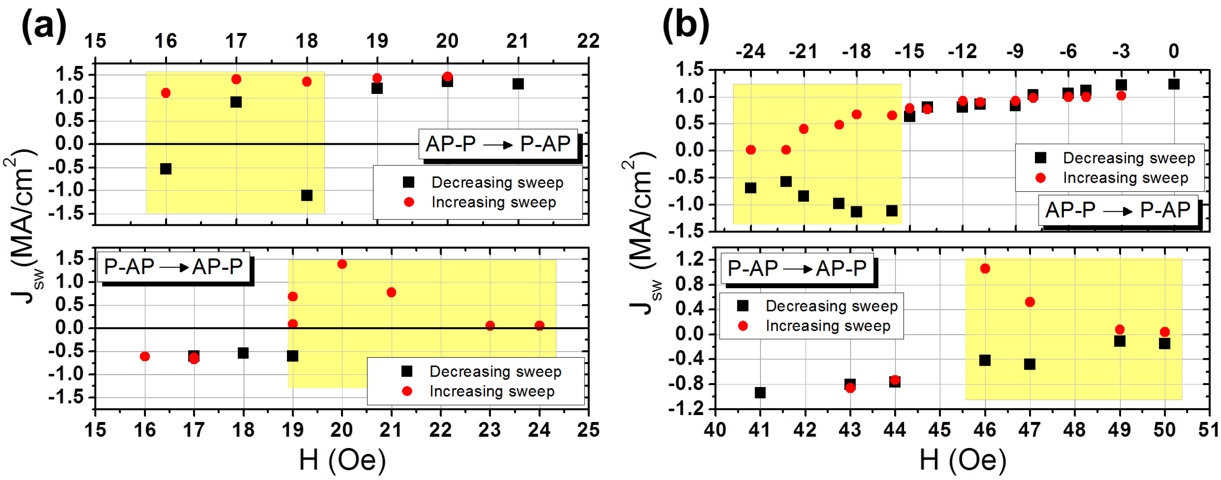

Figure 3.13: Switching current density as a function of the applied field for a symmetric DBMTJ with thick barriers with (a) circular cross section (real diameter = 186 nm) and (b) elliptical cross section (real dimensions 150 nm × 220 nm). The respective R(H) loops are represented in figures 3.12(a) and 3.3(a). Decreasing (black squares) and increasing (red circles) sweeps were performed for both transitions. Yellow colored region represents the area where switching happened for both current polarities due to thermal fluctuations and low energy barrier near the coercive fields.

Once again, the switching current densities as a function of the applied field, $J_{sw}(H)$, were measured for devices with circular and elliptical cross sections as presented in figures.3.13(a) and (b), respectively. Similarly to the previous cases, the data points included inside the yellow boxes correspond to thermally activated transitions. For the two geometries, the J_{sw} values, used in Eq.3.3 to determine J_c, were calculated at H_{off} and obtained by linear extrapolation of the measured current densities for each of the transitions. The determined values are: $J_{sw}^{AP-P \rightarrow P-AP}$ = 1.34 MA/cm^2 and $J_{sw}^{P-AP \rightarrow AP-P}$ = -0.58 MA/cm^2 (circular junction) and $J_{sw}^{AP-P \rightarrow P-AP}$ = 1.64 MA/cm^2 and $J_{sw}^{P-AP \rightarrow AP-P}$ = -2.75 MA/cm^2 (elliptical junction). The differences in J_{sw} between the two geometries were already explained and are related to the larger H_k of elliptical cross section pillars compared with circular ones. For the circular junction, $|J_{sw}^{P-AP \rightarrow AP-P}| < |J_{sw}^{AP-P \rightarrow P-AP}|$, which may be explained by an additional contribution of the field-like torque that favors an AP configuration around the dominant barrier. Since the measured switching current values are higher than the resistance crossover current value, the field-like torque favors the AP-P configuration, thus less energy is needed to induce the reversal of the storage layer. For the case of the ellipse, in all R(I) measurements performed, no resistance crossover between the AP-P and P-AP states was observed [7]. For this reason, and like the asymmetric top thick barrier DBMTJ, field-like torque favors the P-AP state and the transition towards this state is energetically easier. The calculated critical currents J_c for the circular and elliptical devices are, respectively, 0.96 MA/cm^2 and 2.19 MA/cm^2.

Another type of symmetric barriers DBMTJ was also studied, with thinner barriers. The stack composition is the same as for the junctions with thick symmetric barriers, except that the RA of each barrier is 10 $\Omega.\mu m^2$ instead of 45 $\Omega.\mu m^2$. Figure 3.14 presents the switching current density as a function of the

---

[6] In the previous cases, the thicker barrier was also the one with higher TMR.

[7] We also notice that $TMR_{write}(ellipse) < TMR_{write}(circle)$.

applied magnetic field for an elliptical junction set in write mode. The switching current density values obtained at the center of the bi-stable region are $J_{sw}^{AP-P \to P-AP}$ = 2.73 MA/cm^2 and $J_{sw}^{P-AP \to AP-P}$ = -1.97 MA/cm^2 and the critical current density J_c = 2.35 MA/cm^2. These values are similar to the ones obtained for elliptical junctions with thick symmetric barriers. Therefore, we can conclude that the reduction of RA does not affect substantially the efficiency of spin transfer torque switching.

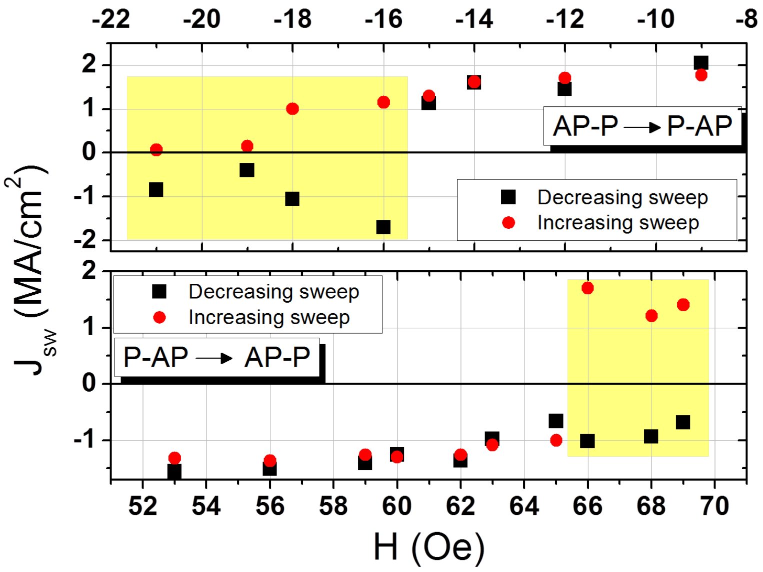

Figure 3.14: Switching current density as a function of the applied field for a junction with thin symmetric barriers and with elliptical cross section (real dimensions 140 nm × 220 nm). The respective R(H) loop is represented in figure 3.3(b). TMR_{write} = 7.1%, H_c = 47Oe and H_{off} = 25Oe. Decreasing (black squares) and increasing (red circles) sweeps were performed for both transitions. Yellow colored region represents the area where switching happens for both current polarities due to thermal fluctuations and low energy barrier near the coercive fields.

3.2.1.D Critical current density comparison with single barrier MTJ

Single barrier MTJs were fabricated in order to compare the switching current density with the above mentioned double barrier MTJs. The stack of the bottom pinned MTJ is illustrated at the center of Fig.3.15. For a more trustworthy comparison, the stack is exactly similar to the studied DBMTJs except that the top MgO barrier and top reference are removed and the storage layer is only capped by a Ta/Ru bi-layer. The oxide barrier has a nominal RA = 35 $\Omega.\mu m^2$. The R(H) cycles of two elliptical junctions are represented in Fig.3.15. Both samples show a TMR higher than 100 %. [8]

In the same way as the DBMTJs, the switching current density of the single barrier devices was measured as a function of the applied magnetic field and the results displayed in Fig.3.16. Following the linear extrapolation method aforementioned, $J_{sw}(H_{off})$ for P → AP and AP → P were determined and are the following: $J_{sw}^{P \to AP}$ = -4.51 MA/cm^2 and $J_{sw}^{AP \to P}$ = 3.64 MA/cm^2 [junction of Fig.3.15(a)] and $J_{sw}^{P \to AP}$ = -6.64 MA/cm^2 and $J_{sw}^{AP \to P}$ = 3.58 MA/cm^2 [junction of Fig.3.15(b)]. Although, for the

---

[8] Note that TMR was found to be higher in SMTJ than DBMTJs with comparable MgO and FL structures, in agreement with previous reports in literature [38, 87, 88]. In the SMTJs, the B rejected from the CoFe phase that was heterogeneously nucleated from the MgO/CoFeB interface diffuses into the adjacent metallic layers (mainly Ta which a well-known B getter.) during annealing. [98–100] In DBMTJs, the double MgO barriers possibly suppress the diffusion of B in the middle CoFeB FL. Another possible reason is the high interface energy at due to lattice mismatch at the CoFeB/MgO interfaces which reduce the nucleation rate and prevent the complete crystallization of the CoFe in the FL. [22].

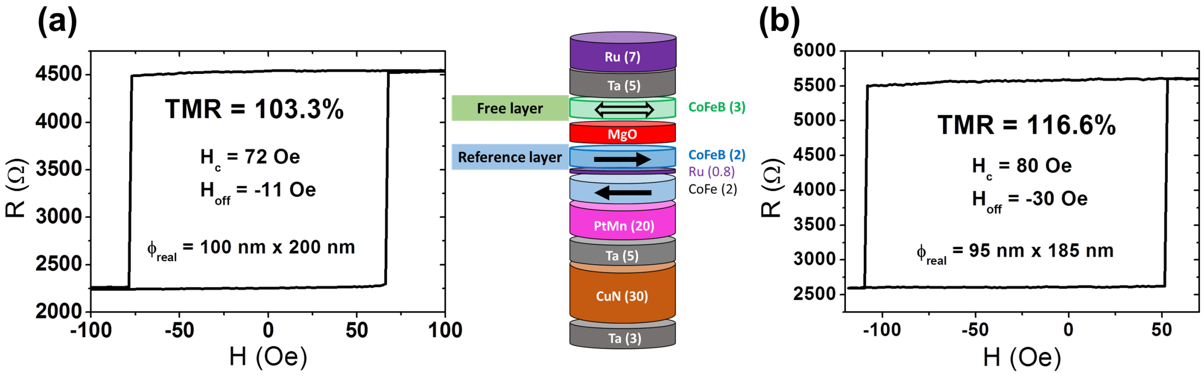

Figure 3.15: The illustration at the center shows the composition of the stack of the single barrier MTJ (thicknesses in nm). On each side are represented the R(H) loops of two junctions with elliptical shape and real dimensions of (a) 100nm × 200nm and (b) 95nm × 185nm. The TMR, coercivity and offset fields are indicated on the graphs.

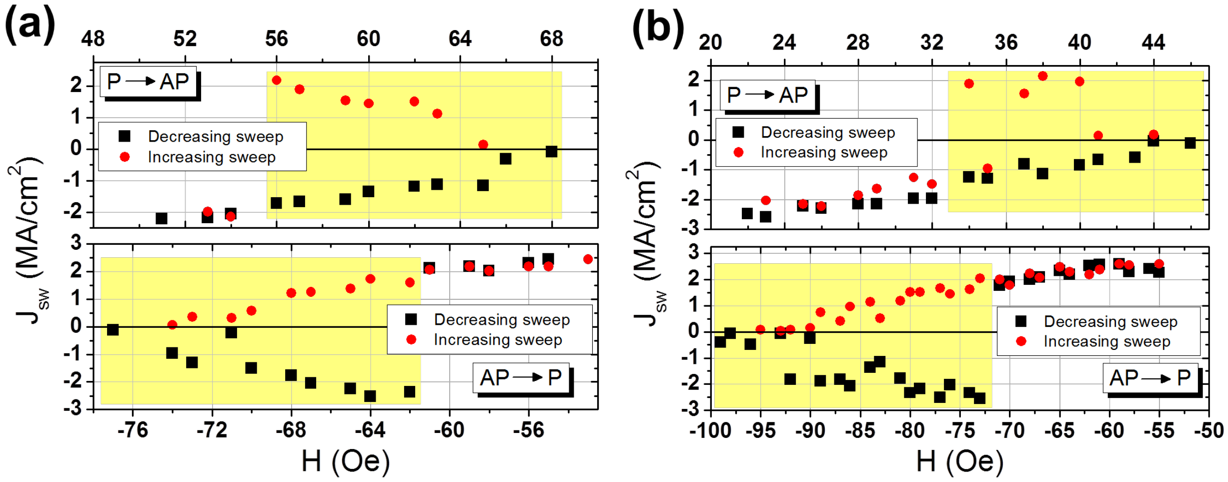

Figure 3.16: Switching current density as a function of the applied field for the single barrier MTJs of (a) Fig.3.15(a) and (b) Fig.3.15(b). Decreasing (black squares) and increasing (red circles) sweeps were performed for both transitions. Yellow colored region represents the area where switching happens for both current polarities due to thermal fluctuations and low energy barrier near the coercive fields.

junction of Fig.3.16(a) no substantial difference exists between J_{sw} for P→AP and AP→P, for the other measured MTJ the ratio between the two switching current densities is almost 2. This asymmetry of switching current density has already been observed [101] and it is caused by the asymmetry of the intrinsic switching current density J_{sw0}. Equation1.22 shows a dependence of J_{sw0} on the spin-transfer efficiency η and assuming an equal spin polarization on both sides of the barrier[9], this quantity can be derived to be [43, 102]:

$$\eta = \frac{P}{2(1 + P^2\, cos\theta)} \tag{3.4}$$

where P is the tunneling spin polarization and θ is the angle between the magnetization of the reference and free layer. This means that magnetic states P and AP do not have the same spin transfer efficiency, the latter being higher for AP than for P configuration. At zero bias, the first order approximation of the tunneling spin polarization is given by [43]:

---

[9] Spin polarization can be considered equal since the free and reference layer are made of the same material, in our case, CoFeB.

$$P_0 = \sqrt{\frac{TMR}{2+TMR}} \tag{3.5}$$

Table 3.3: Analytically calculated and experimental values of the intrinsic switching current density J_{sw0} and switching current density J_{sw} of single barrier MTJs.

		$J_{sw0}(MA/cm^2)$		$J_{sw}(MA/cm^2)$	
Sample	**Transition**	Analytical	Deduced from Experimental	Analytical	Experimental
Figure 3.15(a)	P → AP	-16.1	-7.7	-9.5	-4.5
	AP → P	7.9	6.2	4.7	3.6
Figure 3.15(b)	P → AP	-15.8	-11.5	-9.2	-6.6
	AP → P	7.3	6.2	4.2	3.6

Through the combination of eqs.1.22, 3.4 and 3.5, the proportionality relation between intrinsic switching current density and spin polarization can be translated by $J_{sw0}^{P\to AP} \propto 1+P_0^2$ and $J_{sw0}^{AP\to P} \propto 1-P_0^2$. However, J_{sw0} cannot be directly compared with the values measured by us at room temperature and in large pulse width current regime ($\tau \approx 50ms$). Since the measurements have been performed in the regime where spin transfer torque is mainly a thermally activated process [68, 103], it is necessary to use Eq.1.26 which depends strongly on the pulse width used and the thermal factor ($K_{eff}V/k_BT$) of the sample. Table 3.3 presents the experimental and analytically calculated values of J_{sw0} and J_{sw} for the single barrier MTJs. The following parameters were used to estimate J_{sw0} using Eq.1.22: $\alpha = 0.0055$ [104], $M_s = 1050\, emu/cm^3$ and $t_f = 3\, nm$. The used $H_k \approx H_c$ provides thermal stability factor values $\Delta \approx 40-60$ which are within the expected values for this type of structures [65]. On the other hand, the experimental J_{sw0} was obtained via Eq.1.26 using the experimental J_{sw}. There is a non-negligible discrepancy between experimental and calculated values, specially for the P→AP transition. Besides, the almost 2x difference between $J_{sw}^{P\to AP}$ and $J_{sw}^{AP\to P}$ from the analytical calculations was not observed experimentally, particularly for the junction of Fig.3.15(a).

Figure 3.17 compiles all the critical switching current densities J_{sw} of all the measured DBMTJs and compares them with the analytically calculated values using J_{sw} expression for DBMTJs from equation (1.43)[10]. There is a rather good agreement between the experimental and calculated values of the circular DBMTJs. On the elliptical double junctions the experimental values are higher than those analytically calculated. The divergence observed maybe related with an underestimation of the dimensions of the elliptical DBMTJ which would decrease $J_{sw}\, DB\, Exp.$. Another possibility is an underestimation of H_k for elliptical DBMTJs which would raise the value of $J_{sw}\, DB\, Theory$. However, the imposition of higher H_k would increase K_{eff} which consequently would raise the thermal stability factor Δ to values higher than normal: $\Delta > 70$ for in-plane DBMTJs. Focusing on the experimental values, the average over all the devices is $J_{sw}\, Exp = 1.9\, MA/cm^2$. Among the different types of DBMTJs, there is no clear influence of the symmetry or asymmetry of the MgO barriers on the reduction of the switching current density. The only remarkable influence on J_{sw} lies on the geometry of the devices where circular (**circ**) junctions reveal lower critical switching current density than those with elliptical (**ell**) cross section.

For DBMTJ in write mode, the transitions AP→P and P→AP happen at the same time, one on

---

[10] In the calculations, as both references and storage layer are composed of CoFeB, $P_F = P_R = P_0$ which is given by Eq.3.5

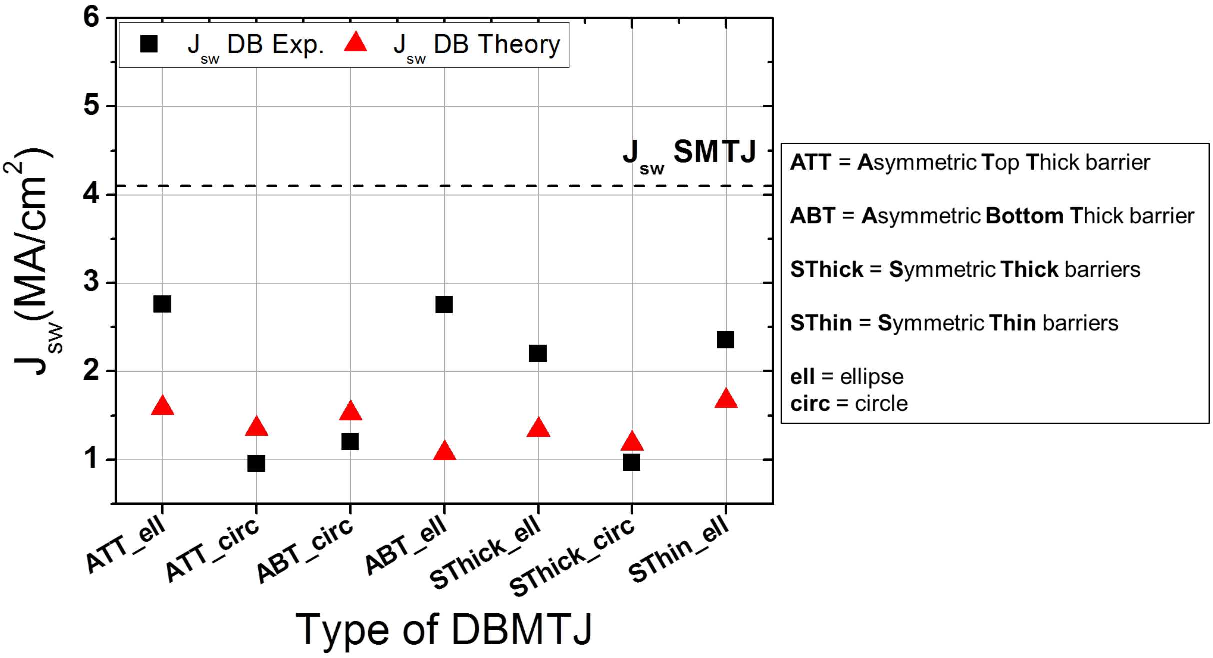

Figure 3.17: Display of the experimental critical current density $J_{sw}\, DB\, Exp.$ (black squares) with respective analytical calculated values $J_c\, DB\, Theory$ (red triangles) for all the measured types of DBMTJs. The acronyms of the different DBMTJs are on the legend box next to the plot. The dashed line correspond, respectively to the critical ($J_{sw}\, SMTJ$) of a single barrier MTJs measured.

each barrier; thus, the two switching current densities of the single barrier were averaged using Eq.3.3. Therefore, in Fig.3.17 the dashed line represent the averaged experimental critical switching current density $J_{sw}\, SMTJ = 4.1\, MA/cm^2$ for the measured single barrier MTJ. The ratio $\frac{J_{sw}\, DBMTJ}{J_{sw}\, SMTJ} \approx 2$ which corresponds to a 2x improvement of the critical switching current density of DBMTJs relative to a single barrier MTJ. This ratio is in agreement with previously obtained results using double barrier MTJs [37][11]. This result proves that the STT-DBMTJ is a suitable device to improve the power consumption of MRAM upon writing.

3.2.2 Read Mode

In this configuration, the magnetizations of the two references are parallel to each other which means that independently of the magnetization direction of the storage layer [parallel or antiparallel to both references, respectively, states 1 and 2 of Fig.3.2(a)], the damping-like torques from each of the references ($T_{\parallel r}$ and $T_{\parallel c}$) have opposite signs. Therefore, the total torque exerted on the storage layer is given by $T_{\parallel total} = \left|T_{\parallel r} - T_{\parallel c}\right|$. Therefore, $T_{\parallel total}$ in read mode is lower than $T_{\parallel total}$ in write mode. This implies that a larger current is needed to flip the magnetization of the storage layer (*i.e.* to write). This magnetic configuration of the two references is not advantageous for writing but rather positive for a more efficient and fast readout process. In addition, the DBMTJs in read mode present maximum TMR since the TMR from each barrier does not subtract in opposition to write mode and it is independent of the symmetry/asymmetry of the barriers (see TMR values on inset of R(H) cycles of Fig.3.3). As mentioned

---

[11] In the publication by Diao et al., for DBMTJs with similar composition and TMR as ours, lower J_{sw} values were obtained. The difference is explained by the substantially lower M_s of their free layer (800 emu/cm^3) CoFeB compared to ours (1050 emu/cm^3).

before, TMR decreases with applied voltage [24, 95], but at a slower rate for DBMTJs [31]. These two last features are essential to yield an effective sense path resistance change (ideally larger than 100%) between the two memory states: 1 (maximum resistance) and 0 (minimum resistance).

P.-Y. Clément [1] has performed similar measurements on DBMTJs in read mode and came across some interesting and unexpected results. Current sweeps performed in DBMTJs with nominally symmetric barriers revealed switchings from P-P $\rightarrow$ AP-AP as shown in the various plots of Fig.3.18. Decreasing sweeps [Fig.3.18(a)-(c)] and increasing sweeps [Fig.3.18(d)-(f)] showed that the switching occurred for both current polarities. These switchings can be attributed to field-like torque since, in read mode, the components coming from the reference and control layers add up. The dual polarity switching is mainly due to the quadratic behavior of the field-like torque with voltage, $T_{\perp} \propto V^2$. Nevertheless, a slight asymmetry exists between switching at negative or positive current. For the same applied field, a smaller negative than positive bias is needed to trigger the switch. The existence of a small (but non-negligible) in-plane torque could explain this bias asymmetry. However, it does not abide by the rules of applied current direction since, according to the measurement configuration (see Fig.3.20), it is the positive current that should help to destabilize the P-P configuration and not negative current as observed. On the other hand, in asymmetric barriers DBMTJ, it has never been observed any switching. More precisely, no storage layer reversal was observed for currents lower than those capable of causing a Joule effect mode switch. Although the absence of switching in read mode is a positive result, in asymmetric barriers structures when the references' magnetizations are set parallel, the damping-like torque is reduced (but not canceled) whereas the field-like torque is enhanced. Therefore, it was expected, at least, a switching from P-P$\rightarrow$AP-AP as field-like torque would tend to destabilize the initial P-P state and favor an AP alignment between storage and reference layers around the dominant barrier. Some possible explanations to the abnormal non-switching were: i) Néel coupling between storage layer and bottom reference due to the low thickness of the bottom MgO barrier; ii) the non-homogeneous oxidation of the bottom barrier may add a non-negligible linear component to the field-like torque [49] and reverse its effects favoring the P alignment between storage and reference layers.

In the following subsections are presented the results of the DC current sweeps performed on the DBMTJs with symmetric and asymmetric barriers. The precision of the applied magnetic field is thence improved compared to that used by P.-Y. Clément, thus in our measurements a considerably higher number of data points was possible to obtain. In addition, we present a brief analysis of the results based on the effects of the two components of the spin transfer torque: damping-like and field-like.

3.2.2.A Asymmetric barriers: top thick barrier

In this subsection the asymmetric top thicker barrier double junctions, which RA properties can be consulted in table 3.2, were set in read mode after an annealing under a 1T applied magnetic field. Similarly to write mode, the samples' resistance was measured while current was swept for both polarities. The switching current densities J_{sw} obtained as a function of the applied magnetic field H are plotted in Fig.3.19. Figures 3.19(a) and (b) correspond, respectively, to junctions with elliptical and circular cross sections which are the same devices as those measured in Fig.3.9. The read mode R(H) loop of the

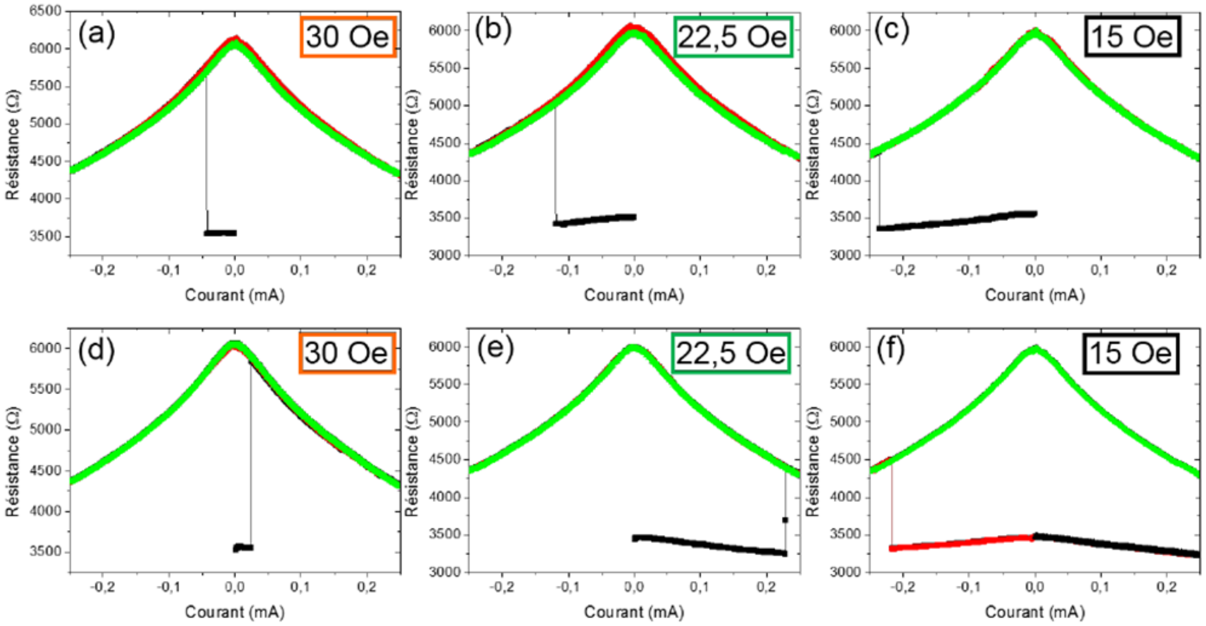

Figure 3.18: [Copy of Fig.IV.18 from [1]]. R(I) cycles of symmetric barriers DBMTJs set in read mode. The initial state of the device is P-P. Switching occurs for both current polarities, except for (f) in which an STT current asymmetry is present.

ellipse is displayed in Fig.3.3(c) and the one for the circular pillar in Fig.3.21(a).

Starting by the analysis of the elliptical junction, positive current favors both the P-P→AP-AP and AP-AP→P-P transitions. Although only the result of a representative DBMTJ is shown, additional measurements on three more junctions (with an elliptical shape and approximately same dimensions) were performed. Among the four junctions the AP-AP→P-P transitions were unilaterally triggered by positive current whereas the P-P→AP-AP transitions were triggered by either only positive, only negative or even both current polarities, depending on the junction, within the same wafer. Considering the direction of the electrons and the effects of incident and reflected ones around each barrier, Fig.3.20 shows which current polarity should favor each transition. Therefore, positive current favors the AP-AP state and negative current favors P-P state. Including the effects of field-like torque, which are maximized in read mode, then the AP-AP state should be extremely stable since it is favored independently of current sign.

Regarding the AP-AP→P-P transition, besides of not following the ideal behavior of the toy model of Fig.3.20, the positive current should strongly stabilize the AP-AP state since, in addition to the damping-like torque, field-like torque also favors the AP state around the dominant top barrier. As a first possible explanation, one may think of the inversion of the sign of $T_{\|}$ for large voltages [49]. However, this theory fails to explain completely the peculiar behavior. Though it allows the AP-AP→P-P transition for large positive current, the transition must also occur for negative current as predicted by STT theory which is not verified. The P-P→AP-AP transition results are quite puzzling since they are junction dependent. In order to dispel possible fabrication induced issues with each junction, each of the four junctions was submitted to similar measurements in write mode configuration. The results were systematic and all the junctions showed the same current polarity/transition correlation as those presented in section 3.2.1.A. Therefore, the inconsistencies come from the torques interplay in read mode configuration and not from

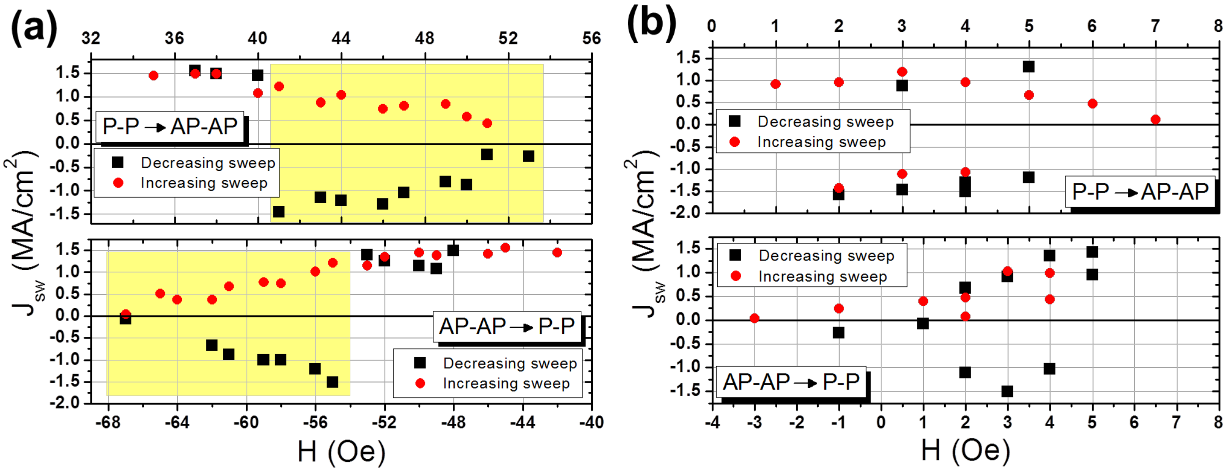

Figure 3.19: Switching current density in function of the applied field for asymmetric top thicker DBMTJs with (a) elliptical cross section (real dimensions: 90 nm x 190 nm) and (b) circular cross section (real diameter: 127 nm). The R(H) loops corresponding to devices (a) and (b) are presented in Fig.3.3(c) and Fig.3.21(a), respectively. Decreasing (black squares) and increasing (red circles) sweeps were performed for both transitions. Yellow colored region represents the area where switching happened for both current polarities due to thermal fluctuations and low energy barrier near the coercive fields.

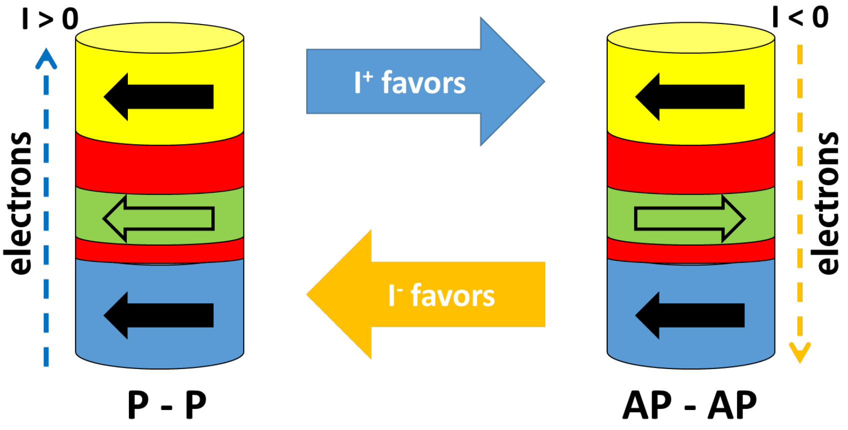

Figure 3.20: The ideal case read mode transitions favored by each current polarity in an asymmetric top thick barrier DBMTJ where $T_{\parallel}^{top} > T_{\parallel}^{bottom}$.

possible damages in the junctions.

For the junction of Fig.3.19(b) (example of a junction showing the most commonly observed behavior), for both the P-P→AP-AP and AP-AP→P-P transitions, there is no prevalence of one current polarity over the other. Moreover, the existence of black squares and red circles for both polarities means that within the sweep associated with the mark (black for decreasing sweep and red for increasing sweep) more than one of that particular transition occurred for the same applied field (usually backhopping or thermally activated switching). As it has already been mentioned in previous subsections, devices with circular cross section possess a lower H_k due to the absence of in-plane shape anisotropy. Thus the field range where bistability is allowed is much smaller than in elliptical junctions and, as J_{sw0} is directly proportional to H_k (see Eq.1.22), their switching current is also smaller. Thus these circular junctions are the only samples in which double transitions could be observed and measured in the same R(I) sweep below breakdown voltage. Figures 3.21(b)-(d) exhibit some R(I) plots performed for applied magnetic fields within the coercive region. Figure 3.21(a) displays several R(H) cycles of the circular junction measured after some R(I) sweeps. As already seen in Fig.3.8*(left)*, due to a lack of thermal stability, H_c varies with successive measurements. Therefore, we defined an effective coercive region that ranges between -1 Oe and 6 Oe where both P-P and AP-AP states exist. Focusing on Fig.3.21(c), the double switch shows clearly which current polarity favors each transition. Negative current favors P-P→AP-AP transition and positive current favors the opposite transition. Once again, the current polarities corresponding to the two possible transitions are opposite to the theoretical behavior of STT according with the direction of the electrons. This scenario could only be explained if there was an inversion of the sign of the $T_{\|}$ which does not seem physically possible for applied currents of this magnitude. On the other hand, all 3 R(I) plots shown in Fig.3.21 exhibit backhopping for large positive current polarities. Despite being unexpected in an ideal read mode setting, and also taking into consideration that the measurements performed on the elliptical junction demonstrate that positive current polarity destabilizes the AP-AP configuration, backhopping is thence just the natural reaction to the competition between in-plane and out-of-plane torques.

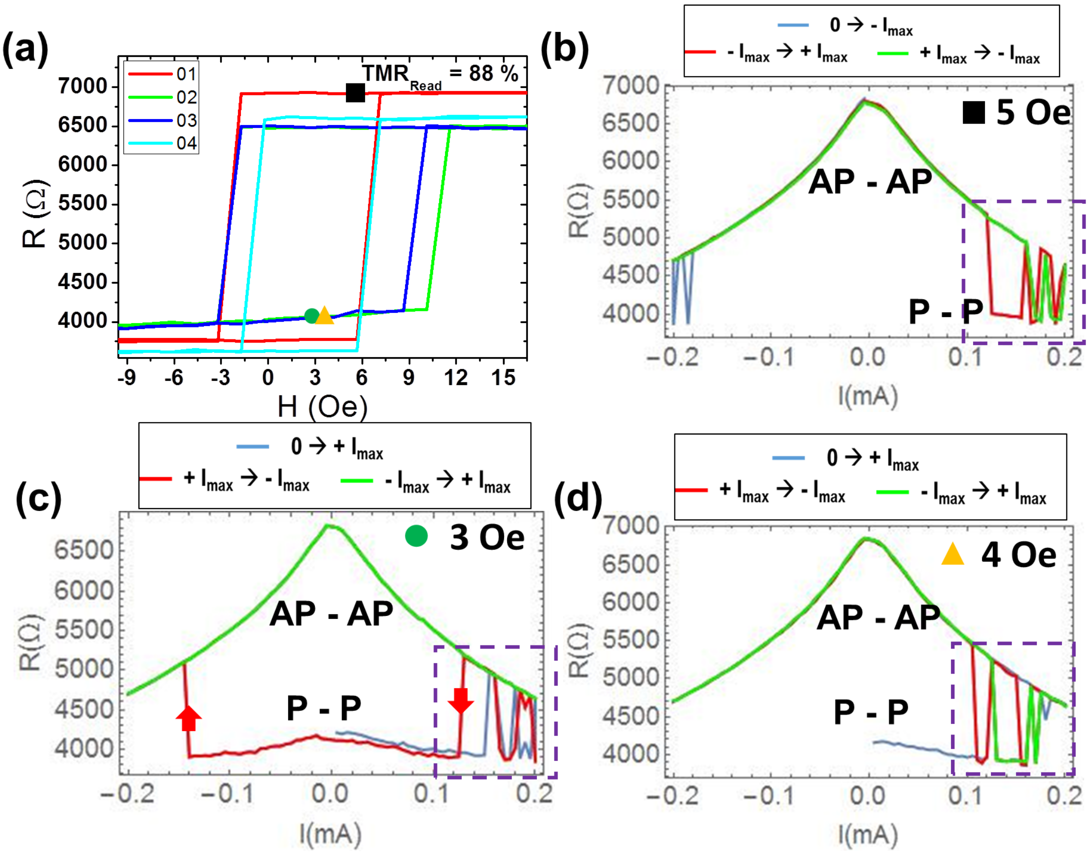

Figure 3.21: (a) Resistance vs. applied magnetic field for a asymmetric top thicker DBMTJ with circular cross section (real diameter = 127 nm). The numbers on the legend represent the sequence of measurement, each one after some current sweep measurements. The device presents a TMR of 88%. The symbols (square,circle and triangle) mark the applied field and initial magnetic state of the current sweep measurements performed. Resistance vs. applied current plots of (b) decreasing current sweeps starting from the AP-AP state and (c)-(d) increasing current sweep starting from the P-P state.

In order to have a base for comparison with write mode, for the elliptical junction, the switching current density at the offset field $J_{sw}(H_{off})$ was determined by extrapolation of the linear fit performed on the data points outside the yellow colored region [see Fig.3.19(a)]. The switching current density values for each transition are the following: $J_{sw}^{P-P \rightarrow AP-AP} =$ 1.60 MA/cm^2 and $J_{sw}^{AP-AP \rightarrow P-P} =$ 2.32 MA/cm^2. Surprisingly, the J_{sw} values obtained for the same asymmetric DBMTJ in write mode are higher than the ones hereby obtained in read mode.

3.2.2.B Asymmetric barriers: bottom thick barrier

We also studied the effects of DC current induced switching in asymmetric bottom thick barrier DBMTJs set in read mode. The R(I) measurements have been performed in several junctions with elliptical and circular cross sections. The obtained switching current densities for one junction of each geometry are displayed in Fig.3.22. For fair comparison, the critical switching current densities J_{sw} were evaluated at the center of the coercive area (H_{off}) where the energy barrier to overcome is supposed to be the same for the two transitions. In the case of the elliptical junction [Fig.3.11(a)], the switching current densities at H_{off} =-1.5 Oe are $J_{sw}^{P-P \rightarrow AP-AP} =$ 2.24 MA/cm^2 and $J_{sw}^{AP-AP \rightarrow P-P} =$ 3.35 MA/cm^2. Whereas for the circular pillar of Fig.3.11(b), H_{off} =-14 Oe and $J_{sw}^{P-P \rightarrow AP-AP} =$ 2.32 MA/cm^2 and $J_{sw}^{AP-AP \rightarrow P-P} =$ 0.85 MA/cm^2. The obtained values, in read mode, for the circular device are higher than those determined for a device of equal geometry in write mode. By contrast, the values obtained for the elliptical junction are similar to J_{sw} values determined in write mode. Despite the difference between read and write mode J_{sw} for the circular junction, the switching current densities in read mode are too close to the ones obtained in write mode to ensure no data corruption while reading.

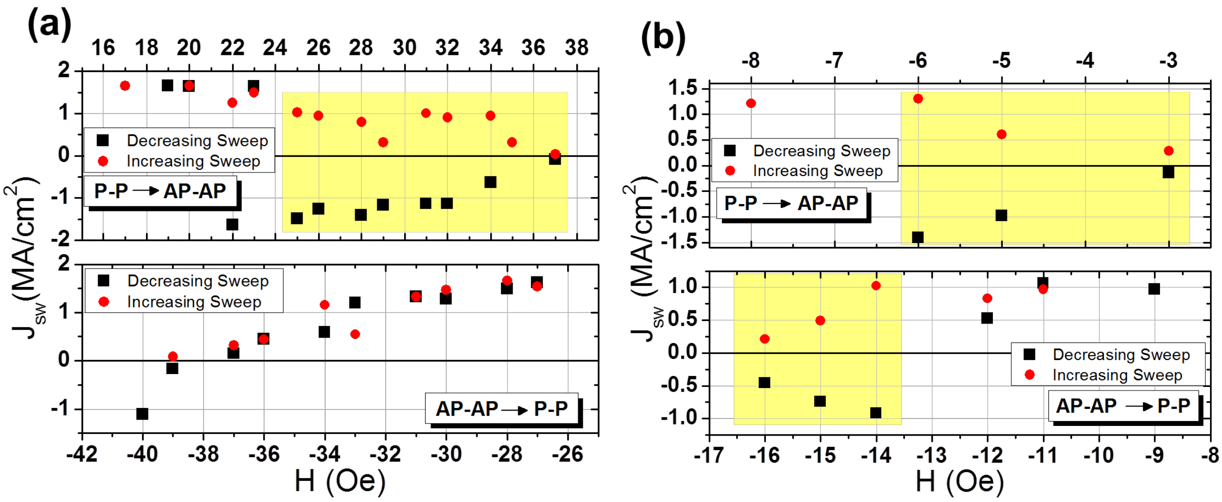

Figure 3.22: Switching current density in function of the applied field for asymmetric bottom thicker DBMTJs with (a) elliptical (real dimensions: 115 nm x 225 nm) and (b) circular cross section (real diameter: 185 nm). Decreasing (black squares) and increasing (red circles) sweeps were performed for both transitions. Yellow colored region represents the area where switching happened for both current polarities due to thermal fluctuations and low energy barrier near the coercive fields.

The bias polarity/transition qualitative analysis of the torques interplay has revealed no clear correlation between the direction of switching and the direction of the electrons. A result that is comparable to the one obtained in the previous subsection for the asymmetric barriers DBMTJ with a thick top barrier. According to theory, and taking into account Fig.3.20, with the position of the barriers inverted, the current bias polarity favoring a certain type of transition also inverts. Consequently, $I > 0$ favors now the P-P state and $I < 0$ favors the AP-AP state. Although in the junctions (chosen as examples) the positive bias favors all the transitions, in other measured junctions the two possible transitions were triggered by both current polarities, similarly to the asymmetric DBMTJs with top thick barrier. Besides not matching the theoretical description, this statistically polarity independent switching does not allow to understand the interplay of the two STT components on magnetization reversal.

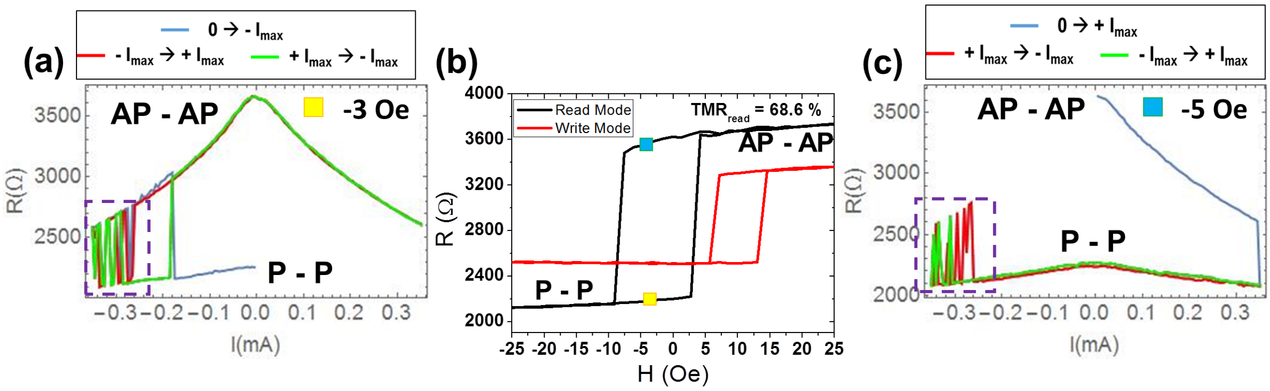

Figure 3.23: Resistance vs. applied current sweeps performed in an asymmetric bottom thick DBMTJ device with circular cross section ($\phi = 160nm$) set in read mode in an initial (a) P-P state and (c) AP-AP state. The purple dashed open squares highlight the zone where backhopping occured. (b) Read/write modes R(H) cycles. The square mark the position inside the coercive region where the displayed R(I) sweeps were performed.

Another way to evaluate the torques in a junction is through the analysis of backhopping events. In one of the measured circular junctions, backhopping was observed. Figures 3.23(a) and (c) display two R(I) plots where this telegraphic transitions were present. As mentioned before, when backhopping is observed for only one polarity of the applied current, it results from the competition between damping and field-like torque. Otherwise, backhopping is considered to be thermally induced. In the cases of the figure, backhopping occurs only for negative current polarity. As above mentioned, this is the same polarity which, according to theory and position of the thicker barrier, favors the P-P→AP-AP transition. Thus, if the results were in line with theory, for negative bias, in-plane and out-of-plane torques favor that same transition and backhopping (from torque competition) should then be observed for the opposite bias polarity. The same disagreement with theory in a circular junction where backhopping was observed happened in section 3.2.2.A.

Although no correlation of the switching events with the bias polarity in both type of asymmetric DBMTJs (top thick barrier and bottom thick barrier) could have been done, the results of the backhopping events showed some coherence with the change of position of the thick barrier of the DBMTJ. Despite the torque mediated backhopping events have only been observed in one circular junction of each type of asymmetric barriers DBMTJ, their consistency in polarity change with dominant barrier position change may allow for a conclusion on the torques interplay in these asymmetric barrier DBMTJ set in read mode. Allowing for an interpretation in opposition to theoretical predictions, for asymmetric DBMTJs with bottom thick barrier, the AP-AP→P-P transition is triggered by negative current. Whereas the same transition is triggered by positive current for asymmetric DBMTJs with top thick barrier. The polarity dependent effects are result from residual in-plane torque while the maximized field-like torque (in read mode) favors the AP-AP state.

Figure 3.24 presents very rare (only observed twice) results of DC current measurements performed in asymmetric DBMTJ with bottom thick barrier. This peculiar result is shown and analyzed in order to record one of the possible consequences of multiple measurements and mode switchings in DBMTJs. First by analyzing the R(H) cycles of Fig.3.24(b) we notice that the resistance of the write mode AP-P state is larger than the resistance of the read mode AP-AP state. Figure 3.3(d) presents normal R(H) read/write mode cycles for asymmetric bottom thicker DBMTJs where the maximum resistance state is the AP-AP. It is, however, important to state that this junction was set initially in write mode by annealing under a 1T magnetic field and R(I) sweeps were performed before it switched to read mode by mode switch caused by Joule effect under applied current and field. Figure 3.24(a) presents resistance as a function of applied current for the junction prepared in read mode. In this specific case, the applied current is not high enough to cause STT switching of the storage layer. However, an interesting and asymmetric resistance dependence with current bias polarity is observed. Resistance decreases with both current polarities but the trend is much more pronounced under positive bias. This asymmetric behavior is translated by the difference of resistance $\Delta R = 45\Omega$ when $|I| = 0.4mA$ at opposite polarities. This asymmetry also exists when the DBMTJ is in the AP-AP state [Fig.3.24(c)] though now $\Delta R < 15\Omega$. This anomalous resistance bias dependence may be connected with structural differences between the ferromagnet/oxide interfaces [105] around top and bottom barriers.

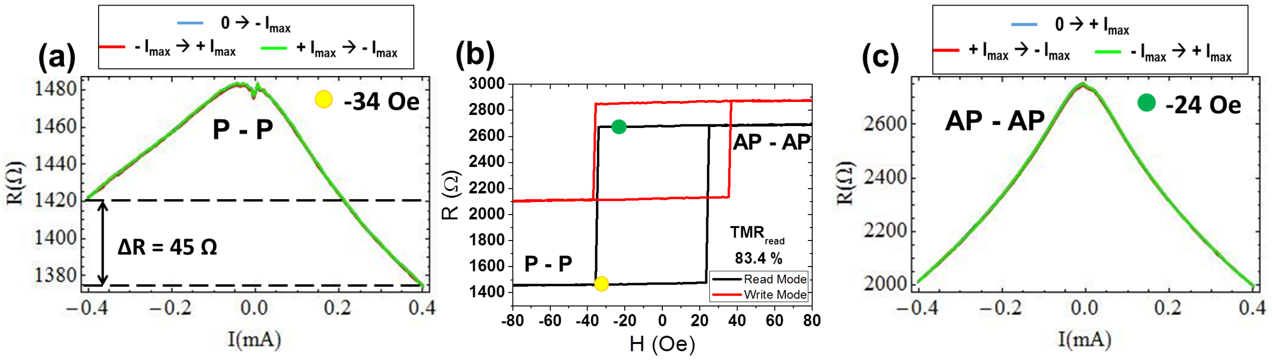

Figure 3.24: R(I) sweeps performed in a selected asymmetric bottom thicker DBMTJ (real dimensions: 115 nm x 225 nm) set in read mode with inital (a) P-P state and (c) AP-AP state. When in the low resistance state, the device present an asymmetric resistance dependence with bias current. (b) The respective read and write mode R(H) cycles. The colored circles point the applied field and initial magnetic state for each of the R(I) sweeps.

As seen before, MTJs have two types of conductivity regimes: ohmic at low bias, whereas for large bias the dynamic conductance has an almost parabolic dependence with DC bias [106]. Resistance and TMR dependence with bias voltage has been heavily studied and several experiments have been conducted around the late 1990s [16, 105, 107–110]. While the cusp-like peak feature at zero bias was attributed to magnon excitations at the ferromagnet-insulator interface ("hot electrons") [95], the behavior at higher bias was thought to be deeply connected with the quality of the interface, barrier type and the materials used for the ferromagnets. Moreover, it was proven that the materials chosen for the insulating barrier and ferromagnets, and thence their interfaces change the sign of the spin polarization of the junction [109, 110]. These factors associated with possible defects on the barrier make that, in the nonlinear regime of conductivity, the tunneling from the bottom electrode to the top electrode is not equivalent to tunneling in the opposite direction. This leads to experimental asymmetric I(V) curves which do not match the theoretical predictions previously made by Simmons [111].

If we focus on Fig.3.24(a) and remember the direction of the electrons for negative and positive current, we can see the spin-dependent electrons experience more spin flip scattering with positive current than with negative. It seems that the electrons which first "see" the bottom barrier ($I > 0$) experience less resistance than those first crossing the top barrier ($I < 0$). Moreover, the resistance asymmetry with bias current was not observed in the same device when in write mode. Therefore, it is possible that the multiple current sweeps combined with an increase in temperature may have caused the deterioration of one of the barriers, rendering it more metallic, hence less resistive.

3.2.2.C Symmetric barriers

STT switching in DBMTJs with symmetric barriers set in read mode has also been studied. Figure 3.25 presents the results of current sweeps performed on two different junctions with symmetric (a) thick barriers (RA = 45 $\Omega.\mu m^2$) and (b) thin barriers (RA = 10 $\Omega.\mu m^2$). The devices chosen are simple examples and do not represent the general results since these did not reveal any clear correlation between current polarity and state transition. In the example junction of Fig.3.25(a), the P-P→AP-AP transition is favored by positive current whereas the AP-AP→P-P transition is favored by negative current. For the chosen example of a junction with symmetric thin barriers [Fig.3.25(b)], both transitions are favored by a positive bias.

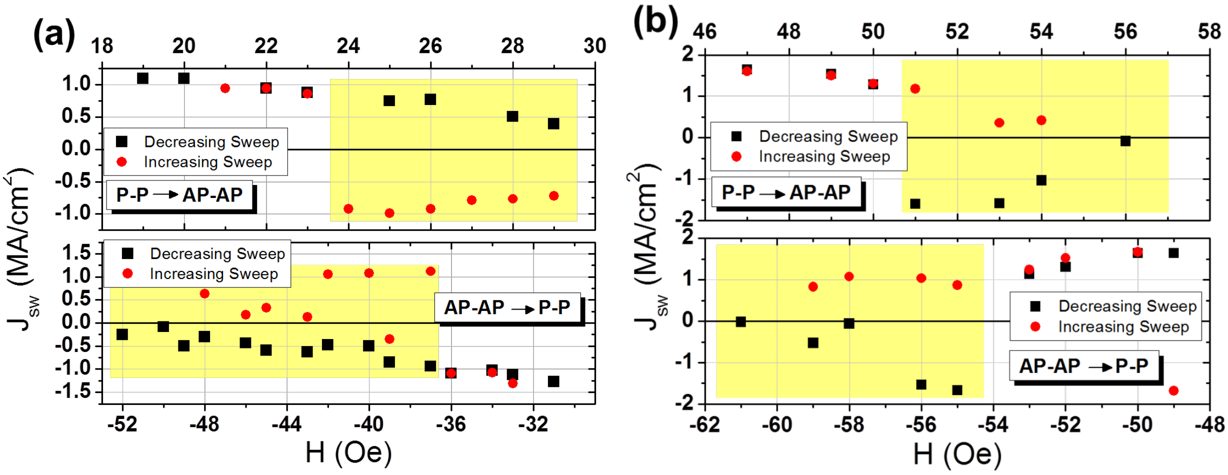

Figure 3.25: Switching current density as a function of the applied field for elliptical cross section symmetric DBMTJs of with: (a) thick barriers - RA = 45 $\Omega.\mu m^2$ and (b) with thin barriers - RA = 10 $\Omega.\mu m^2$ (both junctions present real dimensions of: 170 nm x 250 nm). Decreasing (black squares) and increasing (red circles) sweeps were performed for both transitions. (a) The P-P→AP-AP transition is favored by $I > 0$ and AP-AP→P-P transition is favored by $I < 0$. (b) Both transitions are favored by $I > 0$. Yellow colored region represents the area where switching happened for both current polarities due to thermal fluctuations and low energy barrier near the coercive fields.

According to theoretical predictions, in the case of perfectly symmetric barriers, no STT switching should be observed in this mode as the torques acting on the storage layer, and coming from reference layer $T_{\|r}$ and control layer $T_{\|c}$, cancel each other. Nevertheless, the two barriers are never completely symmetric otherwise $TMR_{write} = 0$, which we have never experimentally observed. As already discussed in section 3.2.1.C, for the majority of the junctions, the top barrier presents slightly higher RA and TMR values than the bottom barrier, thus being the dominating one. Therefore, a residual in-plane component of STT could be responsible for STT switching as described in a theoretical picture by Fig.3.20. For the junction of Fig.3.25(a), the relation between magnetic state and switching current polarity matches the theoretical description. However, the same is not verified for the junction of Fig.3.25(b). In order to improve our interpretation of symmetric DBMTJs in read mode, several more devices were measured. Unfortunately, the destabilization of any of the two states was triggered by either one or the other current polarities with some asymmetries but that change from device to device randomly. Concerning $J_{sw}(H_{off})$, for the device (a): $J_{sw}^{P-P \rightarrow AP-AP}$ = 2.80 MA/cm^2 and $J_{sw}^{AP-AP \rightarrow P-P}$ = -2.15 MA/cm^2, while for device (b): $J_{sw}^{P-P \rightarrow AP-AP}$ = 5.95 MA/cm^2 and $J_{sw}^{AP-AP \rightarrow P-P}$ = 6.03 MA/cm^2. The considerable difference of J_{sw} between symmetric DBMTJs with thick and thin barriers may be related with superior thermal effects present in the DBMTJs with thick barriers. This thermal effect helps on reducing the current needed to trigger STT induced switching.

Despite only showing results on elliptical junctions, we have also tried to perform the same measurements on junctions with circular shape. However, due to their low endurance, we were not able to conclude a complete set of measurements to include here, before reaching breakdown. Moreover, in circular geometry devices, we tried to evaluate backhopping as one of the possible ways to study the interplay of both STT components. Yet, the only backhopping observed was due to thermal fluctuations of the switching field (H_c) (similarly to the one observed in Fig.3.8) since it happened indiscriminately for both current polarities.

In summary, the obtained results are surprising, relatively to the theoretical predictions and do not meet the initial purpose of a ”switching free” mode. The same problems observed by P.-Y. Clément [1] were again retrieved with the aggravating factor of having observed AP-AP→P-P switching besides the P-P→AP-AP. The read mode transitions, in all three types of DBMTJs, do not show any correlation with a bias polarity. Neither the position of the thicker barrier shows any particular influence on the switchings. The only observed exceptions are the backhopping events which exist for opposite polarities with different positions of the thicker barrier. Concerning symmetric barriers DBMTJs, comparatively to those of ref. [80], ours were of superior symmetry ($TMR_{write} < 10\%$), which means that total in-plane torque should be even lower, thus a lower probability of STT switching. Along with the confusing dependence of STT with bias polarity, the J_{sw} values are within the range of those found for DBMTJs in write mode, jeopardizing the reliability of written data. It was also expected that less current would be necessary to switch from P-P to AP-AP since field-like torque (maximized in read mode), should assist the remnant damping-like torque. Though the obtained data does not support this claim. Once again, the bias polarity dependent backhopping events observed in the asymmetric barriers DBMTJs are the only evidence of the competition between damping-like and field-like torque. Globally, the randomness of the obtained results may come from the type of measurements performed where thermally activated switching is dominant and may overshadow the STT induced switching.

3.3 Voltage Pulses Measurements

In the previous chapter, the STT induced switching was triggered by DC current with a large active time τ in the order of milliseconds. This pulse width regime ($\tau > 100\,ns$) is the thermally activated regime in which thermal fluctuations help the magnetization to overcome the energy barrier thus inducing its reversal. Moreover, this type of regime can easily set off undesired thermal backhopping. In the specific case of DBMTJ, the addition of a second barrier also acts as a heat tampon, increasing the temperature inside the junction as well as slowing its dissipation [112]. In spite of the positive results obtained for write mode, the read mode revealed unwanted switchings for all the types of DBMTJs measured. While the P-P→AP-AP transitions could easily be explained by the presence of a strong field-like torque in read mode, those in the opposite direction were completely unexpected and could not be related with theoretical descriptions of STT. However, in some devices, switching occurred regardless of current polarity which hints at the possibility of a strong thermally assisted switching.

In order to tackle the aforementioned temperature issue, similar measurements were performed but with an applied bias voltage with a pulse width $\tau \approx 30 - 100\,ns$. Although not yet in the precessional (or ballistic) regime ($\tau < 10 - 20\,ns$), within this range the switching dynamics is close to macrospin and the thermal fluctuations are reduced. The switching current densities $J_{sw}(\tau)$ are thus expected to increase and to come closer to the intrinsic switching current density J_{sw0} (see Eq.(1.43)).

3.3.1 Experimental Setup and Method

Figure.3.26*(left)* presents a schematic representation of the wafer probing setup used to measure the DBMTJs by applying short voltage pulses. The wafer is placed under the electromagnetic coils with elongated magnetic core that concentrate the magnetic flux in a direction parallel to the plane of the wafer. The current applied to the coils of the electromagnet is supplied by a Kepco power source. This power source is controlled by a wave generator which enables to control the frequency of the input current, and thence the frequency of the applied magnetic field. The field is typically swept at frequencies between 5 - 15 Hz, which are limited by the inductance of the coils. Between the coils, a RF probe is in contact with the wafer: it delivers the applied voltage and it allows a subsequent measurement of resistance at lower bias. The voltage pulses, whose properties are set by the waveform generator, are created at the pulse generator and then sent via the AC port of the bias tee while the low continuous bias to measure the resistance is sent through the DC port of the bias tee. The low DC bias is generated and the junction resistance measured by the sourcemeter.

The phase diagrams shown in the following sections were obtained by performing several R(H) loops for different applied voltages. The measurement method to obtain the phase diagrams is given by the scheme in Fig.3.27. As mentioned in the paragraph above the magnetic field is swept thanks to an electromagnet. At each field step, a pulse generator delivers pulses. In the same field step, the resistance level is measured thanks to a low current delivered by a sourcemeter and the voltage measured thanks

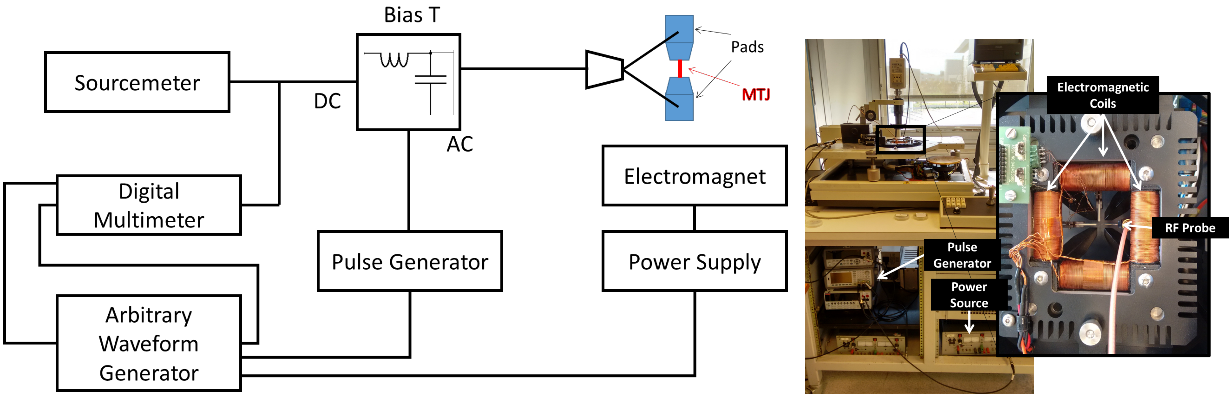

Figure 3.26: *(Left)* Schematic picture of the experimental setup used to measure the Voltage-Field Resistance phase diagrams. Adapted from [113]. *(Right)* Photo of the experimental setup with all the apparatus. Zoom of the electromagnetic coils and RF probe under which the wafer is placed.

to a digital multimeter. The field loops are repeated with a varying pulse voltage amplitude. The pulse voltage sequence starts from low amplitude pulses of positive voltage followed by same amplitude pulse but of negative voltage, increasing its amplitude from there on. While maintaining the intermittence between positive and negative voltage. The resistance level calculated as a function of voltage and field showed in the final diagram is an average value of the multiple cycles performed for each voltage pulse amplitude value.

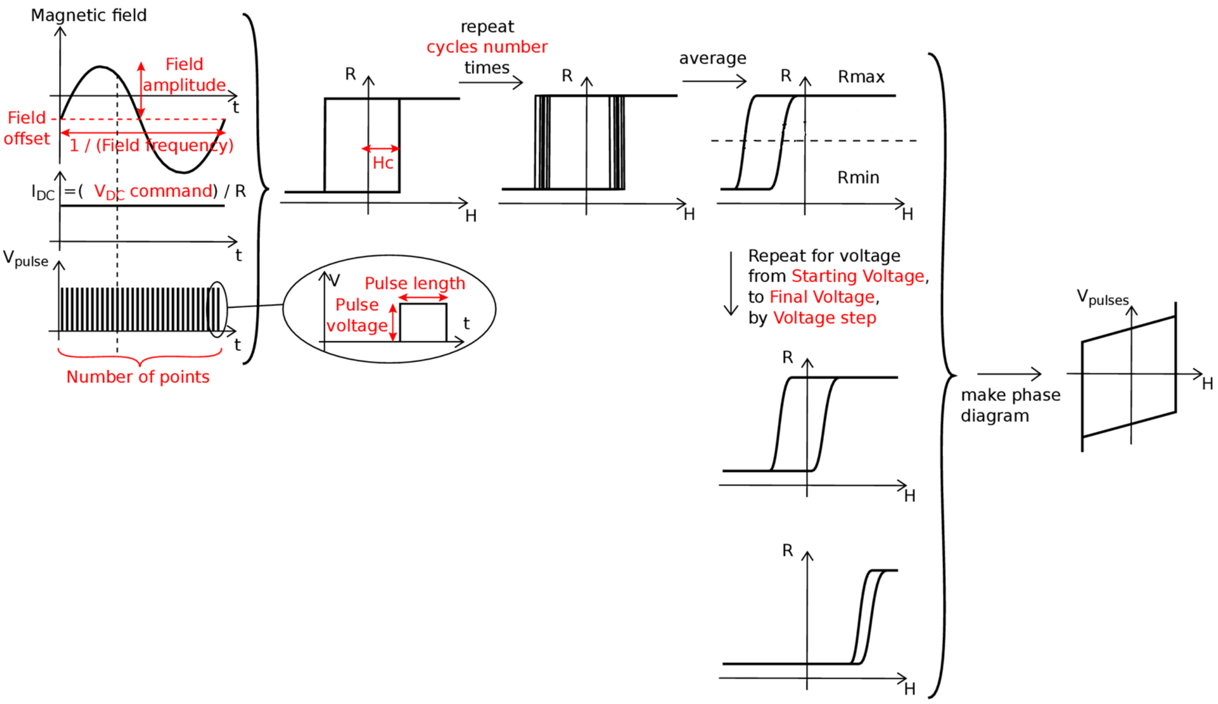

Figure 3.27: Measurement method for pulsed voltage switching phase diagram.

The two possible output phase diagrams present resistance in two different sets of units: arbitrary (a.u) or S.I. units in Ohms. Figure 3.28(a) presents one example of the phase diagram with resistance in arbitrary units. In this phase diagram, the measured resistance R is normalized to 0-1 range through a simple calculation $\frac{R-R_{min}}{R_{max}-R_{min}}$. Therefore, the color code gradient varies from 1 - red (corresponding to R_{max}) down to 0 - blue (corresponding to R_{min}). Whereas in Fig.3.28(b) the same color code is used but attached value scale shows the measured resistance values.

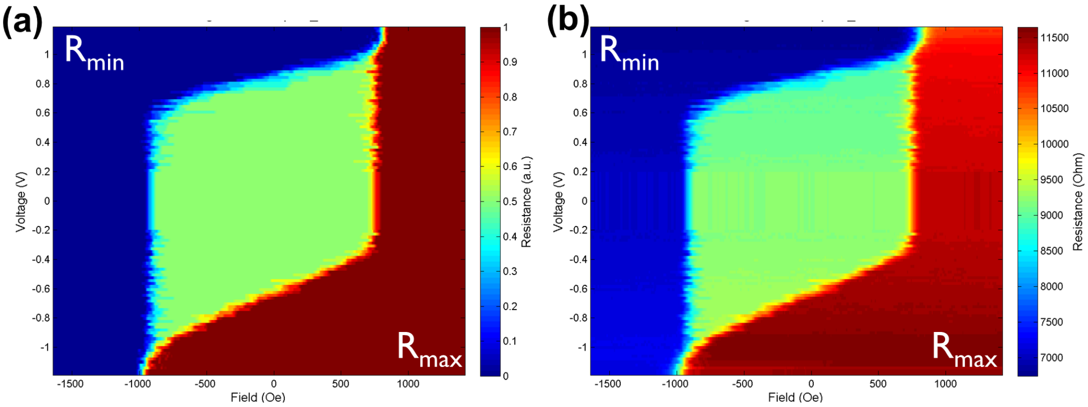

Figure 3.28: Example phase diagram of the resistance as a function of voltage and field where the color code corresponds to (a) a normalized value of resistance or (b) the real measured resistance in S.I. units.

3.3.2 Write Mode

For the measurements of this section, the DMTJs were set in write mode via annealing under applied magnetic field. Some parameters were fixed: pulse width $\tau = 100\,ns$ and frequency of the magnetic field $f_H = 7\,Hz$. The number of R(H) loops varied between 8-10. The devices measured in the automatic wafer probing setup are not exactly the same as those measured in the DC current setup since only two-point probe measurements were allowed. As the lithographic masks used for the in-plane anisotropy DBMTJs were specially designed for four-points measurements, only some devices could be tested. Nonetheless, statistically, the measured devices can be compared to those of section 3.2 since they still belong to same wafers. Regarding the polarity of the applied voltage pulses and the direction of electrons, the measurements were performed as represented in Fig.3.4. Exceptions to this configuration are carefully indicated in the text and in the caption of the concerned phase diagrams.

3.3.2.A Phase diagrams: global qualitative analysis

In this section, we present a global qualitative analysis of the different phase diagrams measured for each type of in-plane DBMTJ set in write mode as well as a single barrier MTJ used for comparison. Figures 3.29, 3.30, 3.31 and 3.32 present representative phase diagrams of DBMTJs with, respectively, asymmetric thicker top barrier, asymmetric thick bottom barrier, symmetric thick barriers and symmetric thin barriers. For each type of DBMTJ (except for the DBMTJ with symmetric thin barriers), we present two different phase diagrams with (a) a rarely or (b) a more commonly observed STT behavior. We measured: 26 asymmetric DBMTJs with a thicker top barrier (23% presented the rare behavior), 20 asymmetric DBMTJs with a thicker bottom barrier (30% presented the rare behavior), 13 symmetric DBMTJS with thick barriers (23% presented the rare behavior) and 3 symmetric DBMTJS with thin barriers. Regarding the uniformity of the measured devices, for each type of DBMTJ, the deviations in resistance (for devices with the same nominal dimensions) are below 15% which reveals a DBMTJ size variation with the same percentage. This result allows to compare STT among the presented devices since they present very similar thermal stability factors Δ.

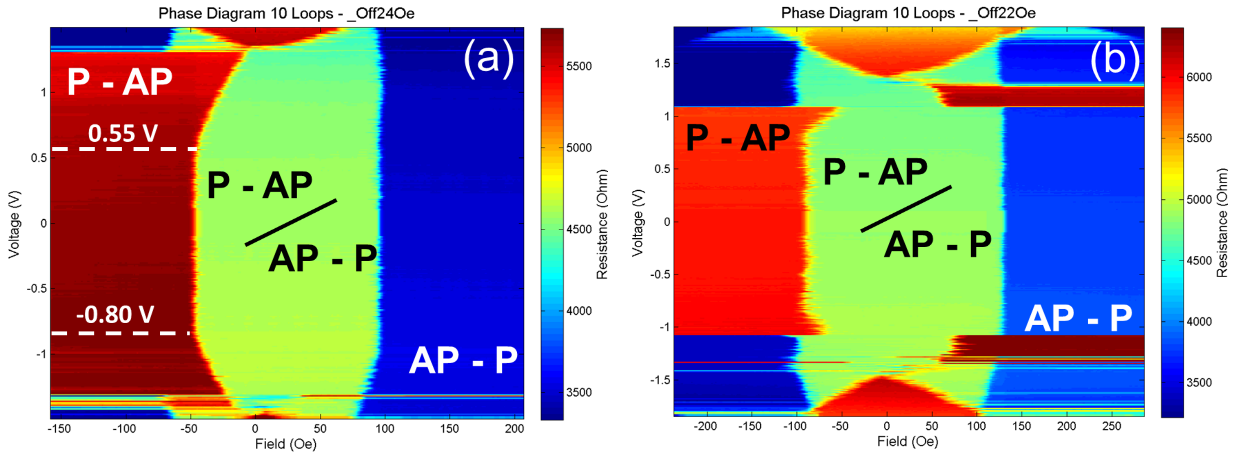

Figure 3.29: Phase diagrams of asymmetric barriers DBMTJs with a thicker top barrier with a (a) rarer and (b) more common STT behaviors, set in write mode. Both devices have elliptical cross section and nominal dimensions of $140\,nm \times 40\,nm$. The maximum applied voltages were (a) 1.5 V and (b) 1.85 V. The color gradient represents the resistance, from high (red) to low (blue) resistances. The strange color inversion happening at high voltages correspond to mode switch.

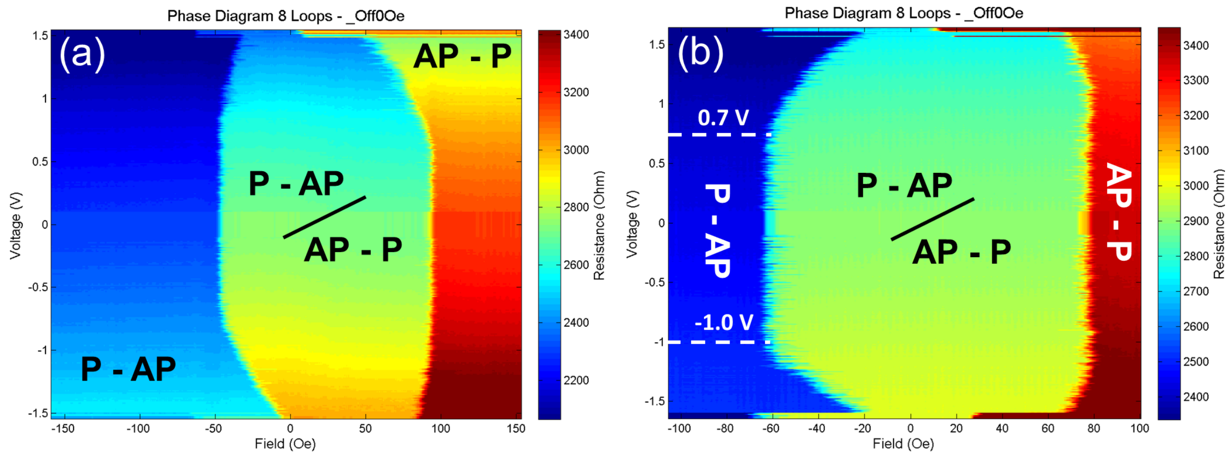

Figure 3.30: Phase diagrams of asymmetric barriers DBMTJs with a thicker bottom barrier, set in write mode, with a (a) rarer and (b) more common STT behaviors. Both devices have elliptical cross section and nominal dimensions of $140\,nm \times 40\,nm$. The maximum applied voltages were (a) 1.5 V and (b) 1.65 V. The color gradient represents the resistance, from high (red) to low (blue) resistances. Note: The voltage polarity is inversed in (a).

Before comparing the different phase diagrams, it is important to clarify the strange behavior observed at high voltages in the phase diagrams of Fig.3.29(a)-(b), Fig.3.31(b) and Fig.3.32(a)-(b). For large absolute voltage amplitudes, some color inversions occur and a stable state P-AP or AP-P reverses to P-P or AP-AP which suggests that the control layer reverses. In fact, the colors intermixing suggests that the DBMTJ has changed mode, thus leading to an inversion of the high/low resistance states with field. This has already been mentioned before and it is called mode switch whose origin is explained later in section 3.3.5. Figure 3.33 shows the R(H) loops measured at voltage pulse amplitudes (± 1.4 V) where the mode switch happens for the asymmetric DBMTJ with thicker top barrier of Fig.3.29. For both cases, four states in resistance exist within the same loop which means that the free layer rotates together with the control layer. Therefore, the beginning of the color inversion points to the maximum value in voltage where the write mode is stable. Our analysis of the phase diagrams is thus

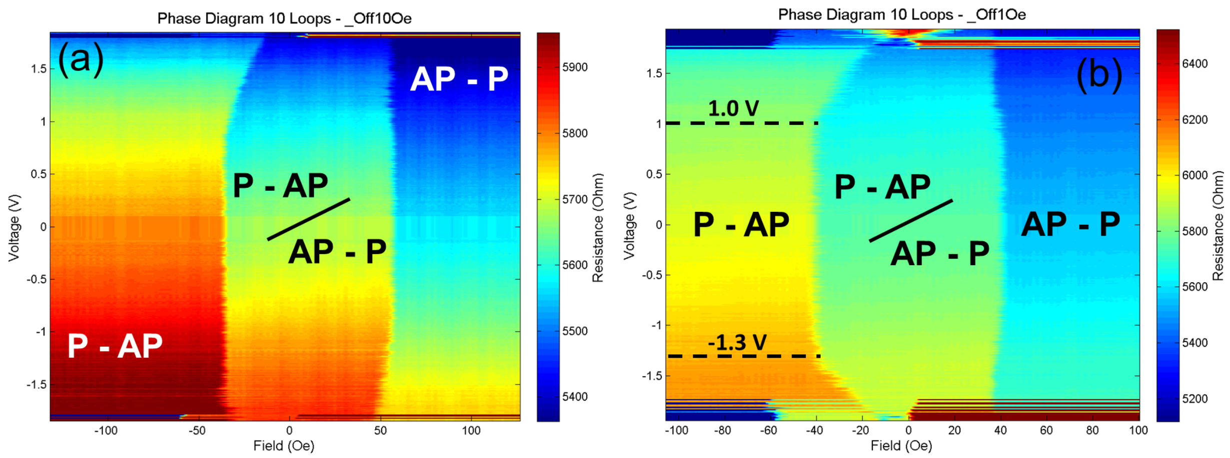

Figure 3.31: Phase diagrams of DBMTJs with symmetric thick barriers ($RA_{top} = RA_{bottom} = 45\,\Omega\mu m^2$), set in write mode, with a (a) rarer and (b) more common STT behaviors. Both devices have elliptical cross section and nominal dimensions of $140\,nm \times 40\,nm$. The maximum applied voltages were (a) 1.85 V and (b) 1.95 V. The color gradient represents the resistance, from high (red) to low (blue) resistances.

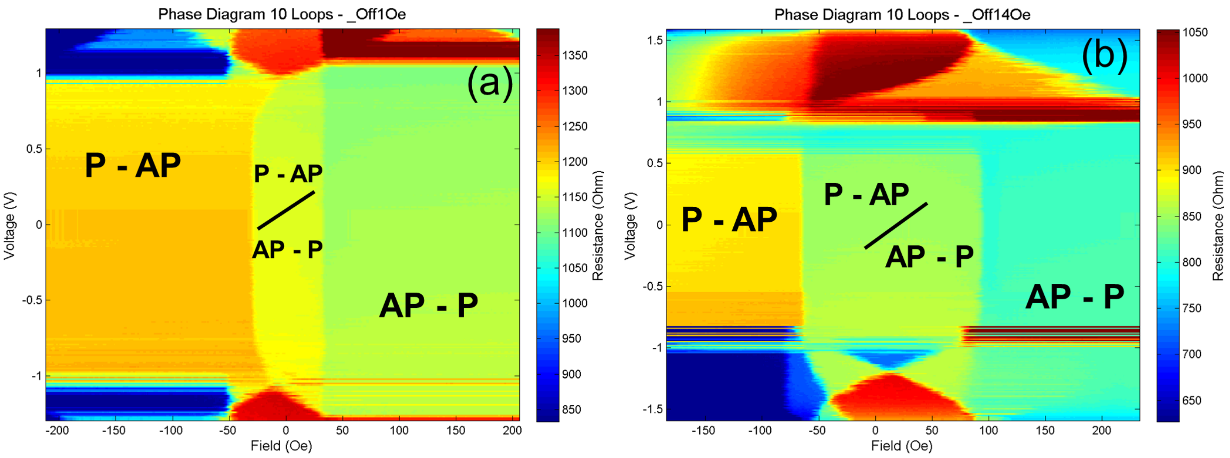

Figure 3.32: Phase diagrams of DBMTJs with symmetric thin barriers ($RA_{top} = RA_{bottom} = 10\,\Omega.\mu m^2$), set in write mode. Mode switch happens for (a) $|V| > 1$ V and (b) for $|V| > 0.5$ V Both devices have elliptical cross section and nominal dimensions of $140\,nm \times 40\,nm$. The maximum applied voltage was 1.3 V for both devices. The color gradient represents the resistance, from high (red) to low (blue) resistances.

confined to voltages below this mode switch triggering point.

First, we analyze the common feature among the phase diagrams with a rarer STT behavior. In fact, the shared feature is the presence of an observable damping-like torque which presents a linear dependence with applied voltage $T_{\|} \approx a_1 V$. In the phase diagrams of figs.3.29(a), 3.30(a) and 3.31(a), the P-AP state is favored by positive voltage and the AP-P state by negative voltage [12]. The direction of the electron flow is coherent with the theoretical description of STT with the usual polarity convention and follows the results obtained from the R(I) sweeps of subsection 3.2.1. Nevertheless, among the referred phase diagrams, only those belonging to asymmetric DBMTJs with a thicker bottom barrier and a DBMTJ with symmetric thick barriers show exclusively the linear trend with voltage of the damping-like torque. In the phase diagram of Fig.3.29(a) (asymmetric DBMTJ with thicker top barrier), the P-AP state

---

[12] This is not true in Fig.3.30(a) because the measurement was conducted with probes in the inverse position of the standard measurement of Fig.3.4. Therefore the electrons direction was inverted and the P-AP and AP-P states are favored by the opposite polarities of a normal measurement.

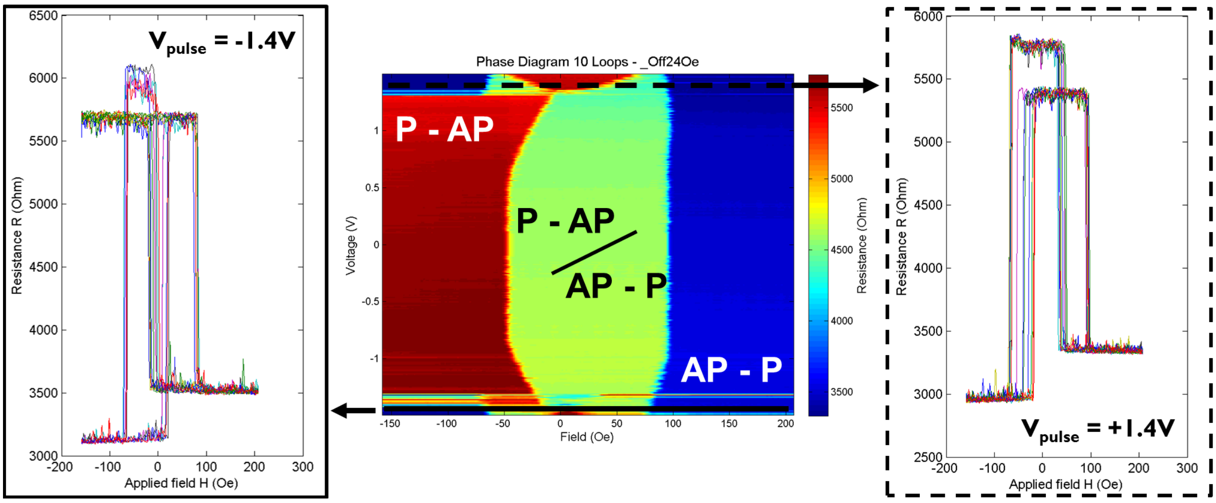

Figure 3.33: R(H) loops for voltage pulse amplitudes -1.4 V and +1.4 V of the phase diagram of Fig.3.29(a) where mode switch effect is visible.

is also favored by negative voltage. This even dependence with voltage is typical of field-like torque which, besides being of the form $T_\perp \approx b_2V^2$, favors the AP state around the dominant barrier [114], consequently favoring P-AP. A more careful look on this phase diagram shows that the effects of STT do not start at the same voltage amplitude for positive and negative polarity. The white dashed lines mark the starting point where coercivity starts to drop. The torque exerted for a positive polarity is stronger than for negative since its effect starts at ≈0.55 V, while for negative polarity the torque effects only start at ≈-0.80 V. This asymmetry is due to the presence of a field-like torque component which is expected when the barriers are asymmetric since $|T_\perp^r - T_\perp^c| \neq 0$.

The most observed behavior in the majority of the phase diagrams [figs.3.29(b), 3.30(b), 3.31(b) and 3.32(a)] shares the even dependence in voltage favoring the AP-P→P-AP transition. In the cases of the asymmetric DBMTJ with top thicker barrier and the two types of DBMTJ with symmetric (thick and thin) barriers, the result is explained by the presence of a strong field-like torque which favors the AP state around the thicker barrier. Although this explanation is easily accepted for the case of the asymmetric barriers DBMTJ, for the DBMTJs with symmetric barriers it deviates more from theory which states that, in write mode, the two torques cancel each other out ($T_\perp^r - T_\perp^c = 0$). This result only adds to the previous ones which demonstrate an asymmetry in the two barriers RA, even if they were set nominally symmetric. In our nominally symmetric barriers DBMTJs, it is the top barrier which demonstrates an higher RA product. The linear in-plane torque component is non-negligible in the symmetric barriers DBMTJ of Fig.3.31(b) and eases the storage layer switching towards a P-AP state. The free layer full STT (damping-like + field-like) assisted reversal is possible for V $>$ 1.0 V, whereas field-like torque only enables switching for V $<$ -1.3 V. The case of the phase diagram of Fig.3.30(b) is much more complex to analyze. A quick, though inattentive, analysis suggests that the bipolar favoring in voltage of the P-AP state could be attributed to either field-like torque either thermal effects since the latter are non-dependent of the voltage polarity. The thermal effect is clearly present since we are in the thermally assisted switching regime however they do not explain why the P-AP state is favored under lower voltages than the AP-P state. Pure thermal effects would shrink the bi-stable region [in green in

Fig.3.30(b)] evenly with increasing applied voltage. In addition, this scenario is not easily explicable via a normal field-like torque since an antiparallel magnetic configuration between reference and storage layers was expected around the thicker barrier, corresponding to the AP-P state. According to Bernert *et al.* [60] simulations, the only way to have the curvature of the boundary favoring the low resistance state (P state, in their case with single barrier MTJ) was to set the field-like torque negative. For the moment, no reports in literature suggest the possibility of a negative field-like torque prefactor with quadratic dependence on voltage that favors the parallel alignment of two magnetizations around the tunnel barrier. Another possible explanation is to assume the top barrier to be the dominant one for STT. Taking into account the conical shape of the DBMTJ (effect of ion milling angles on the pillar shape), the top barrier should have a smaller area. For a same current, it corresponds to a higher current density J on that barrier and since torque is carried by the electrons, a higher number of electrons traveling across the top barrier would mean a higher torque being applied from the top barrier interface with the free layer.

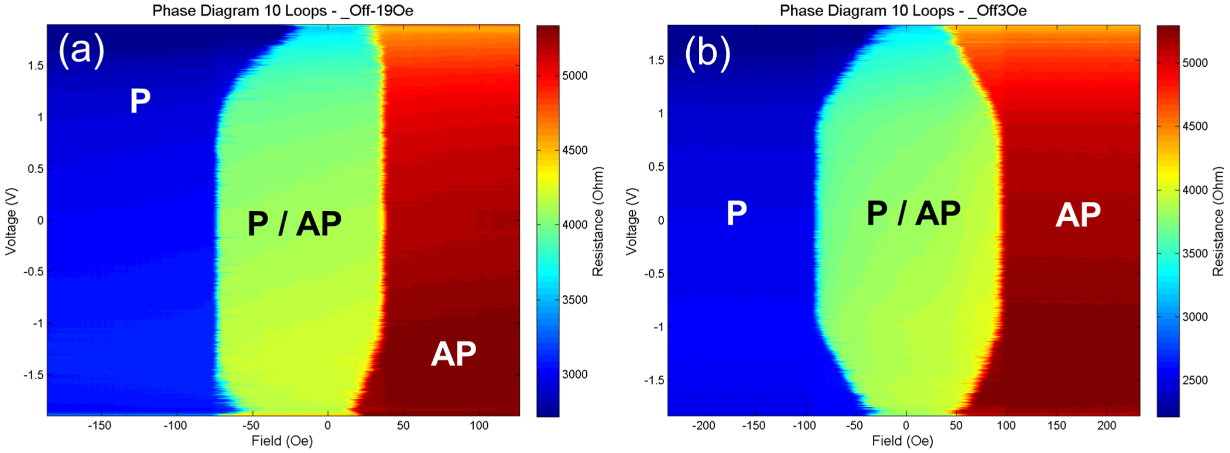

Figure 3.34: Phase diagrams of single barrier MTJs ($RA = 35\,\Omega.\mu m^2$) with (a) expected STT behavior and (b) predominance of thermal switching. Both devices have elliptical cross section and nominal dimensions of $140\,nm \times 40\,nm$. The maximum applied voltages were (a) 1.9 V and (b) 1.85 V. The color gradient represents the resistance, from maximum (red) to minimum (blue) resistances.

We performed similar measurements on single barrier MTJs with ($RA = 35\,\Omega.\mu m^2$). Figure 3.34 presents the phase diagrams of two chosen MTJs that exhibit (a) the expected STT behavior and (b) a quasi-absence of STT, with the storage layer switching being mostly driven by thermal effects. Relatively to voltage polarity and STT, in Fig.3.34(a), positive voltage favors the stabilization of a parallel (P) alignment between free and reference layers whereas negative voltage favors the antiparallel (AP) alignment between them. This is in agreement with the theoretical description of an active in-plane torque. On phase diagram (b) from $|V| > 1\,V$ the coercivity H_c of the free layer reduces linearly with voltage. In this case, we do not observe any dependence on the direction of injected electrons (voltage polarity), therefore no correlation with STT. This H_c reduction is a consequence of Joule heating due to current injection that will induce a reduction of the magnetic anisotropy H_k of the system. The coercivity evolution with temperature T [115] may be expressed by adapting the Néel-Brown formula [66, 116] as follows:

$$H_c(T) = H_k \left(1 - \sqrt{\frac{2k_b T ln(f_0/f_H)}{M_s H_k V}}\right), \tag{3.6}$$

where f_H is frequency of the magnetic field, f_0 is the attempt frequency ($10^{10}\,s^{-1}$) and V is the volume of the free layer.

3.3.2.B Determination and analysis of critical switching quantities

Besides the qualitative analysis on the phase diagrams, we have also determined the critical switchings voltages (V_c) for AP-P→P-AP and P-AP→AP-P transitions in DBMTJs and for P→AP and AP→P transitions in the case of single barrier MTJ. The critical switching voltages were obtained by linear fitting the phase boundaries of the phase diagrams. Figures 3.35 and 3.36 shows examples of the extracted phase boundaries and respective linear fits performed, for the case an asymmetric DBMTJ with thicker top barrier and single barrier MTJ, respectively. In order to visually isolate the effects of the damping and field-like torques, the data points corresponding to even effects in voltage (around V = 0) and mode switch (usually for $|V| \gg 1$) were deleted from the extracted phase boundaries and not considered for fitting. The critical switching voltages (one for each boundary) were determined at $H = H_{off}$ which is the center of the bi-stable region thus equally spaced in field from either of the static field switching boundaries (*i.e.* coercive field). At the center of the bi-stable region, the effect of the magnetic field on switching should be the same for both transitions therefore at this point the switching should only be driven by STT. The phase boundaries linear fittings were also performed for other selected DBMTJs of each type (asymmetric or symmetric).

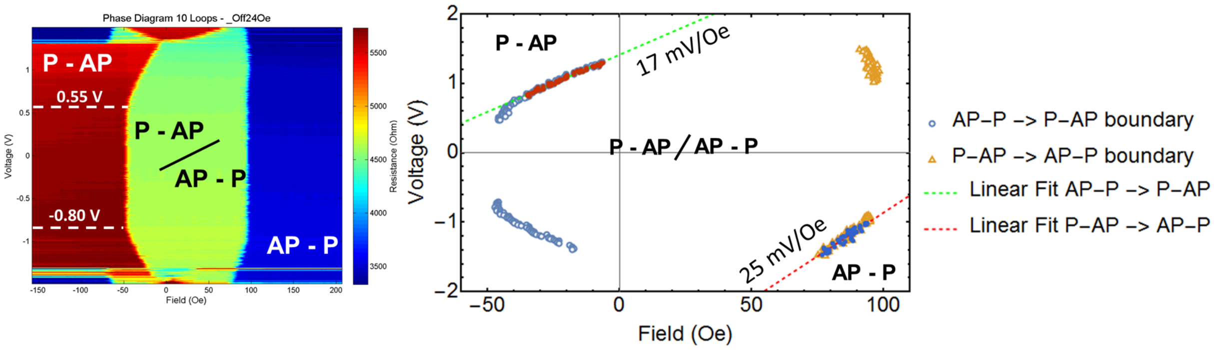

Figure 3.35: Linear fits of the boundary lines of phase diagram at the left side [same as in Fig.3.29(a)]. The data points used for the fit are represented by the full circles in red and blue colors. The fitted slopes are displayed next to each fitted dashed line.

Table 3.4 presents the critical switching voltages, for both transitions, for the analyzed DBMTJs set in write mode. The critical switching current density (J_c) is derived from V_c and also shown in the table. In order to have an indicator of the STT efficiency, we chose to calculate the figure of merit Δ/I_c. Since all the chosen junctions have similar areas and the free layer thickness is the same, we fixed the value of thermal stability factor $\Delta = 40$ (based on the values obtained in section 3.2) both for DBMTJ and single barrier MTJ. The last two rows of the table show the results obtained for the single barrier MTJ which serve as reference for comparison.

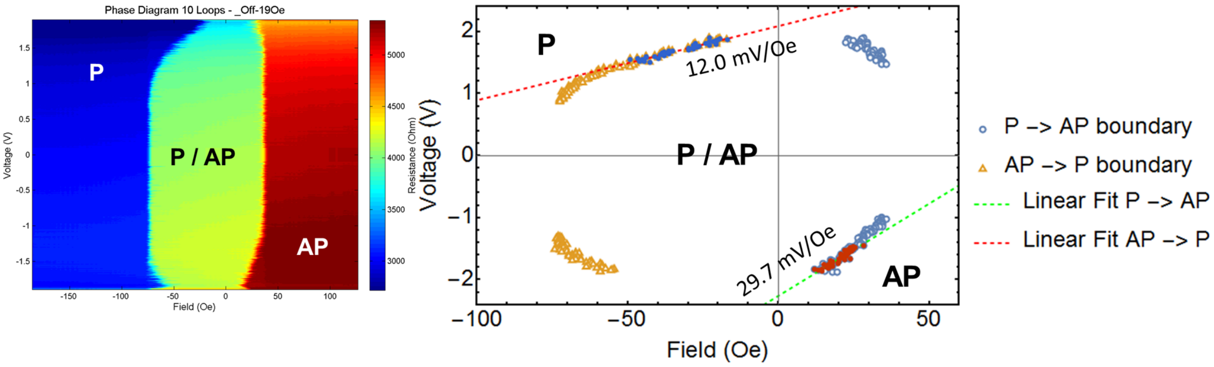

Figure 3.36: Linear fits of the boundary lines of phase diagram at the left side [same as in Fig.3.34(a)]. The data points used for the fit are represented by the full circles in red and blue colors. The fitted slopes are displayed next to each fitted dashed line.

Table 3.4: Critical switching voltage (V_c) obtained from linear fitting the phase boundaries of the different phase diagrams for selected DBMTJs with asymmetric and symmetric barriers and a single barrier MTJ. The critical current density (J_c) presented is calculated from V_c. The last column presents the STT efficiency figure of merit. The thermal stability factor $\Delta = 40$ was used for all DBMTJs and MTJs considering that there are not considerably large deviations in size of the elliptical pillars. Note: The critical switching quantities for the phase boundaries of the phase diagram from Fig.3.30(a) present here the correct signal despite the boundaries being inverted in polarity in the phase diagram.

Phase Diagrams	Type of MTJ	Transition	V_c(V)	J_c (MA/cm^2)	$\Delta/I_c(\mu A^{-1})$
Fig.3.29(a)	Double Asymmetric Top Thick Barrier	AP-P→P-AP	1.84	4.11	0.08
		P-AP→AP-P	-2.76	-3.80	0.08
Fig.3.30(a)	Double Asymmetric Bottom Thick Barrier	AP-P→P-AP	1.92	2.94	0.07
		P-AP→AP-P	-1.91	-4.04	0.05
Fig.3.30(b)	Double Asymmetric Bottom Thick Barrier	AP-P→P-AP	2.15	3.10	0.06
		P-AP→AP-P	2.97	5.87	0.03
Fig.3.31(a)	Double Symmetric Thick Barriers	AP-P→P-AP	2.57	1.93	0.09
		P-AP→AP-P	-4.21	-3.03	0.06
Fig.3.31(b)	Double Symmetric Thick Barriers	AP-P→P-AP	2.29	1.72	0.10
		P-AP→AP-P	-4.75	-3.33	0.05
Fig.3.32(a)	Double Symmetric Thin Barriers	AP-P→P-AP	1.27	1.41	0.13
Fig.3.34(a)	Single Barrier	P→AP	-2.83	-8.08	0.04
		AP→P	1.86	3.10	0.11

Focusing first on the similarities among the DBMTJs, the asymmetric DBMTJ with top thicker barrier and the symmetric thick barriers present a 1.5x to 2x lower V_c(AP-P→P-AP) than V_c(P-AP→AP-P). This result demonstrates clearly the assistance of field-like torque in switching towards the P-AP state, since all these DBMTJ have a dominating top barrier. The latter contrasts with the double asymmetric bottom thick barrier MTJ from phase diagram 3.30(a) which presents almost symmetric V_c for the two transitions. Moreover, the phase boundary slopes are also very similar: 13.1 mv/Oe (AP-P→P-AP) and 13.7 mV/Oe (P-AP→AP-P) - an additional result which reinforces the predominance of damping-like torque along with an almost zero influence of field-like torque in spin torque assisted switching, in this particular junction. Between the two types of asymmetric barriers DBMTJs, a comparison in critical voltages (possible since the total RA is the same) suggests a more suitable behavior in torque for the DBMTJ with the bottom thicker barrier [Fig.3.30(a)], both transitions occur at similar voltages (in absolute value) and they are lower in magnitude than in asymmetric DBMTJs with top thick barrier. Moreover, it was for this type of DBMTJs that a larger percentage of junctions were found to present a behavior dominated by the in-plane torque and not by field-like torque which is not suitable for memory applications. A comparison between the two types of DBMTJs with symmetric barriers (thick and thin) is not possible since, for the DBMTJ with symmetric thin barriers, only phase diagrams with a phase boundary even in voltage favoring the P-AP state were observed. A comparison of V_c between the selected DBMTJs and the single barrier MTJ does not reveal any advantages apart from a slight improvement in the symmetry of the values for the two transitions. In consequence, the critical switching current density J_c is a much more interesting quantity to compare regarding the different RA products involved.

First of all, the critical switching current density is given by:

$$J_c^{i \to k} = \frac{I_c^{i \to k}}{A} = \frac{V_c^{i \to k}}{R_s^i A} \tag{3.7}$$

where i, k represent each one of the write mode states in DBMTJ (P-AP or AP-P) or (P or AP) in the case of single barrier MTJ, A is the electrical area of the junction obtained from $A = \frac{RA_{total}^{nominal}}{R_{min}^{read}}$ and R_s^i is the resistance of the equilibrium state from where the transition occurs. In order to confirm the possibility to compare junctions with different RA products, an analysis of J_c for the same transition AP-P→P-AP for symmetric DBMTJ with thick and thin barriers shows very similar values despite the DBMTJ with thick barriers ($RA_{total} = 90\,\Omega.\mu m^2$) presenting a more than 4x larger RA than the DBMTJ with thin barriers ($RA_{total} = 20\,\Omega.\mu m^2$). Among the DBMTJs, is for the one with symmetric thick barriers that J_c values are the lowest within the same transition. On other end is the double asymmetric bottom thick barrier DBMTJ from phase diagram 3.30(b) where P-AP state (low write mode resistance) is favored by both voltage polarities. Globally, the DBMTJs in write mode, present lower J_c in both transitions than the more energy consuming transition in a single barrier MTJ (P→AP). Comparing just with the rare phase diagrams 3.29(a),3.30(a), 3.31(a) with the P→AP transition in a single barrier MTJ, the reduction in J_c goes from 2x (for both types of asymmetric barriers DBMTJs) up to 4x (AP-P→P-AP in DBMTJ with symmetric thick barriers). Another interesting observation is the reduction of J_c asymmetry between transitions for DBMTJs when compared to the single barrier MTJ. While $|\frac{J_c(P \to AP)}{J_c(AP \to P)}| \approx 2.5$ for the single barrier MTJ, $|\frac{J_c(P-AP \to AP-P)}{J_c(AP-P \to P-AP)}|$ varies between 2 for the DBMTJ with symmetric thick barriers [phase diagram 3.31(b)] and 1 for the asymmetric DBMTJ with thick top barrier [phase diagram 3.30(a)]. A result which is in agreement with previous measurements [37] of J_c made in DBMTJs.

Regarding STT efficiency, we now focus on the figure of merit Δ/I_c (last column of table 3.4). Among DBMTJs, it is for the AP-P→P-AP transition that the efficiency is higher, which is justified by the double action of damping and field-like torques assisting on this particular transition. The highest values of this figure of merit are exhibited by the double junctions with symmetric barriers. Comparing only with the DBMTJs where field-like torque effect is less strong, the gains in efficiency are as high as 2x (AP-P→P-AP in symmetric DBMTJ with thick barriers) in relation to the less efficient transition (P→AP) in the single barrier MTJ. Likewise the critical switching current density, the symmetry in efficiency of both write mode transitions in a DBMTJ is far superior than in a single barrier MTJ.

Although the results shown in this section correspond to measurements performed using short voltage pulses where the thermal effects are reduced in comparison with the DC measurements performed

Table 3.5: Dissipated power during critical switching for selected DBMTJs with asymmetric and symmetric barriers and a single barrier MTJ. Last column presents the calculated voltages values in DBMTJs necessary to dissipate the same power as in a P→AP transition for the single barrier MTJ.

Phase Diagram	**Type of MTJ**	Transition	Dissipated Power (mW)	V (V) power of MTJ
Fig.3.29(a)	Double Asymmetric Top Thick Barrier	AP-P→P-AP	0.97	2.6
		P-AP→AP-P	1.34	3.31
Fig.3.30(a)	Double Asymmetric Bottom Thick Barrier	AP-P→P-AP	1.15	2.10
		P-AP→AP-P	1.62	2.47
Fig.3.30(b)	Double Asymmetric Bottom Thick Barrier	AP-P→P-AP	1.38	2.17
		P-AP→AP-P	3.61	2.54
Fig.3.31(a)	Double Symmetric Thick Barriers	AP-P→P-AP	1.19	3.27
		P-AP→AP-P	3.05	3.34
Fig.3.31(b)	Double Symmetric Thick Barriers	AP-P→P-AP	0.94	3.27
		P-AP→AP-P	3.79	3.39
Fig.3.32(a)	Double Symmetric Thin Barriers	AP-P→P-AP	1.44	1.47
Fig.3.34(b)	Single Barrier	P→AP AP→P	1.93 0.77	

in section 3.2, they are not negligible. In fact, we observed phase diagrams where thermal effects are predominant, for example phase diagram 3.34(b). As mentioned before, pure thermal effects cause a reduction of coercivity with increasing applied voltage for both polarities. This type of behavior was mostly observed for single barrier MTJ than for DBMTJs. Therefore, we calculated the dissipated power at the critical switching voltages for both single and double MTJs. The results are presented in table 3.5. From the dissipated power expression $P = \frac{V_c^2}{R}$, one may think that dissipated power would be higher for the single barrier MTJ since resistance is smaller than in DBMTJs for similar V_c. An idea verified only for the low to high resistance transition of all DBMTJ relative to the single barrier MTJ. However the scenario reverses dramatically for the high to low resistance state transition where the power dissipated by the DBMTJs is 2x-3x higher than for the single barrier MTJ. In addition, we have also calculated the voltage necessary to apply to the DBMTJs in write mode to have the same dissipated power as in the P→AP transition of the single barrier MTJ. The results show that the obtained voltages are very close to critical switching voltages of table 3.4, being even lower for the P-AP→AP-P transition. Therefore, the heating effect is quite similar in both type of devices, single or double barrier. Although the effect of temperature does not seem very visible in the reduction of bi-stable region width in field, it may be one of the root causes for the mode switch effect present in the phase diagrams of some DBMTJs.

A well-known advantage of dual barrier MTJ in diffusive regime is that it acts as a voltage divider. In practical terms, this means that for the same voltage applied to top and bottom electrodes of the junction, in a DBMTJ, each barrier is exerted by a fraction of the total applied voltage depending on the RA symmetry between barriers. Therefore, in a DBMTJ with symmetric barriers, each one of them is subjected to half of the total applied voltage to the electrodes. The voltage acting on each barrier is given by:

$$V_i = V\frac{RA_i}{RA_i + RA_k} \tag{3.8}$$

Table 3.6: Calculated voltage drop values at each of the barriers for selected DBMTJs with asymmetric and symmetric barriers. The single barrier values are exhibited as reference for comparison.

Phase Diagram	Type of MTJ	RA$_{Top}$ ($\Omega.\mu m^2$)	RA$_{Bottom}$ ($\Omega.\mu m^2$)	Transition	V$_c$ (V)	V (V) Top barrier	V (V) Bottom Barrier
Fig.3.29(a)	Double Asymmetric Top Thick Barrier	35	10	AP-P→P-AP	1.84	1.43	0.41
				P-AP→AP-P	-2.76	-2.15	-0.61
Fig.3.30(a)	Double Asymmetric Bottom Thick Barrier	10	35	AP-P→P-AP	-1.91	-0.42	-1.48
				P-AP→AP-P	1.93	0.43	1.50
Fig.3.31(a)	Double Symmetric Thick Barriers	45	45	AP-P→P-AP	2.57	1.29	1.29
				P-AP→AP-P	-4.21	-2.10	-2.10
Fig.3.34(a)	Single Barrier	35		P→AP AP→P	-2.83 1.86		

, where V is the total applied voltage and i = Top (Bottom) and k = Bottom (Top) correspond to the position of the barriers. The voltages acting on each barrier of some selected DBMTJ (rare behavior) and on the single barrier MTJ associated to phase diagram 3.34(a) were calculated and are summarized in table 3.6. The only valid comparison between the single barrier MTJ and DBMTJ is for the barriers with an RA close to 35 $\Omega.\mu m^2$. By directly comparing the lower (higher) V_c transition in the single MTJ with the lower (higher) V_c transition in the DBMTJs, each of the barriers in all DBMTJs are subjected to less voltage than the barrier of the single MTJ. Independently of the type of DBMTJ, the stress which each barrier is under can be reduced by a factor of 2 relative to a single barrier MTJ with comparable RA. In conclusion, the operating window ($V_{breakdown} - V_c$) is considerably larger for a DBMTJ than for a single barrier junction which is extremely advantageous for writing. Similar findings in DBMTJs have been recently reported in literature [40].

3.3.3 Read Mode

The measurements in this section were performed in the same conditions as those in subsection 3.3.2, with the exception that the DBMTJs are set in read mode.

3.3.3.A Phase diagrams: global qualitative analysis

Figure 3.37 presents the phase diagrams of DBMTJs that display the general behavior observed in asymmetric barriers junctions with (a) top thick barrier and (b) bottom thick barrier; and symmetric barriers junctions with (c) thick and (d) thin barriers. The represented read mode behaviors were observed for all DBMTJs measured, independently of their behavior in write mode. Starting with an initial analysis of the phase diagrams, in all DBMTJs, the AP-AP state is favored by both voltage polarities. In addition, the transition boundary line evolves quadratically with voltage, thus suggesting the implication of a b_2V^2 field-like torque. As mentioned before, in read mode, $T_\perp$ should be maximized since both contributions from top and bottom reference add up. On the contrary, $T_\parallel$ is expected to be minimized or even canceled in the case of perfect barrier symmetry. However, the field-like torque seems to be dominant for all types of DBMTJs and almost no visible influence of damping-like torque exists even though, in theory, the latter does not completely cancel for DBMTJs with asymmetric barriers. In principle, if damping-like torque would play a role on read mode switching, it would induce minimum (P-P) to maximum (AP-AP)

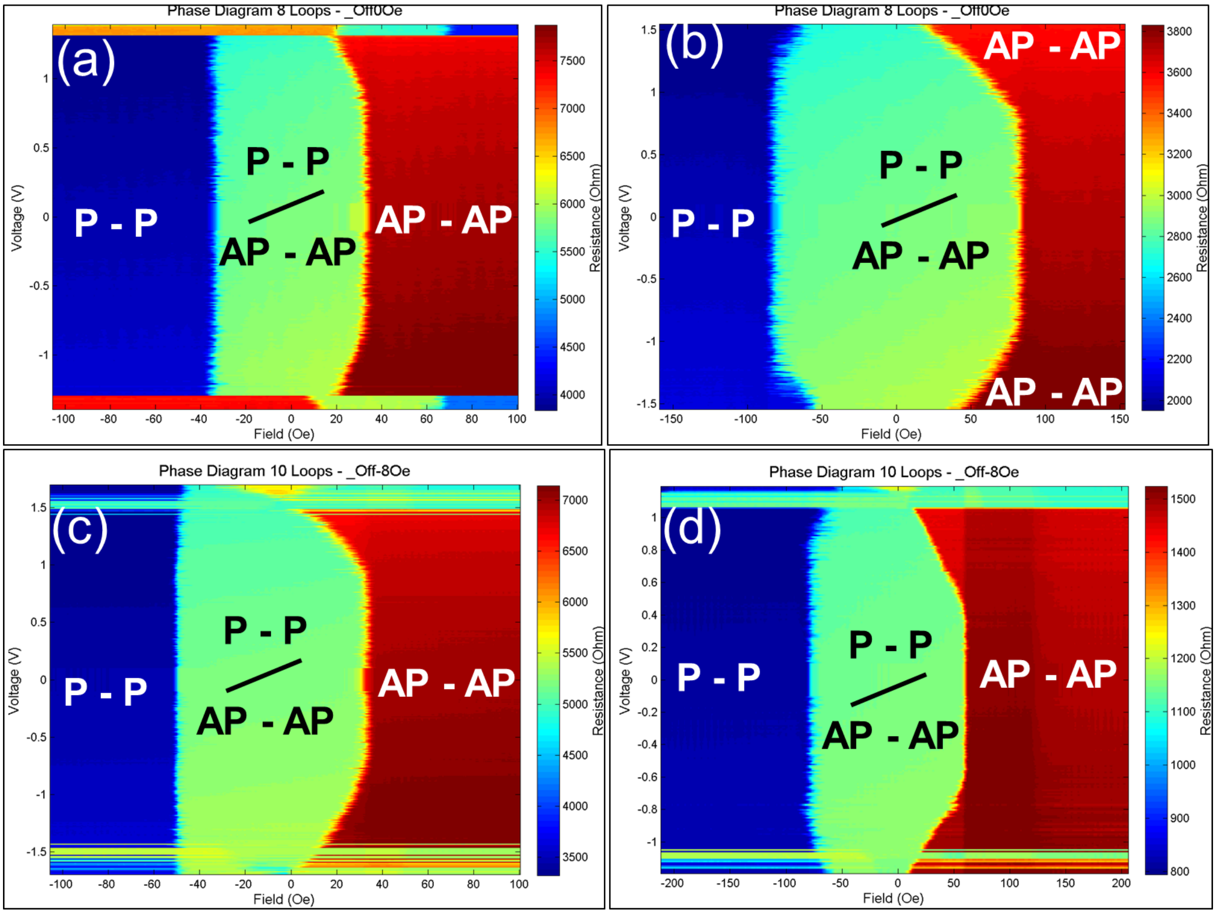

Figure 3.37: Phase diagrams of representative asymmetric DBMTJs with (a) top thick barrier and with (b) bottom thick barrier and symmetric DBMTJs with (c) thick and (d) thin barriers. All pillars have elliptical cross section and nominal dimensions of $140\,nm \times 40\,nm$. The maximum applied voltages were (a) 1.4 V, (b) 1.55 V, (c) 1.77 V and 1.2 V. The color gradient represents resistance, from maximum (red) to minimum (blue) values.

(and vice-versa) resistance state switching for opposite voltage polarities. Nevertheless, only switching towards AP-AP was observed. The AP-AP→P-P switching boundaries which start to appear for high voltages are mostly certainly created by thermal effects since they occur independently of the voltage polarity. The analysis of the P-P→AP-AP switching voltages at H = H_{off} may help to better understand the torques interplay on DBMTJs in read mode.

3.3.3.B Analysis of critical switching quantities

Table 3.7 compiles the two critical switching voltages for the P-P→AP-AP transition which occur for all types of DBMTJs, together with other quantities of interest (J_c and dissipated power) computed from voltage. Among all DBMTJs, only the asymmetric barriers DBMTJ with top thick barrier and the symmetric DBMTJ with thin barriers demonstrate a very good symmetry in positive and negative switching voltages. A good indicator of the single influence of a torque proportional to V^2, thus field-like torque. On the other hand, the asymmetric barriers DBMTJ with bottom thick barrier and the symmetric DBMTJ with thick barriers present a discrepancy between V_c+ and V_c-. In this case, a lower V_c for one polarity may indicate that an additional (to the field-like torque) torque linear with voltage helps to switch. In those junctions which only field-like torque induced transitions were observed, the theory only matches the experimental results for the symmetric DBMTJ with thin barriers since $T_{\|} \approx 0$. For the asymmetric DBMTJ with top thick barrier, $T_{\|}$ should not be totally zero and the positive voltage should favor more the AP-AP state while negative voltage should favor the P-P state, as represented in the ideal case of Fig.3.20. The possible of non-zero $T_{\|}$ for the symmetric DBMTJ with thick barriers can be explained by the dominant behavior of one barrier over the other. In this case, and judging by the fact that $V_c+ > V_c-$, the top barrier would be the ruling one. The read mode switching behavior of the asymmetric DBMTJ with bottom thick barrier, though revealing the presence of a $T_{\|} \neq 0$, the fact that $V_c+ > V_c-$ does not follow the theoretical description for which the AP-AP state should be more favored by negative voltage. However, it does support the hypothesis of a dominant top barrier (even if smaller in RA than the bottom) which has already been observed for the same type of DBMTJ in write mode. The dominating effect of the top barrier may be justified by its smaller area than the bottom barrier due to fabrication but also due to better growth conditions (supported by previous observations in DBMTJs by Feng *et al.* [39]) which confer an higher TMR to the top barrier than the bottom one.

Table 3.7: Positive (V+) and negative (V-) critical switching voltages (V_c) obtained from linear fitting the P-P→AP-AP phase boundaries of the different phase diagrams for selected DBMTJs with asymmetric and symmetric barriers, set in read mode. The critical current densities (J_c) presented are calculated from V_c. The last column presents the dissipated power by the DBMTJs at the critical voltages for both polarities.

Phase Diagram	Type of MTJ	Transition	V_c (V)	J_c (MA/cm^2)	Dissipated Power (mW)
Fig.3.37(a)	Double Asymmetric Top Thick Barrier	P-P→AP-AP (V+)	1.79	3.99	0.80
		P-P→AP-AP (V-)	-1.80	-4.00	0.81
Fig.3.37(b)	Double Asymmetric Bottom Thick Barrier	P-P→AP-AP (V+)	1.71	3.81	1.44
		P-P→AP-AP (V-)	-1.94	-4.31	1.84
Fig.3.37(c)	Double Symmetric Thick Barriers	P-P→AP-AP (V+)	1.65	1.83	0.79
		P-P→AP-AP (V-)	-1.85	-2.06	0.99
Fig.3.37(d)	Double Symmetric Thin Barriers	P-P→AP-AP (V+)	1.38	6.92	2.35
		P-P→AP-AP (V-)	-1.33	-6.67	2.18

Between the two symmetric barriers there is a difference on the critical switching voltages in read mode. Although one might think that the lower V_c obtained for the DBMTJ with thin barriers could be justified by a stronger field-like than for the DBMTJ with thicker barrier, thermal effects cannot be neglected. In fact, according to the values of the dissipated power in table 3.7, the thermal effects are 2x higher for the symmetric DBMTJ with thin barriers than for the one with thicker barriers. These effects may be the real reason behind the lower V_c values obtained for these type of DBMTJ. In addition, the AP-AP→P-P switching boundaries which start to appear for high voltages on the asymmetric DBMTJ with thick bottom barrier and symmetric DBMTJ with thin barriers coincide with the highest dissipated power values also demonstrated by those DBMTJ, supporting substantially the thermal nature of those transitions.

3.3.4 Conclusion: Field-like torque in write and read modes

From the performed measurements on the DBMTJs and analysis of their respective phase diagrams, there is one effect common to them all: field-like torque.

In write mode, the most surprising result was the observation of field-like torque induced switching in DBMTJ with symmetric barriers. According to theory, in a double barrier MTJ with the control and reference layers' magnetizations in antiparallel alignment (*i.e.* write mode), the two field-like torque components of the torques acting on the free layer should subtract. Moreover, in a structure with symmetric barriers, the cancellation should be perfect, thus $T_{\perp} = 0$. However, for the majority of the symmetric DBMTJs measured, with thick or thin barriers, the field-like torque even dependence with V dominates the switching and favors the antiparallel alignment around the top barrier, therefore favoring the P-AP state. Even for the small group of symmetric barriers double junctions [example in Fig.3.31(a)] where the damping-like torque induced switching is visible, the field-like torque is non-negligible and allows for a more efficient transition towards P-AP. The non-zero $T_{\perp}$ may have two possible origins. One is the shape of the DBMTJ pillar which is most probably conical (due to ion beam etching) therefore creating a top barrier with a smaller area than the bottom barrier. This creates an asymmetry of the current density across the two oxide barriers. The larger J on top the barrier translates on a larger number of electrons carrying torque per unit area corresponding to a larger field-like torque coming from the control layer than from the bottom reference layer. The other reason is related with the quality of the barriers. It is possible that the top barrier may have a superior texture quality than the bottom, providing higher TMR on top than on bottom barrier. Comparison with previous works is difficult since there are not many reports on DBMTJs. Furthermore the existing reports are somehow contradictory. Feng *et al.* [39] report that, despite the amorphous state of the middle CoFeB (free layer) due to a lack of B diffusion because of the existence of two MgO barriers, they see evidence of the formation of lattice planes along the upper CoFeB/Top MgO interface. Their proposed explanation for an higher TMR of the top barrier than the bottom barrier in nominally symmetric barrier double junctions. On the other hand, Gan *et al.* [38] report a lower TMR on the top barrier than the bottom barrier since the degree of crystallization of the top CoFeB (control layer) is slightly less than the bottom CoFeB reference layer. The other peculiar STT behavior observed in write mode was for asymmetric DBMTJ with thick bottom barrier. In spite of few double junctions presenting the expected behavior dominated by the damping-like torque, in many others switching towards the P-AP state occurred for both voltage polarities [Fig.3.30(b)]. An unexpected observation even considering a dominant field-like torque. Theory suggests that field-like torque favors an antiparallel alignment between free and reference layers around the dominating barrier. In this type of DBMTJs it was thought that the dominant barrier would be the bottom one since it presents the highest RA. However, if the aforementioned explanations are true, there is the possibility of the top barrier, even if it presents a lower RA, to be the dominant one. That would fit with the experimental observations. Another possibility, yet much less probable, it is to consider a negative field-like torque $T_{\perp} = b_2 V^2$, where $b_2 < 0$. This scenario was only verified in simulations performed by Bernet *et al.* [60], with no experimental reports to sustain this claim.

In read mode, field-like torque is expected to be maximized since $T_{\perp total}^{Read} = T_{\perp}^{Control} + T_{\perp}^{Reference}$. Therefore, favoring the AP-AP configuration, where the free layer is antiparallel to both control and reference layers. The experimental results of all DBMTJs are in agreement with theoretical predictions. The only divergence with theory concerns damping-like torque specially in the asymmetric DBMTJ with bottom thick barrier. Here again, although the presence of a remaining $T_{\parallel}$ was expected (no complete cancellation between $T_{\parallel}^{Reference}$ and $T_{\parallel}^{Control}$), the voltage polarity for which the P-P→AP-AP transition is benefited is not in agreement with a dominating bottom barrier. Nevertheless, it matches a situation where the top barrier is dominant which goes along with the results observed in write mode and sustain the dominance of the top barrier.

Another very interesting point is the fact that field-like torque induced switching has never been observed in our measured single barrier MTJs. In fact, the main difference between single and double junction is that the latter has an extra oxide barrier grown on top of the free layer. Consequently, this result points to a direct correlation between the top barrier and the strong field-like torque induced switching observed for the majority of the in-plane anisotropy DBMTJs. It is possible that the top barrier grown on top of amorphous CoFeB may possess particular qualities that boost field-like torque in planar double barrier magnetic tunnel junctions.

3.3.5 Mode switch

In this section, we investigate the *mode switch* by applying voltage pulses for different initial states of the DBMTJ, either in read or write mode. The mode switch is defined as an undesired rotation of the control layer while trying to write the storage layer through current induced STT. This phenomenon has been firstly observed by P.-Y. Clément [1] while applying large DC currents in order to trigger switching by STT. The current necessary to cause the reversal of the control layer is, in general, comprised between the critical current for STT switching and the breakdown current. In our experiments, mode switch was observed on several occasions while performing DC current sweeps and voltage pulses measurements, independently of the type of DBMTJ. Fig.3.38 presents one example of a write to read mode switch and Fig.3.39 an example of a read to write mode switch, while performing DC current sweeps. In the R(I) plot of fig3.38, the measurement starts with the DBMTJ in write mode at an initial AP-P state and switches towards the read mode AP-AP state when the applied current reaches -0.34 mA. In the corresponding R(I) plot of Fig.3.39, there are field-like torque (or thermally) induced P-P⇄AP-AP switchings for negative and positive currents until current reaches +0.34 mA and the DBMTJ switches from AP-AP towards the P-AP state which corresponds to write mode.

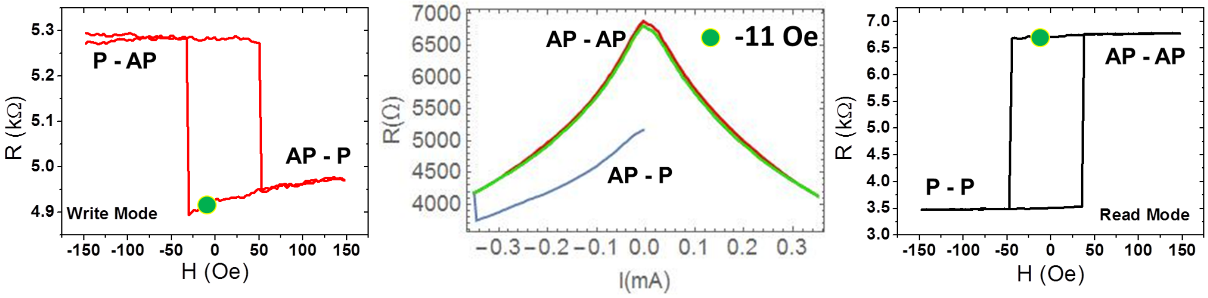

Figure 3.38: Example of a mode switch while performing R(I) sweeps with DC current, in a symmetric DBMTJ with thick barriers. *(Left)* The device is an initial AP-P state in write mode. *(Center)* The applied field is constant, $H = -11\,Oe$, and R(I) sweep is performed. A jump in resistance happens for I = -0.34 mA. The DBMTJ does not switch from AP-P to P-AP. Instead, it switches from AP-P (write mode) to AP-AP (read mode). *(Right)* R(H) loop after the R(I) sweep shows the device is effectively in read mode.

For the voltage pulses measurements, mode switch can be observed in figs.3.29(a)-(b), 3.31(b), 3.32 and 3.37(a),(c)-(d). The oscillation between the two modes, usually observed for $|V| > 1\,V$, are characterized by sudden color changes in the phase diagrams. Figure 3.33 shows the R(H) loops of the mode switch regions where both write and read mode R(H) curves exist. In the phase diagrams of DBMTJs with a thicker top barrier, the mode switch is easier to detect because the stables states of maximum and minimum resistance of read mode exist for magnetic fields of opposite sign in write mode. For example, in Fig.3.29(b), the stable write mode P-AP state (high resistance, in orange color) exist for $H \ll 0$ as well as the stable read mode P-P state (minimum resistance, in dark blue color).

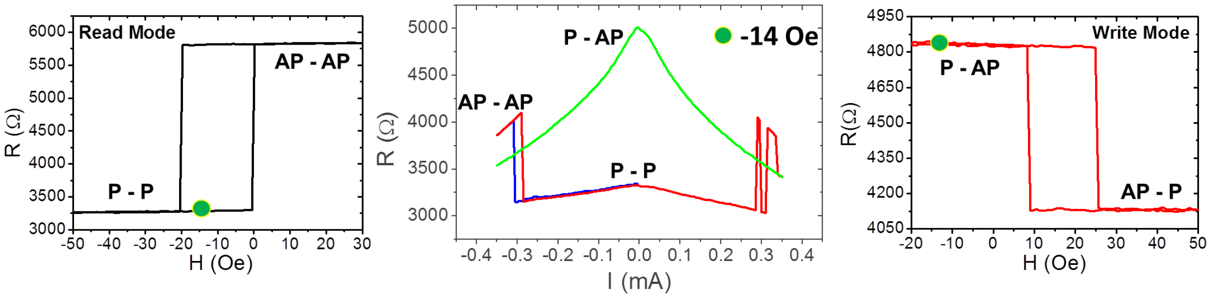

Figure 3.39: Example of a read to write mode switch while performing R(I) sweeps with DC current, in a symmetric DBMTJ with thick barriers. *(Left)* The DBMTJ is an initial P-P state in read mode. *(Center)* The applied field is constant, $H = -14\,Oe$, and R(I) sweep is performed. STT switching happens for negative currents, however for I = 0.34 mA the junction switches from AP-AP to P-AP state. Therefore switching from read to write mode. *(Right)* R(H) loop after the R(I) sweep shows the device is effectively in write mode. Moreover, at H = -14 Oe the DBMTJ is in a stable P-AP state, outside the bi-stable region.

The first attempt to explain this effect was also proposed by P.-Y. Clément [1] who claimed that it was caused by thermal effects. More precisely, the applied current would increase locally the temperature of the double junction above the blocking temperature of the FeMn (see section 3.1.1), unpinning the hard layer of the top SAF. Upon the rupture of the exchange coupling between the antiferromagnet and the adjacent ferromagnet, even a small applied magnetic field would be strong enough to reverse the control layer. According to this explanation and considering the effect to be purely caused by high temperatures, the mode switch should also happen for applied magnetic fields outside the coercive region and given the field is in the direction which enables to reverse the control layer from its original configuration: parallel (read mode) or antiparallel (write mode) to the bottom reference layer. In order to verify this hypothesis, we conducted experiments using voltage pulses in different DBMTJ states both for read and write modes. Unlike the DC current measurements, the temperature effects are minimized using short pulses, thus higher voltages should be needed to attain temperatures superior to T_b^{FeMn}. For the aforementioned purpose, we studied the regions of field around -500 Oe and 500 Oe (marked by dashed boxes) on the left side R(H) cycles of figs.3.40 and 3.41). In these regions, the free layer cannot switch by STT or by applied magnetic field.

Figure 3.40 presents the tests realized with the DBMTJ set in read mode. The R(H) cycles at the left show the initial state of the DBMTJ and the tested zone (red dashed square). For the case on the top, where the DBMTJ stable states are either AP-AP or AP-P in the tested field range (due to the rotation of the control layer), mode switch happens for V = +1.22 V and the control layer does not switch back even for higher voltages. The R(H) plot of the top left shows that the antiferromagnetic RKKY coupling between the ferromagnetic layers of the top SAF is broken around 500 Oe. In the top phase diagram,

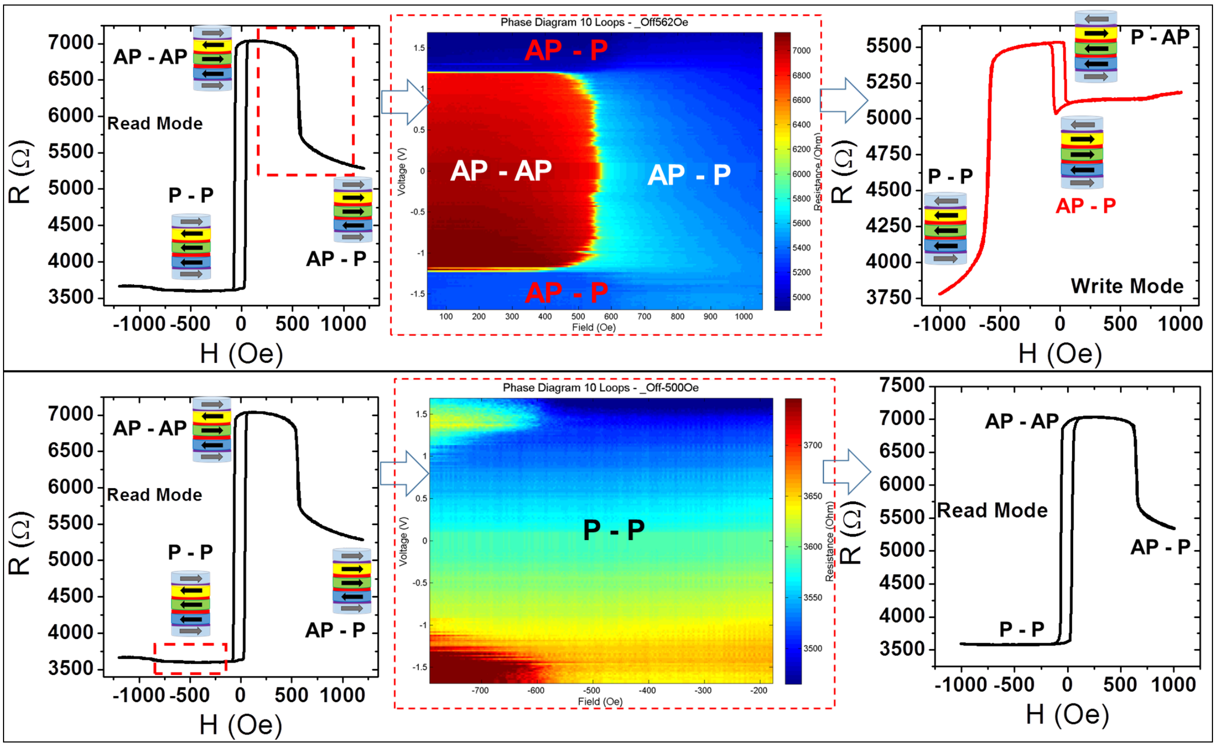

Figure 3.40: Mode switch investigation using voltage pulses for magnetic fields outside the free layer coercive region. The symmetric DBMTJ with thick barriers was initially set in read mode. *(Top)* The zone marked by the red dashed square in the left R(H) cycle, corresponds to the AP-AP and AP-P states, where the control layer rotates, was submitted to 100 ns voltage pulses $0 < |V| < 1.7\,V$. The phase diagram, at the center, shows a mode switch happening at $V = 1.22\,V$. The right R(H) cycle shows the stable mode of the DBMTJ after the voltage pulses, which is write mode. *(Bottom)* The zone marked by the red dashed square in the left R(H) cycle, the P-P state, was submitted to 100 ns voltage pulses $0 < |V| < 1.7\,V$. The phase diagram, at the center, shows no evidence of mode switch, only small resistance variations. The right R(H) cycle shows the stable mode of the DBMTJ after the voltage pulses, which is read mode. The stacks on the inset of the R(H) plots are represented by the following (bottom to top): bottom pinned layer (light blue), Ru spacer (purple), reference layer (blue), MgO barrier (red), storage layer (green), MgO barrier, control layer (yellow), Ru spacer, top pinned layer (light blue).

up to V = ±1.22 V, the exchange coupling between the FeMn and the top pinned layer still exists and the sweeps of magnetic field allow the rotation of the control layer. For $|V| > 1.22\,V$, the control layer remains stable and aligned along the positive field direction even for fields below 500 Oe (within the red dashed box). When the voltage pulse is no longer applied, the RKKY coupling is reestablished. The R(H) cycle on the right was measured after the voltage pulses and shows the DBMTJ in write mode. In opposition, for the bottom case of Fig.3.40, the voltage pulses were applied for negative magnetic fields below $-H_c$. In this case, for the same range of voltage as the top one, no mode switch happened which is confirmed by the static R(H) loop, measured after the voltage pulses, at the right of the bottom phase diagram. In fact, the control layer is already aligned in the same direction of the applied field. So the heating from the applied voltage only breaks the exchange coupling but the antiferromagnetic coupling in the SAF is reestablished the moment the voltage pulse is turned off.

A similar study was performed for the DBMTJ set in write mode and its results are presented in Fig.3.41. The case on top shows that when the pulses were applied with the DBMTJ in a stable AP-P state, no mode switch was observed for $0 <| V |< 1.7\,V$. On the other hand, for the case at the bottom, when the pulses were applied for the DBMTJ between the P-AP and P-P states, mode switch

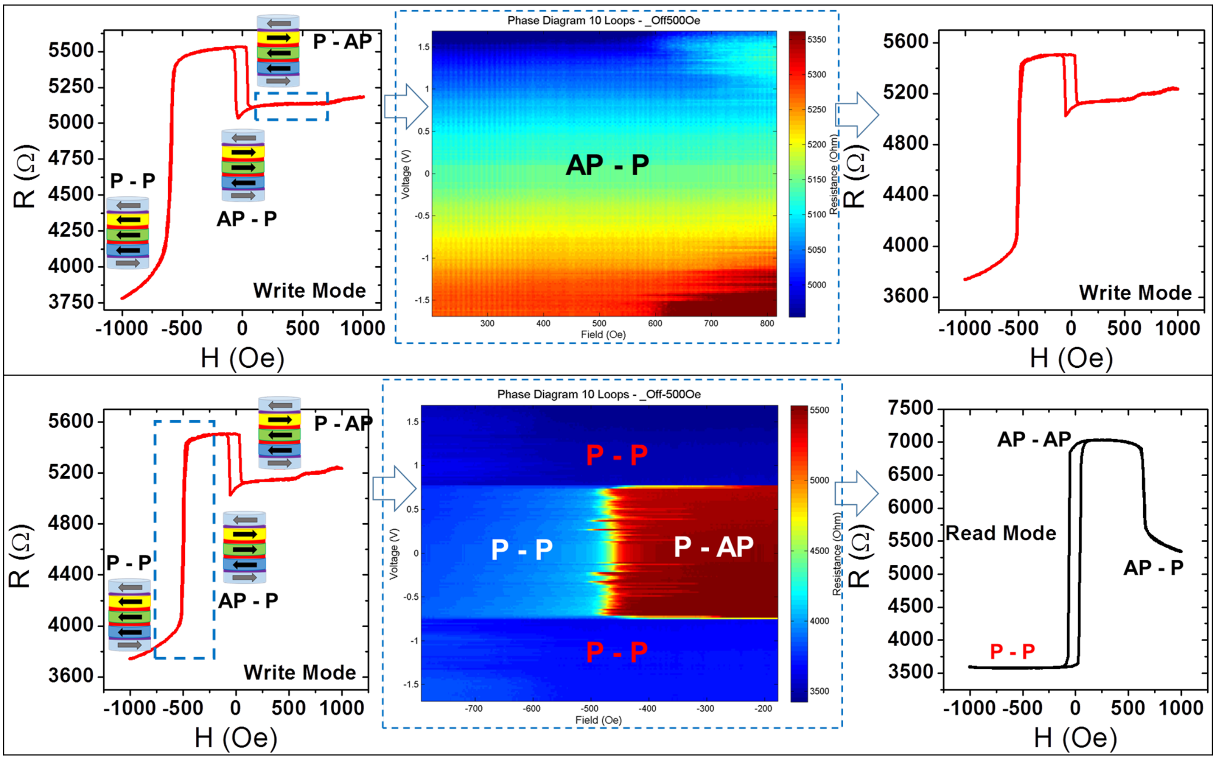

Figure 3.41: Mode switch investigation using voltage pulses for magnetic fields outside the free layer coercive region. The symmetric DBMTJ with thick barriers was initially set in write mode. *(Top)* The zone marked by the red dashed square in the left R(H) cycle, the AP-P state, was submitted to 100 ns voltage pulses $0 < |V| < 1.7\,V$. The phase diagram, at the center, shows no evidence of mode switch, only small resistance variations. The right R(H) cycle shows the stable mode of the DBMTJ after the voltage pulses, which is write mode. *(Bottom)* The zone marked by the red dashed square in the left R(H) cycle, corresponds to the AP-P and P-P states, where the control layer rotates, was submitted to 100 ns voltage pulses $0 < |V| < 1.7\,V$. The phase diagram, at the center, shows a mode switch happening at $V = 0.78\,V$. The right R(H) cycle shows the stable mode of the DBMTJ after the voltage pulses, which is read mode.

was triggered at $V = 0.78\,V$. This case is similar to mode switch in read mode where the control layer magnetization rotates to become parallel with the direction of the applied field and it remains stable for values above the mode switch trigger voltage. Again the RKKY coupling is reestablished before the exchange coupling and the pinned layer magnetization is aligned in the direction opposite to the direction of the applied field.

The mode switch observations for applied magnetic fields within the coercive region ($-H_c < H < H_c$) corresponding to the figs.3.38 and 3.39 do not match the observations for absolute magnetic fields larger than H_c corresponding to figs.3.40 and 3.41. The mode switches observed from the write mode AP-P state towards the read mode AP-AP state in Fig.3.38 and from the read mode P-P state towards the write mode P-AP state in Fig.3.39 have never been observed, respectively, in figs.3.41 and 3.40. In order to have a better and clear insight on the probable mechanisms behind the two types of observed mode switches, we designed two model scenarios where the pinned layer (Fig.3.42) or the control layer (Fig.3.43) are, respectively, the more stable layers.

As it has already been mentioned, our DBMTJ possess two electrodes composed both by a SAF. In this type of structures two kinds of coupling exist: (i) the exchange coupling between the antiferromagnets (PtMn and FeMn) and the contiguous ferromagnet (pinned/hard layer) and (ii) the interlayer

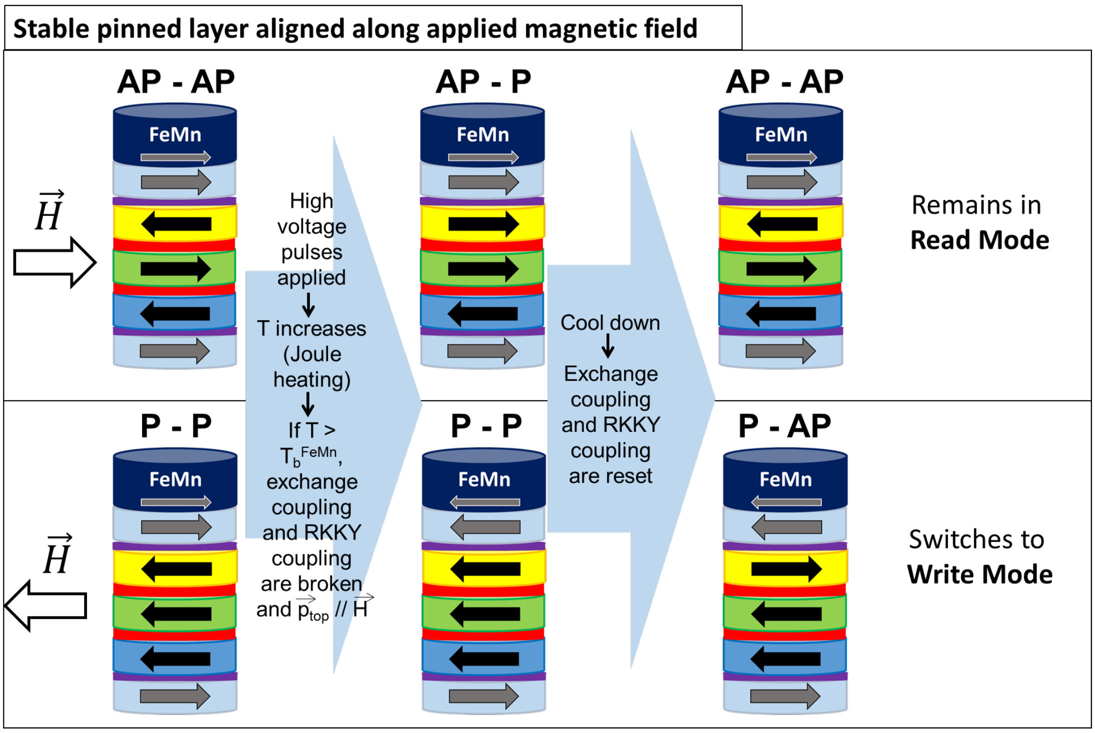

Figure 3.42: Description of mode switch caused by Joule heating, in a DBMTJ in read mode, considering the top pinned layer aligns along the applied magnetic field $\vec{H}$. *(Top)* Double junction at an initial AP-AP state where $\vec{H} > 0$. After the applied pulses and subsequent cool down, the junction remains in read mode. *(Bottom)* Double junction at an initial P-P state where $\vec{H} < 0$. After the applied pulses and subsequent cool down, the junction switches to write mode.

(RKKY) coupling between the pinned layer and the reference/control layer. In both proposed scenarios, we chose initial read mode states but the a similar explanation would fit initial write mode states. Besides this and for simplicity, we have also chosen initial configurations where the applied field direction is parallel to the direction of the magnetization of the free layer. Lets first focus on the scenario of Fig.3.42. We start from an AP-AP configuration stabilized by a positive applied field. When high current (or voltage) is applied, the temperature T increases due to Joule effect. If $T > T_b^{FeMn}$, the exchange coupling between FeMn and the SAF pinned layer ceases to exist. If H is high enough to overcome the RKKY coupling between pinned layer and control layer, then the magnetizations of the top pinned layer $\vec{p}_{top}$ and control layer $\vec{p}_{control}$ align with the direction of $\vec{H}$. Upon cool down and with the applied field off, the exchange is reset with the pinned layer magnetization aligned in the positive field direction and RKKY coupling is reestablished so the control layer becomes again antiparallel to the pinned layer. The structure remains in read mode. At the bottom part of Fig.3.42, on the other hand starting with a P-P state, stabilized by a negative field, the outcome is different. After exchange loss due to Joule heating, the top pinned layer and control layer magnetizations align with $\vec{H}$, which later results in a reversal of the control layer upon cool down, leading to mode switch. The final state is a P-AP state corresponding to write mode. If the DBMTJ was prepared in a write mode state, the proposed mechanism would provide the following results: (i) if the DBMTJ was in a stable AP-P state under a positive applied field, it would switch to a read mode AP-AP state. Whereas the DBMTJ in a stable P-AP state under negative applied field would not switch mode.In fact, this mechanism mimics the annealing process used to switch the operation mode of a whole set of DBMTJs on a sample. However, instead of using a magnetic annealer (oven) to heat up the DBMTJ, it is the current that increases locally the temperature of the DBMTJ by Joule effect.

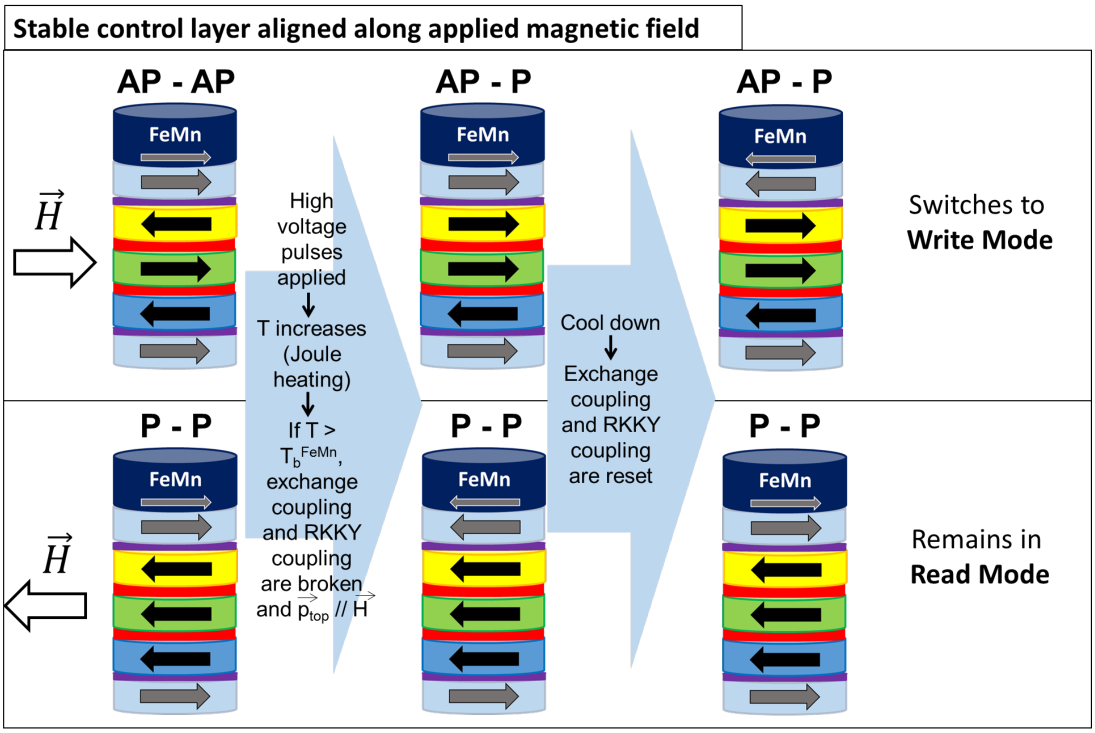

Figure 3.43: Description of mode switch caused by Joule heating, in a DBMTJ in read mode, considering the control layer aligns along the applied magnetic field $\vec{H}$. *(Top)* Double junction at an initial AP-AP state where $\vec{H} > 0$. After the applied pulses and subsequent cool down, the junction switches to write mode. *(Bottom)* Double junction at an initial P-P state where $\vec{H} < 0$. After the applied pulses and subsequent cool down, the junction remains in read mode.

The model scenario presented in Fig.3.43 is based on the assumption of the control layer being the most stable and magnetically harder layer. On the top part of the figure, the system is in read mode in a the AP-AP state where the free layer is aligned in the direction of a positive applied field. Again, when subjected to a strong enough voltage which is able to increase temperature above T_B^{FeMn}, the exchange coupling between top pinned layer and the antiferromagnet is broken. If the field H is high enough to break the interlayer coupling of the SAF, then the two ferromagnetic layers magnetizations' become parallel to each other and the DBMTJ changes to the AP-P state. Upon cool down and considering the control layer to be the hardest layer of the SAF thus not rotating against $\vec{H}$, the RKKY coupling is reestablished by forcing the magnetization of the top pinned layer to become antiparallel to the control layer. The exchange coupling is then reset and the final state of the junction is a write mode AP-P state. Mode switch happens in this case. On the bottom part of the figure, the initial state is the read mode P-P where the control layer has already the same direction of the negative applied field $\vec{H}$. In this particular case, even after the loss of both couplings, the control layer will not rotate. So when high voltage is no longer applied, the DBMTJ does not change mode and remains at P-P state. Like in the previous model, similar conclusions could be taken if the DBMTJ was prepared in a write mode state. If the DBMTJ was in a stable AP-P state under a positive applied field, it would not switch mode. Whereas the DBMTJ in a stable P-AP state under negative applied field would switch to the read mode P-P state.

The mode switch events observed during the DC current measurements (figs.3.38and3.39) are in agreement with the model of the more stable pinned layer of Fig.3.42. Whereas the mode switch events observed from the voltage pulses for applied magnetic fields far from the coercive region (figs.3.40 and 3.41) are in agreement with the model of the stable control layer of Fig.3.43. Although the mode switch events observed for fields below H_c follow a model similar to a mode switch process by magnetic annealing, they do not recreate the process completely since the cool down is performed under a very strong magnetic field 1T (10 kOe) and on the measurements the fields are much smaller. Therefore the demagnetizing fields from the magnetic layer below may influence the sense of rotation of the magnetic layers of the SAF. On the contrary, the mode switch experiments with short voltage pulses were performed for larger fields ($|H| \gg |H_c|$) so the free layer is not able to rotate. The model attached to this experiment lies on a reliable fact: control layer magnetically harder than the pinned layer. The top SAF ferromagnetic layers are composed by different materials: control layer composed of 2 nm of CoFeB and the top pinned layer composed by a (1.5 nm NiFe/ 0.5 nm CoFe) bilayer. The saturation magnetization of the CoFeB is ≈1100 emu/cm^3. The saturation magnetization of the bilayer can be calculated, given M_s(NiFe)≈800 emu/cm^3 and M_s(CoFe) ≈1400 emu/cm^3, by:

$$M_s(NiFe + CoFe) = \frac{M_s(NiFe)t_{NiFe} + M_s(CoFe)t_{CoFe}}{t_{NiFe} + t_{CoFe}} \tag{3.9}$$

After calculation, $M_s(NiFe + CoFe)$ ≈950 emu/cm^3 which is lower than $M_s(CoFeB)$. Therefore, the for applied fields around ±500 Oe, the control layer rotates if set against the applied field direction and when the exchange coupling is broken by heat, rests as the hard magnetic layer of the SAF. So the RKKY antiferromagnetic coupling is reset before the exchange coupling. The second model (Fig.3.43) may be the more reliable explanation on the mechanism behind mode switch. However, if the applied fields are very large (H $>$ 1kOe) then the RKKY coupling is not reset before the exchange and we have a mechanism just like the magnetic annealing which is described by the first model (Fig.3.42).

3.4 Macrospin Simulations

It is crucial to compare the experimental results with a theoretical model. In this section, we present the results obtained by performing macrospin (single-domain) simulations of a double barrier MTJ subjected to short voltage pulses. The macrospin simulations program was developed by Andrey Timopheev.

3.4.1 Model and LLGS equation

The model system designed is represented in Fig.3.44(a). For simplicity, the volume of the three layers was not taken into account and only the dimensions of the storage layer was considered for calculation of its demagnetizing field. Each one of the arrows represents one of the torques $T_{\parallel}$ and $T_{\perp}$ acting on the storage layer stemming from one of the two polarizers (control and reference layers). In

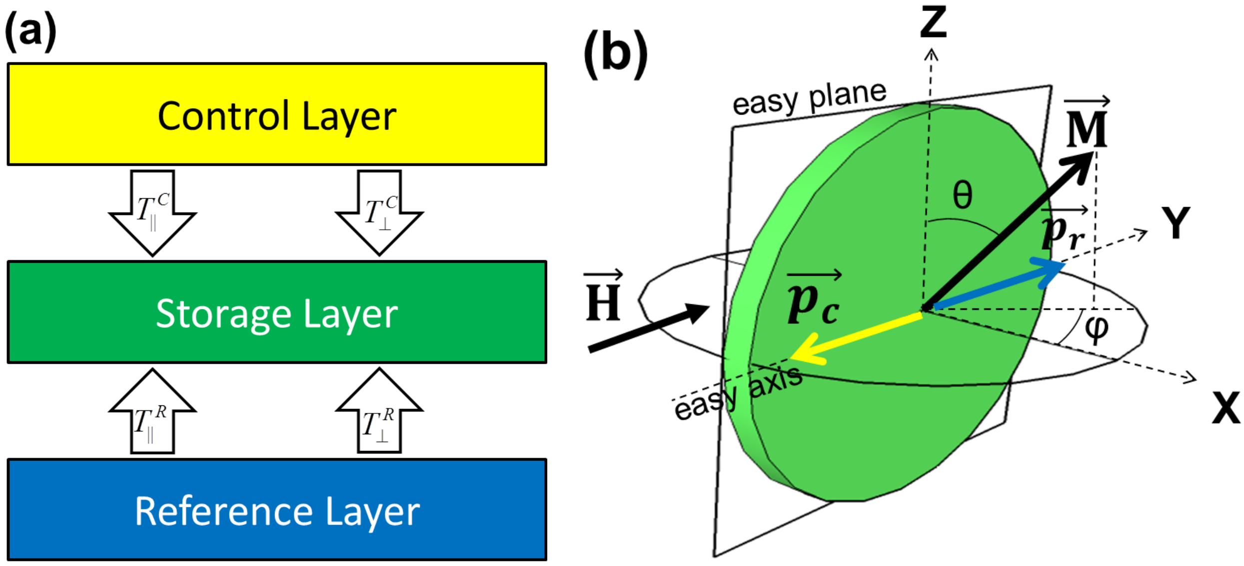

Figure 3.44: (a) Illustration of the trilayer model system designed for the macrospin simulations. The in-plane $T_{\parallel}$ and out-of-plane $T_{\perp}$ torques coming from control (C) and reference (R) layers are exerted on the storage layer. (b) Geometry of the ellipsoidal cross section of the storage layer (green) lying on the z-y plane. Its magnetization is represented by a macrospin $\vec{M}$ that can point in any direction. The unit vectors along the direction of the magnetizations of the control and reference layers (not shown) are represented by $\vec{p}_c$ (yellow) and $\vec{p}_r$ (blue), respectively. Their magnetizations lie on the easy axis $\vec{e}_y$ and can be in a parallel or antiparallel alignment depending on the operation mode.

fact, these are the most important variables of the model and their interplay was studied through the simulations.

Our macropsin model of the system mimicking a double barrier MTJ shown in Fig.3.44(b) assumes that the magnetization of the storage layer is uniformly distributed with a saturation value M_s. In our model, the unit vector $\vec{m} = \frac{\vec{M}}{M_s}$ gives the direction of the storage layer magnetization: it can point to any direction in space. We are using the spherical coordinate system in which θ is the polar angle, $\theta \in [0, \pi]$, and φ is the azimuthal angle, $\varphi \in [0, 2\pi]$. Therefore, $\vec{m}$ in the Cartesian basis is given by,

$$\vec{m} = \sin\theta\cos\varphi\,\vec{e}_x + \sin\theta\sin\varphi\,\vec{e}_y + \cos\theta\,\vec{e}_z. \tag{3.10}$$

If we consider the Cartesian coordinates, $i = x, y, z$ while in our local spherical coordinates, $\mu = m, \theta, \varphi$, then the rotation matrix [117] transforming Cartesian into our spherical coordinates, $\vec{e}_\mu = R_{\mu i}\vec{e}_i$ is,

$$R_{\mu i} = \begin{bmatrix} \sin\theta\cos\varphi & \sin\theta\sin\varphi & \cos\theta \\ \cos\theta\cos\varphi & \cos\theta\sin\varphi & -\sin\theta \\ -\sin\varphi & \cos\varphi & 0 \end{bmatrix} \tag{3.11}$$

We describe the dynamics of a 0 K macrospin $\vec{m}$ under constant spin-polarized current, using Landau-Lifshitz-Gilbert-Slonczewski (LLGS) equation [44, 62, 63],

$$\begin{aligned} \frac{d\vec{m}}{dt} &= -\gamma\left(\vec{m} \times \vec{H}_{eff}\right) + \alpha\left(\vec{m} \times \frac{d\vec{m}}{dt}\right) \\ &\quad - \gamma T_{\parallel}^{c}\,\vec{m} \times (\vec{m} \times \vec{p}_c) - \gamma T_{\perp}^{c}\,\vec{m} \times \vec{p}_c - \gamma T_{\parallel}^{r}\,\vec{m} \times (\vec{m} \times \vec{p}_r) - \gamma T_{\perp}^{r}\,\vec{m} \times \vec{p}_r, \end{aligned} \tag{3.12}$$

where $\vec{H}_{eff}$ is the effective field (which accounts for magnetostatics, external field and uniaxial anisotropy), $\vec{p}_c$ and $\vec{p}_r$ are the unit vectors along the magnetization direction of control and reference layers, respectively, γ is the gyromagnetic ratio, α is the Gilbert damping constant, $T_{\parallel}^{c,r}$ and $T_{\perp}^{c,r}$ are in-plane and out-of-plane STT prefactors, respectively, whose subscripts c, r stand for control and reference which represent the origin of the torque.

In a geometric point of view, in-plane and out-of-plane torque terms of Eq.(3.12) are equivalent to the damping and precession terms, respectively, of the Landau-Lifshitz (LL) equation. Following a similar procedure as done in Ref. [115], Eq.(3.12) can be transformed into LL form by performing a cross product of $\vec{m}$ on both sides of the equation,

$$\begin{aligned}\vec{m}\times\frac{d\vec{m}}{dt} &= -\gamma\,\vec{m}\times\left(\vec{m}\times\vec{H}_{eff}\right)+\alpha\,\vec{m}\times\left(\vec{m}\times\frac{d\vec{m}}{dt}\right)\\ &-\gamma\,T_{\parallel}^{c}\,\vec{m}\times\left[\vec{m}\times\left(\vec{m}\times\vec{p}_c\right)\right]-\gamma\,T_{\perp}^{c}\,\vec{m}\times\left(\vec{m}\times\vec{p}_c\right)\\ &-\gamma\,T_{\parallel}^{r}\,\vec{m}\times\left[\vec{m}\times\left(\vec{m}\times\vec{p}_r\right)\right]-\gamma\,T_{\perp}^{r}\,\vec{m}\times\left(\vec{m}\times\vec{p}_r\right).\end{aligned} \tag{3.13}$$

Substituting the second term (damping term) of Eq.(3.12) with the result of Eq.(3.13) and following the vector triple product relationship [13], it yields,

$$\begin{aligned}\frac{\left(1+\alpha^2\right)}{\gamma}\frac{d\vec{m}}{dt} &= -\vec{m}\times\left[\vec{H}_{eff}-\left(\alpha\,T_{\parallel}^{c}-T_{\perp}^{c}\right)\vec{p}_c-\left(\alpha\,T_{\parallel}^{r}-T_{\perp}^{r}\right)\vec{p}_r\right]\\ &-\vec{m}\left\{\vec{m}\times\left[\alpha\,\vec{H}_{eff}+\left(\alpha\,T_{\perp}^{c}+T_{\parallel}^{c}\right)\vec{p}_c+\left(\alpha\,T_{\perp}^{r}+T_{\parallel}^{r}\right)\vec{p}_r\right]\right\}.\end{aligned} \tag{3.14}$$

Besides the advantages for further analytical treatment, the numerical integration of the LLGS equation in the form of Eq.(3.14) is faster. Moreover, and to reduce the number of input equations to compute from three (Cartesian base: x, y, z) to two, Eq.(3.14) was converted to spherical coordinates [117,118]. Thus, in terms of θ and φ, the modified LLGS can be written as,

$$\begin{aligned}\frac{\left(1+\alpha^2\right)}{\gamma}\frac{d\theta}{dt} &= H_{eff,\varphi}+\alpha\,H_{eff,\theta}-T_{\parallel}^{c}\left(\alpha\,p_{c,\varphi}-p_{c,\theta}\right)-T_{\perp}^{c}\left(p_{c,\varphi}+\alpha\,p_{c,\theta}\right)\\ &-T_{\parallel}^{r}\left(\alpha\,p_{r,\varphi}-p_{r,\theta}\right)-T_{\perp}^{r}\left(p_{r,\varphi}+\alpha\,p_{r,\theta}\right),\\[2ex] \frac{\left(1+\alpha^2\right)}{\gamma}\sin\theta\frac{d\varphi}{dt} &= \alpha\,H_{eff,\varphi}-H_{eff,\theta}+T_{\parallel}^{c}\left(\alpha\,p_{c,\theta}+p_{c,\varphi}\right)+T_{\perp}^{c}\left(p_{c,\theta}-\alpha\,p_{c,\varphi}\right)\\ &+T_{\parallel}^{r}\left(\alpha\,p_{r,\theta}+p_{r,\varphi}\right)+T_{\perp}^{c}\left(p_{r,\theta}-\alpha\,p_{r,\varphi}\right)\end{aligned} \tag{3.15}$$

Here $H_{eff,\theta}$, $H_{eff,\varphi}$ and $p_{c,\theta}$, $p_{r,\varphi}$, $p_{c,\theta}$, $p_{r,\varphi}$, are the $\vec{e}_\theta$ and $\vec{e}_\varphi$ components of $\vec{H}_{eff}$ and $\vec{p}_{c,r}$, respectively.

Besides the demonstration of a more solvable form of the LLGS equation, it is convenient to further describe some of its terms, notably those involving H_{eff} and the STT terms, $T_{\parallel}$ and $T_{\perp}$. The first term (precessional) of the right-hand side of (3.12) has the form of a torque. The torque is exerted by an effective field which is derived from the total energy E of the storage layer with volume V [14],

---

[13] In particular: $\vec{m}\times\left(\vec{m}\times\frac{d\vec{m}}{dt}\right)=\vec{m}\left(\vec{m}\cdot\frac{d\vec{m}}{dt}\right)-\frac{d\vec{m}}{dt}\left(\vec{m}\cdot\vec{m}\right)=-\frac{d\vec{m}}{dt}$ and $\vec{m}\times\left(\vec{m}\times\vec{p}\right)=\vec{m}\left(\vec{m}\cdot\vec{p}\right)-\vec{p}$

[14] The volume V is used here in the energy expressions, though it is unitary in our simulations for simplicity of calculations.

$$\vec{H}_{eff} = -\frac{1}{V}\frac{\partial E}{\partial \vec{M}} \tag{3.16}$$

The potential energy [15] for the storage layer [64, 119] is $E = E_d + E_z$, where E_d is the self-demagnetizing energy due to the shape of the storage layer and E_z is the Zeeman energy from the external applied field H. The self-demagnetizing energy coming from shape anisotropy is defined as,

$$E_d = \frac{1}{2}VM_s\left(\vec{m}\cdot\vec{H}_d\right) = \frac{1}{2}VM_s\left(\vec{m}\cdot\boldsymbol{N}\cdot\vec{m}\right) = \frac{1}{2}VM_s^2 4\pi\left(N_x\cos^2\theta\sin^2\varphi + N_y\sin^2\theta\sin^2\varphi + N_z\cos^{\theta}\right), \tag{3.17}$$

where $\vec{H}_d = M_s\boldsymbol{N}\cdot\vec{m}$ is the demagnetizing field and $\boldsymbol{N}$ is the demagnetizing tensor. The demagnetizing factors are N_x, N_y, N_z, respectively, for $\vec{e}_x$, $\vec{e}_y$, $\vec{e}_z$ and were calculated following Ref. [120] for an ellipsoid with 140nm×130nm×3nm (in order to have an $H_c < 50Oe$). Finally, the Zeeman energy due to a field H applied along $\vec{e}_y$ is expressed by,

$$E_z = 4\pi VM_s\left(\vec{m}\cdot\vec{H}\right) = 4\pi M_s H\sin\theta\sin\varphi. \tag{3.18}$$

The $H_{eff,\theta}$ and $H_{eff,\varphi}$ components in expression (3.15) may be then found by applying $\nabla E(\theta,\varphi) = (\partial E/\partial\theta)\,\vec{e}_\theta + (\partial E/\partial\varphi)\,\vec{e}_\varphi$ on Eq.(3.16).

Relatively to the STT terms, we need to defined the dependence of the STT components $T_\parallel$ and $T_\perp$ with voltage V. For positive voltage, electrons flow from reference to free layer and from free layer to control layer. Thus, the effect of current on the free layer, due to STT, is reversed. Therefore we chose the following convention: torque stemming from reference layer is function of V, whereas torque stemming from control layer is function of $-V$. Finally, the STT components are defined as,

$$\begin{aligned}
T_\parallel^c &= a_1^c(-V) + a_2^c(-V)^2\\
T_\perp^c &= b_1^c(-V) + b_2^c(-V)^2\\
T_\parallel^r &= a_1^r V + a_2^r V^2\\
T_\perp^r &= b_1^r V + b_2^r V^2.
\end{aligned} \tag{3.19}$$

In addition, it is important to stress that the voltage applied to each barrier individually is not purely V. In fact, V is the total voltage applied to the DBMTJ. In eqs.(3.19), the fraction of V applied to each barrier is controlled by the prefactors a_1, a_2, b_1, b_2, where the attached subscripts r and c are respectively connected to the bottom and top barriers, the ones respectively closer to the reference (r) and control (c) layers. For example, for an asymmetric barriers DBMTJ with a bottom barrier 2x more resistive than the top barrier ($RA_{bottom} = 2\,RA_{top}$), the prefactors should respect a similar ratio: $a_{1,2}^r = 2\,a_{1,2}^c$ and $b_{1,2}^r = 2\,b_{1,2}^c$.

This choice was made to have an extra degree of freedom in the definition of the torque components. The parameters used for the simulation are presented in table 3.8.

The simulations were realized in order to mimic the phase diagrams of section 3.3, using finite writing voltage pulses with $\tau = 100\,ns$. For each value of voltage V, the field H was swept from -100 Oe to 100

---

[15] The uniaxial anisotropy energy is defined as $E_u = K_u\sin^2\theta\sin^2\varphi$, albeit its influence is negligible, thus it is not included in our model.

Table 3.8: The values used for the assigned parameters of the macrospin simulations.

Parameters	Value
γ	$1.85 \times 10^{-7}\, s^{-1} Oe^{-1}$
α	0.0055
M_s	$1000\, emu/cm^3$

Oe and then back to -100 Oe. The phase diagrams shown are a superposition of the two phase diagrams corresponding to each of the field sweeps. The colors of the phase diagram represent resistance and are directly associated to one of the possible magnetic states of the DBMTJ, P-AP or AP-P (write mode) and P-P or AP-AP (read mode). The integration time was $0.6\, \mu s$ in each field point.

Another important difference between these $T = 0\, K$ simulations and the phase diagrams obtained experimentally at room temperature is the starting voltage of the STT driven boundaries. While in the simulations, the starting point in voltage of the STT boundary solely depends on the strength of the torque (ex. starting from $V = 0$ when $\Delta b_2 \neq 0$ in write mode and $\Sigma b_2 \neq 0$ in read mode), in the experimental phase diagrams the STT switching boundaries never start from $V = 0$. In the initial stage, when all the magnetizations are collinear, the torque is very weak which results in very low STT-induced dynamics. In fact, without any thermal fluctuations to trigger a non collinearity between the magnetizations, the switching time of the storage layer would be infinite for any spin-polarized currents [64, 121]. Therefore, in experimental phase diagrams, the STT switching boundaries do not start for voltage values around 0 because there is no significant misalignment between the storage layer and polarizers magnetizations. In the macrospin simulations, a small misalignment ($0.1°$) between $\vec{m}, \vec{p}$ and $\vec{H}$ was introduced in the system in order to avoid infinite switching time.

3.4.2 Influence of In-plane and Out-of-plane torques on STT switching

To better understand the interplay between the two components of the spin torque in a dual reference system, we start by introducing individually the most accepted dependencies of the in-plane and out-of-plane torque with applied voltage. Thus, a linear dependence with V for the Slonczewski torque [44, 122], a_1^c and a_1^r factors from Eq.(3.19), and a quadratic dependence with V for the field-like torque [53–55, 123], b_2^c and b_2^r factors from Eq.(3.19). In the study that follows, we used, as an example, the resistance and TMR values of a symmetric barriers DBMTJ: $R_{Bottom} = R_{Top} =$ 2000Ω, $TMR_{Bottom} =$ 94% and $TMR_{Top} =$ 84% [16] Consequently, the stable AP-P and AP-AP states exist for $H > 0$ and the stable P-AP and P-P states exist for $H < 0$.

In Fig.3.45, we analyze the in-plane torque linear prefactors a_1^r and a_1^c in write mode. On the main diagonal of the matrix, both prefactors increase in absolute value from 10 to 60 Oe/V while remaining equal. As the absolute value increases, the critical switching voltage V_{sw} [17] decreases. The same happens if we fix one of the prefactors and increase the other one (on Fig.3.45, in a line: going from left to right / in a column: going from top to bottom). In the case where $a_1^r = 60\, Oe/V$ and $a_1^c = 10\, Oe/V$, V_{sw} is higher than when $a_1^r = 60\, Oe/V$ and $a_1^c = 30\, Oe/V$. The torque is more efficient in second case, as

---

[16] Asymmetry in TMR of top and bottom barriers was chosen so TMR in write mode was not null.

[17] V_{sw} is calculated at $H = 0$ since there is no offset field.

the sum of two linear prefactors, $\Sigma a_1 = a_1^r + a_1^c = 90\,Oe/V$, is larger than for the first pair of prefactors, $\Sigma a_1 = 70\,Oe/V$. These results confirm that the two in-plane torques add up ($T_\parallel^r + T_\parallel^c$) when the DBMTJ is set in write mode.

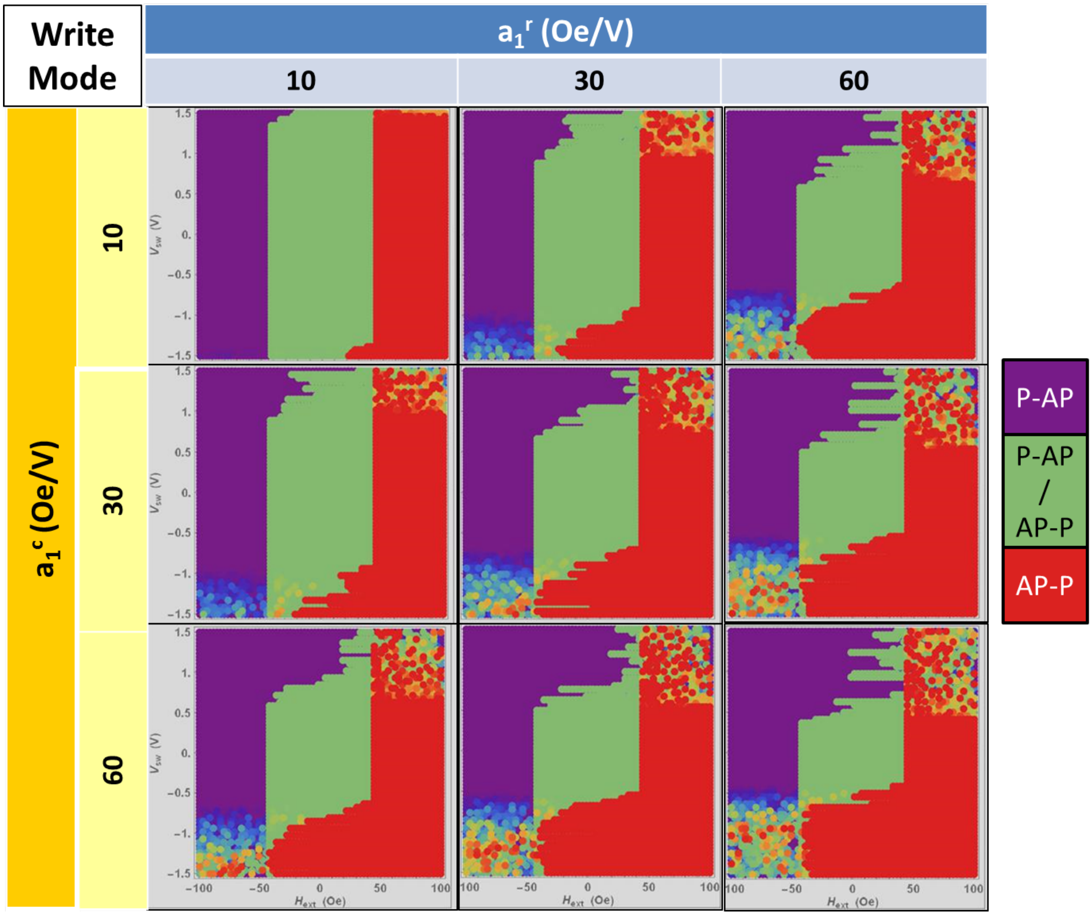

Figure 3.45: Finite writing pulse phase diagrams of a double barrier/double reference MTJ configured in write mode operation. The only torque prefactors acting on the storage layer are a_1^r and a_1^c, the remaining prefactors of eqs.(3.19) are set to zero. The applied magnetic field varies between $\pm 100\,Oe$ and the applied voltage varies between $\pm 1.5\,V$. The red color corresponds to the high resistance state, the purple color to the low resistance state and the green color to the bi-stable state.

Afterwards, we have studied the influence of the linear in-plane torque prefactors when the magnetizations of reference and control layers are set parallel to each other (read mode). In this configuration, the two torques are expected to subtract, $T_\parallel^r - T_\parallel^c$. Therefore, if we consider the main diagonal (Fig.3.46) where both prefactors have the same value ($\Delta a_1 = a_1^r - a_1^c = 0$), there is no sign of STT switching since no change on the phase diagrams has been observed whatever the applied voltage. This is the expected behavior of an ideal symmetric barriers DBMTJ in read mode. As a matter of fact, for the chosen range of applied voltages, only when $|\Delta a_1| > 50\,Oe/V$ it is possible to observe signs of STT switching (see phase diagrams at the bottom left and top right corners in Fig.3.46). Moreover, also for these two phase diagrams, it is also interesting to notice that the voltage sign that favors AP-AP or P-P states reverses when changing the origin of the dominant torque. For the top right corner phase diagram in Fig.3.46 which represents the case of a large RA asymmetry between the two barriers with bottom barrier being the thickest ($a_1^r \gg a_1^c$), the positive voltage favors P-P and negative voltage favors AP-AP. On the other extreme of the anti-diagonal (bottom left corner), the case of an asymmetric barriers DBMTJ with thicker top barrier ($a_1^r \ll a_1^c$), the STT switching voltages change polarity and follow the theoretical predictions for the ideal case of this type of asymmetric barriers DBMTJ represented by in Fig.3.20 in section 3.2.

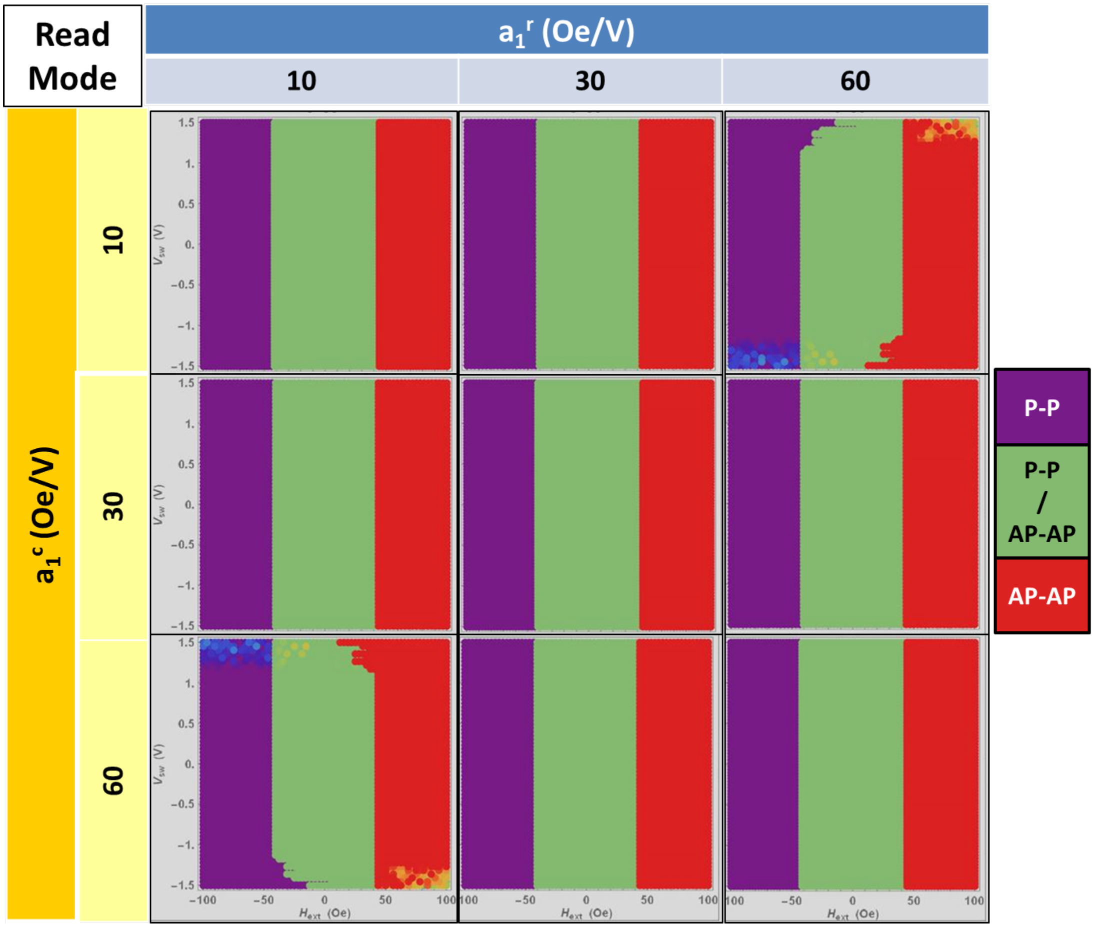

Figure 3.46: Finite writing pulse phase diagrams of a double barrier/double reference MTJ configured in read mode operation. The only torque prefactors acting on the storage layer are a_1^r and a_1^c, the remaining prefactors of eqs.(3.19) are set to zero. The applied magnetic field varies between $\pm 100\,Oe$ and the applied voltage varies between $\pm 1.5\,V$. The red color corresponds to the high resistance state, the purple color to the low resistance state and the green color to the bi-stable state.

Concerning the quadratic prefactors of the out-of-plane torque, we started by studying their influence when the DBMTJ is set in write mode. According to theory, when the magnetizations of both polarizers are in an antiparallel alignment, then $T_\perp^r - T_\perp^c$. This is confirmed for the ideal case of a DBMTJ with perfectly symmetric barriers ($b_2^r = b_2^c$) corresponding to the main diagonal in Fig.3.47. In this case, the total torque is zero and no spin torque switching is observed. When $b_2^r \neq b_2^c$ then the total field-like torque is non-zero, and two scenarios are possible. Considering that in our case, the bottom barrier is thicker (larger voltage drop), it seems coherent to assume that $b_2^r > b_2^c$. In this case, the AP-P state is favored for both voltage polarities (top right corner and adjacent phase diagrams in Fig.3.47). On the other hand, when $b_2^r < b_2^c$ then it is the P-AP state that is favored by both voltage polarities. For the phase diagrams of Fig.3.47, the P-AP state corresponds to the low resistance state while in the case of a top thicker barrier DBMTJ, the P-AP state would correspond to a high resistance state (in red color). In fact, the phase diagrams at the bottom left corner are those most in agreement with the most common experimental phase diagrams obtained for an asymmetric bottom thick barrier DBMTJ in write mode [see Fig.3.30(b)].

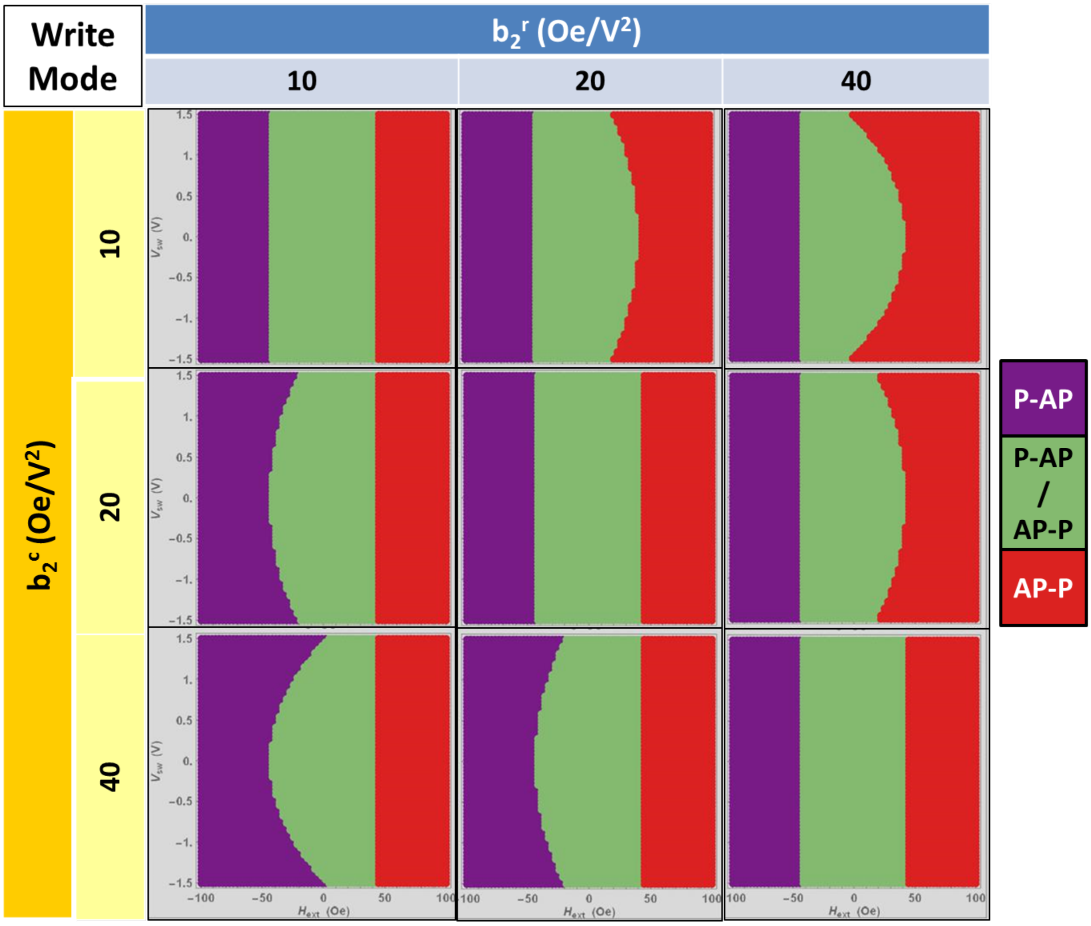

Figure 3.47: Finite writing pulse phase diagrams of a double barrier/double reference MTJ configured in write mode operation. The only torque prefactors acting on the storage layer are b_2^r and b_2^c, the remaining prefactors of eqs.(3.19) are set to zero. The applied magnetic field varies between $\pm 100\,Oe$ and the applied voltage varies between $\pm 1.5\,V$. The red color corresponds to the high resistance state, the purple color to the low resistance state and the green color to the bi-stable state.

Finally, we studied the effects of b_2^r and b_2^c in read mode. The field-like torque in read mode follows the same principle of damping-like torque in write mode, *i.e.* $T_\perp^r + T_\perp^c$. Its most visible effect can be observed by following the main diagonal of Fig.3.48. For the phase diagram of the top left corner, $\Sigma b_2 = 20\,Oe/V^2$, though the effect of quadratic torque favoring the AP-AP state can already be observed, it remains minimal. By contrast, for the phase diagram at the other extreme of the main diagonal, $\Sigma b_2 = 80\,Oe/V^2$, which is the maximum field-like torque (for the chosen values), the AP-AP state is stabilized for much lower applied voltages.

Although a direct quantitative comparison cannot be made with the results of section 3.3 since the macrospin simulations are done for $T = 0\,K$ while the measurements were performed at room temperature, we can comment qualitatively on the torques interplay on the various dual MTJ systems. Figure 3.49 presents simulated phase diagrams with a_1 and b_2 parameters adjusted in order to emulate the experimental results for the three types of DBMTJs, in write and read modes. Firstly focusing on write mode, both asymmetric top thick barrier and symmetric barriers DBMTJ present a similar behavior with

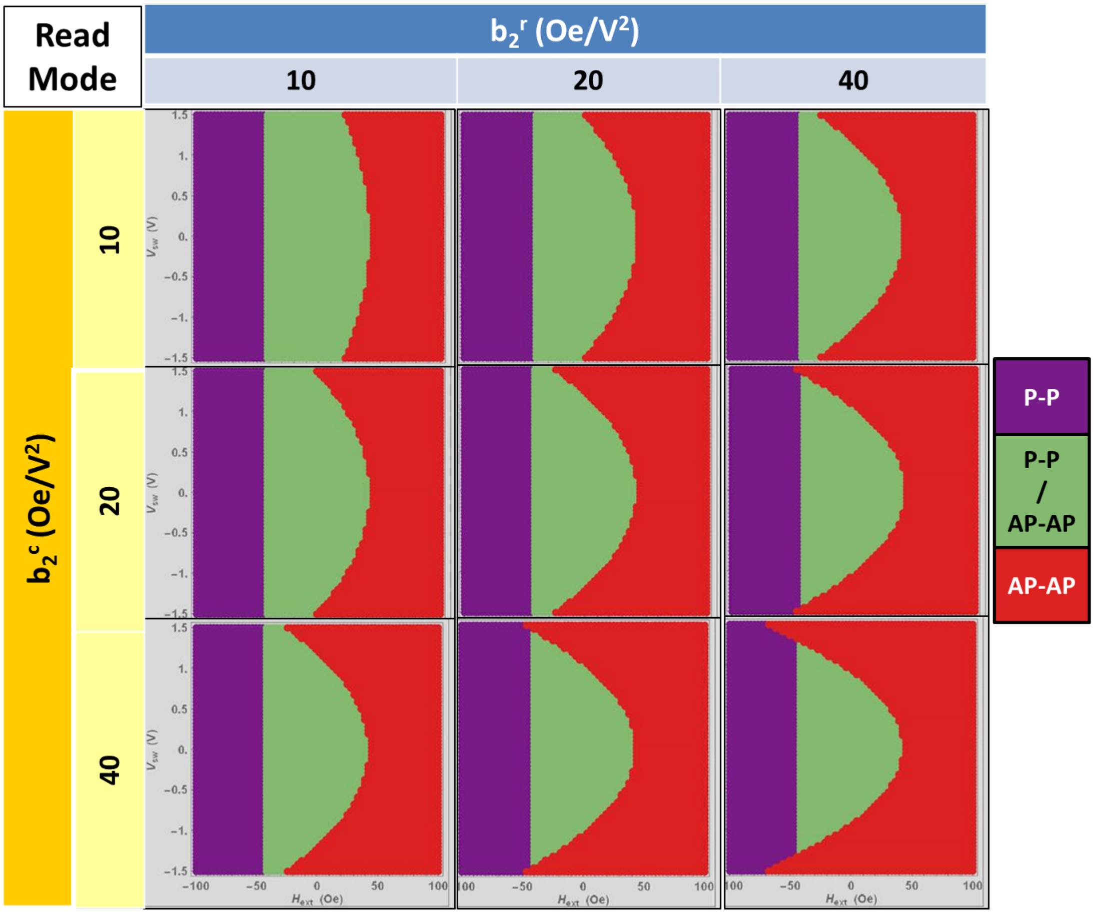

Figure 3.48: Finite writing pulse phase diagrams of a double barrier/double reference MTJ configured in read mode operation. The only torque prefactors acting on the storage layer are b_2^r and b_2^c, the remaining prefactors of eqs.(3.19) are set to zero. The applied magnetic field varies between $\pm 100\,Oe$ and the applied voltage varies between $\pm 1.5\,V$. The red color corresponds to the high resistance state, the purple color to the low resistance state and the green color to the bi-stable state.

each voltage polarity favoring one particular state. The larger Δa_1 (with $a_1^c > a_1^r$) imposed for the asymmetric top thick barrier DBMTJ than for the symmetric barriers one is reasonable since $RA_{top} > RA_{bottom}$ for the first and $RA_{top} \approx RA_{bottom}$ for the latter [18]. The effects of field-like torque are visible in the asymmetric top thick barrier DBMTJ but not in the case of symmetric barriers. As seen before, the quadratic field-like torque in write mode only plays a role if $\Delta b_2 \neq 0$. For asymmetric barriers $\Delta b_2 = 20\,Oe/V^2$ (first case) and for symmetric barriers $\Delta b_2 = 0$ for the latter. The case of the asymmetric thick bottom barrier DBMTJ is the most curious: to reproduce the experimental trend, thus to allow the low resistance state (P-AP) to be stabilized by both voltage polarities, the larger b_2 prefactor must belong to the polarizer adjacent to the thin barrier of the DBMTJ.

In read mode, the field-like torque is dominant since $T_\perp^{total} = T_\perp^c + T_\perp^r$ and the stabilization of AP-AP state is obtained for all type of DBMTJs.

Comparing our simulations with the numerical simulations performed on in-plane MTJs by Bernert *et al.* [60], we found good agreement on the relationship between the torques and the magnetic configurations they favor. One of the most interesting results, which was also observed by us, is the favoring

---

[18] Note: Though $RA_{top} \approx RA_{bottom}$, as P-AP corresponds to high resistance state in write mode, then either $RA_{top} > RA_{bottom}$ or $TMR_{top} > TMR_{bottom}$.

Type of DBMTJ	Asym. Top Thick Barr.	Asym. Bottom Thick Barr.	Symmetric Barriers
a_1^c and a_1^r (Oe/V)	40 and 10	10 and 30	30 and 10
b_2^c and b_2^r (Oe/V^2)	30 and 10	20 and 10	20 and 20

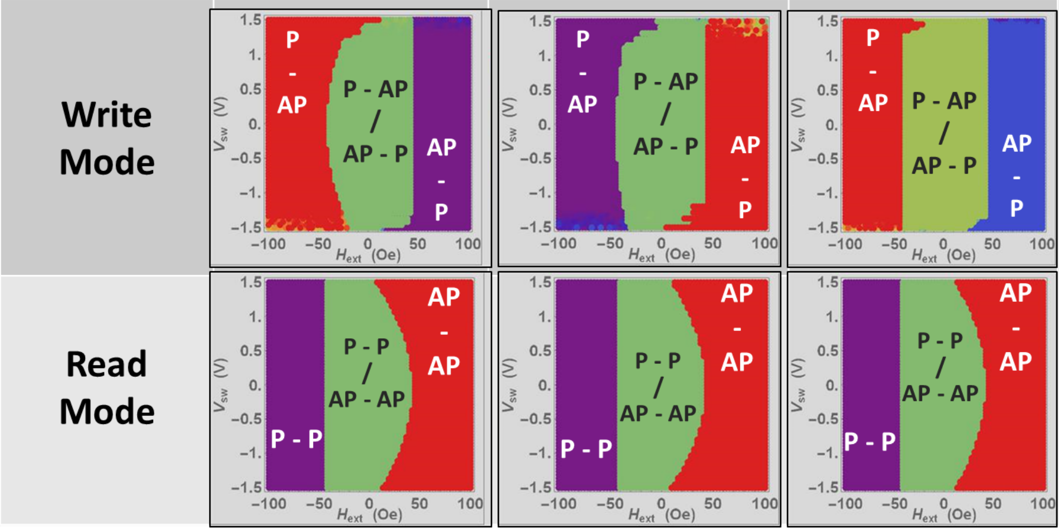

Figure 3.49: Phase diagrams with tuned linear in-plane and quadratic out-of-plane torques in order to mimic the experimental results for: asymmetric top thick barrier[write mode: Fig.3.29(a); read mode: Fig.3.37(a)], asymmetric bottom thick barrier [write mode: Fig.3.30(a); read mode: Fig.3.37(b)] and symmetric barriers [write mode: Fig.3.31(a); read mode: Fig.3.37(c)]

of AP state of the MTJ when a field-like torque term proportional to V^2 is included. Similarly to us, and particularly in read mode (Fig.3.48) where this torque term is maximized, the P→AP phase boundary presents a curvature favoring the AP state (AP-AP state in our case for a DBMTJ). Nevertheless, in the phase diagram obtained by them (see phase diagram of Fig.1.11), the AP→P also presents a curvature favoring the AP state, while our simulated phase diagrams do not show any curvature favoring any state on the AP-AP→P-P phase boundary. In addition, they claim that the two boundary curvatures are due to the quadratic field-like torque term which is also included in our model, though the curvature is only seen in one of the phase boundaries. The difference between the two phase diagrams, besides theirs corresponding to a single barrier MTJ and ours to a DBMTJ, is the computation method used for the simulations. In fact, their simulations are simple numerical integrations of the LLGS equation with a particular integration time per point and at constant voltage during this time. Whereas in our case, in our numerical integration the voltage is applied by pulses of 100 ns within an integration time per point of 600 ns. In simple terms, the magnetic state acquired for each magnetic field and voltage point is done with the torque always applied. Whereas in our simulations, the magnetic state obtained for each magnetic field-voltage point is the stable state after the torque is applied. Therefore, the P-P→AP-AP transition evolves with V^2 (due to field-like torque), thus the curvature, while the AP-AP→P-P transition is not favored by the torque and no change with voltage happens to left (negative in field) phase boundary. Since the voltage is not always ”on” during the full integration time, in the positive towards negative field sweep, the AP-AP is the stable state, no matter the amplitude of the voltage pulse, thus no change of the phase boundary. For the case of Bernert *et al.*, the voltage is always ”on” in every field sweep and during the full integration time, so is the torque. Since the field-like torque favors the

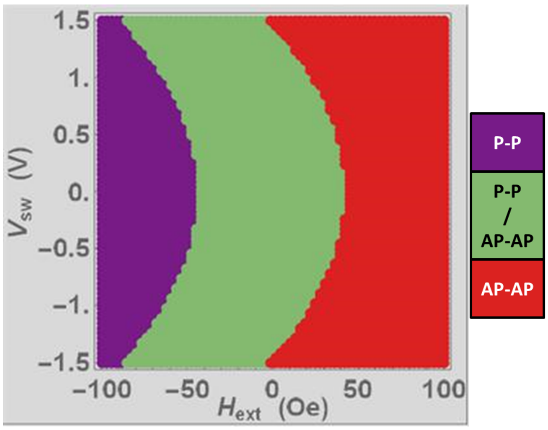

Figure 3.50: Phase diagram of DBMTJ set in read mode, obtained by simulation where voltage is applied constantly instead by 100 ns pulses. Therefore, reproducing the phase diagrams obtained by Bernert *et al.* [60].

AP state and it increases its strength with increasing voltage, whether is a negative towards positive or a positive towards negative field sweep, the junction will want to stay in the AP state. In their phase diagram, if the voltage is increased, both switching fields shift to the left for both voltage polarities, but the width of the loop remains twice the anisotropy. Switching to the AP state will thus require less field to be applied while the field necessary to induce the opposite transition will be increased in the presence of a finite bias voltage [60]. In order to validate our statements we performed a simulation of DBMTJ in read mode, applying constant voltage instead of 100 ns pulses, as shown in Fig.3.50. We obtained a phase diagram with curvature in both phase boundaries similarly to Bernert *et al.*. Since the phase diagrams in section 3.3 where obtained using pulsed voltage, our simulations reproduce the experiment (except the temperature effects) and the simulated phase diagrams are, in general, in good agreement with the experimental results obtained.

3.4.3 Linear dependence of Out-of-plane torque

Though on the vast majority of theoretical and experimental studies, the perpendicular STT is described as being proportional to V^2, some other claim the existence of a linear voltage dependent prefactor which also plays a role on the applied torque. Measurements in frequency [56] and switching current in symmetric [57] and asymmetric MTJs [91] revealed that this out-of-plane torque was proportional to the bias current and changed sign with bias voltage. Therefore a linear term in the dependence of field-like torque effective field on bias voltage should exist in addition to a quadratic one, which is in agreement with former theoretical predictions [48].

As a base scenario, we have chosen to set initial quadratic field-like torque prefactors, $b_2^c = 20\,Oe/V^2$ and $b_2^r = 10\,Oe/V^2$, which are the quadratic prefactors that better fit the experimental phase diagrams in the case of a bottom thicker asymmetric barriers DBMTJs. In addition to the quadratic fixed prefactors, we have included and studied the effects of the linear prefactor b_1 on the spin torque switching, both in write and read modes. The corresponding phase diagrams are shown in Fig.3.51.

Analyzing first the write mode, we can observe that the inclusion of the b_1 prefactor improves the efficiency of switching towards the P-AP state for positive voltages while reducing it for negative voltages, scaling with Σb_1. For the plots of the b_1^r/b_1^c pairs: 20/10, 10/20 and 20/20, we observe an additional curvature of the P-AP→AP-P boundary favoring the AP-P state. In Fig.3.47(bottom left corner phase diagrams), the curvature favoring the P-AP state has only been seen for the AP-P→P-AP boundary, meaning that when the junction is at an initial P-AP state, it does not switch with STT and only with field when $H > H_c$ for any bias voltage. The torque stabilizes the P-AP state. The inclusion of the linear b_1 prefactor acts similarly to the linear damping-like torque prefactor a_1: favors P-AP for positive voltage and seems to favor AP-P for negative voltage. However, the inner curvature seen for negative voltages seems to be opposite to the linear damping like torque behavior. For voltages near zero, the slope starts strong but it decreases as voltage becomes more negative. Apparently, this b_1 torque acts in two ways: linear dependence with voltage combined with a favoring of the P-AP state. So for negative voltage, the linear dependence favors the AP-P state while struggling to favor the P-AP with increasing voltage. Thus, as V increases the necessary field to switch towards AP-P also increases unlike the case of Fig.3.47(bottom left corner phase diagrams).

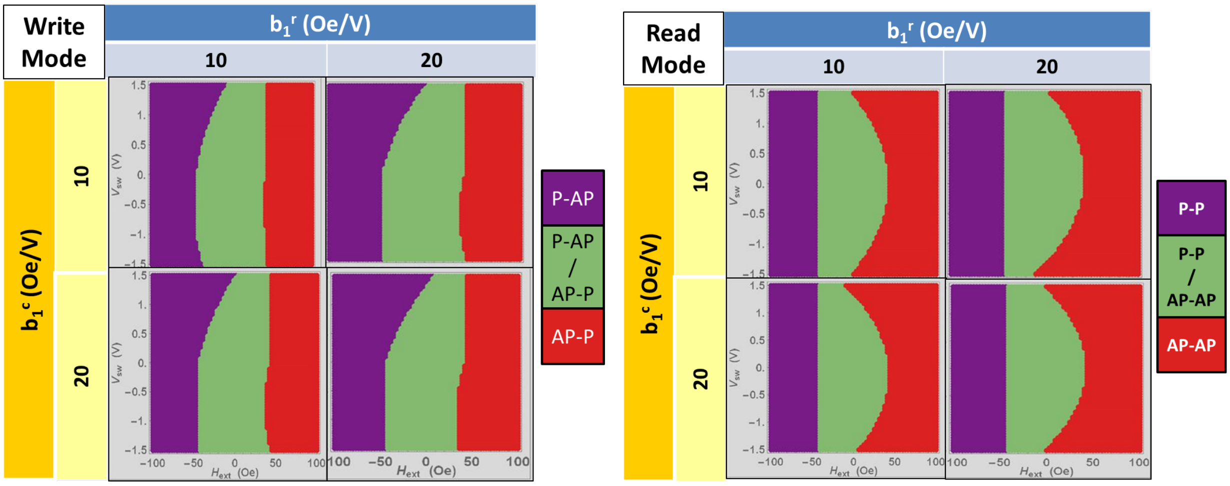

Figure 3.51: Phase diagrams of the DBMTJ under the influence of variable linear (b_1^c and b_1^r) and fixed quadratic ($b_2^c = 20\,Oe/V^2$ and $b_2^r = 10\,Oe/V^2$) field-like torque components. All the other torque components were set to zero. The phase diagrams were performed for both (*Left*) write and (*Right*) read modes.

Now focusing our attention on the read mode phase diagrams of Fig.3.51, we immediately remark that both phase diagrams from the main diagonal are equal. This implies that the perpendicular torque linear with voltage components cancel in read mode since $\Delta b_1 = 0$ and an increasing Σb_1 does not produce any change on the phase diagrams. On the other hand, when $\Delta b_1 \neq 0$ the phase diagrams are slightly different depending which component b_1^r or b_1^c is larger. In these phase diagrams the curvature of the two parabolas change with a shift of their minima away from $V = 0$ contrary to the case when $\Delta b_1 = 0$. When $b_1^c > b_1^r$ the minima shifts towards negative voltages while the shift happens for the opposite voltage polarity for $b_1^c < b_1^r$. Consequently, if $b_1^c > b_1^r$ the positive voltage favors more efficiently the AP-AP state, while in the opposite cases, the negative voltage is the most effective. A similar result was found by Bernert *et al.* [60] when adding a linear perpendicular torque component to their single MTJ model.

By comparing the simulated phase diagrams with experimentally obtained ones, we conclude that the presence of a linear voltage dependence of the out-of-plane torque (even if small in magnitude) may explain the slight asymmetries in voltage of the parabolas boundaries favoring P-AP (in write mode, see figs.3.29,3.30 and 3.31) and AP-AP (in read mode, see Fig.3.37).

3.4.4 Quadratic dependence of In-plane torque

Although it is unlikely to happen, we found interesting to study the effects of a quadratic component of in-plane torque component (a_2) in our dual MTJ system. The only quasi-quadratic behavior measured for the damping-like torque was observed by Kubota *et al.* [59] and Sankey *et al.* [53] for CoFeB/MgO/CoFeB MTJs where this torque would reverse its sign under very large positive voltages. This trend of in-plane torque with bias voltage had been predicted theoretically [50, 51, 124] for half-metals with an exchange splitting $\Delta \approx 1 - 1.5$ [19]. The quadratic dependence with voltage as only been accounted in theory for the particular case of 1/4 majority band filling and $\epsilon^{\downarrow} = 4.2$ ev (see as an example Fig. 4 from [51]). This situation is described, by Chshiev *et al.* [51], to be only possible due to a maximum in charge current as a function of band filling so that the appropriate exchange splitting between $\epsilon^{\uparrow}$ and $\epsilon^{\downarrow}$ around the maximum causes the corresponding charge currents to be equal.

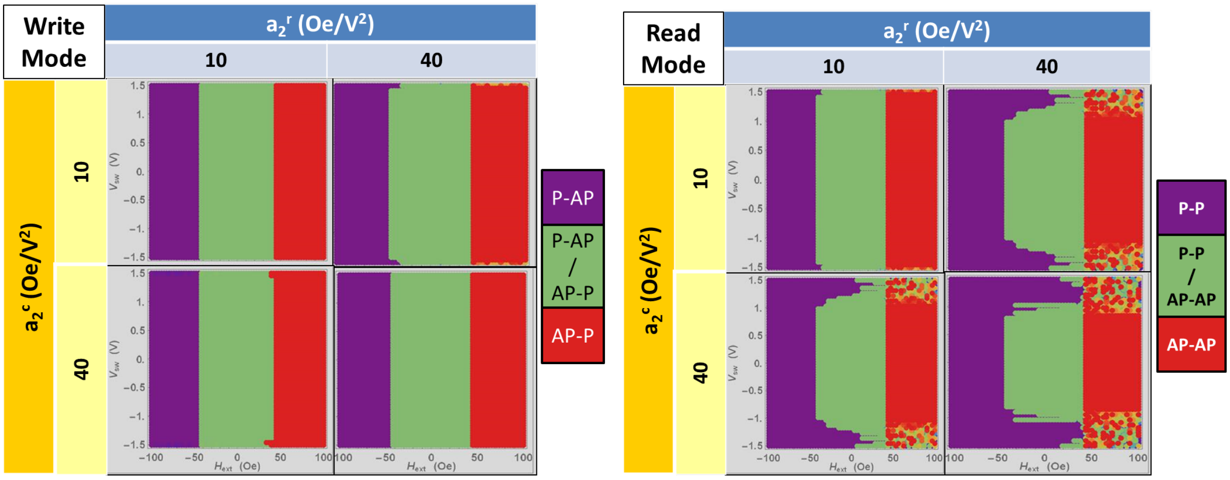

Figure 3.52: Phase diagrams of the DBMTJ under the influence of variable (a_2^c and a_2^r) in-plane torque components. All the other torque components were set to zero. The phase diagrams were performed for both (*Left*) write and (*Right*) read modes.

Figure 3.52 shows the phase diagrams for variable paired values of a_2^c and a_2^r set in write and read modes. For the case of the DBMTJ in write mode, no current induced switching occurs for the phase diagrams on the main diagonal corresponding to $\Delta a_2 = 0$. For the phase diagrams of the anti-diagonal, depending on the dominant prefactor a_2^c or a_2^r, the AP-P or P-AP state is favored for both voltage polarities, respectively. In fact, contrary to what happens with the field-like torque b_2 component in write mode (see Fig.3.47), the favored state is the one for which the storage layer is in antiparallel alignment to the reference carrying the lowest a_2 value. Judging from the phase diagrams for which $\Delta a_2 = 0$ and those with $\Delta a_2 \neq 0$, we can conclude that the quadratic components of damping-like torque subtract in write mode, as expected.

---

[19] The exchange splitting is defined as $\Delta = \varepsilon^{\downarrow} - \varepsilon^{\uparrow}$ for Ref. [50] while $\Delta = (\varepsilon^{\downarrow} - \varepsilon^{\uparrow})/2$ for Refs. [51, 124].

In read mode, the introduction of the a_2 prefactor favors and stabilizes the P-P state. Similarly to the b_2 prefactor of field-like torque, a_2^c and a_2^r add up. With the increase of Σa_2, the AP-AP→P-P switching is more efficient. For different Δa_2, conserving a similar Σa_2 (phase diagrams on the anti-diagonal), the phase diagrams present no differences. Although the opposite behaviors of the quadratic in-plane and out-of-plane torques are explained by the opposite signs of these two torques with bias voltage, the shapes of their read mode phase diagram parabolas are quite distinct. In the case of an acting quadratic field-like torque (see Fig.3.48), the variation of the switching voltage with applied field is rather smooth and the P-P→AP-AP boundary parabola's concavity closes more with increasing Σb_2 though conserving a quadratic curve behavior. On the contrary, for the case of a quadratic damping-like torque, the switching voltage does not start from $V = 0$, yet there is a trigger voltage for which the switching begins. This trigger voltage V_{trigg} reduces with increasing Σa_2, with $V_{trigg} = 1.4\,V$ for $\Sigma a_2 = 20\,Oe/V^2$ decreasing to $V_{trigg} = 0.9\,V$ for $\Sigma a_2 = 80\,Oe/V^2$. In addition, the switching boundary is almost linear and the slope (in V/Oe) reduces with increasing Σa_2.

In our experiments, none of the measured DBMTJs presented phase diagrams similar to those of Fig.3.52. As mentioned at the beginning of this section, this in-plane torque component was only considered in theoretical publications.

3.5 Summmary

In this chapter we have characterized and performed current/voltage induced switching measurements of double barrier magnetic tunnel junctions with in-plane anisotropy with different RA ratios between top and bottom barrier: asymmetric bottom thick barrier ($RA_{top} = 10\,\Omega.\mu m^2$ and $RA_{bottom} = 35\,\Omega.\mu m^2$), asymmetric top thick barrier ($RA_{top} = 35\,\Omega.\mu m^2$ and $RA_{bottom} = 10\,\Omega.\mu m^2$), thick ($RA_{top} = RA_{bottom} = 45\,\Omega.\mu m^2$) and thin ($RA_{top} = RA_{bottom} = 10\,\Omega.\mu m^2$) symmetric barriers.

First, STT switching measurements were performed using DC current, for the dual barrier MTJs set in write and read operation modes. In write mode, the results did not reveal a correlation between the RA ratios of the DBMTJs and the switching current densities. Backhopping events were observed for circular DBMTJs, independently of the degree of RA symmetry between the oxide barriers. Its origin is mainly connected with the interplay between the in-plane and perpendicular torques. Nevertheless, the DBMTJs presented approximately two times lower switching current densities ($J_{sw}^{DBMTJ} = 1.9\,MA/cm^2$) than a single barrier MTJ ($J_{sw}^{SBMTJ} = 4.1\,MA/cm^2$). Thus showing that the DBMTJ is a reliable alternative to reduce power consumption in STT-MRAM devices. In read mode, additionally to the P-P→AP-AP transitions reported by P.-Y. Clément [1] for symmetric barriers structures, we have also observed switchings in the opposite direction for all measured devices. The calculated switching current densities were of the same magnitude of those reported for write mode.

In order to mitigate the temperature effects during switching, we performed finite voltage pulse ($\tau = 100\,ns$) measurements on the same types of DBMTJs. In write mode, the DBMTJs presented two types of behaviors: i) a predominant effect of linear damping-like torque ($T_{\|} \propto a\,V$) where each of the voltage polarities stabilizes a different state and ii) a predominant effect of a quadratic perpendicular torque component ($T_{\perp} \propto bV^2$) which favors the antiparallel alignment between the storage layer and reference (or control) layer around the thicker barrier. The only exception was verified for the case of the asymmetric barriers DBMTJ with thick barrier adjacent to the bottom reference layer. Here the perpendicular torque favored the antiparallel alignment between the storage and control layers adjacent to the thinner barrier, in opposition to what was observed for the other two DBMTJs and in disagreement with theoretical predictions. The critical switching current densities were determined from the linear fitting of the phase boundaries of the phase diagrams. The switching current density for the DBMTJs varied between $J_{sw}^{DBMTJ} = 1.4 - 5.9\,MA/cm^2$ for both transitions while for the single barrier MTJ the more energy consuming transition P→AP registered a $J_{sw}^{SMTJ} = 8.1\,MA/cm^2$. Thus conserving the 2x reduction in critical switching current density for the double barrier MTJs. The symmetric barriers DBMTJs present slightly lower J_{sw} than those with asymmetric barriers. The J_{sw} asymmetry between AP-P⇄P-AP transitions in the DBMTJs was also reduced compared to the P⇄AP transitions in a single barrier MTJ. In addition, the stress (applied voltage) on each of barriers of the DBMTJ is reduced by a factor of 2 relatively to a single barrier MTJ. Therefore showing that DBMTJs have a larger operating window ($V_{breakdown} - V_c$) than comparable single barrier MTJs. In read mode, all the DBMTJs exhibited an unanimous behavior: P-P→AP-AP switching being favored with V^2. This effect is due to a dominant field-like torque acting on the storage layer. In both read and write modes, we have observed a very dominant effect of field-like. While expected to be maximum in read mode ($T_{\perp total}^{Read} = T_{\perp}^{Control} + T_{\perp}^{Reference}$), it was supposed to be minimum or even zero (symmetric barriers) in write mode ($T_{\perp total}^{Write} = T_{\perp}^{Control} - T_{\perp}^{Reference}$). Besides, in write mode, the favored state, by both voltage polarities, is the antiparallel alignment between the storage layer and the control layer around the top barrier. Two hypothesis were proposed to explain these observations: i) conical shape of the DBMTJ pillar which would make the top barrier smaller in area than the bottom barrier thus a larger number of electrons carrying torque (higher field-like torque) around that barrier and ii) a better texture quality of the top barrier than bottom barrier which would increase TMR on the first one thus enhancing the effects of torque around this one, even if the RA of the top barrier is smaller than the bottom one.

We have also studied an undesired event, which compromises the application of the in-plane anisotropy DBMTJ as an MRAM, the current induced mode switch. The experimental results obtained were not totally conclusive. In fact, we proposed two models that can explain the obtained results depending on which of the SAF ferromagnetic layer is more stable. The mode switch phenomenon results from the loss of exchange between the top pinned layer and the top antiferromagnet (FeMn) due to Joule heating. However, we have showed that the reversal of the control layer magnetization (mode switch) depends on the magnetic configuration of the DBMTJ and the applied magnetic field. In fact, this physical effect does not happen always if the DBMTJ is in a state and under a magnetic field that does not favor the reversal of the control layer magnetization.

Finally, the interplay between in-plane and perpendicular torques in a trilayer system with one free layer in between two polarizers was studied using macrospin simulations. The influence of the linear and quadratic prefactors of the two torques were analyzed for the simulated DBMTJ, either in write and read modes. The two linear in-plane torques coming from reference and control layers were shown to add up in write mode and subtract in read mode. While the opposite happens for the quadratic components of the out-of-plane torque. The reproduction of the experimental results was possible by setting a larger value to the torque prefactors coming from the polarizer adjacent to the thickest barrier. Except for the case of the asymmetric bottom thick barrier whose phase diagrams were only replicated if $b_2^c > b_2^r$, *i.e.*, a larger perpendicular torque coming from the control layer adjacent to thinner barrier. The inclusion of a perpendicular torque linear with the bias voltage was shown to explain the small shifts in voltage of the parabolas' concavities (not centered in $V = 0$), for both write and read modes. A V^2 dependent damping-like torque was also studied but its behavior did not show any resemblance with the experimental results, proving this torque dependence is not present in the double barrier system.

4

Development and optimization of a new functional top reference for DBMTJs with perpendicular anisotropy

Contents

4.1 Introduction

In section 1.5.4, the advantages of STT-MRAM based on magnetic tunnel junctions with perpendicular magnetic anisotropy (PMA) have been described. In spite of TMR or damping not yet comparable to those attained by in-plane magnetized systems, scalability, data retention (thermal stability) and power consumption are the key features of this technology for industrial applications. In order to further reduce the switching current density without compromising the thermal stability, one of the strategies lies on a double barrier/double reference system. As already been demonstrated for in-plane [80] and, more recently, for perpendicular [76] anisotropy DBMTJs, the STT acting on the storage layer is enhanced when the two references magnetizations are in antiparallel alignment. High quality perpendicular MTJs with bottom reference (showing high TMR and good thermal stability of the reference layer) have been vastly demonstrated due to the high effective anisotropy ($K_{eff} \approx 10^7 erg/cm^3$) displayed by bottom references based on Co/Pt multilayers ([Co/Pt]$_n$) grown on Pt and Ru seed layers [125–129]. While high thermal stability was obtained for these [Co/Pt]$_n$ acting as bottom electrode with well textured seed layers, the same does not happen when the growth is made on top of FeCoB/MgO/FeCoB under-layers due to a poor fcc (111) texture [when (Co/Pt) is deposited directly in FeCoB electrode] [130, 131]. Therefore, the development of a DBMTJ with perpendicular anisotropy is rather challenging, mainly due to the complex engineering of a top electrode with high PMA.

In this chapter, we present part of the work developed in direct collaboration with fellow PhD student Jyotirmoy Chatterjee. The objective of our research was to develop and optimize a functional stack with high PMA to be used as a top reference in a DBMTJ with perpendicular anisotropy (p-DBMTJ). The development of such novel seedless multilayers (NSML) [1] with high PMA is addressed in the thesis manuscript of J. Chatterjee [132]. Here we describe the optimization of the top reference with the novel multilayers included as one part of the SAF structure and show characterization of the full p-DBMTJ stacks.

4.2 Perpendicular Magnetic Anisotropy

In magnetic materials, magnetization may align into certain preferential directions. This phenomenon is called magnetic anisotropy. The control of anisotropy is thus crucial for applications using the properties of magnetic systems. For MRAM, two stable positions should exist in the absence of external stimulus, which can be obtained by inducing an anisotropy axis in the materials. This preferred axis is called easy axis. The volume energy of the system is defined as

$$E = -K_{eff} \cos^2(\theta) \tag{4.1}$$

where θ is the angle between the magnetization and the anisotropy axis and K_{eff} is the effective magnetic anisotropy energy constant. In fact magnetic anisotropy has different contributions: magnetocrystalline, magnetoelastic, shape and surface anisotropies. Thus, K_{eff} is defined by $K_{eff} =$

---

[1] The composition of the NSML cannot be disclosed because of intellectual property issues.

$K_v - 2\pi M_s^2 + \frac{2K_s}{t}$, where K_v is the volume anisotropy energy (magnetocristalline and magnetoelastic anisotropies), $-2\pi M_s^2$ is the shape anisotropy related to the demagnetizing field, K_s the surface anisotropy energy and t the thickness of the magnetic element.

PMA is obtained when the easy axis is normal to the magnetic film/layer. The following sections address the different sources of PMA.

4.2.1 PMA from spin-orbit interactions and metal/oxide interface

Spin-orbit interaction is the main and common origin of PMA in magnetic multilayers and magnetocrystalline anisotropy in bulk magnetic materials. This interaction connects the electron's spin with its orbital motion and gives rise to an orbital moment L_z. The lattice arrangement plays an important role in this phenomenon since the spin moment couples with the lattice [133]. Large values of L_z were predicted for transition metal monolayers (Co, Ni,...) [134] and magnetic multilayers [135, 136] including heavy metals (ex. Pt, Pd, Au, Ta, rare earths,...) which display strong spin-orbit coupling.

In fact, this type of materials is of particular interest for Hard Disk Drive perpendicularly magnetized media. Chemically ordered transition metal alloys like CoPtCr, L1$_0$ ordered FePt, FePd and CoPt [137, 138] present PMA due to the spin-orbit-coupling of Pt and Pd associated with low crystal symmetry which results in a high magnetocrystalline anisotropy. In these cases, PMA is said to have a bulk origin. However, the FePt and FePd alloys require very high (and stack incompatible) annealing temperatures to exhibit high PMA. And, along the CoPtCr and CoPt, they have a large damping factor, not suitable to the free layer.

With the reduction of thickness of magnetic films and their arrangement in multilayers, interface effects become measurable, contrary to bulk materials where these effects are negligible compared to the volume contributions. The role played by surface anisotropy is now put into evidence. This anisotropy was first predicted by L. Néel [116] and was attributed to a change in the symmetry at the interfaces. The most studied and interesting multilayers were [Co/NM]$_n$ where NM stands for non magnetic metal. By manipulating the local distribution of the Co atoms at the interfaces, it is possible to change the physical and magnetic properties of the multilayers (ex. new crystallographic phases and new anisotropy directions may appear). The discovery of PMA in (Co/Pd) multilayers [140], followed by (Co/Pt) [141] and (Co/Au) [142] has triggered a large interest in these type of multilayers since they profit both from the strong spin-orbit coupling (Pt, Pd and Au elements) but also from the interfacial effects at the ferromagnet/heavy metal interfaces. Besides the theoretical interest of these multilayers as model systems, they also present advantages for the spintronics industry:

- large K_{eff} of the order $10^7\, erg/cm^3$ which allows to fabricate devices with lateral size as small as $10\, nm$ with sufficient thermal stability.
- high flexibility of their physical features by adjusting their growth parameters, layer thickness and annealing treatments.
- deposition of the multilayers may be performed using multiple technologies, from sputtering deposition(compatible with industrial requirements) to molecular beam epitaxy (more complex and

expensive).

Despite the weak spin-orbit coupling, another form of interface anisotropy was observed at the metal/oxide interface, displaying similar magnitudes as those reported for [Co/Pt]$_n$. It was first found in Pt/CoFe/AlOx stacks [143] with a strong dependence on the degree of oxidation at the interface. In fact, for the same stack, the variation in oxidation time may turn the magnetization from out-of-plane to in-plane and *vice-versa* [144]. This phenomenon has been observed for a large variety of oxides (AlOx, TaOx, MgO,...), either crystalline or amorphous, both for plasma and natural oxidation [145]. The origin of this interface anisotropy has been attributed to the hybridization between the 3d orbitals of the transition metal and the 2p orbitals of oxygen [146]. Moreover, it also been demonstrated that annealing the sample to temperatures higher than $300°C$ also improves the PMA at the metal/oxide interface by easing the migration of oxygen atoms towards the interface [147].

Although [Co/Pt]$_n$ and [Co/Pd]$_n$ are very good candidates for a hard perpendicular reference layer due to their high values of K_{eff}, their use as storage layer in a MTJ is not ideal. They present large M_s and damping factor α, which do not allow to reduce the critical switching current. By contrast, metal/oxide interface anisotropy allows that even materials with weak spin-orbit coupling but low M_s and α, which is the case of FeCoB/MgO, are used in a p-MTJ [148]. Furthermore, the use of a MgO layer (capping layer) on top of FeCoB has proven to reinforce its PMA [149, 150], allowing for larger thicknesses and thus larger TMR. These properties therefore enable the development of double barrier tunnel junctions with FeCoB-based storage layers.

4.2.2 Methods for effective anisotropy determination

The saturation magnetization M_s of a particular magnetic stack can be measured using a superconducting quantum interference device (SQUID) or Vibrating sample magnetometry (VSM). This parameter together with the anisotropy field H_k are essential to determine K_{eff} since, in its simplest form K_{eff} may be expressed as

$$K_{eff} = \frac{M_s H_k}{2}. \tag{4.2}$$

K_{eff} corresponds to the energy needed to trigger the reversal of the magnetization from the easy axis to the hard axis. As shown in Fig.4.1, it can be extracted from VSM curves measured along easy and hard axes: K_{eff} is given by the difference between the areas below the easy and hard axes, which corresponds to the colored area in Fig.4.1.:

$$K_{eff} = \int_{Easy\,Axis} M\,dH - \int_{Hard\,Axis} M\,dH \tag{4.3}$$

The K_{eff} values presented in this section are the average of the areas between the easy and hard axes of M(H) plots, for both $H < 0$ and $H > 0$. The possible sources of error come mostly from the determination of $M_s = \frac{\mathcal{M}}{A\,t}$ where $\mathcal{M}$ is the magnetic moment measured, A is the area and t the thickness of the magnetic layer.

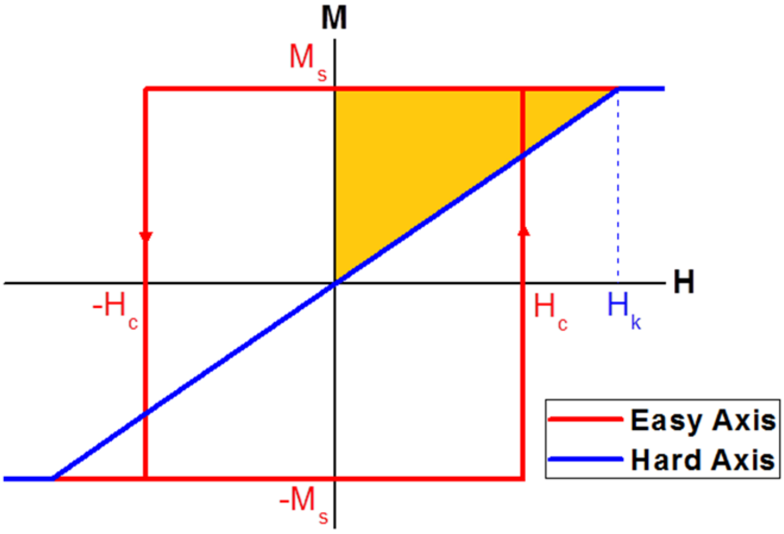

Figure 4.1: Measurement of the magnetization M as a function of magnetic field H applied parallel (red) and perpendicular (blue) to the easy axis of anisotropy. The effective anisotropy energy K_{eff} is equivalent to the area in orange. H_c is the coercive field.

4.3 Perpendicular DBMTJ with improved top reference

In this section we present the experimental results obtained from the integration of the novel seedless multilayers (more details in Ref. [132]) in a top reference single barrier p-MTJ, up to the development of a full perpendicular DBMTJ.

4.3.1 Development of a top reference in a single perpendicular MTJ

As mentioned before, [Co/Pt]$_n$ has very high K_{eff}. As for other type of multilayers, growth conditions are of paramount importance in order to ensure a strong effective anisotropy. One of the factors responsible for the growth quality and type of texture is the deposition technique. Epitaxial (100) [Co/Pd]$_n$ revealed higher values of K_v and K_s than polycrystalline (111) multilayers [151]. Another important factor is the buffer/seed layer whose type and thickness influence the PMA of (Co/NM) multilayers. (Co/Pt)$_n$ [130, 131] and (Co/Ni)$_n$ [152] demonstrated higher PMA when grown on top of thick Pt buffer layers. [Co/Pt]$_n$ (or [Co/Ni]$_n$) fcc (111) crystal structure is not compatible with MgO (001). Therefore, the use of these multilayers as MTJ top reference would cause a severe loss of TMR. The strategy is to keep FeCoB at the interface with MgO to preserve a high TMR, and add the Co-based multilayer to reinforce PMA. A texture breaking layer (TBL) is thus needed to decouple the crystallization of FeCoB from (Co/NM) fcc (111) multilayer without losing the ferromagnetic coupling of the two layers so they behave as a single macrospin [153]. Previous works [154,155] demonstrated that [Co/Pd]$_n$ can be used as top reference, since PMA is considerably higher than [Co/Pt]$_n$ ($6 \times 10^6\, erg/cm^3$ for [Co/Pd] instead of $1 \times 10^6\, erg/cm^3$ for [Co/Pt]) in the absence of a well textured seed layer. Our novel seedless multilayers (NSML) have also demonstrated a unique potential to be used as top reference since they display higher K_{eff} when grown on top of a TBL than on top a of proper buffer layer [132].

4.3.1.A Optimization of the texture breaking layer

In order to choose the best material as TBL we have deposited half top reference MTJ consisting of: Ta 3/FeCoB 0.3/MgO/FeCoB 1.1/TBL/NSML/Ru 5 (thickness in nm) where TBL = Ta or W. We have also studied the effect of the annealing temperature on K_{eff}. Figure 4.2 shows M_s [2] and K_{eff} as a function of TBL thickness [3] for stacks with the two types of TBL and for two different annealing temperatures, 350°C and 400°C. While Ta has been widely used as TBL between [Co/Pt]$_n$ and FeCoB in bottom references of p-MTJ [153], W has recently been found to improve PMA when used as cap layer on top of FeCoB storage layers, enhancing the thermal stability [156].

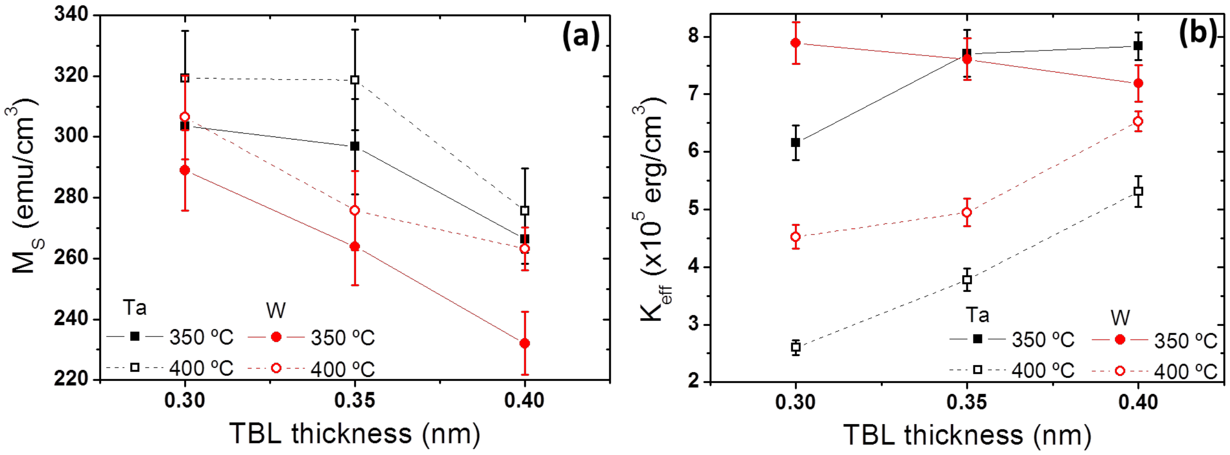

Figure 4.2: (a) Saturation magnetization and (b) effective PMA as a function of the texture breaking layer (TBL) thickness for half top reference p-MTJ Ta 3/FeCoB 0.3/MgO/FeCoB 1.1/TBL/NSML/Ru 5 (nm). The TBL elements are Ta (black squares) and W (red circles). The stacks were annealed at two different temperatures 350°C (solid markers) and 400°C (open markers).

In Fig.4.2(a), M_s decreases with increasing TBL thickness, independently from the TBL composition or annealing temperature. Moreover on average, its value is lower for W than Ta. In fact, for a 0.35 nm TBL,the stack with W has a smaller M_s than the one with Ta, even when annealed at 400°C. Besides the effective anisotropy can be viewed as the competition between two main factors, the intrinsic anisotropy K_u (that includes K_v and $\frac{2K_s}{t}$) and the demagnetization energy $2\pi M_s^2$. Since M_s decreases with increasing TBL thickness, K_{eff} consequently increases with TBL thickness as observed in Fig.4.2(b). The increase of K_{eff} with TBL thickness is verified for Ta (for both annealing temperatures) and for W annealed at 400°C. By contrast, for W annealed at 350°C, the trend is inverted. It seems that, despite the decrease of M_s, K_u is also affected, thus leading to the slight decrease of K_{eff} with increasing TBL thickness.

Although stacks with 0.3 nm W and 0.4 nm Ta annealed at 350°C show the highest K_{eff}, we chose a TBL of W with 0.4 nm. In fact, annealing at 400°C is preferred in order to obtain a high TMR ratio. Therefore, our choice of TBL is the best option to obtain both a strong perpendicular anisotropy and a good TMR ratio. The integration of this texture breaking layer in the top reference p-MTJ is discussed in the following section.

---

[2] In the M_s calculation, the total thickness used for the volume calculation is the sum of the thicknesses of FeCoB and various layers of Co and Pt of the NSML.

[3] The small range of thicknesses studied was chosen after an optimization over a larger range using only W [132]. The objective here was to compare W with Ta and also study the influence of annealing temperature on K_{eff}.

4.3.1.B p- MTJ with SAF top reference

After the optimization of the texture breaking layer, we present the first tests on perpendicular MTJs with a top reference in a SAF configuration. The SAF is used to reduce the dipolar coupling in small size pillars. While in MTJ with planar anisotropy the stray fields (acting on the free layer) are cancelled out by magnetic compensation (nearly same M_s for both ferromagnetic layers within the SAF), that is not the case for a SAF in a p-MTJ. In the latter, the ratio of magnetizations needs to be adjusted as a function of the size of the device [157]. Anyway, in general, magnetization of the ferromagnet further away from the free layer is larger than that of the ferromagnet closer to it due to a distance effect. Thus, the side of the SAF with higher magnetization is called *hard layer* while the other one is called *soft layer*.

Two different stacks were deposited. For the first one, the NSML is used both as soft and hard layer of the SAF, with the following composition of the full top reference p-MTJ stack: Ta 3/FeCoB 1.2/MgO/FeCoB 1.1/W 0.6/[NSML]$_4$/Co 0.6/Ru 0.9/Co 0.6/[NSML]$_8$/Ru 5 (in nm). The other one has the same soft layer but a hard layer composed of (Co/Pt) multilayer: its composition is the same as the hard layer of a bottom reference SAF [81, 153]. The stack is the following: Ta 3/FeCoB 1.2/MgO/FeCoB 1.1/W 0.5/[NSML]$_4$/Co 0.6/Ru 0.9/Co 0.6/Pt 0.25/[Co 0.5/Pt 0.25]$_7$/Ru 5 (in nm). The two stacks were annealed at 400°C.

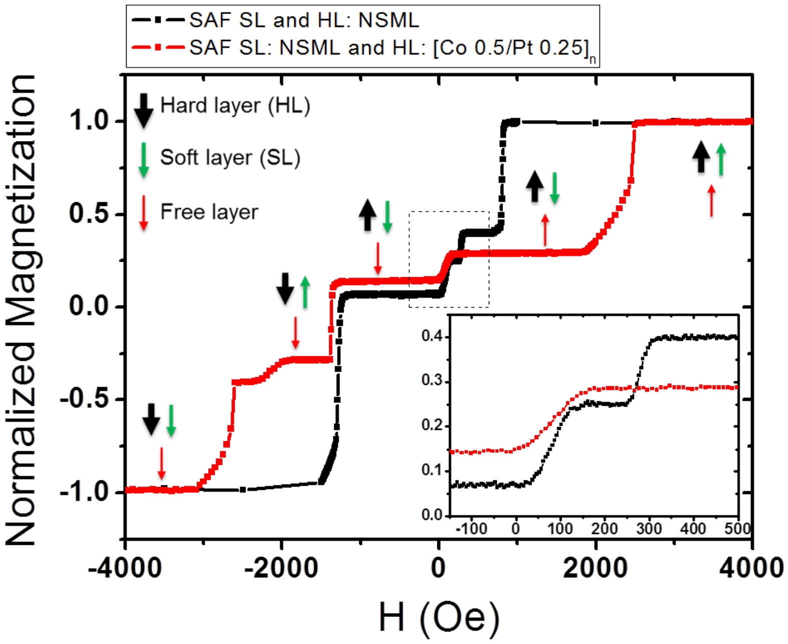

Figure 4.3: Normalized magnetization as a function of a decreasing perpendicular magnetic field, for two different top reference p-MTJs, with the following composition (thickness in nm): Ta 3/FeCoB 1.2/MgO/FeCoB 1.1/W 0.6/[NSML]$_4$/Co 0.6/Ru 0.9/Co 0.6/[NSML]$_8$/Ru 5 (black) and Ta 3/FeCoB 1.2/MgO/FeCoB 1.1/W 0.5/[NSML]$_4$/Co 0.6/Ru 0.9/Co 0.6/Pt 0.25/[Co 0.5/Pt 0.25]$_7$/Ru 5 (red). The inset is a zoom of the zone defined by the dashed square.The magnetic configuration of the plateaus of the red curve is described by arrows corresponding to the magnetization of each layer (legend on the top left corner). The black curve is described in the text.

Figure 4.3 shows the normalized magnetization as a function of the applied field for the two different top reference p-MTJs. Let us first analyze the black curve (full NSML SAF): coming from positive applied magnetic field, the rotation of the soft layer happens at 850 Oe and a second jump in magnetization at 300 Oe (see inset of Fig.4.3). In fact, these two jumps show that the ferromagnetic coupling between

FeCoB and NSML in the soft layer is broken; the two layers can no longer be described as a macrospin but are two separated layers with different spin-flop fields (the smaller one corresponding to the FeCoB). The free layer rotates at 150 Oe with an offset field of $\approx$100 Oe. Finally, the hard layer rotates at -1125 Oe to reach a full negative saturation state. For the other stack with [Co/Pt]$_n$ as hard layer, the rotation of the layers is described by arrows at each plateau of the red curve in Fig.4.3. This second stack presents multiple advantages when compared with the first one. First, coming from positive fields, the rotation of the soft layer happens at much higher field (2500 Oe) with no sign of decoupling between FeCoB and NSML. Moreover the plateau between this rotation and the onset of the rotation of the free layer (2320 Oe) is 3x larger than the one of the black curve (690 Oe). This means that a thinner W layer [4] ensures good ferromagnetic coupling within the soft layer and high PMA. In this case, the hard and soft layer do not switch together. In fact, near H = -1320 Oe, there is a double reversal or crossover of the hard and soft layers. When the hard layer rotates towards the direction of negative fields, the soft layer switches in the opposite direction due to the strong RKKY coupling that forces an antiferromagnetic coupling between the two layers. Finally, the rotation towards negative saturation of the soft layer takes place in two steps, which suggests that even 0.5 nm of W are not thin enough to guarantee ferromagnetic coupling between the two constituents of the SAF soft layer.

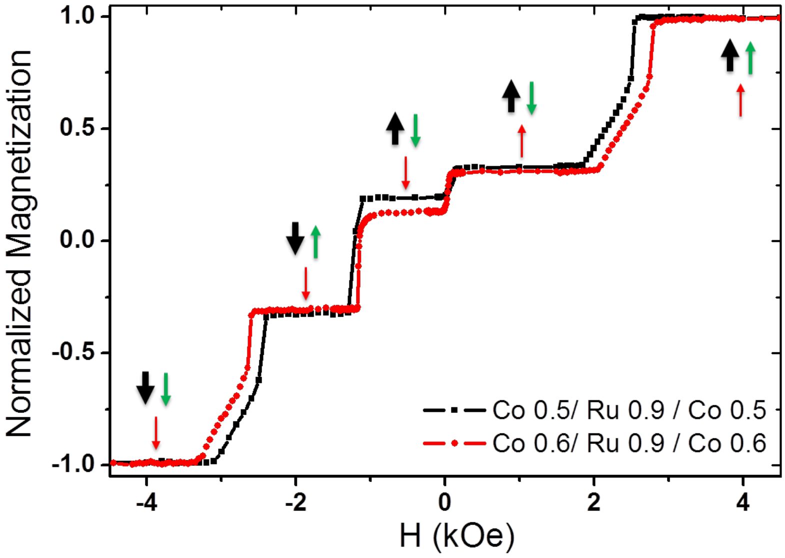

Figure 4.4: Normalized magnetization as a function of the decreasing perpendicular field H for top reference p-MTJs with the following structure: Ta 3/ FeCoB 1.2/MgO/FeCoB 1.1/W 0.4/[NSML]$_3$/Co x/Ru 0.9/Co x/Pt 0.25/[Co 0.5/Pt 0.25]$_6$/Ru 5 (in nm), where x = 0.5 nm for the black points and x = 0.6 nm for the red points. The arrows represent the magnetizations of the hard (black), soft (green) and free (red) layers.

Another important point that was shortly studied for improving the top reference SAF was the inter-layer coupling across the Ru spacer. Likewise the previously optimized bottom SAF [155], we have fixed the Ru thickness at 0.9 nm to ensure a stable antiferromagnetic coupling between the two layers of the SAF. Although larger RKKY coupling amplitudes could be reached with a smaller Ru thickness ($\approx$0.4 nm), the spacing between antiferromagnetic and ferromagnetic coupling peaks is rather small [158] and

---

[4] At this stage of our work, the optimized W TBL was 0.6 nm at multilayer level. When inserted in the full top reference p-MTJ, it showed to be too thick to keep the ferromagnetic coupling between FeCoB and NSML within the soft layer. Later it was optimized to 0.4 nm.

reproducibility issues may occur when targeting very small Ru thicknesses by sputtering deposition. While the Ru thickness is fixed, we study the influence of the thickness of the adjacent Co layers. In Fig.4.4 we compare two different thicknesses of the Co layers, 0.5 nm and 0.6 nm, in top reference p-MTJ. When using 0.6 nm of Co instead of 0.5 nm, the rotation of the soft layer (green arrow) with decreasing field happens at 2800 Oe instead of 2550 Oe. This means that RKKY coupling energy increases, probably due to a better defined Co lattice structure [130]. Nevertheless, a compromise must be found since Co films exhibit in-plane magnetocrystalline anisotropy [159] and PMA decreases for thicker Co layer.

The initial optimization of the TBL made at the multilayer level [132] showed that increasing W thickness increases PMA until a thickness of 0.6 nm, above which the ferromagnetic coupling between FeCoB and NSML is broken. However, in Fig.4.3 (red plot), we observe that the coupling is broken for a TBL of W 0.5 nm when integrated into the full top reference p-MTJ. Therefore, it is important to further optimize the top reference TBL thickness within the p-MTJ. Magnetization vs. perpendicular applied field plots for p-MTJs with varying TBL (W and Ta) thicknesses are presented in Fig.4.5.

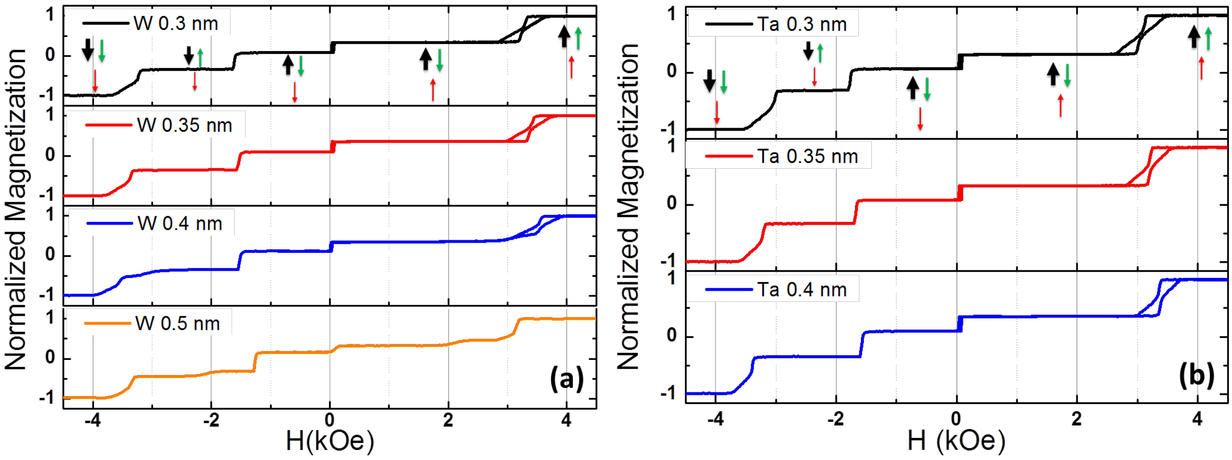

Figure 4.5: Normalized magnetization vs.field for top reference MTJs with the following stack: Ta 3/ FeCoB 1.2/MgO/FeCoB 1.1/TBL/$[\mathrm{NSML}]_3$/Co 0.6/Ru 0.9/Co 0.6/Pt 0.25/$[\mathrm{Co}\ 0.5/\mathrm{Pt}\ 0.25]_6$/Ru 5 (in nm) where (a) TBL = W with 0.3 nm (black), 0.35 nm (red), 0.4 nm (blue) and 0.5 nm (orange) and (b) TBL = Ta with 0.3 nm (black), 0.35 nm (red) and 0.4 nm (blue). All the stacks were annealed at 350°C. The arrows represent the magnetizations of the hard (black), soft (green) and free (red) layers.

In Fig.4.5(a), with a TBL of W, the squareness of the transitions improves as the W thickness reduces in agreement with the dependence of K_{eff} with TBL thickness: in Fig.4.2(b), PMA increases with decreasing W thickness for an annealing temperature of 350°C. However, the RKKY coupling energy of the SAF seems to reduce with decreasing W thickness: the minor loop associated with the reversal of the SAF soft layer is centered at 3560 Oe for W 0.4 nm, 3400 Oe for W 0.35 nm and 3260 Oe for W 0.3 nm. Therefore, a compromise needs to be found to have, simultaneously, strong PMA in all p-MTJ layers and strong RKKY coupling in the SAF. W 0.5nm and 0.4 nm are not good candidates since FeCoB in the soft layer is not coupled with the NSML. Moreover the PMA of the free layer starts to be affected too: the transition of the free layer is no more steep, especially for W 0.5 nm. The W thickness that ensures a good balance between high PMA and stable RKKY coupling is thus 0.35 nm.

For the same annealing temperature (350°C), Ta as TBL does not behave as W. In Fig.4.5(b), the minor loop becomes steeper for larger Ta thickness, indicating that PMA increases with increasing Ta thickness. In addition, the interlayer exchange coupling between soft and hard layer of the SAF also improves: the soft layer minor loop is centered at 3045 Oe for Ta 0.3 nm, 3215 Oe for Ta 0.35 nm and 3370 Oe for Ta 0.4 nm.

In conclusion, for an annealing temperature of 350°C, a TBL of Ta 0.4 nm shows the best properties, followed closely by W 0.35 nm. For the top reference of the DBMTJ, we chose a TBL of 0.35 nm W because the overall thermal stability is higher [156] which consequently allows high temperature annealing as a guarantee of higher TMR without a major loss in PMA.

One of the key aspects of the development of a double barrier magnetic tunnel junction is the storage layer. Its optimization aims to improve important p-MTJ parameters for memory applications such as thermal stability, TMR and PMA. In order to improve TMR and, more importantly thermal stability, one strategy lies on the increase of the storage layer thickness [160]. However, this increase must not compromise PMA.

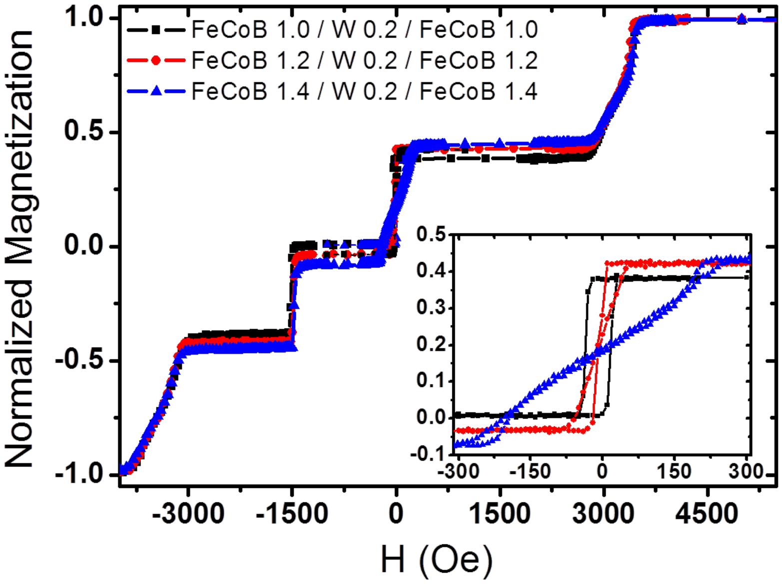

Figure 4.6: Normalized magnetization as a function of decreasing perpendicular field for top reference p-MTJ with a composite free layer with the following composition: Ta 3/FeCoB 0.3/MgO/FeCoB x/W 0.2/FeCoB x/MgO/FeCoB 1.1/W 0.4/[NSML]$_3$/Co 0.6/Ru 0.9/Co 0.6/Pt 0.25/[Co 0.5/Pt 0.25]$_6$/Ru 5 (in nm), where x = 1.0 (black), x = 1.2 (red) and x = 1.4 (blue). The inset shows the zoom of the storage layer minor loop.

Since the storage layer PMA originates at the FeCoB/MgO interface, the use of two FeCoB/MgO interfaces doubles the interface anisotropy, allowing an increase of the storage layer thickness (see section 4.2.1). In fact, it has been reported a 2x increase of the thermal stability factor when using a composite storage layer of the form FeCoB/Insertion/FeCoB [149] in comparison with a single FeCoB layer. The principal function of the insertion layer between the two FeCoB layers is to help their crystallization by attracting/absorbing boron [100]. The two most used materials are Ta and W. Recently, the use of W as an insertion layer has proven to enable higher TMR [161] and the boron extraction has proven to improve the perpendicular anisotropy of storage layer [162].

Even though the total thickness of the storage layer can be increased, the thickness of each of the FeCoB layers needs to be carefully adjusted in order to maintain high PMA. Figure 4.6 shows the normalized M(H) plots of top reference p-MTJs with composite storage layer and two MgO barriers with the following composition: Ta 3/FeCoB 0.3/MgO/FeCoB x/W 0.2/FeCoB x/MgO/FeCoB 1.1/W 0.4/[NSML]$_3$/Co 0.6/Ru 0.9/Co 0.6/Pt 0.25/[Co 0.5/Pt 0.25]$_6$/Ru 5 (in nm), with x varying between 1.0 nm and 1.4 nm. Focusing on the inset of Fig.4.6, as the FeCoB thickness increases from 1.0 up to 1.4 nm the squareness of the minor loop starts fading. For 1.0 nm, the free layer presents a coercivity of 25 Oe, decreasing to 2.5 Oe for 1.2 nm, whereas for 1.4 nm the free layer anisotropy becomes mostly in-plane. Therefore, the thickness of each of the FeCoB layers of the storage layer should not exceed 1.1-1.2 nm. However, we expect a reduction of TMR ratio for very thin free layer; a balance between TMR and PMA must thus be found. No changes were observed in the top SAF.

4.3.2 Analytical calculations of offset field: towards zero field Read/Write mode operation in p-DBMTJ

Zero field operation is a primordial requirement for MTJ to be used as a STT-MRAM in industrial applications. All research towards decreasing the device's critical switching current is useless otherwise. Although the junction might operate at very low currents, the overall power consumption may increase if the addition of a current line is necessary to induce an Oersted field in order to compensate for the hysteresis loop offset field of the free layer. The offset field H_{off} may be expressed as:

$$H_{off} = H_{cp} - H_d. \tag{4.4}$$

The first term (H_{cp}) of this equation corresponds to the coupling between the magnetic layers. This term contains different contributions: Néel "orange peel" coupling [163], which may be either ferromagnetic (for low PMA) or antiferromagnetic (for high PMA) [164] and interlayer exchange coupling, mediated by electrons, which is usually antiferromagnetic [165]. The second term accounts for the effect of the stray fields (H_d) arising from the reference layers (two in case of a DBMTJ).Whereas the coupling field is independent of the junction size, the dipolar field starts dominating for diameters below 200 nm [157] which covers our target sizes range (20 - 150 nm). Thus, the offset field expression (4.4) may be approximated to $H_{off} \approx -H_d$.

More recently, it has been demonstrated by Bandiera *et al.*, for a bottom reference perpendicular MTJ, [157] that the stray field of the SAF on the free layer cannot be exactly canceled. Only the spatial average of the stray field can be reduced to zero. Moreover, they showed that the distance between the SAF layers and the storage layer needs to be taken into account. Thus, in order to have zero offset field, the hard layer must have a larger $M_s t$ than the soft layer (see section 4.3.1.B) and the ratio between them must be adjusted as a function of the device lateral size.

Here we perform simple analytical calculations of the stray fields acting at the center of the free layer, coming from the bottom and top references. The number of repetitions n of the multilayers from the soft and hard layers of the top reference are varied in order to have the lowest H_{off} for both modes of operation (read and write) of the DBMTJ.

4.3.2.A Analytical calculations of the stray field

In a domain where there is no free current, $\nabla \times \boldsymbol{H} = 0$, thence the dipolar field may expressed using a magnetic scalar potential ψ:

$$\boldsymbol{H_d} = -\nabla\psi. \tag{4.5}$$

The expression of the scalar potential at position $\boldsymbol{r}$ is thus given by

$$\psi(\boldsymbol{r}) = \frac{1}{4\pi}\left(\int \frac{\rho_m(\boldsymbol{r'})}{|\boldsymbol{r}-\boldsymbol{r'}|}d\boldsymbol{V'} + \oint \frac{\sigma_m(\boldsymbol{r'})}{|\boldsymbol{r}-\boldsymbol{r'}|}d\boldsymbol{S'}\right), \tag{4.6}$$

where $\rho_m = -\nabla.\boldsymbol{M}$ and $\sigma_m = -\boldsymbol{M}.\boldsymbol{n}$ are the density and surface magnetostatic charges. First, considering only one magnetic layer for the reference under the free layer [Fig.4.7(a)] and assuming the magnetization of the reference layer is uniform, then $\rho_m = 0$ and $\sigma_m = \pm M_s$. The magnetic potential is calculated by integrating over the two surfaces at the top and bottom of the reference layer:

$$\psi(\boldsymbol{r}) = \frac{1}{4\pi}\left(\iint_{top} \frac{+M_s}{|\boldsymbol{r}-\boldsymbol{r'}|}d\boldsymbol{S'} + \iint_{bottom} \frac{-M_s}{|\boldsymbol{r}-\boldsymbol{r'}|}d\boldsymbol{S'}\right). \tag{4.7}$$

Considering the symmetry axis z with its origin at the center of the free layer, the magnetic potential on z becomes:

$$\psi(z) = \frac{1}{4\pi}\left(\int_{r'=0}^{R} \frac{+M_s}{\sqrt{(d_1+z)^2+r'^2}}2\pi r' d\boldsymbol{r'} + \int_{r'=0}^{R} \frac{-M_s}{\sqrt{(d_2+z)^2+r'^2}}2\pi r' d\boldsymbol{r'}\right), \tag{4.8}$$

where d_1 and d_2 are the distances from the center of the free layer to the top and bottom surface of the reference, respectively, and R is the radius of the circular cross section of the cylinder [Fig.4.7(a)]. The first term refers to the top surface while the second term refers to the bottom surface. Solving Eq.(4.8), $\psi(z)$ turns out as

$$\psi(z) = \frac{M_s}{2}\left[\sqrt{(d_1+z)^2+R^2} - |d_1+z| - \sqrt{(d_2+z)^2+R^2} + |d_2+z|\right] \tag{4.9}$$

Finally, the dipolar field can be calculated by replacing $\psi(z)$ in Eq.(4.5), thus $\boldsymbol{H_d} = -\frac{\partial\psi}{\partial z}\vec{e}_z$. Therefore,

$$\boldsymbol{H_d}(z) = \frac{M_s}{2}\left[\frac{d_2+z}{\sqrt{(d_2+z)^2+R^2}} - \frac{d_1+z}{\sqrt{(d_1+z)^2+R^2}}\right]\vec{e}_z \tag{4.10}$$

At the center of the free layer (r=0, z = 0),

$$\boldsymbol{H_d}(z) = \frac{M_s}{2}\left(\frac{d_2}{\sqrt{d_2^2+R^2}} - \frac{d_1}{\sqrt{d_1^2+R^2}}\right)\vec{e}_z \tag{4.11}$$

Nevertheless, the reference layers of our devices are SAFs which means that we need to consider two magnetic layers for the reference, thence the soft and hard layers where the latter is further away from the free layer than the soft layer. Figure 4.7(b) shows an illustration of the tetralayer structure.

Since the dipolar field is addictive, the expression for our SAF reference is

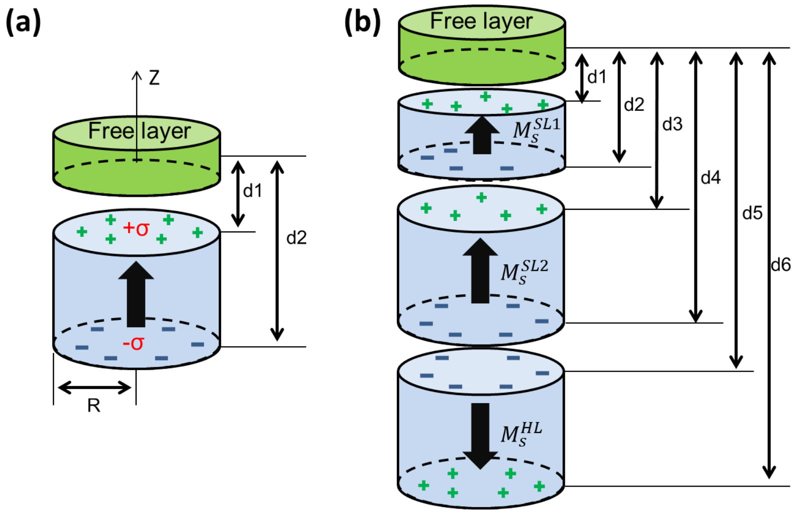

Figure 4.7: Illustration of the surface charge distribution on a MTJ with (a) single layer reference (blue) and (b) a SAF reference (blue). The thick black arrows represent the direction of the magnetization. M_s^{SL1}, M_s^{SL2} and M_s^{HL} are the saturation magnetizations of the first half of the soft layer (FeCoB), the other half of the soft layer ([Co/Pt]$_n$) and hard layer of the SAF, respectively. The pairs d_1-d_2, d_3-d_4 and d_5-d_6 are the distances from the center of the free layer to the top and bottom surfaces of the the first half of the soft layer (FeCoB), the other half of the soft layer ([Co/Pt]$_n$) and hard layer of the SAF, respectively. R represents the radius of the cylindrical structures.

$$\begin{aligned}\boldsymbol{H_d} = &\frac{M_s^{SL1}}{2}\left(\frac{d_2}{\sqrt{d_2^2+R^2}} - \frac{d_1}{\sqrt{d_1^2+R^2}}\right) + \frac{M_s^{SL2}}{2}\left(\frac{d_4}{\sqrt{d_4^2+R^2}} - \frac{d_3}{\sqrt{d_3^2+R^2}}\right)\\ &- \frac{M_s^{HL}}{2}\left(\frac{d_6}{\sqrt{d_6^2+R^2}} - \frac{d_5}{\sqrt{d_5^2+R^2}}\right),\end{aligned} \tag{4.12}$$

where M_s^{SL1}, M_s^{SL2} and M_s^{HL} are the saturation magnetizations of the first half of the soft layer (FeCoB), the other half of the soft layer ([Co/Pt]$_n$) and hard layer of the SAF, respectively. The pairs d_1-d_2, d_3-d_4 and d_5-d_6 are the distances from the center of the free layer to the top and bottom surfaces of the the first half of the soft layer (FeCoB), the other half of the soft layer ([Co/Pt]$_n$) and hard layer of the SAF, respectively. Notice that the soft and hard layer terms have opposite signs since the magnetizations are antiparallel to each other, therefore the two stray fields subtract.

Equation (4.12) accounts for the stray fields created by a bottom reference. In the case of a DBMTJ, one needs to take into account a second reference on top of the free layer, thus the total dipolar fields acting of the DBMTJ free layer may be expressed as $H_d^{DBMTJ} = H_d^{bottom} + H_d^{top}$, where H_d^{bottom} and H_d^{top} have the form of Eq.(4.12). The signs of the magnetizations are adjusted according to the operation mode. In read mode, the magnetizations of the bottom and top SAF soft layers are parallel, thus they must have the same sign while the the two hard layers must also have the same sign but opposite to the soft layers one. In write mode, the magnetizations of the bottom and top SAF soft layers are antiparallel, thus they must have opposite signs, as well as the magnetizations of the two hard layers.

4.3.2.B Top reference optimization for zero offset field in Read/Write modes

First, the offset fields H_d have been calculated for p-MTJs with composite free layer and with a single (bottom or top) reference. Figure 4.8 shows the stray fields as a function of the pillar diameter for both types of p-MTJs. The saturation magnetizations used for the bottom reference were: $M_s^{SL1} = 1100\,emu/cm^3$ (relative to the 1.2 nm FeCoB layer), $M_s^{SL2} = 1000\,emu/cm^3$ and $M_s^{HL} = 1000\,emu/cm^3$ (based on experimental measurements). The distances d_1 to d_6 can be easily calculated from the bottom pinned p-MTJ stack illustration placed between figs.4.8(a) and (b). Figs.4.8(a) and (b) present the stray field calculation for the two possible configurations of the bottom reference SAF. By analyzing the plots, we can distinguish two different critical diameters. One is 45 nm, for which the offset field is zero; below this diameter the offset field is negative (resp. positive) for M_s^{HL} oriented in the positive (resp. negative) direction of the z axis (positive for M_s^{HL} oriented in the negative direction), thus meaning that the stray field of the soft layer dominates for this device size range. The other critical diameter is 80 nm for which the stray field is maximum (90 Oe) for positively oriented M_s^{HL} [minimum (-90 Oe) for negatively oriented M_s^{HL}], then for larger diameters, the absolute value of the offset field decreases.

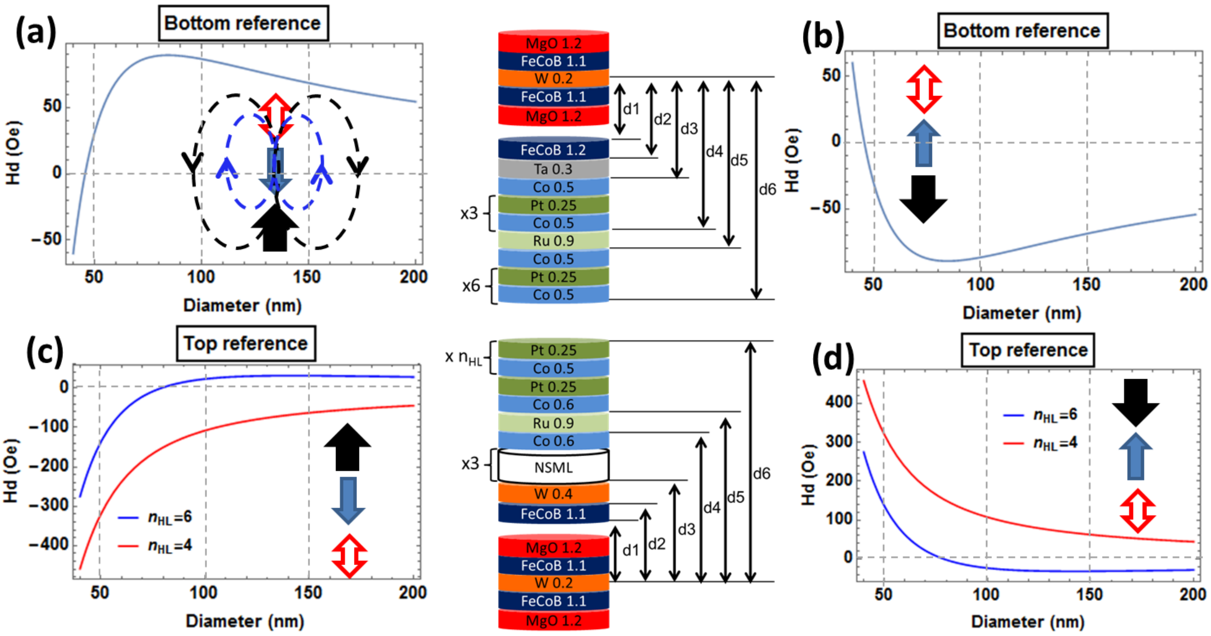

Figure 4.8: Stray field H_d as a function of the MTJ diameter for: p-MTJ with a bottom reference SAF whose HL magnetization is oriented in the (a) positive or (b) negative direction of the z axis and p-MTJ with a top reference SAF whose HL magnetization is oriented in the (c) positive or (d) negative direction of the z axis. The stack illustrations represent *(top)* the bottom and *(bottom)* the top reference p-MTJs. n_{HL} represents the multilayer repetitions of the hard layer. d_1 to d_6 represent the distances of each marked layer surface to the center of the free layer. The arrows represent the magnetizations of the free (red), SAF soft (blue) and SAF hard (black) layers.

For the case of the top pinned p-MTJ, the saturation magnetizations used for the top reference were: $M_s^{SL1} = 1100\,emu/cm^3$ (relative to the 1.1 nm FeCoB layer), $M_s^{SL2} = 400\,emu/cm^3$ and $M_s^{HL} = 800\,emu/cm^3$ (based on experimental measurements) [5]. The distances d_1 to d_6 can be easily calculated from the top pinned p-MTJ stack illustration placed between figs.4.8(c) and (d). Likewise the bottom pinned p-MTJ, figs.4.8(c) and (d) correspond to the two possible magnetic configuration of the top SAF. For this particular case, we have studied the stray field as a function of the MTJ diameter for 4 and 6

---

[5] The used M_s^{SL2} is higher than the $M_s^{SL2} \approx 300\,emu/cm^3$ obtained in section 4.3.1.A because the latter was measured only for the NSML while the one used here was determined from the top reference p-MTJ M(H) loop, where texture effects are more significant. In addition, in the stack used in this section, there is an additional 0.6 nm Co layer which also justifies for the higher M_s^{SL2} value obtained. Regarding the hard layer, the M_s obtained for the [Co/Pt] multilayers in a top pinned p-MTJ was found to be smaller than in a bottom pinned p-MTJ which possesses a thick Pt buffer layer which may justify the difference between the two M_s^{HL} values.

repetitions of the hard layer [Co/Pt] multilayers (n_{HL}). The general behavior is a fast increase (resp. decrease), for M_s^{HL} oriented positively (resp. negatively), of the stray field from very large negative (positive) values towards zero until 80 nm, thereon the increase (decrease) is rather smooth, approaching saturation for diameters above 150 nm. A smaller net stray field is obtained when using $n_{HL} = 6$ instead of $n_{HL} = 4$. This is due to the increase of the hard layer thickness, which generates a larger stray field than the hard layer with $n_{HL} = 4$. The increase of the hard layer stray field is large enough to completely cancel out the stray field coming from the soft layer for MTJ diameters around 75-80 nm.

Comparing the stray field values for both type of p-MTJs, we observe that the stray field stemming from the top reference is far stronger than the one coming from the bottom reference. For the bottom SAF, $M_s^{SL} = M_s^{HL}$ and the number of repetitions of [Co/Pt] has been previously optimized to reach compensation. It is not the case for the newly developed top SAF reference. Therefore, it seems more important to study the impact of the top reference stray field on the DBMTJ and consequently optimize it to reduce the offset field as much as possible.

To do so, we calculated the stray fields in a full DBMTJ, configured in read mode (soft layers magnetizations in parallel alignment) and write mode (soft layers magnetizations in antiparallel alignment). The full stack used is the superposition of the two p-MTJs stacks illustrated in Fig.4.8. The parameters used for the bottom reference were the same as used for the calculations of the bottom reference p-MTJ relative to the results of Fig.4.8(a) (see first paragraph of this section 4.3.2.B). For the top reference, we considered a SAF with a soft layer containing a NSML with 3 repetitions and a hard layer made of [Co/Pt] with n_{HL} repetitions. For this study, we assume that the M_s of the hard layer does not significantly vary with the number of repetitions. By contrast, for the soft layer, M_s^{SL2} (corresponding to the NSML) is considered as a free parameter since the growth of the NSML is expected to be different at the top of the stack and at the bottom. The two free parameters are therefore M_s^{SL2} and n_{HL}.

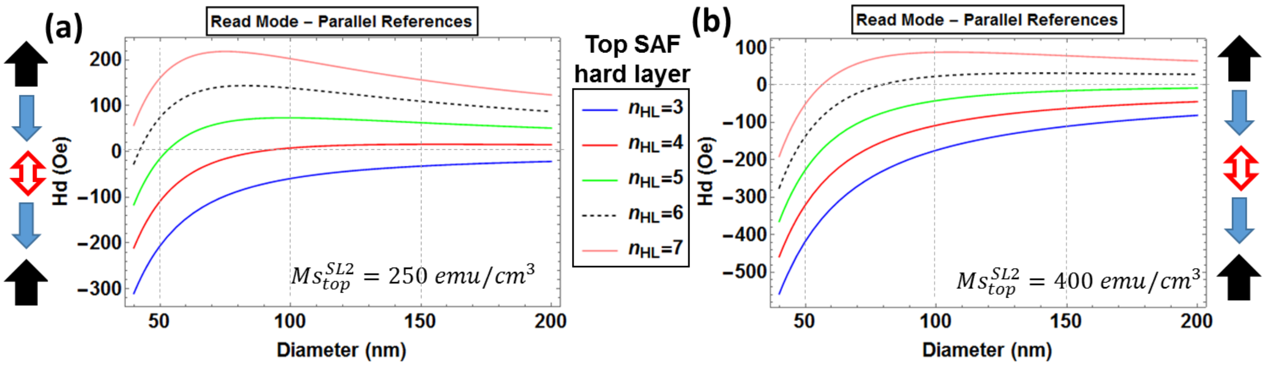

Figure 4.9: Stray field evolution with device diameter for a DBMTJ in read mode using two different values for the saturation magnetization of the NSML of the top SAF soft layer M_s^{SL2}: (a) 250 emu/cm^3 and (b) 400 emu/cm^3. The calculations have been performed for different number of repetitions of [Co/Pt] (n_{HL}) within the top SAF hard layer. The arrows represent the magnetizations of the free layer (red), soft layer (blue) and hard layer (black). The blue and black arrows above and below the red arrow correspond to the top and bottom references, respectively.

Figure 4.9 shows the evolution of the stray fields as a function of the device diameter for the DBMTJ set in read mode (parallel references). The stray field behavior is presented for n_{HL} varying from 3 to 7 and for two different values of M_s^{SL2}: (a) a rather low value of 250 emu/cm^3 and (b) another value of 400 emu/cm^3, closer to experimental measurements. Again comparison between the results of Fig.4.9(a) and (b) is done for two size ranges, below and above 70 nm for which the stray field is maximum. For $M_s^{SL2} = 250\,emu/cm^3$ and small size junctions, using $n_{HL} = 4 - 6$ appears to be a good solution to obtain low offset field (below 150 Oe). For larger sizes, the lowest offset field is obtained for 4 repetitions of [Co/Pt] in the hard layer. In Fig.4.9(b), when M_s^{SL2} is fixed at 400 emu/cm^3, all calculated stray fields decrease towards negative values when the junction diameter decreases. For junction diameter smaller than 70 nm, the smallest offset field is obtained for $n_{HL} = 7$ whereas for larger junctions, it is nearly zero for 6 multilayer repetitions.

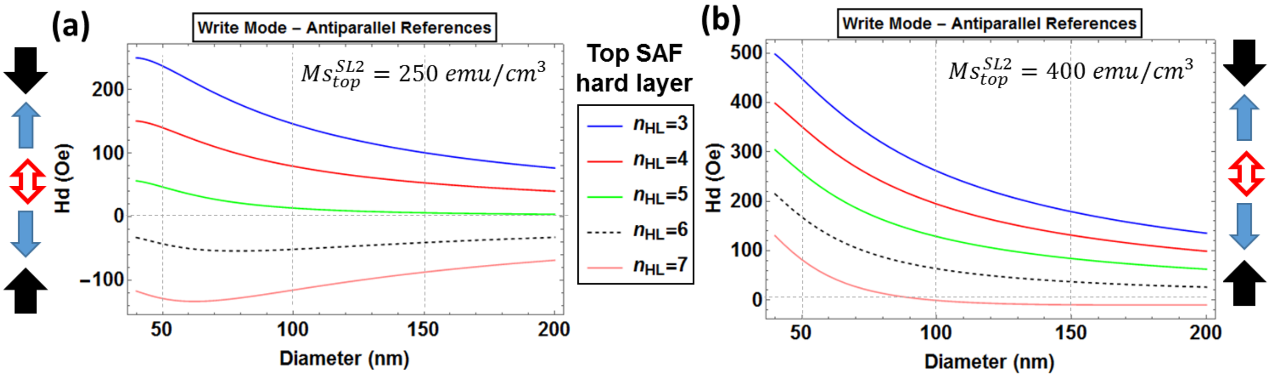

Figure 4.10: Stray field evolution with device diameter for a DBMTJ in write mode using two different values for the saturation magnetization of the NSML of the top SAF soft layer M_s^{SL2}: (a) 250 emu/cm^3 and (b) 400 emu/cm^3. The calculations have been performed for different number of repetitions of [Co/Pt] (n_{HL}) within the top SAF hard layer. The arrows represent the magnetizations of the free layer (red), soft layer (blue) and hard layer (black). The blue and black arrows above and below the red arrow correspond to the top and bottom references, respectively.

Figure 4.10 presents similar stray field calculations as Fig.4.9 but now for the DBMTJ set in write mode (antiparallel references). In Fig.4.10(a) where $M_s^{SL2} = 250\,emu/cm^3$, two types of behavior exist: for $n_{HL} \leq 5$ the stray field decreases with increasing diameter, while for $n_{HL} \geq 6$, H_d decreases for small junction diameter and reaches a minimum around 65 nm and then increases back. Here, two size ranges exist as well: for diameters smaller than 50 nm, 6 multilayer repetitions provides the lowest stray field in absolute values while 5 repetitions is the optimal choice for diameters superior to 50 nm. The scenario is simpler in Fig.4.10(b) with $M_s^{SL2} = 400\,emu/cm^3$: in all cases, the stray field decreases with increasing device size. Moreover, for the whole size range, H_d decreases with increasing n_{HL}. Therefore, the smallest offset field is obtained for $n_{HL} = 7$; $n_{HL} = 6$ is also close to the optimum, especially for very large diameters ($>$ 150 nm).

In order to choose the number of [Co/Pt] repetitions in the top SAF hard layer to obtain read and write mode operations centered around zero field, we compiled, in table 4.1, the read/write mode stray field values calculated for two characteristic device diameters, 50 nm and 100 nm. These values were extracted from the curves of figs.4.9(b) and 4.10(b) since they were calculated using an M_s^{SL2} value extracted from experimental measurements performed in top reference p-MTJs. Moreover, we also calculated two other quantities to have a combined picture of the more balanced read and write mode offset fields. One is $< |H_d| >$ which is the average of the absolute stray field values in read and write mode, defined as $< |H_d| >= (|H_d(read)| + |H_d(write)|)/2$. The other one is the simple average of the read and write mode stray fields. The closer to zero are these two quantities, the better is the corresponding n_{HL}. Therefore, for devices with 50 nm diameter, the optimum number of repettions is

n_{HL} is 7. This same choice is also recommended for devices with 100 nm diameter, along with $n_{HL} = 6$ that provides very low offset fields as well.

	$H_d(50nm)$ (Oe)				$H_d(100nm)$ (Oe)			
n_{HL}	**Read**	**Write**	$<\lvert H_d\rvert>$	Average	**Read**	**Write**	$<\lvert H_d\rvert>$	Average
3	-416	450	433	17	-172	258	215	43
4	-326	352	339	13	-107	192	149	43
5	-223	254	238	16	-35	125	82	43
6	-134	166	150	16	23	63	43	43
7	-49	75	62	13	85	-2	43	42

Table 4.1: Stray fields H_d values for 50 nm and 100 nm diameter DBMTJs in read and write mode for different [Co/Pt] repetitions in the top SAF hard layer (n_{HL}). $M_s^{SL2} = 400\, emu/cm^3$ has been used for this calculation.

4.3.3 Magnetic characterization of perpendicular DBMTJs

4.3.3.A Newly Developed DBMTJ vs. Co/Pd-based multilayers top SAF DBMTJ

After having optimized the top reference, we assembled the three different building blocks, the storage layer between the two references, to create a double barrier magnetic tunnel junction with perpendicular anisotropy. For easy visualization, we separate the DBMTJ stack into three main parts: bottom reference SAF (hard layer/Ru spacer/soft layer), storage layer and top reference SAF (soft layer/Ru spacer/hard layer). The composition of our first deposited p-DBMTJ stack is the following (thicknesses in nm):

- Bottom reference SAF: Ta 3/Pt 5/[Co 0.5/Pt 0.25]$_6$/Co 0.5/Ru 0.9/[Co 0.5/Pt 0.25]$_3$/Co 0.5/Ta 0.3/FeCoB 1.2
- Bottom barrier: MgO 1.2 (30s low pressure oxidation)
- Storage layer: FeCoB 1.0/W 0.2/FeCoB 1.0
- Top barrier: MgO 0.8 (10 s low pressure oxidation)
- Top reference SAF: FeCoB 1.1/W 0.4/NSML/Co 0.6/Ru 0.9/Co 0.6/Pt 0.25/[Co 0.6/Pt 0.25]$_6$/Ru 5

Figure 4.11 shows the magnetic loop obtained for this DBMTJ annealed for 10 min. at 400°C. The magnetization direction of the different magnetic parts of the DBMTJ are illustrated by the arrows above (or below) each stable magnetic state as shown in the sketch of the stack.

Starting from positive magnetic field, the first transition corresponds to the reversal of both SAF soft layers (of bottom and top references). This switch is due to the reestablishment of the antiferromagnetic RKKY coupling between the soft and hard layers. The transition around zero field corresponds to the free layer reversal. At -1270 Oe, the top SAF hard layer switches. However, the variation of magnetic moment is too small to correspond to a hard layer reversal. In fact, when the magnetization of the top hard layer switches towards the negative direction, the top soft layer magnetization simultaneously switches up in order to preserve the RKKY coupling of the SAF (we have called this phenomenon *crossover* in section 4.3.1.B). Finally, at -2150 Oe the bottom SAF hard layer and top SAF soft layer switch towards full DBMTJ saturation in the negative direction.

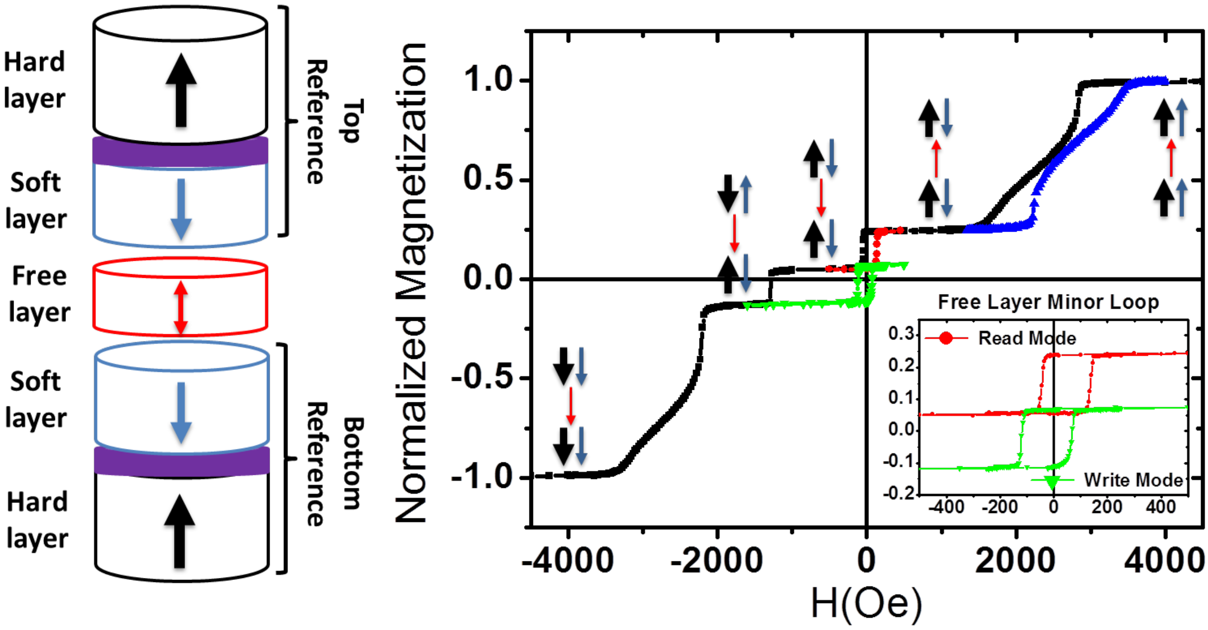

Figure 4.11: Magnetic cycle measured by VSM with perpendicular field for the newly developed perpendicular DBMTJ. The inset shows the minor loops performed on the free layer with either parallel (red) or antiparallel (green) configuration of the references, corresponding, respectively, to read and write modes. The stack represented on the left side of the plot serves as legend for the arrows, describing the magnetization direction of the different magnetic parts of the DBMTJ.

Similarly to in-plane anisotropy DBMTJ, the perpendicular DBMTJ has also two modes of operation: read and write. As shown in the inset of Fig.4.11, minor loops can be performed on the storage layer with either parallel (red) or antiparallel (green) alignment of the reference layers. The two configurations can be achieved by applying the proper field sweep. Coming from positive field saturation and decreasing the applied field until ≈-1000 Oe allows both the reference layers (top and bottom SAF soft layers) to be aligned parallel, *i.e.* in read mode. The free layer hysteresis loop is obtained by increasing the field again towards positive values. If the field is further increased, the hysteresis loop of the soft layers can also be performed (blue triangles in Fig.4.11). To set the two references antiparallel to each other (*i.e.* write mode), it is necessary to decrease the field down to ≈-1500 Oe. The minor loop of the free layer, in write mode, can then be measured by increasing the field towards positive values.

It is possible to extract the coupling fields (H_{cp}) acting on the storage layer from both interfaces, from the minor loops in inset of Fig.4.11. When the DBMTJ is in read mode, the coupling fields add up while they subtract in write mode. So in read mode, $H_{off}^{read} = H_{cp,bottom} + H_{cp,top} = 47Oe$ and $H_{off}^{write} = H_{cp,bottom} - H_{cp,top} = -27Oe$, in write mode. After solving the two equations, $H_{cp,bottom} = 10Oe$ and $H_{cp,top} = 37Oe$. Both couplings are ferromagnetic which means that that some Néel "orange peel" coupling exists at both MgO interfaces. The ferromagnetic coupling is considerably larger for the top barrier and can be attibuted to metallic pinholes since the top barrier is the thinnest.

Let us now compare this perpendicular DMTJ with new top reference to previous samples. L. Cuchet *et al.* [81] were the first to grow perpendicularly magnetized DBMTJ. They have developed a double barrier MTJ using (Co/Pt) multilayer based bottom reference and (Co/Pd) multilayer top reference. Their DBMTJ stack composition is the following:

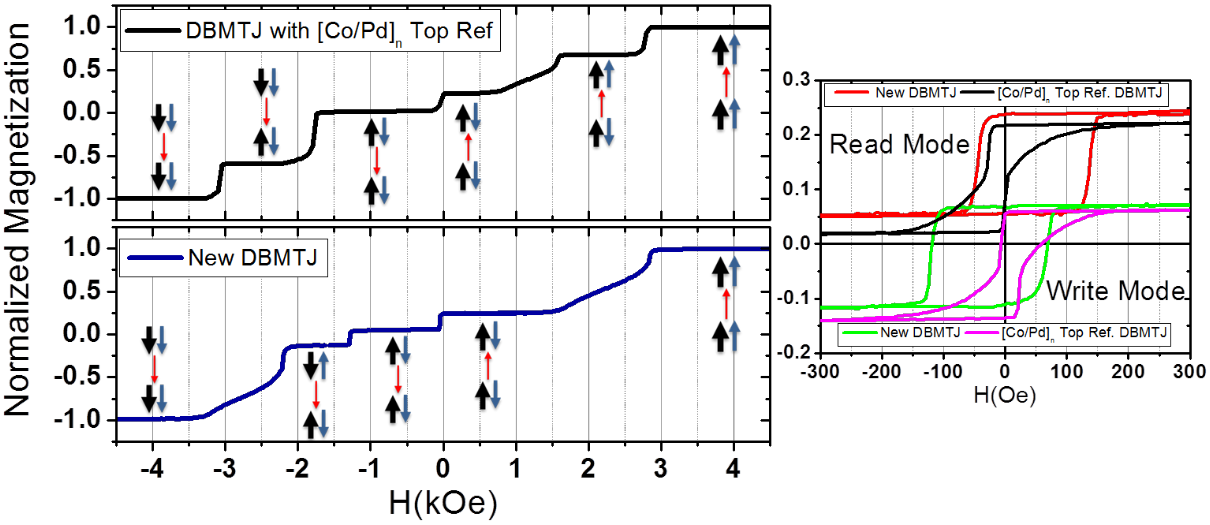

Figure 4.12: *(Left)* Normalized magnetization as a function of perpendicular applied field for the first realized DBMTJ with (Co/Pd) multilayers on the top reference (black line, data is courtesy from L. Cuchet *et al.* [81]) compared with our new DBMTJ (blue line). *(Right)* Minor loops of the free layer in read/write modes for the DBMTJ with (Co/Pd) multilayers on the top reference (black/magenta lines) and for the new DBMTJ (red/green lines). The arrows represent the magnetizations of the main magnetic blocks of the DBMTJ,with the same legend as in Fig.4.11.

- Bottom reference SAF: Ta 3/Pt 5/[Co 0.5/Pt 0.25]$_6$/Co 0.5/Ru 0.9/[Co 0.5/Pt 0.25]$_3$/Co 0.5/ Ta 0.3/FeCoB 1.2
- Bottom barrier: MgO 1.4 (10s high pressure oxidation)
- Storage layer: FeCoB 1.1/Ta 0.3/FeCoB 1.1
- Top barrier: MgO 1.1 (30 s low pressure oxidation)
- Top reference SAF: FeCoB 1.2/Ta 0.3/[Co 0.4/Pd 1.2]$_4$/Co 0.4/Ru 0.9/[Co 0.4/Pd 1.2]$_8$/Co 0.4/ Pd 2

Figure 4.12 compares the M(H) loops of (Co/Pd)-based top reference DBMTJ with the one developed by us (new DBMTJ). One of the main differences between the two DBMTJs is the number of stable magnetic states. Our DBMTJ has 5 stable states whereas the one develop by L. Cuchet *et al.* has 6 stable states. Coming from positive fields, a transition happens around 2800 Oe where only the bottom SAF soft layer switches for the (Co/Pd)-based top reference DBMTJ, while in our DBMTJ both top and bottom soft layer switch together. The existence of this plateau between 2650 and 1600 Oe means that the RKKY coupling energy of the top (Co/Pd) SAF is lower than the RKKY coupling of our new DBMTJ top SAF. Another proof of this statement is the transition that happens at -1750 Oe where the top SAF hard layer magnetization switches towards the negative direction. Unlike our new DBMTJ, there is no crossover, since the RKKY coupling is too weak to restore the antiferromagnetic coupling. Indeed, this weaker RKKY coupling may be due to the use of Co 0.4 nm at the interface with Ru in the top SAF, compared to Co 0.6 nm used in our new DBMTJ.

On the right side of Fig.4.12, the minor loops of the storage layers, in both read and write modes, can be compared for both types of DBMTJs. For (Co/Pd)-based top reference DBMTJ, read mode can be obtained by the same field sweep as for our new DBMTJ. By contrast, to set the DMTJ in write mode requires to decrease the field down to -2500 Oe and then increase it back to positive values. The immediate difference between both storage layers is their coercivity: in our DBMTJ, H_c = 90 Oe while for the DBMTJ of Ref. [81], H_c = 19 Oe. This fact and the improved squareness of the minor loops of the new DBMTJ indicated a higher PMA for FeCoB 1.0/W 0.2/FeCoB 1.0 (nm) storage layer than FeCoB 1.1/Ta 0.3/FeCoB 1.1 (nm). Besides the obvious fact that PMA of FeCoB increases as thickness is reduced, the use of W as an insertion layer may also reinforce it. On the other hand, the coupling fields of the (Co/Pd)-based top reference DBMTJ storage layer are negative and low [155] which means that a weak antiferromagnetic coupling exist across the MgO barriers. Nonetheless, it reveals a better quality of the MgO barrier than in our DBMTJ.

4.3.3.B PMA improvement of p-DBMTJ and influence of the MgO barriers on the storage layer

Although read and write mode can be well set in our p-DBMTJ, the rotation of top and bottom SAF layers magnetizations at similar fields reduces the number of stable magnetic states, compared to the (Co/Pd)-based top reference DBMTJ. Besides the strong RKKY couplings, possibly the similarity of bottom and top K_{eff} is contributing to these almost simultaneous switchings. Hence, a larger difference between top and bottom reference K_{eff} must be found. Since improving K_{eff} of the top SAF is extremely challenging, the easier strategy is to increase the PMA of the bottom SAF via a thicker Pt buffer layer. Therefore, the Pt buffer layer thickness has been increased by a factor 5-6 compared with the first sample (Pt 5 nm). In addition, we also compare the storage layer minor loops for three types of double barrier configuration: symmetric barriers, asymmetric top thick barrier and asymmetric bottom thick barrier. The stacks are the following (thickness in nm):

- Bottom reference SAF: Ta 3/Pt **X**/[Co 0.5/Pt 0.25]$_6$/Co 0.5/Ru 0.9/[Co 0.5/Pt 0.25]$_3$/Co 0.5/Ta 0.3/FeCoB 1.2
- Bottom barrier: MgO **Y**
- Storage layer: FeCoB 1.1/W 0.2/FeCoB 1.1
- Top barrier: MgO **Z**
- Top reference SAF: FeCoB 1.1/W 0.35/NSML/Co 0.6/Ru 0.9/Co 0.6/Pt 0.25/[Co 0.5/Pt 0.25]$_6$/Ru 5

For symmetric barriers: **X** = 30, **Y** = **Z** = 1.2 (30s low pressure oxidation) ; for asymmetric top thick barrier: **X** = 25, **Y** = 1.2 (30s low pressure oxidation) and **Z** = 1.4 (10s high pressure oxidation); for asymmetric bottom thick barrier: **X** = 25, **Y** = 1.4 (10s high pressure oxidation) and **Z** = 1.2 (30s low pressure oxidation). All the p-DBMTJs were annealed at 350°C in order to improve the PMA of the top reference (see section 4.3.1.A).

Figure 4.13(a) compares the magnetization as a function of perpendicular applied field of symmetric barriers and asymmetric bottom thick barriers [6] p-DBMTJs. We observe several differences between

---

[6] Asymmetric bottom and top thick barrier DBMTJs have very similar M(H) cycles with only differences on the free layer read/write minor loop. The choice of the asymmetric bottom thick barrier p-DBMTJ was just representative of an asymmetric barriers p-DBMTJ.

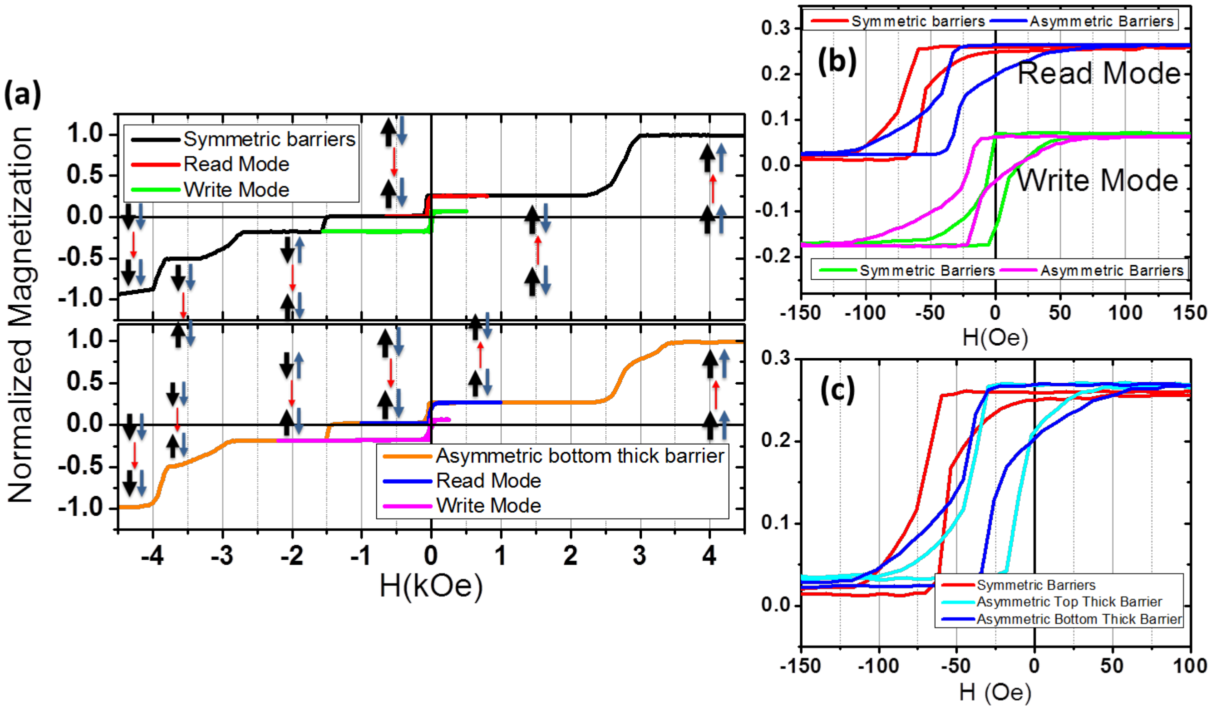

Figure 4.13: (a) VSM magnetic cycles of the p-DBMTJ with symmetric barriers (black line) and asymmetric bottom thick barrier (orange line). The arrows represent the magnetizations of the main magnetic blocks of the DBMTJ (legend in Fig.4.11). (b) Minor loops of the free layer in read/write modes for the DBMTJ with symmetric barriers (red/green lines) and with asymmetric bottom thick barrier (blue/magenta lines).(c) Read mode minor loops comparing symmetric (red), asymmetric with top (cyan) and bottom (blue) thick barrier.

these samples and the previously studied DMTJ with thinner Pt buffer layer. The first difference is the field at which reversal occurs for both soft layers: 3500 Oe for the asymmetric barriers p-DBMTJ and 3000 Oe for the symmetric barriers one. The second is related with the appearance of a new stable state after the top SAF crossover: this new state is created by the rotation of the top SAF soft layer magnetization towards the negative field direction. This rotation occurs at H = -2650 Oe and H = -2850 Oe for symmetric and asymmetric barriers p-DBMTJ, respectively. Consequently, the new state has a stable plateau of 500 Oe for symmetric barriers and of 200 Oe for asymmetric barriers. These differences between the new samples and the initial one result from the use of a thicker Pt buffer layer. The thickest layer (30 nm) has been used for the symmetric barriers structure. However, a Pt buffer of 25 nm seems a better choice since it delays the rotation of the top SAF after the crossover, which increases the field range for stable write mode state by 700 Oe compared to the initial DBMTJ of Fig.4.11.

In Fig.4.13(b), the free layer minor loops, for read and write modes, are shown. In terms of coercivity, both types of DBMTJs present similar values for read and write modes. The symmetric barriers p-DBMTJ displays $H_c^{read} = H_c^{write} = 8.5\,Oe$ and the asymmetric bottom thicker p-DBMTJ exhibits $H_c^{read} = H_c^{write} = 9\,Oe$. The most interesting differences come from the offset fields. The one with symmetric barriers presents an $H_{off}^{read} = -63.5\,Oe$ while the $H_{off}^{write} = -0.5\,Oe$. For the bottom thick barrier p-DBMTJ, $H_{off}^{read} = -32\,Oe$ and $H_{off}^{write} = -17.5\,Oe$. By separating the effect of each interface as in section 4.3.3.A, we find that $H_{cp,bottom} = -32\,Oe$ and $H_{cp,top} = -31.5\,Oe$ for the case of symmetric barriers whereas $H_{cp,bottom} = -25\,Oe$ and $H_{cp,top} = -7.25\,Oe$ for the case of thick bottom barrier.

For the first case, $H_{cp,bottom} \approx H_{cp,top}$ which means that the barriers are almost indentical and that the growth conditions did not differ that much from bottom to top. For the asymmetric barriers, the antiferromagnetic coupling is larger at the bottom barrier than at the top barrier. Despite the fact that the top barrier is nominally the same for both types of p-DBMTJ, the antiferromagnetic coupling is much weaker when the bottom barrier is thicker and oxidized under higher pressure. It thus possible that the thicker bottom barrier may have an improved texture that allows a better growth of the storage layer and hence provide a smoother top barrier interface.

Finally, Fig.4.13(c) presents the read mode free layer minor loops of the three types of p-DBMTJs: symmetric barriers (red), asymmetric top thick (cyan) and asymmetric bottom thick (blue) barriers. Regarding coercivity, the p-DBMTJ with thicker barrier on top is the one which presents the highest coercivity, $H_c = 16.5\,Oe$, almost 2 times larger than the coercive fields of the other two p-DBMTJ ($H_c \approx 9\,Oe$). In perpendicular DBMTJ, higher easy axis coercivity is also synonym of high PMA. Therefore, we can conclude that in asymmetric p-DBMTJ, it is recommended to have the thicker barrier on top of the storage layer in order to improve its perpendicular anisotropy. The use of a thicker MgO barrier probably increases the interfacial anisotropy arising at the FeCoB/MgO interface. Nevertheless, the coercive field is smaller than the one observed in the initial sample and the minor loop cycles are much less steep. In these samples, the storage layer is composed of two layers of CoFeB 1.1 nm instead of 1.0 nm in the initial sample. Since TMR is expected to improve when the layer thickness is increased, the choice of the optimum thickness is a delicate tradeoff between TMR and PMA.

4.3.3.C Alternative p-DBMTJ with thin bottom SAF reference

Recently, J. Chatterjee *et al.* [166] has developed a new type of RKKY coupling layer in order to improve the PMA of the FeCoB polarizing layer in the bottom reference and simultaneously couple it antiferromagnetically with the hard layer. Therefore, the soft layer of the bottom SAF is just composed of a single FeCoB layer instead of [Co/Pt]$_n$/Co/Ta/FeCoB. This new bottom SAF composed of [Co/Pt]$_n$/Co/Ru/W/FeCoB is called ”thin SAF”, since it is substantially thinner than a conventional perpendicular bottom SAF. Considering the successful implementation of the thin SAF in bottom reference p-MTJ, we tried replacing the conventional bottom SAF of our p-DBMTJs by the thin SAF. Figure 4.14 presents the normalized magnetization cycle of the first realization of a perpendicular double barrier MTJ with a thin SAF as a bottom reference. The composition of this alternative p-DBMTJ is the following:

- Bottom reference SAF: Ta 3/Pt 5/[Co 0.5/Pt 0.25]$_3$/Co 0.5/Ru 0.4/W 0.2/FeCoB 1.2
- Bottom barrier: MgO 1.2 (30s low pressure oxidation)
- Storage layer: FeCoB 1.0/W 0.2/FeCoB 1.0
- Top barrier: MgO 0.8 (10 s low pressure oxidation)
- Top reference SAF: FeCoB 1.1/W 0.4/NSML/Co 0.6/Ru 0.9/Co 0.6/Pt 0.25/ [Co 0.5/Pt 0.25]$_6$/Ru 5

In order easily visualize the difference between this alternative p-DBMTJ and the normal one, the M(H) loop of the latter (Fig.4.11) was added to Fig.4.14 as a blue dashed line.

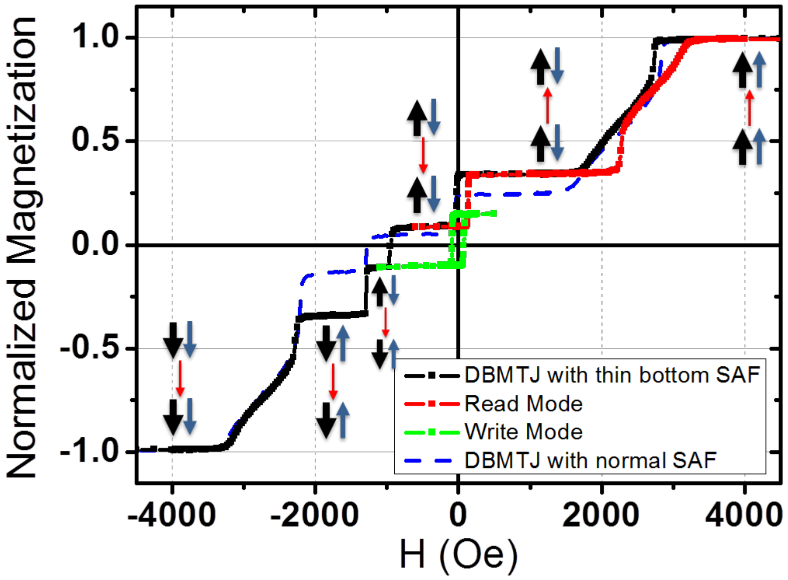

Figure 4.14: Magnetic cycle of the perpendicular DBMTJ with thin bottom SAF (in black). The write (green) and read (red) mode free layer minor loops were also measured, with an extension in positive field of the latter allowing also to measure the minor loop corresponding to the two SAF soft layers rotation. The M(H) cycle of the new p-DBMTJ with a conventional bottom SAF reference, already presented in Fig.4.11 (blue dashed line) is included for comparison. The arrows represent the magnetizations of the main magnetic blocks of the DBMTJ (legend in Fig.4.11.

While the read mode minor loop can be measured in the exact same way as described in section 4.3.3.A for the conventional p-DBMTJ, the same does not happen for write mode. The write mode configuration is also obtained by applying a negative magnetic field sweep to the p-DBMTJ, but instead of stopping at -1500 Oe as previously mentioned, the applied field must not overcome -1250 Oe. The write mode plateau of 700 Oe once measured for the normal DBMTJ is now reduced to 250 Oe. Indeed, for this thinner p-DBMTJ, the hard layer/soft layer crossover does happen not only for the top reference but also for the bottom one, the latter corresponding to the transition at $\approx$ -900 Oe. After this first crossover, the two reference layers magnetizations are in antiparallel alignment. Then, around -1270 Oe, happens the crossover of the top SAF hard and soft layers, similarly to what has been observed for the conventional p-DBMTJ (blue dashed line).

In conclusion, we demonstrated write and read mode configurations in the thin bottom SAF p-DBMTJ. Despite the less stable write mode configuration, this alternative p-DBMTJ presents a substantial advantage to the conventional DBMTJ, a reduced total thickness. Since the physical etching process of such a thick stack is a challenging task, this thinner p-DBMTJ may pave a way towards an easier integration of the p-DBMTJ as an STT-MRAM by reducing its nanofabrication complexity.

4.4 Summary

This chapter describes all the steps followed in the development of a new DBMTJ, from the integration of the NSML as top reference to the full realization of the double barrier magnetic tunnel junction.

First, we have shown that use of W as texture breaking layer improves the magnetic properties, mainly PMA, of the NSML even for annealing at 400°C. Towards the development of a functional top reference, we have demonstrated that a top SAF structure where the soft layer is constituted by FeCoB/W/NSML and the hard layer composed of [Co/Pt]$_n$ has better performances than a top SAF where both layers contain NSML. For the top reference p-MTJ, composition and thickness of the texture breaking layer and storage layer have been tested in order to enhance the perpendicular anisotropy. The best option is an insertion layer of W 0.35 nm and a composite storage layer of the form FeCoB/W/FeCoB, where W has 0.2 nm and the FeCoB thickness should lie between 1.0 and 1.2 nm.

Analytical calculations of the stray field have been performed to dimension the p-DBMTJ stack, aiming at read and write mode operations centered around zero field. Since the top SAF is the thicker part of the p-DBMTJ, our study mainly addresses the effect of the number of multilayer repetitions in this reference, for junctions of different diameters. Based of the experimental value of the top SAF soft layer saturation magnetization (400 emu/cm^3), the optimal number of [Co/Pt] repetitions in the top SAF hard layer is 7. For these parameters and for devices diameters between 50 and 100 nm, the read and write mode offset fields, are expected to be inferior than 100 Oe.

We have also demonstrated the realization of a new p-DBMTJ using a top SAF reference including the NSML in the soft layer and [Co/Pt]$_n$ as hard layer. Setting these junctions into read and write mode magnetic configurations has also been shown. This new p-DBMTJ has been compared to the first perpendicular DBMTJ reported by L. Cuchet *et al.* [81] where (Co/Pd) multilayers is used for the top reference. Our p-DBMTJ displays a storage layer with higher perpendicular anisotropy and write mode operation can be set by sweeping field down to -1500 Oe instead of -2500 Oe.

With the objective of increasing the field window where the write mode state is stable, we have decided to increase the thickness of the bottom reference Pt buffer layer to improve this reference perpendicular anisotropy. By increasing the Pt buffer thickness from 5 nm up to 25 nm, the plateau where the references are in antiparallel configuration rises from 800 Oe up to 1300 Oe. The impact of the symmetry or asymmetry of the MgO barriers on the PMA of the storage layer has also been studied. The highest coercivity has been observed for the case where the top barrier is thicker than the bottom barrier which is explained by an improvement of the FeCoB/MgO interfacial anisotropy. The analysis of the coupling fields around each barrier also showed that the growth of the second barrier is affected by the thickness of the first one. In fact the top barrier coupling fields have shown to be smaller when the bottom barrier is rather thick.

Finally, we have demonstrated the first realization of perpendicular DBMTJ using a bottom thin SAF of the form [Co/Pt]$_n$/Co/Ru/W/FeCoB, where Ru/W is a new type of RKKY coupling layer developed by J. Chatterjee *et al.* [166], instead of the conventional bottom SAF of the form [Co/Pt]$_n$/Ru/[Co/Pt]$_n$/Ta/FeCoB. Although the write mode magnetic field window is smaller than with the conventional bottom SAF, read and write mode minor loop could be performed, demonstrating that the two mode operations are still possible. Moreover, the overall thickness of the stack is smaller than for conventional p-DBMTJ and consequently less challenging for device nanofabrication.

5

Spin Transfer Torque in Perpendicular DBMTJ

Contents

5.1 Setting read and write modes in p-DBMTJ nanometric devices

After the realization of the perpendicular DBMTJ stacks and demonstration of the two possible magnetic configurations - parallel and antiparallel references - we proceeded to the patterning of the full sheet stacks into nanometric size pillars with nominal diameters ranging from 300 nm down to 20 nm (detailed nanofabrication process chapter 2).

As seen in section 4.3.2.B, with the reduction of the lateral size of the devices comes an increase of the stray fields acting on the storage layer. The target magnetic fields to set the read and write modes in a patterned p-DBMTJ device should not be the same for a thin film. In order to isolate these two modes in nanometric sized p-DBMTJ devices, measurements of resistance (R) as a function of applied magnetic field (H) were performed in a Physical Properties Measurement System (PPMS) where magnetic fields up to ±17 kOe could be reached. The R(H) sweeps were performed for two types of DBMTJs with different top references. Figure 5.1 shows the measurements made for p-DBMTJ provided by L. Cuchet *et al.* [81] with (Co/Pd) multilayers based top reference, whose full stack composition is (thickness in nm):

- Bottom reference SAF: Ta 3/Pt 5/[Co 0.5/Pt 0.25]$_6$/Co 0.5/Ru 0.9/[Co 0.5/Pt 0.25]$_3$/Co 0.5/Ta 0.3/FeCoB 1.2
- Bottom barrier: MgO 1.2 (30 s low pressure oxidation)
- Storage layer: FeCoB 1.2/Ta 0.3/FeCoB 1.2
- Top barrier: MgO 1.2 (30 s low pressure oxidation)
- Top reference SAF: FeCoB 1.2/Ta 0.3/[Co 0.4/Pd 1.2]$_4$/Co 0.4/Ru 0.9/[Co 0.4/Pd 1.2]$_8$/Co 0.4/Pd 2

Whereas Fig. 5.2 presents the measurements performed in our newly developed p-DBMTJ with a top reference based on NSML whose full stack is the following (thickness in nm):

- Bottom reference SAF: Ta 3/Ru 15/W 3/Ta 1/Pt 5/[Co 0.5/Pt 0.25]$_6$/Co 0.5/Ru 0.9/[Co 0.5/Pt 0.25]$_3$/Co 0.5/Ta 0.3/FeCoB 1.2
- Bottom barrier: MgO 1.2 (30s low pressure oxidation)
- Storage layer: FeCoB 1.05/W 0.2/FeCoB 1.05
- Top barrier: MgO 1.2 (30s low pressure oxidation)
- Top reference SAF: FeCoB 1.1/W 0.4/NSML/Co 0.6/Ru 0.9/Co 0.6/Pt 0.25/[Co 0.6/Pt 0.25]$_6$/Ru 8

First of all, the sample used in Fig.5.1 was saturated under a very large negative field (-12 kOe) in order to set all the magnetizations aligned in the same direction. The first field sweep was performed from -4 kOe to +4 kOe [Fig.5.1(a)]. The first rotation happens around -1.5 kOe where the top SAF recovers its antiferromagnetic coupling with the soft layer magnetization reversing towards the positive

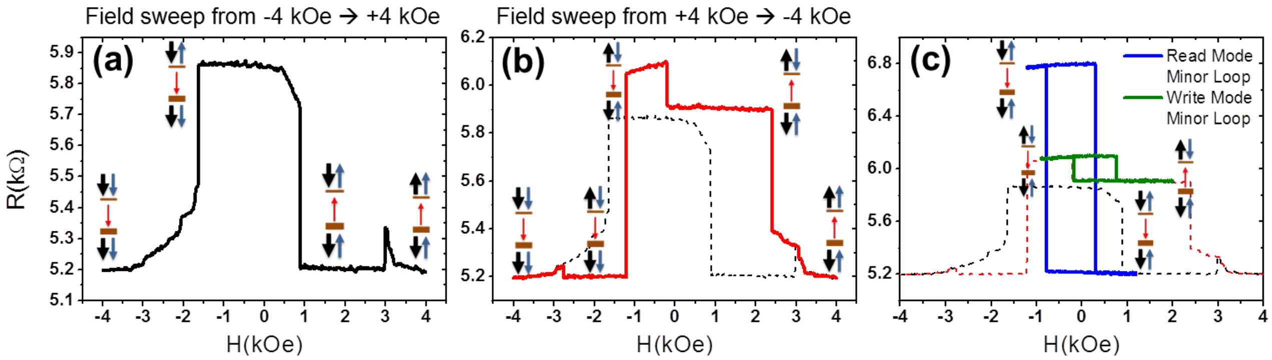

Figure 5.1: Resistance as function of applied field measurements performed in the p-DBMTJ of Ref. [81] with $(Co/Pd)_n$ based top reference. The p-DBMTJ device is initially saturated with an applied magnetic field of -12 kOe. (a) Field sweep from -4 kOe to +4 kOe. (b) Field sweep from +4 kOe to -4 kOe. (c) The free layer minor loops performed with the p-DBMTJ set in read mode (blue line) and write mode (green line). The p-DBMTJ has two symmetric barriers ($RA_{bottom} = RA_{top} = 10\,\Omega.\mu m^2$). The device has an electric diameter of 70 nm. The magnetoresistance values in each operation mode are $TMR^{read} = 30.20\,\%$ and $TMR^{write} = 3.15\,\%$. The arrows represent the magnetization of the main magnetic blocks of the DBMTJ, its legend may be seen in the schematic of Fig.4.11.

field direction. Then a double rotation of the bottom SAF soft layer and free layer magnetizations start at ≈400 Oe, being complete at ≈890 Oe. From the latter until ≈3 kOe, the p-DBMTJ is set in read mode (top and bottom references magnetizations in parallel alignment). At 3 kOe, there is a sudden oscillation in resistance ($\Delta R \approx 130\,\Omega$) equivalent to an MR = 2.5 $\%$. This small "jump" in resistance is due to the reversal of the top SAF hard layer which may induce a giant magnetoresistance effect. Then, the field was swept in the opposite direction (back to -4 kOe) as shown in Fig.5.1(b). Coming from +4 kOe, the first magnetization reversal occurs for the top SAF soft layer (at H ≈ 2.41 kOe) corresponding to the reestablishment of the RKKY coupling of the top SAF. From this point, the p-DBMTJ is set in write mode since both references magnetizations are in antiparallel alignment. At -200 Oe happens the rotation of the storage layer which corresponds only to a $\Delta R = 190\,\Omega$ and consequently a TMR = 3.15$\%$ since the two barriers are almost symmetric [1]. Write mode ceases to exist from -1.2 kOe which corresponds to the magnetic field that induces the rotation of the bottom SAF soft layer and resistance falls to its minimum. After this, around -2.7 kOe the little "jump" in resistance happens once again due to the reversal of the top SAF hard layer towards negative fields, with the p-DBMTJ back to full negative saturation. Figure 5.1(c) presents the read and write mode minor loops. The read mode is prepared by performing the field sweep (black line) of Fig.5.1(a) but stopping at H = +2 kOe and the free layer minor loop is done by sweeping the field between ±1.2 kOe. The measured TMR is 30.2% in read mode. The write mode is also prepared by performing the field sweep of Fig.5.1(a) all the way up to +4 kOe and then going back towards negative fields following the red line of Fig.5.1(b) but stopping at H = +2kOe. This procedure ensures the antiparallel alignment of the two references magnetizations. The write mode free layer minor loop can be made by sweeping field between -1 kOe and +2 kOe.

We have repeated the same type of measurements for our newly developed p-DBMTJ and the results are presented in Fig.5.2. Once more, the initial full saturation of the p-DBMTJ was done under a strongly negative applied magnetic field (-17 kOe). In Fig.5.2(a), coming from -4 kOe and contrary to

---

[1] If the two barriers were exactly equal, TMR = 0 for antiparallel references. For this particular device RA and/or TMR are slightly higher for the bottom barrier

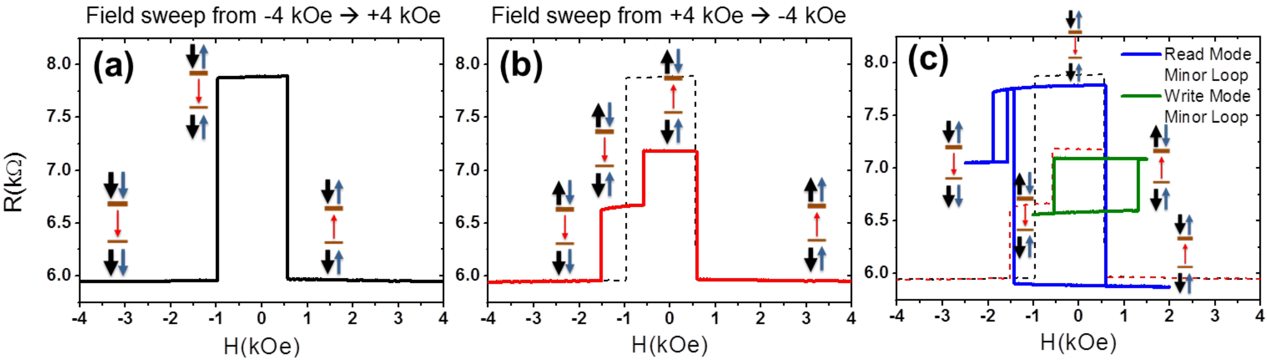

Figure 5.2: Resistance as function of applied field measurements performed in the newly developed p-DBMTJ with NSML based top reference. The p-DBMTJ device is initially saturated with an applied magnetic field of -17 kOe. (a) Field sweep from -4 kOe to +4 kOe. (b) Field sweep from +4 kOe to -4 kOe. (c) The free layer minor loops performed with the p-DBMTJ set in read mode (blue line) and write mode (green line). The p-DBMTJ has two symmetric barriers ($RA_{bottom} = RA_{top} = 8.5\,\Omega.\mu m^2$). The device has an electric diameter of 53 nm. The magnetoresistance values in each operation mode are $TMR^{read} = 32\,\%$ and $TMR^{write} = 8\,\%$. The arrows represent the magnetizations of the main magnetic blocks of the DBMTJ, its legend may be seen in the schematic of Fig.4.11.

what was observed in Fig.5.1(a), both top and bottom SAF soft layers rotate at similar field (H ≈ -970 Oe), recovering the antiferromagnetic coupling of both SAFs. The double junction is then at maximum resistance with the storage layer antiparallel to both references. It returns back to a parallel alignment for H = 570 Oe. After reaching +4 kOe, by performing the sweep in the opposite direction, a different path in resistance is also found as presented in Fig.5.2(b). In fact, when the field is increased past +3 kOe, similarly to the p-DBMTJ in Fig.5.1, the top SAF hard layer magnetization reverses. However, unlike the previous p-DBMTJ, there is no apparent change in resistance due to this reversal. Going back towards negative fields, close to H = 600 Oe, the p-DBMTJ reaches an intermediate state of resistance corresponding to the reestablishment of the RKKY coupling between the two magnetic parts of the top SAF. Therefore the device is set in write mode. The free layer rotates around -560 Oe. And the p-DBMTJ is back to minimum resistance when H = -1500 Oe due to the reversal of the bottom SAF soft layer. Finally, in Fig.5.2(c), we have isolated the two possible free layer minor loops. The read mode can be obtained in exactly the same way as for (Co/Pd) multilayers p-DBMTJ: initial saturation at very large negative fields and field towards positive values stopping around +2 kOe. The minor loop results from a sweep between ±1.5 kOe. Notice that in Fig.5.2(c), the field was swept past -2 kOe which led to the reversal of the bottom SAF soft layer at a larger negative value of switching field (-1860 Oe) than when the p-DBMTJ was set in write mode [red line in Fig.5.2(b)] due to the different stray fields involved. The write mode is also prepared in a similar way as the other p-DBMTJ where the double junction needs to be swept from large negative fields up to +4 kOe and then reduce the field down to -1 kOe [follow red line in Fig.5.2(b)]. The free layer minor loop was obtained by sweeping the field between -1 kOe and +1.5 kOe. In addition and despite both studied p-DBMTJs having nominal symmetric barriers, the write mode minor loops of figures 5.1(c) and 5.2(c) are different. This is due to a slight difference of RA and/or TMR between the two barriers caused by different growth conditions and as a consequence of the nanofabrication process. The bottom barrier of the p-DBMTJ of Fig.5.1 and top barrier of the p-DBMTJ of Fig.5.2 dominate comparatively to the other barrier.

5.2 Spin Transfer Torque

After having fixed the method to set the two operation modes of the p-DBMTJ, spin transfer torque was studied via the application of finite voltage pulses and subsequent analysis of the stability phase diagrams.

The experimental setup is similar to the one described in section 3.3.1 except for the direction of the applied magnetic field which is perpendicular to the plane of the sample. The phase diagrams were also obtained by the same method as described in aforementioned section. At each magnetic field point, a 100 ns voltage pulse with a determined amplitude was applied to the p-DBMTJ pillar. Immediately after, the resistance was measured under a small dc bias current, and the next magnetic field point was set. In order to reduce stochasticity in the switching field values, each MR loop was measured 10 times, and their average used for switching field determination. The same procedure was used for all voltage pulse amplitudes, and the final phase diagrams were constructed from these averaged MR loops. The frequency used for the magnetic field was 7 Hz.

5.2.1 Write Mode

In this subsection, all the studied p-DBMTJs were prepared in write mode. The measured phase diagrams are analyzed and comparisons made between p-DBMTJs with different stacks as well as with two types of single p-MTJs.

5.2.1.A Influence of the composite free layer spacer on STT of a p-DBMTJ

We start by comparing two types of p-DBMTJs with, not only different free layer compositions but also with distinct top references. Hereafter, these two samples will be simply labeled by their free layer composition. Figure 5.3(a) presents the read/write mode R(H) loops of an exemplar p-DBMTJ with a FeCoB/Ta/FeCoB free layer and (Co/Pd) multilayers based top reference whose stack composition can be found in section 5.1. [2]. Whereas the read/write mode R(H) loops of Fig.5.3(b) were measured from the best device of the sample with the following composition (thickness in nm):

- Bottom reference SAF: Ta 3/Pt 30/[Co 0.5/Pt 0.25]$_6$/Co 0.5/Ru 0.9/[Co 0.5/Pt 0.25]$_3$/Co 0.5/Ta 0.3/FeCoB 1.2
- Bottom barrier: MgO 1.2 (30s low pressure oxidation)
- Free layer: FeCoB 1.1/W 0.2/FeCoB 1.1
- Top barrier: MgO 1.2 (30s low pressure oxidation)
- Top reference SAF: FeCoB 1.1/W 0.4/NSML/Co 0.6/Ru 0.9/Co 0.6/Pt 0.25/[Co 0.5/Pt 0.25]$_6$/Ru 8

As mentioned above, both studied p-DBMTJs have nominal symmetric barriers. However, mainly due to fabrication caused device-to-device differences, the TMR in write mode mode is not the same for

---

[2] The sample used for fabrication was deposited and provided as courtesy of L. Cuchet *et al.* [81]

both devices. Despite the very close TMR^{read} values, the RA and/or TMR disparity between the two barriers is higher for the p-DBMTJ with W spacer layer in the free layer [Fig.5.3(b)] than for the p-DBMTJ with Ta insertion layer [Fig.5.3(a)]. It is also important to note that the dominant barrier is the bottom one for Fig.5.3(a) and the top one for Fig.5.3(b).

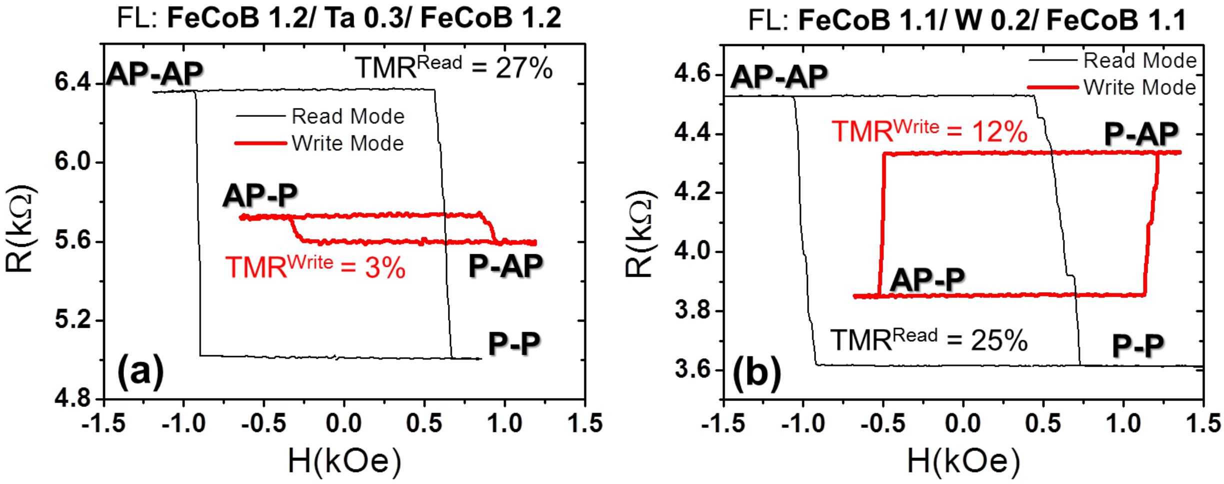

Figure 5.3: Resistance vs. applied magnetic field loops for p-DBMTJs with (a) FeCoB/Ta/FeCoB and (b) FeCoB/W/FeCoB composite free layers (FL) both in read (black line) and write mode (red line). The TMR values are indicated. The write mode loops offset fields are (a) 303 Oe and (b) 327 Oe, respectively and the coercive fields are (a) 615 Oe and (b) 834 Oe. The devices electric diameters are (a) 71 nm and (b) 76 nm.

The phase diagrams of the two perpendicular double MTJs are shown in Fig.5.4. Since the two p-DBMTJs have similar total RA values [3] [20 $\Omega.\mu m^2$ for the p-DBMTJ corresponding to Fig.5.4(a) and 17 $\Omega.\mu m^2$ for that used for the phase diagram in Fig.5.4(b)], and electric diameters, the respective boundary slopes can be compared.

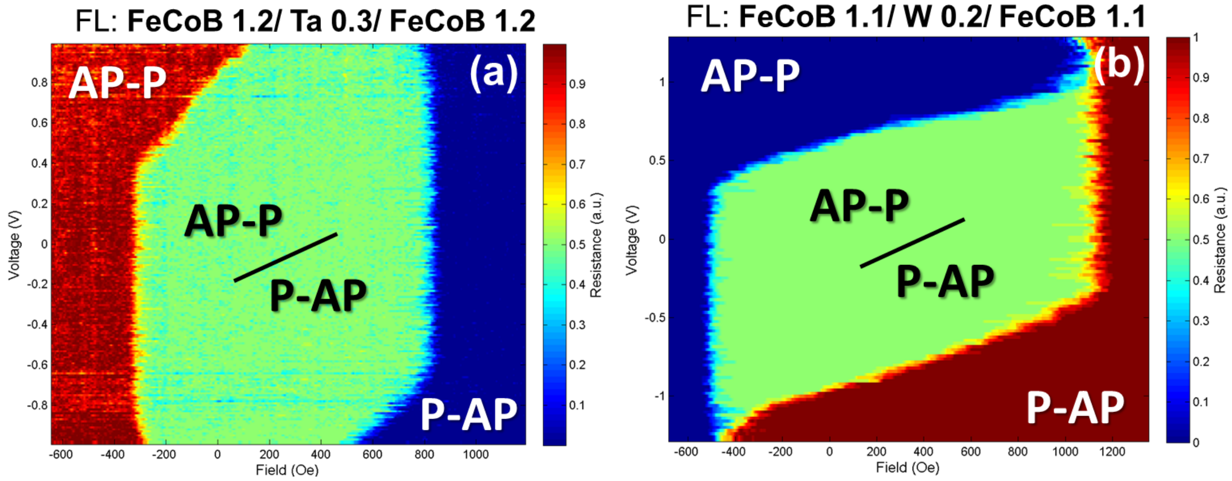

Figure 5.4: Phase diagrams for p-DBMTJs with (a) FeCoB/Ta/FeCoB and (b) FeCoB/W/FeCoB composite free layers (FL) set in write mode. The color corresponds to the normalized resistance, going from high (red) to low (blue) resistance.

The extracted phase boundaries are shown in Fig.5.5. The voltage driven parts of the phase diagrams are linear and almost parallel to each other. As far as possible, only the central points (closer

---

[3] The total RA results from the sum of the RA values of each barrier. The RA of one barrier was measured by CIPT in a single barrier MTJ with the same MgO thickness and oxidation conditions.

to the offset field) were used in the fitting in order to reduce the influence of small nonlinearities at the edges of the boundaries. The fitted slopes are 1.07 (AP-P→P-AP) and 1.29 mV/Oe (P-AP→AP-P) for the p-DBMTJ with a FeCoB/Ta/FeCoB composite free layer and 0.47 (AP-P→P-AP) and 0.32 mV/Oe (P-AP→AP-P) for the p-DBMTJ with a FeCoB/W/FeCoB composite free layer.

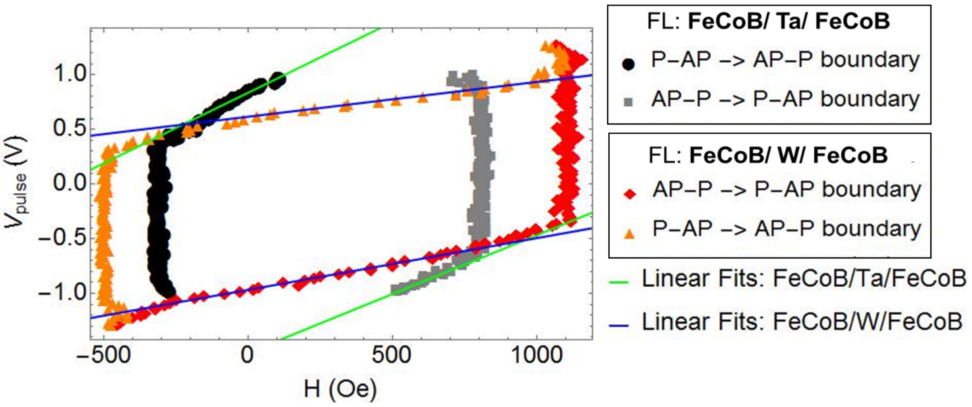

Figure 5.5: Extracted phase diagram boundaries from Fig.5.4(a) and (b). The linear fittings for both P-AP→AP-P and AP-P→P-AP boundaries are displayed by the solid lines.

With the obtained slopes (dV/dH), it is possible to calculate the STT conversion efficiency factor $s_{t\|}$. Transforming Eq.(1.22) to a current density J_{sw} and applying the derivative in respect to the field H, we obtain:

$$\frac{dJ_{sw}}{dH} = \frac{\alpha}{s_{t\|}} = \frac{2e}{\hbar}\frac{t_f \alpha M_s}{\eta}. \tag{5.1}$$

Applying the condition $V_{sw} = J_{sw}\,RA$ to Eq.(5.1), $s_{t\|}$ can be defined as

$$s_{t\|} = \frac{\alpha}{dV/dH} RA_{write} \tag{5.2}$$

where α is the damping factor, RA_{write} is the measured RA of the p-DBMTJ when set in write mode which consists on the product between the resistance of the P-AP state for the p-DBMTJ of Fig.5.3(a) [AP-P state for the device of Fig.5.3(b)] and the electric area of the pillar. Based on a recent study of p-MTJs with a composite free layer of the type FeCoB/spacer/FeCoB [167] and taking into consideration the large magnetic thickness of the free layers (>2 nm), the damping factor used for the calculations was α = 0.005. Therefore the values obtained for $s_{t\|}$ were 103 (AP-P→P-AP) and 86 $Oe\,\mu m^2/A$ (P-AP→AP-P) for the p-DBMTJ with FeCoB/Ta/FeCoB free layer, while for the FeCoB/W/FeCoB free layer p-DBMTJ the values obtained were 187 (AP-P→P-AP) and 278 $Oe\,\mu m^2/A$ (P-AP→AP-P). In summary, the perpendicular DBMTJ with a composite free layer with 0.2 nm W spacer layer presents a gain in STT of approximately 2 and 3 times, respectively for the AP-P→P-AP and P-AP→AP-P transitions, when compared to the p-DBMTJ with Ta spacer in the composite free layer.

The previous analysis is only valid in the assumption of a similar damping factor for both free layers. It is possible that the calculated STT gain might be slightly overestimated, if the damping for the FeCoB/W/FeCoB free layer p-DBMTJ was overestimated, too. According to Devolder *et al.* [167], damping depends on the concentration of Ta impurities within the FeCoB layers and the thickness of the spacer in the composite free layer. Actually, damping was shown to be lower when using a composite free layer with Ta spacer and MgO as a cap layer instead of thick Ta capping. Indeed, the latter would intermix with the FeCoB layers of the free layer and increase its damping. Increasing the composite free layer spacer thickness has also shown to increase the damping factor. Therefore, a lower damping is expected for the p-DBMTJ with higher STT efficiency factor for two reasons: i) it has a thinner spacer than the other p-DBMTJ (0.2 nm instead of 0.3 nm) and more importantly ii) W was used as spacer instead of Ta. This material presents a reduced interdiffusion [156] with FeCoB when compared to Ta, thus enabling a potential reduction of the damping constant.

Despite the possible overestimation of the STT efficiency, the p-DBMTJ with FeCoB/W/FeCoB exhibits critical switchings voltages 40% lower than in p-DBMTJs with a FeCoB/Ta/FeCoB. Therefore, reducing significantly the energy consumption of the p-DBMTJ STT-MRAM.

5.2.1.B Double barrier vs. single barrier perpendicular MTJ

We compare some fundamental STT-MRAM properties between the double and single magnetic tunnel junctions, more precisely writing current (I_c) and current density (J_c), thermal stability factor (Δ) and the spin torque switching efficiency, in the form of the figure of merit Δ/I_c.

In this section, two types of DBMTJs were used, one with nominally symmetric barriers ($RA_{bottom} = RA_{top} = 8.5\,\Omega.\mu m^2$) and another with the bottom barrier thicker than the top barrier ($RA_{bottom} = 60\,\Omega.\mu m^2$ and $RA_{top} = 8.5\,\Omega.\mu m^2$)[4]. The general stack of the two p-DBMTJs used is the following (thickness in nm): *Bottom electrode* - Ta 3/Pt 25/[Co 0.5/Pt 0.25]$_6$/Co 0.5/Ru 0.9/[Co 0.5/Pt 0.25]$_3$/Co 0.5/Ta 0.3/FeCoB 1.2/MgO, *Free layer* - FeCoB 1.1/W 0.2/ FeCoB 1.1 and *Top electrode* - MgO/FeCoB 1.1/W 0.35/NSML/Co 0.6/Ru 0.9/Co 0.6/Pt 0.25/[Co 0.5/Pt 0.25]$_6$/Ru 8. The patterned devices of the p-DBMTJ with symmetric barriers presented a $TMR^{read} = 35 \pm 8\%$ and a $TMR^{write} = 9 \pm 5\%$. The devices of the p-DBMTJ with a bottom thicker barrier presented a $TMR^{read} = 54 \pm 4\%$ and $TMR^{write} = 34 \pm 4\%$. In addition, data on two types of single p-MTJ stacks were provided by J. Chatterjee [132] for comparison with the p-DBMTJs described above [5]. One of the p-MTJ possesses a single FeCoB free layer and thin bottom SAF [166] (see section 4.3.3.C for more details) with the following full stack composition (thickness in nm): Ta 3/Pt 20/Ta 3/Pt 10/[Co 0.5/Pt 0.25]$_3$/Co 0.5/Ru 0.4/W 0.2/FeCoB 1.15/MgO 1.2 (30s low pressure oxidation)/FeCoB 1.5/W 2/Pt 5. The other one has a composite free layer (similar to the p-DBMTJ) followed by a thin MgO cap layer to increase the PMA of the thick free layer and it presents the following full stack composition (thickness in nm): Ta 1/Pt 5/[Co 0.5/Pt 0.25]$_6$/Co 0.5/Ru 0.9/[Co 0.5/Pt 0.25]$_3$/Co 0.5/Ta 0.3/FeCoB 1.2/MgO 1.2 (30s low pressure oxidation)/FeCoB 1.05/W 0.2/FeCoB 1.05/MgO 0.85 (10s low pressure oxidation)/W 2/Pt 5. The p-MTJ with single free layer has a $RA = 8.5\,\Omega.\mu m^2$ and the one with composite free layer has a full $RA = 12.5\,\Omega.\mu m^2$ [6]. The patterned devices display an average $TMR = 59 \pm 2\%$ and $TMR = 70 \pm 5\%$, respectively, for the p-MTJ with single and composite free layers.

Next, we present a description of the expressions and methods used for the calculation of the above

---

[4] The nominal values are obtained from full CIPT measurements

[5] Notice that the perpendicular double and single MTJs were deposited in the same sputtering tool, thus avoiding machine-to-machine stack properties differences.

[6] The main barrier has a $RA = 8.5\,\Omega.\mu m^2$ and the thin MgO cap has a $RA = 4\,\Omega.\mu m^2$

mentioned STT-MRAM properties from the parameters retrieved from the 100ns voltage pulses phase diagrams. The critical switching current density J_c is given by $J_c = V_c/RA$, where V_c is the critical switching voltage obtained at the offset field (center of the bistable zone) for both transitions. In the case of the DBMTJ, the used RA is RA^{write} which is calculated from the product between the lower resistance state in write mode and the electrical area of the device. The critical current I_c is given by $I_c = V_c/R$ where R is the resistance of the initial state of the junction in a certain transition (ex. for the AP→P switching, the used resistance is R_{AP}). The thermal stability factor Δ (or data retention) is extracted via the Switching Field Density (SFD) method for 300 switching events. The Δ obtained is estimated using the following formula [168]:

$$SFD(H) = \frac{1}{R_h \tau_0} \exp\left(-\frac{H_k}{2\tau_0 R_h}\right) \sqrt{\frac{\pi}{\Delta}} erfc\left[\sqrt{\Delta}\left(1 - \frac{H}{H_k}\right)\right] \exp\left[-\Delta\left(1 - \frac{H}{H_k}\right)^2\right] \tag{5.3}$$

, where R_h is the magnetic field sweeping rate, τ_0 (~1 ns) is the inverse of the attempt frequency and H_k is the magnetic anisotropy field of the free layer. SFD was chosen as a reliable retention accelerated extraction method [169]. Finally the figure of merit Δ/I_c is simply the ratio between the thermal stability factor and the critical switching current [7].

The J_c, I_c and Δ on p-DBMTJs are the average values of AP-P→P-AP and P-AP→AP-P transitions since the energy necessary to switch from one to the other state is approximately the same [76]. Whereas, for the single p-MTJs the presented values correspond to the most energy consuming transition P→AP.

Figure 5.6 presents the STT-MRAM properties: (a) J_c, (b) I_c, (c) Δ and (d) Δ/I_c as a function of junction size (electric diameter) for an asymmetric barriers p-DBMTJ with a bottom thicker barrier, p-DBMTJ with nominally symmetric barriers, single p-MTJ with single free layer and single p-MTJ with composite free layer (described above).

First, concerning the critical switching current density J_c [Fig.5.6(a)], the two p-DBMTJs with asymmetric or symmetric barriers present the lowest values for devices above 50 nm. For the asymmetric barriers p-DBMTJ with thick bottom barrier, the switching current densities vary between 2 to 3.5 MA/cm^2 for devices ranging from 100 nm down to 45 nm. By contrast, the largest switching current density is observed for the p-MTJ with single FL whose J_c varies between 6 to 10 MA/cm^2 for the same size range. This corresponds to a switching current density reduction up to 3x for a double p-MTJ in comparison to a single MTJ. The reduction is in agreement with the improvement of STT in p-DBMTJ relative to the single barrier ones. Despite the presence of two barriers in the symmetric barriers p-DBMTJ, the reduction of switching current density is only of 1.5x if compared to the single FL p-MTJ. Despite the RA symmetry or asymmetry of the barriers not being determinant in write mode since both torques add up, the difference in J_c between asymmetric and symmetric barriers p-DBMTJ is due to the larger TMR of the first one in comparison to the second one. In fact, P(asymmetric p-DBMTJ) = 0.46 while for the other one P(symmetric p-DBMTJ) = 0.38 where P is calculated from TMR^{read} using the expression $P = \sqrt{\frac{TMR}{2+TMR}}$. The reduction (increase) of the spin polarization, increases (reduces)

---

[7] It is convenient to notice that Δ/I_c is not the standard figure of merit for spin torque switching efficiency which is usually given by Δ/I_{c0} where I_{c0} is the switching current measured for a writing pulse width of 1 ns.

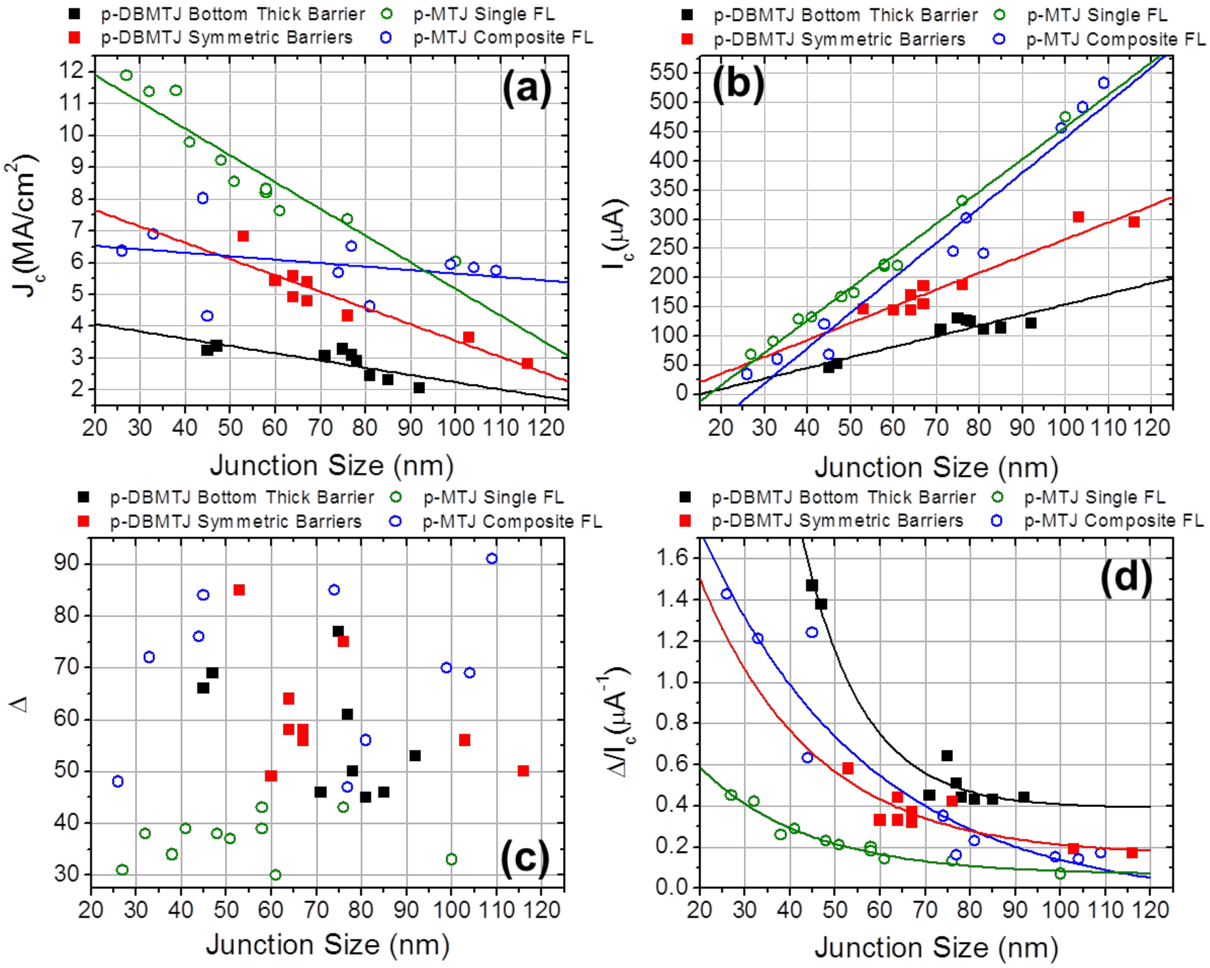

Figure 5.6: Multiple STT-MRAM fundamental properties - (a) critical current density J_c, (b) critical current I_c, (c) thermal stability factor Δ and (d) STT efficiency figure of merit Δ/I_c - as function of the junction electric size, for two types of p-DBMTJs (solid squares) and two types of single p-MTJs (open circles). The presented values were determined from data obtained from voltage writing pulse phase diagrams. The lines in (a),(b) and (d) are guides to the eye.

the switching current (as shown by Eq. (1.40) supposing that $P_F = P_R = P$). Nevertheless, J_c reduction factor is smaller (1.5x-2x) if we compare the p-DBMTJs with the p-MTJ with composite FL. With exception of the p-MTJ with composite FL, the double and single p-MTJs exhibit an increasing J_c with reducing junction size, which is abnormal since J_c should be constant regardless of the junction dimensions. This unexpected trend is due to the linear increase of critical switching current I_c with junction diameter, as presented in Fig.5.6(b). According to eqs.(1.23)-(1.40) and supposing an almost constant H_k with junction size, I_c was expected to scale linearly with area A and consequently to scale with r^2 where r is the radius of a circular junction. Although the expected trend has been observed in previous reports of p-MTJs [170, 171], it has also been reported that, outside the macrospin model (diameter $>$ 30 nm), device-to-device variations on the thermal stability factor Δ affect I_c. In term of absolute values, I_c reduction is of $\sim$3x when using the asymmetric barriers p-DBMTJ instead of a single FL p-MTJ. On the other hand, between single barrier p-MTJs the difference is not that drastic (similarly to ref. [149]), even though the use of a composite free layer p-MTJ slightly improves I_c.

Figure 5.6(c) presents the variation of the thermal stability factor Δ with junction size for the different structures. For the double and single p-MTJs with composite free layer, the values oscillate between 50 and 90. For the single 1.5 nm free layer p-MTJ, the experimental values vary between 30 - 40. Therefore, the employment of the composite free layer provides a gain in the thermal stability factor. A result that goes along with a previous report by Sato *et al.* [149]. In a more general picture, for the device size range studied, Δ has shown to be almost constant [171, 172]: there is no apparent trend of Δ with junction size. There are two types of switching depending on the lateral dimensions of the junction. For device diameters above the nucleation size ($> 30 - 40\,nm$), the switching process consists in nucleating a reversed domain in the free layer and propagating a domain wall. For smaller sizes, the magnetization switches coherently, following a macrospin description. For large structures, the first process requires much less energy than the coherent magnetization reversal [173]. While the energy to create a domain wall increases linearly with diameter, the needed energy for a coherent rotation scales quadratically with the diameter. The single-domain model and nudged elastic band simulations [174] have predicted a linear increase of Δ with junction lateral size (even for large sizes), which goes against experimental observations. A subvolume nucleation mechanism [172] as well as a edge nucleation mode [175] have been reported as possible explanations for the conservation of Δ for large areas. More recently a $\Delta(H)$ model extension to the domain wall mediated switching [176] has corroborated the linear increase of thermal stability with device diameter, in line with the above mentioned simulations.

Finally, Fig.5.6(d) presents the ratio between the thermal stability factor and the critical switching current (Δ/I_c). A closer analysis to Eq.(1.23) shows that I_c is actually proportional [8] to Δ (Eq.(1.28)), thus affected by variations of the latter. According to ref. [171], the variations can be mitigated if one considers the figure of merit Δ/I_c. This ratio was described as a measure of effective damping, characterizing the energy loss of spin transfer switching, or as a measure of the efficiency of STT switching [170]. Our Δ/I_c data, for all the studied perpendicular double or single MTJs, scales with inverse of the diameter (at least for device diameters larger than 30 nm) following a similar trend as previous reports [170, 171, 177]. Moreover, the same authors reported a saturation of this ratio for sizes below transition to quasi-uniform regime. Unfortunately, due to fabrication limitations, we do not have a sufficient amount of devices with diameters below 30 nm to confirm the Δ/I_c saturation. Comparing the various types of p-MTJs, again the p-DBMTJ with a thicker bottom barrier presents the higher STT efficiency along the whole studied size range. The contrast between this type of structure and the single FL p-MTJ increases as dimensions reduce. For junctions sizes of ≈80 nm, the gain in efficiency is of ≈4x, whereas for devices ≈45 nm, the gain rises to ≈6x. On the other hand, the gain in STT efficiency drastically declines to 1.5x when comparing the asymmetric p-DBMTJ with single p-MTJs with a composite free layer. This figure of merit can also be perceived as the inverse of an effective damping, and as discussed in section 5.2.1.A, the damping factor (α) of a FeCoB/Spacer/FeCoB free layer is actually smaller than in a single free layer. Therefore, in a composite FL, I_c reduces due to a lower α and Δ increases since the thickness (and consequently the volume) of the free layer is almost two times larger, enabling the enhancement of Δ/I_c. The symmetric barriers p-DBMTJ also presents a higher STT efficiency than the single FL

---

[8] Under the macrospin model, the critical switching current can be re-written including the thermal stability factor: $I_c = \frac{4e}{\hbar}\Delta\frac{\alpha k_B T}{\eta}$

p-MTJ, however it does not overcome the one with composite FL probably due to the low TMR (low spin polarization) which is detrimental for the critical switching current values.

5.2.2 Read Mode

In this subsection, the perpendicular double barrier MTJs were prepared with the references aligned in parallel. In this configuration, as mentioned in section 1.5.4.C, the torques coming from bottom and top references (acting on the storage layer) subtract. Therefore, this is the ideal magnetic configuration to access (*i.e.* read) the device memory state ("1" or "0") with reduced chances of data disturbance and also with the possibility of using higher readout voltages. The behavior with voltage of p-DBMTJs prepared in read mode was also evaluated through applied voltage pulses phase diagrams.

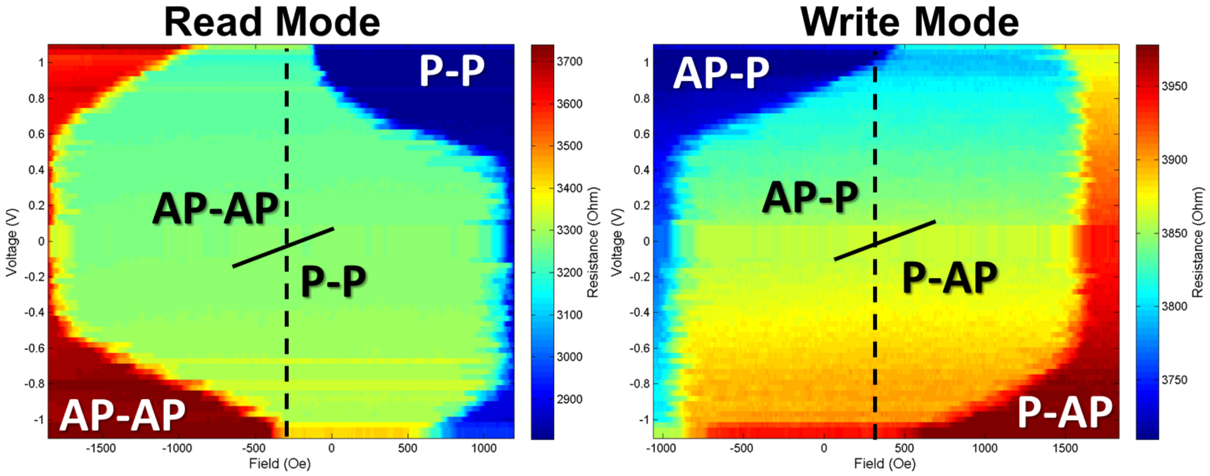

Figure 5.7: Voltage-Field-Resistance phase diagrams of a perpendicular DBMTJ device with nominally symmetric barriers ($RA_{bottom} = RA_{top} = 8.5\,\Omega.\mu m^2$), prepared in read and write modes. The device has an electric diameter of approx. 75 nm. The read and write mode TMR values are 30% and 5%, respectively. The dashed lines are along the offset fields, $H_{off}^{read} = -315$ Oe and $H_{off}^{write} = 376$ Oe.

Figure 5.7 presents the read and write mode phase diagrams of a perpendicular symmetric double barriers MTJ (example representing the most common observed behavior). In the read mode phase diagram, a decrease in coercivity with increasing amplitude applied voltage pulses is observed. The phenomenon is perfectly visible for the positive voltage linear boundary between -1800 Oe and -1000 Oe and the negative voltage linear boundary between 500 Oe and 1100 Oe. Contrary to the behavior observed in the write mode phase diagram, the transitions occur for both voltage polarities. Even if a small asymmetry is observed between the slopes of the phase boundary for each polarity, the observed transitions probably correspond to thermal effects, thus independent of the voltage polarity. Besides, the very good symmetry between the two barriers (related to a very low $TMR^{write} = 5.4\,\%$) should imply $T_{total} \approx 0$, since $T_{\parallel r} \approx T_{\parallel c}$ and torques subtract in read mode. Thus, the possibility of STT induced switching is reduced in this mode. A similar behavior was also noticed in asymmetric p-DBMTJ with thick bottom barrier, set in read mode [Fig.5.8(a)]. The decrease of coercivity with increasing voltage is more pronounced in the positive voltage linear boundary between 0 Oe and 1200 Oe and the negative voltage linear boundary between -1700 Oe and -500 Oe). Despite the undesired thermal effects, for both symmetric and asymmetric barriers p-DBMTJs, the read mode phase diagrams are different from the write mode phase diagrams. At the center of the coercive region (H_{off}) and for the same range of voltage, P-P⇄AP-AP switchings are not possible in read mode [Fig.5.7(a) and Fig.5.8(a)]. On the contrary, for the asymmetric junction [see Fig.5.8(b)], switching from AP-P to P-AP is observed and switching from P-AP to AP-P is expected for a voltage just beyond the experimental values range. For these switching voltages, the magnetic state is stable in read mode [Fig.5.8(a)]. Therefore, the read and write modes show the expected behaviors, even if their performances are not completely satisfactory.

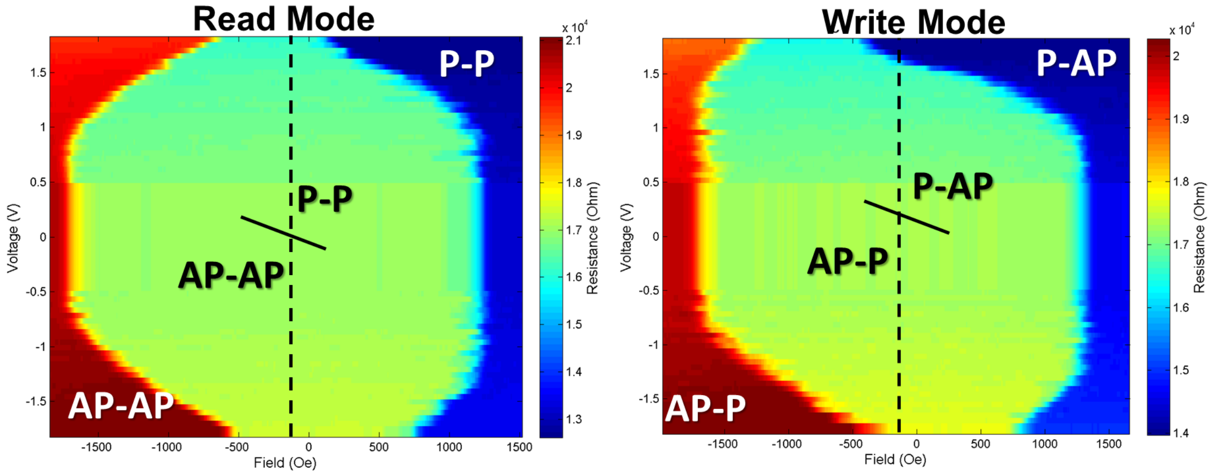

Figure 5.8: Voltage-Field-Resistance phase diagrams of an asymmetric barriers perpendicular DBMTJ with a thicker bottom barrier ($RA_{bottom} = 60\,\Omega.\mu m^2$ and $RA_{top} = 8.5\,\Omega.\mu m^2$), prepared in read and write modes. The device has an electric diameter of approx. 80 nm. The read and write mode TMR values are 57% and 36$\%$, respectively. The dashed lines are along the offset fields, $H_{off}^{read} = -133$ Oe and $H_{off}^{write} = -109$ Oe.

Besides, there is a non-linear behavior of the switching boundary with applied voltage pulses, clearly present in the AP-AP→P-P boundary in the read mode phase diagram of the symmetric barriers p-DBMTJ (Fig.5.7). Indeed, between 0.5 V and 0.6 V the boundary is straight but as the voltage pulse amplitude increases, the boundary becomes curved, closing at a field of ∼150 Oe instead of only closing at the free layer negative switching field ($H_{sw} = H_{off} - H_c$). This phenomenon is not exclusive of devices set in read mode: even the write mode P-AP→AP-P boundary (Fig.5.7) begins to lose its linearity at $V > 1\,V$. In addition, the boundary curvature with high voltage has not been observed in all measured devices [Fig.5.4(b) is an example], thus possibly being associated to device defects caused by nanofabrication. This phase diagram boundary curvature corresponds to a loss of STT efficiency with increasing applied voltage.

In order to better understand the effect of heating, we have extracted and plotted, from the read mode phase diagram of Fig.5.8, some of the resistance hysteresis loops measured after each voltage pulse. The average of 10 loops measured for (a) positive and (b) negative voltage pulses, from 0.5 V to 1.75 V are plotted in Fig.5.9. The decrease of coercivity with a voltage pulse of increasing amplitude is specially visible for the positive polarity voltage pulse [Fig.5.9(a)]. This reduction of H_c is nearly symmetric with respect to the center of the loop. It favors the AP-AP state for H $<$ 0 and the P-P state for H $>$ 0. For V $>$ 0, it is mostly a thermal effect. On the other hand, for V $<$ 0 in Fig.5.9(b), the reduction of H_c is not symmetric. Here, there is a mixture of thermal effects and STT. Since the measured p-DBMTJ has asymmetric barriers, in theory, there is no complete cancellation of the two torques acting on the storage

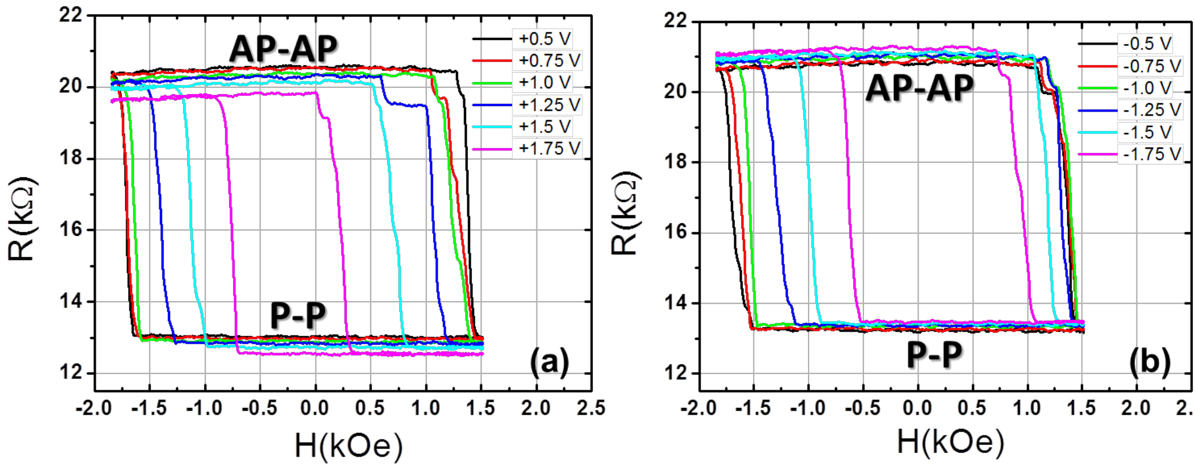

Figure 5.9: Average of 10 hysteresis loops measured after application of (a) positive and (b) negative polarity voltage pulses of increasing amplitude from 0.5 V to 1.75 V in steps of 0.25V. The loops are part of the read mode phase diagram of Fig.5.8, thus measured from the same device. The small resistance variations and the observed steps of the free layer switching fields are measurement setup artifacts.

layer, thus switching is possible even in read mode. Taking into consideration the direction of the injected current, the negative voltage facilitates the P-P→AP-AP transition.

The behavior described above has already been reported by Bandiera *et al.* (see Fig.3 from [73]) in perpendicular magnetized single barrier MTJs with a CoFeB 1.2/[Pd 1.2/Co 0.3]$_3$ (thicknesses in nm) free layer. In their work, the thermally induced reorientation of the FL magnetic anisotropy from perpendicular to in-plane helps the STT switching of the FL magnetization. Curiously, similar phase diagrams have been measured at Spintec by J. Chatterjee [132] in single barrier p-MTJs with composite free layer with an extra thin MgO layer as capping. Figure 5.10 presents two representative phase diagrams for devices with different diameters, where the thermal effect appears to be considerably stronger for Fig.5.10(a) and almost inexistent in Fig. 5.10(b). A closer look to Fig.5.10(a) shows that the decrease of coercivity due to heating happens for voltage pulses with an amplitude larger than 0.45 V (for both polarities). The common feature between this p-MTJ and the p-DBMTJ is the free layer which is composite (FeCoB/W/FeCoB) and sandwiched between two MgO barriers. In fact, the latter may be the source of the thermal effect, at such low voltages, as the MgO layers could be acting as thermal barriers concentrating heat within the composite free layer. Another interesting recurring observation is that the thermal effect is stronger for larger diameter devices. The most probable explanation lies on the Joule effect which is stronger for the junctions with smaller R since the dissipated power (for the same voltage) scales with 1/R.

In some cases, phase diagrams show an even stronger distorsion with a clear curvature observed on the switching boundaries, mainly for high amplitude voltage pulses [see Fig.5.11(a)]. The observed curvature in write mode, at high voltage, is synonym of loss of STT efficiency since the window of field where the STT induced free layer reversal is possible is reduced. In the read mode phase diagram of Fig.5.11, the curvature of the boundary is observed for applied voltage pulses larger than 1V (white dashed line in the figure). This curvature may be related to a thermal effect or to the beginning of the rotation of one the polarizing layers (control or reference), as a result of STT exerted on the polarizer.

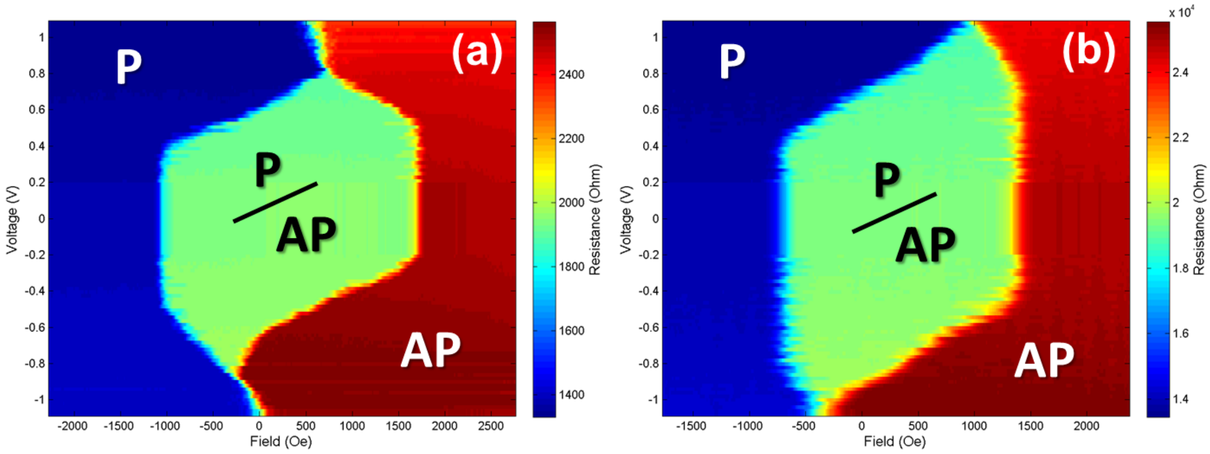

Figure 5.10: Phase diagrams of representative p-MTJ devices with composite free layer (full stack in section 5.2.1.B). The junctions have an electric diameter of (a) 105 nm and (b) 33 nm and TMR values of (a) 81.8 % and (b) 79.6 %. The presented data are courtesy of J. Chatterjee [132].

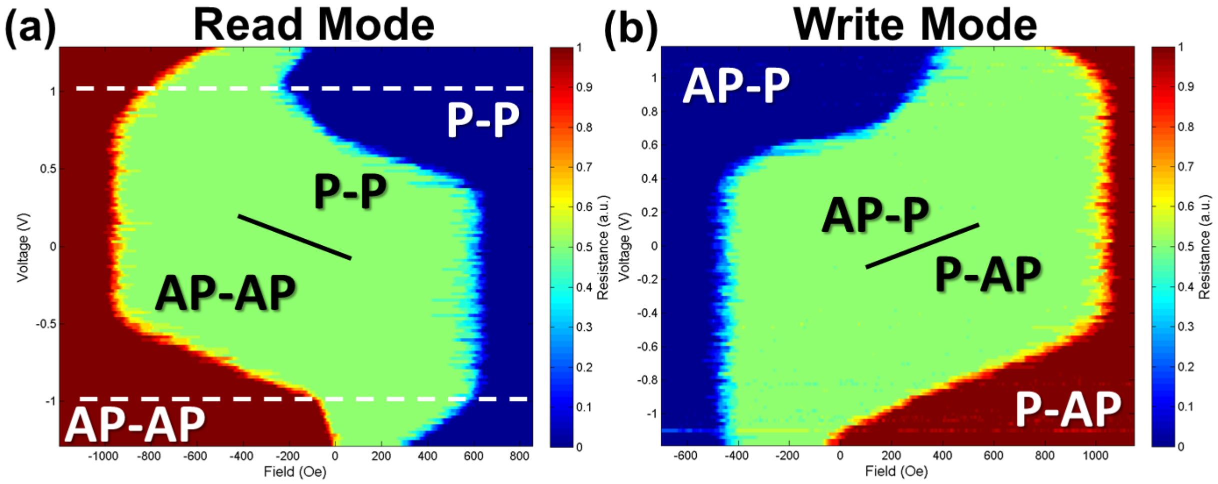

Figure 5.11: Phase diagrams of representative p-DBMTJ devices with nominally symmetric barriers (full stack in section 5.2.1.B). ($RA_{bottom} = RA_{top} = 8.5\,\Omega.\mu m^2$), prepared in (a) read and (b) write modes. The double junction has an electric diameter of approx. 100 nm. The read and write mode TMR values are 26% and 2%, respectively.

A similar curvature of the phase diagram boundaries at high voltage was also observed by J. Chatterjee [132] for single barrier p-MTJs with a single FeCoB free layer, as shown in Fig.5.12(a). However, this specific feature is not systematically observed due to device to device variation: Fig.5.12(b) shows the phase diagram of a nominally equivalent junction which does not demonstrate these curious curvatures. Contrary to what happens for the p-DBMTJ, for these single barrier p-MTJs the curvature does not influence the efficiency of the STT since it only happens for voltages larger than the maximum voltage necessary to switch the free layer magnetization through the entire bi-stable window of field [-1200 Oe to 1000 Oe in Fig.5.12(a) and -350 Oe to 600 Oe in Fig.5.12(b)].

The aforementioned behaviors are as unexpected as they are undesired since the first reduces the STT efficiency of the p-DBMTJ while writing and the second disturbs the magnetic stability of the device while being read. In the next section, the origin of these phenomena are discussed among several hypothesis.

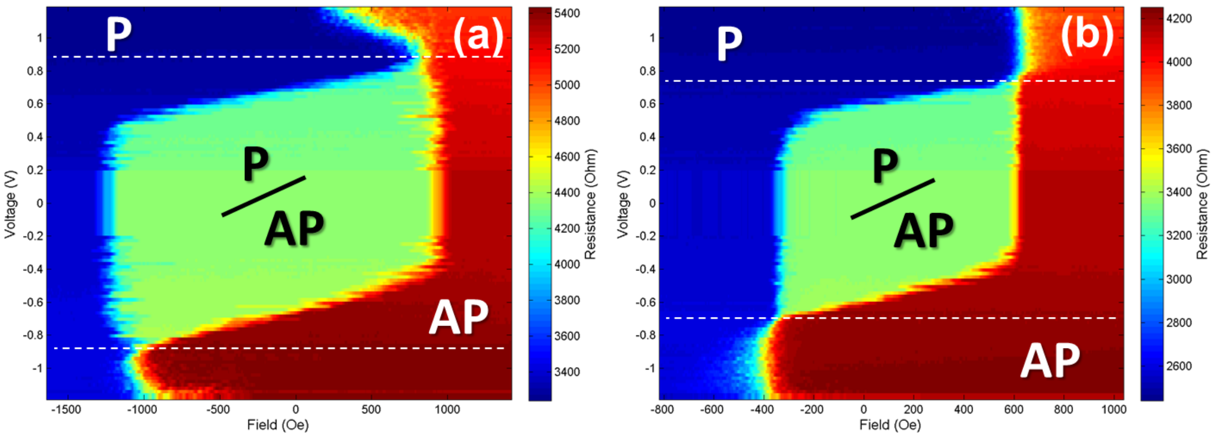

Figure 5.12: Phase diagrams of representative p-MTJ devices with single free layer (full stack in section 5.2.1.B). The junctions have an electric diameter of (a) 56 nm and (b) 65 nm and TMR values of (a) 57.0 % and (b) 62.6 %. The presented data is courtesy of J.Chatterjee [132].

5.2.3 Possible reasons for unexpected phase diagrams of p-DBMTJs

The spin transfer torque mechanism in the read and write modes (see section 1.5.4.C) in a double MTJ (planar or perpendicular anisotropy) only works under the assumption of having the fundamental ferromagnetic blocks - control, reference and free layers - behaving as a macrospin. Moreover, the torques subtraction and addition predicted by the theoretical model for read and write modes, respectively, are only valid if the magnetizations are nearly collinear. A substantial misalignment among these magnetizations may enhance or curtail the STT effect depending on the mode of operation. Therefore, a loss (or reduction) of the perpendicular magnetic anisotropy of one of the reference layers and/or the free layer may explain the unexpected phase diagrams in one or both operation modes. Figure 5.13 shows a schematic of a perpendicular double MTJ with arrows coming from the layers where the magnetization is more prone to lose its orthogonality and, in the small boxes, the possible causes.

5.2.3.A Thermal induced anisotropy reorientation (TIAR)

The thermally induced anisotropy reorientation (TIAR) is defined as an heat assisted method that reorients the direction of the magnetization of a magnetic layer. The TIAR has been demonstrated to assist the STT switching of the free layer in a magnetic tunnel junction [73]. In fact, the magnetization of a perpendicularly magnetized layer may fall into the thin film plane when this layer heats up because of the different temperature dependence of the PMA and the demagnetizing energy [178]. In a STT-MRAM, the heating always occurs when a current is applied to the MTJ due to the inelastic relaxation of the tunneling electrons (Joule effect).

The phenomenon of TIAR-assisted switching is particular interesting for the STT-MRAMs because the STT effect is the strongest since the moment carried by the spin polarized electrons from the electrodes is almost perpendicular to the magnetization of the free layer (already tilted due to heat). In this particular case, thermal fluctuations are not necessary to trigger STT, thus resulting in a more reliable switching process. This type of assisted switching is advantageous in terms of energy consumption when the current required to increase the junction temperature up to its anisotropy reorientation point is

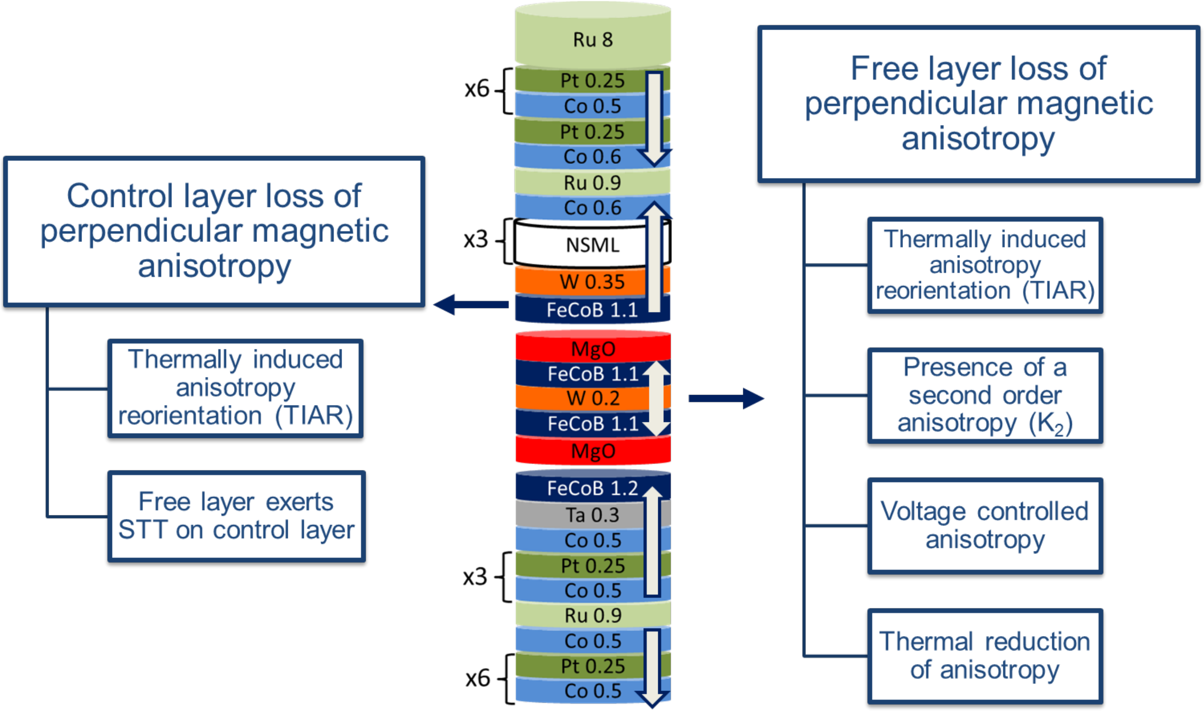

Figure 5.13: Schematic of the possible reasons behind the reduction of perpendicular magnetic anisotropy of the free layer and control layer, which may explain the undesired switchings in read mode and STT efficiency loss of the p-DBMTJ in write mode.

lower than the MTJ critical switching current. This condition has higher probabilities of being fulfilled in a double barrier MTJ since the two MgO barriers act as thermal barriers [179] confining heat, especially within the free layer.

Fig.5.14 shows a comparison between the phase diagram of Fig.5.8(a) of an asymmetric barriers p-DBMTJ in read mode and the phase diagram obtained in a p-MTJ where TIAR-assisted current-induced switching was observed [180]. The similarity between the two phase diagrams is substantial. In fact, the behavior of the phase boundaries for both voltage polarities is identical. The only difference is that in the phase diagram of Fig.5.14(a) the phase boundaries do not intersect the dashed line (center of the loop) since higher voltage were not tried to avoid the double junction breakdown. Therefore, TIAR-assisted switching may also be present in our p-DBMTJs.

5.2.3.B STT exerted on a polarizing layer

The reference magnetization, like the storage layer one, is subjected to STT but it is usually not sufficient to induce magnetization dynamics or reversal. If the current is still applied after the free layer switch, the torque on the reference may destabilize it (”back-torque”). In literature, the dynamics of the reference layer (in perpendicularly magnetized MTJs) were seldom studied. Recently, L. Thomas *et al.* [181] have reported experimental data on STT-induced dynamics of a SAF reference layer in p-STT-MRAM devices. They observed mutual switching of the free and reference layers when the voltage increases. This mutual torque is described as reminiscent of the Slonczewski windmill. Indeed, this windmill torque effect with switching of both layers is only possible if, in the reference SAF, the soft layer (adjacent to the MgO barrier) has higher magnetic moment than the hard layer. In the other scenario,

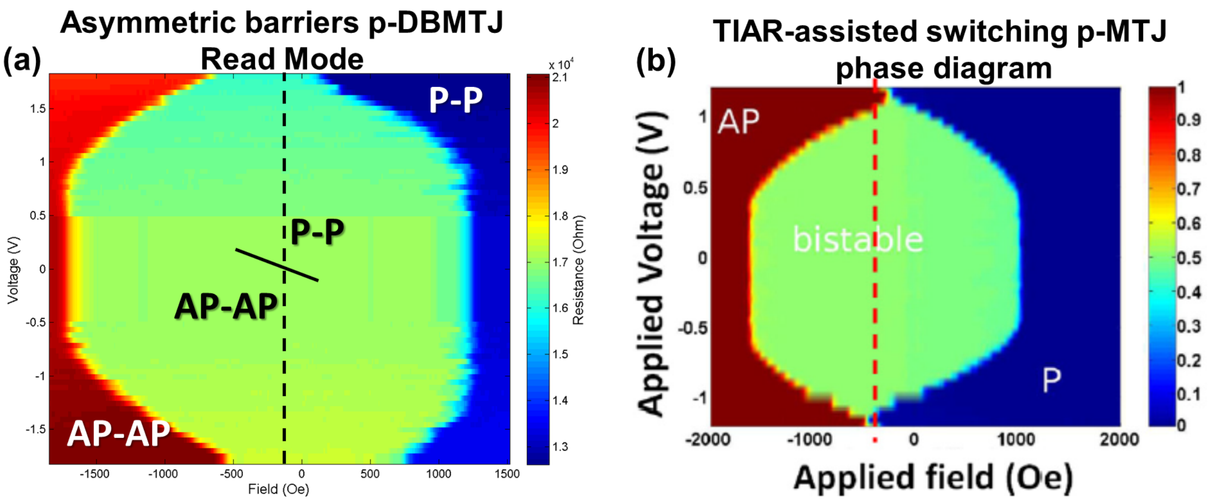

Figure 5.14: (a) Phase diagram of an asymmetric barriers perpendicular DBMTJ with a thicker bottom barrier ($RA_{bottom} = 60\,\Omega.\mu m^2$ and $RA_{top} = 8.5\,\Omega.\mu m^2$), prepared in read mode. Same as in Fig.5.8(a). Next to (b) the phase diagram of a 110 nm diameter pillar of a single barrier p-MTJ where the switching happening at the applied field marked by the dashed red line is TIAR-assisted. This phase diagram correspond to Fig.17 in the paper [180] by Prejbeanu *et al.*

hard layer magnetic moment larger than soft layer one (same as the SAFs used in our p-DBMTJs), the windmill is preceded by another dynamical regime, in which the soft layer magnetization tilts from and precesses around the out-of-plane axis. This magnetization reorientation is the result of interplay between the STT and the SAF exchange field.

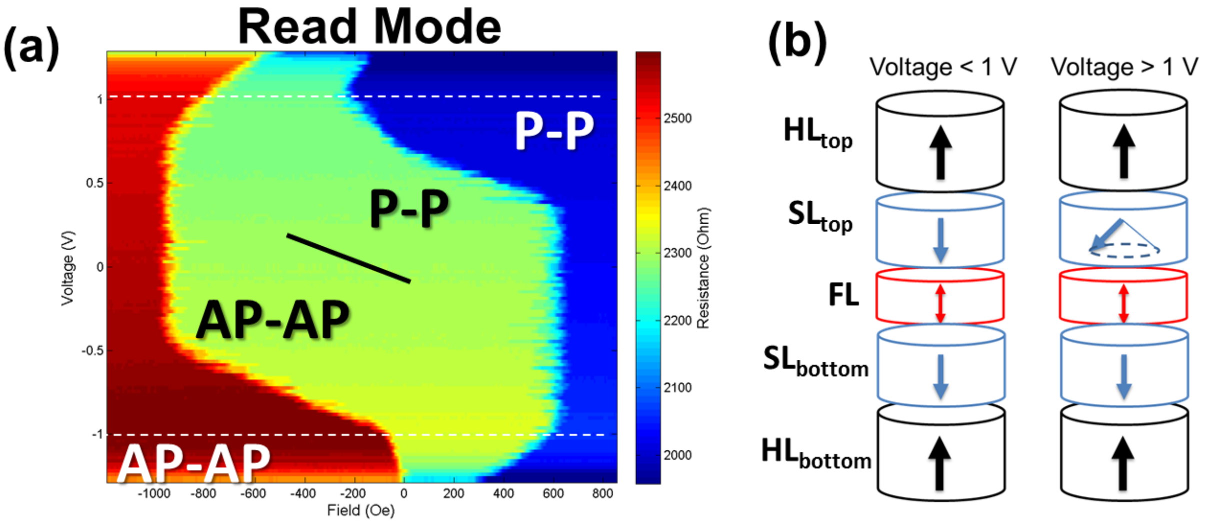

Figure 5.15: Phase diagrams of a p-DBMTJ with nominally symmetric barriers (full stack in section 5.2.1.B). ($RA_{bottom} = RA_{top} = 8.5\,\Omega.\mu m^2$), prepared in read mode. The junction has an electric diameter of approx. 100 nm. The read mode TMR is 26% (b) Illustration of the possible magnetization configuration of the p-DMTJ device in read mode for voltages above and below 1 V.

Unlike Ref. [181] we did not perform time-resolved resistance measurements, but some of the performed finite voltage pulse phase diagrams showed evidence of an initial rotation of the reference layer. A concrete example in p-DBMTJs is the curvature of the bi-stable area [in green in read mode phase diagram of Fig.5.15(a)] for voltages above (below) 1 V (-1 V). Since the phase diagram only shows the resistance change due to the reversal of the free layer, a small tilt of the reference does not change significantly the measured resistance. On the other hand, it does affect the stray fields which act on the free layer, thus changing its offset field which is translated by the observed curvature of the bi-stable area at high voltages. Figure 5.15(b) shows an illustration of the different magnetizations of the p-DBMTJ in read mode (parallel soft layers of top and bottom references). While for voltages below 1 V only the free layer reverses by STT, for pulses amplitudes larger than 1 V, there may be an analogy with the results of Ref. [181]: the magnetization of the reference with lower PMA may slightly tilt towards the plane of the layer and (possibly) precesses around the perpendicular axis. The magnetization reorientation of that reference is probably induced by STT from the free layer.

The probability of this effect being responsible for the unexpected behavior of the p-DBMTJ phase diagrams is rather low. In general, the resistance variation is too low to ensure that there is a deviation of the magnetization of one of the references. In addition, in case of inclination of the control (or reference) magnetization, the torque efficiency should probably increase, instead of the observed loss.

5.2.3.C Presence of second order anisotropy (K$_2$)

The introduction of a noncollinearity between the reference and storage layers has already been proved to be one of the methods to decrease the stochasticity of the switching. Ultra-fast energy efficient switching [182] was demonstrated in orthogonal spin-transfer MRAM (OST-MRAM) which is a type of MRAM with its spin-polarizing layer magnetized perpendicularly to the free layer magnetization [183]. Moreover, the aforementioned noncollinearity can be induced by implementing an easy-cone anisotropy in one of the MTJ magnetic blocks, more commonly the free layer [184]. In fact, the PMA energy density of interfacial origin may be expressed as $E_{PMA} = -\frac{K_1 \cos^2\theta + K_2 \cos^4\theta + ...}{t}$ where K_1,K_2,... are constants of the first and second order surface anisotropy energy per unit area, t is the thickness of the ferromagnetic layer and θ is the angle between the magnetization and perpendicular to plane axis. The easy-cone regime (or canted state) corresponds to a ground state where $K_1 > 0$, $K_2 < 0$ and $0.5 < -K_2/K_1 < 1$. The angle θ_c that the canted magnetization makes with the out-of-plane axis is given by $\cos^2\theta_c = -K_1/2K_2$. In most part of magnetic systems where interface anisotropy is present, the K_1 term dominates over K_2. The second order anisotropy term results from anomalies in the atomic structure at the interface, from interfacial non-uniform stress due to large crystallographic mismatch [184] and can also be a result from spatial fluctuations of first order anisotropy [185]. As previously stated, the small misalignment of the free layer, in the form of this easy-cone state, contributes to a more efficient STT switching in p-MTJs since the thermal stochasticity is mitigated.

The reported K_2 was measured in p-MTJ structures with a composite free layer capped by a thin MgO layer: FeCoB 0.9/Ta 0.3/FeCoB 0.8/MgO 0.4 (thicknesses in nm) [184] which are similar to the ones used in our p-DBMTJs. Therefore, the existence of K_2 anisotropy term in p-DBMTJs cannot be excluded. More recently, N. Strelkov *et al.* [186] have reported the interesting results and analysis of finite voltage pulse measurements performed on the same p-MTJs of Ref. [184]. They have performed V-H resistance phase diagrams (in a similar way as those performed by us) for a variety of applied magnetic field orientations, from $\theta_H = 0°$ (along the out-of-plane axis) until $\theta_H = 90°$ (along the in-plane axis), as shown

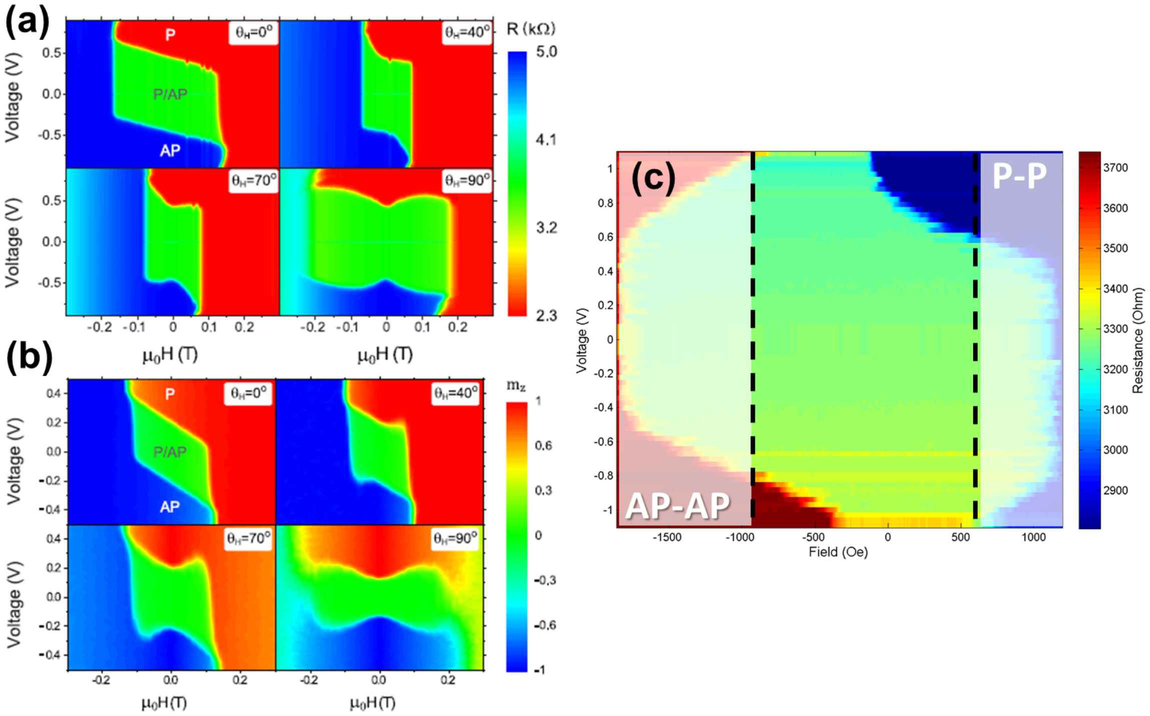

Figure 5.16: (a) Experimental stability V-H diagrams of 80 nm diameter MTJ at room temperature for $\theta_H = 0°, 40°, 70°$, and $90°$. Voltage pulse length was 100 ns. Reprinted with permission of Strelkov *et al.* [186].(b) Numerical stability diagrams at 300K with $K_1 = 778\,kJ/m^3$ and $K_2 = -150\,kJ/m^3$. Reprinted with permission of Strelkov *et al.* [186].(c) Manipulated read mode phase diagram of Fig.5.7. The field region in between the dashed lines is the operational bistable region after the coercivity reduction with applied voltage.

in Fig.5.16(a). Moreover, they have found good agreement with experimental results, when including $K_2 \approx -K_1/5$ instead of $K_2 = 0$ (as in standard systems), as presented in Fig.5.16(b). Comparing the referred phase diagrams with those measured for p-DBMTJs, we found some similarities on the STT switching boundaries, more precisely with the phase diagrams corresponding to $\theta_H = 40°$ and $\theta_H = 70°$. In fact, the curvature (sign of STT efficiency loss) of switching boundary for higher voltages is also observed, which reinforces the theory of a misalignment of the storage layer magnetization. Figure 5.16(c) shows a manipulated p-DBMTJ read mode phase diagram, where the effects of the coercivity reduction with increasing voltage are concealed. The area in between the dashed lines presents some resemblance with the $\theta_H = 40°$ and $\theta_H = 70°$ phase diagrams of figs.5.16(a) and (b).

Nevertheless, the phase diagrams of Ref. [186] do not fit completely with the ones measured for p-DBMTJs. One of the differences is that in the measurements performed on the p-DBMTJs the curvature of the STT switching boundary was observed on measurements carried out with an applied field angle of $\theta_H = 0°$. Whereas for in figs.5.16(a) and (b), the same type of boundaries were observed for $\theta_H = 40°$ and $\theta_H = 70°$. Another major difference is the coercivity (or width of the bi-stable region). While in figs.5.16(a) and (b), the coercivity is visibly reduced when the magnetic field orientation changes from perpendicular($\theta_H = 0°$) towards in-plane, for the p-DBMTJs the coercivity starts reducing from a trigger voltage point upwards and it seems to have linear dependence with voltage.

In conclusion, even if from a stack point of view the presence of a non negligible second order anisotropy in the storage layer seems possible, the phase diagram measurements do not confirm this possibility. The angle reorientation of the magnetization does not appear to be consistent with an easy-cone state but dependent of the amplitude of the applied voltage pulses.

5.2.3.D Voltage Controlled Magnetic Anisotropy

As previously mentioned Fe-rich FeCoB presents high perpendicular magnetic anisotropy at the interface with oxides as MgO which is, consequently, sensitive to voltages applied across the dielectric layer [187]. The PMA of FeCoB varies with its thickness and near the critical transition (perpendicular to in-plane), the magnetization configuration is more sensitive to external voltages [188] and thus enabling the realization of electric-field-controlled MTJ devices. This possibility of changing the PMA at ferromagnet/oxide interface by applying an electric field is often called voltage controlled magnetic anisotropy (VCMA).

Despite the enormous potential of STT-MRAM as a versatile non-volatile memory, it still presents some drawbacks in energy efficiency. The need for driving significant charge currents through the device to switch by STT, together with a nonzero voltage drop across the MTJ leads to a considerable power dissipation. The use of voltage rather than current to control magnetization allows for a decrease of the dissipated power since no charge flow is usually required in such type of structures based on voltage controlled effects. Although most of the electric field controlled PMA effects have been demonstrated in samples grown by molecular beam epitaxy, Wang *et al.* [189] presented the first device, deposited by sputtering, whose magnetization could be reversed by an electric field. Moreover, the manipulation of magnetic anisotropy through voltage has been proven to be dependent on its polarity [190]. Thus, the direction of the applied electric field dictates the increase or decrease of the magnetic anisotropy energy.

In our p-DBMTJs, the used voltages to switch the free layer magnetization correspond to energies of the order 10^{-11} J which are some orders of magnitude higher than the ones used in VCMA experiments (10^{-15} J) [191]. Moreover, the MgO barriers used are quite thin, corresponding to RA values, at least, two orders of magnitude lower than the ones used in VCMA reported experiments. In fact, the VCMA effect was mostly observed in high-resistance MTJs, where the STT is suppressed due to small leakage currents [187]. Unlike STT-MRAM, in VCMA memory devices the leakage current is small, thus the electric field across the tunnel barrier (*i.e.* the applied voltage) is able to control the switching behavior. Besides the previous reasons, VCMA is polarity dependent which does not agree with our obtained results (see figs.5.7 and 5.11) where the loss of PMA happens for both voltage polarities.

In conclusion, although applied voltage (translated as an electric field) has been proven to control the magnetization spatial orientation of ferromagnetic layers, VCMA stands as the least probable reason for the loss of STT efficiency and unexpected behaviors observed in our p-DBMTJs.

5.2.3.E Thermal reduction of anisotropy

In Fig.5.17, we observe an important reduction of coercivity with applied voltage. At negative field, this reduction of coercive field is nearly the same for positive and negative voltage [9]. This independence with voltage sign suggests Joule heating and a subsequent decrease of perpendicular anisotropy with

---

[9] At positive field, the interplay between thermal effect and residual STT is more visible

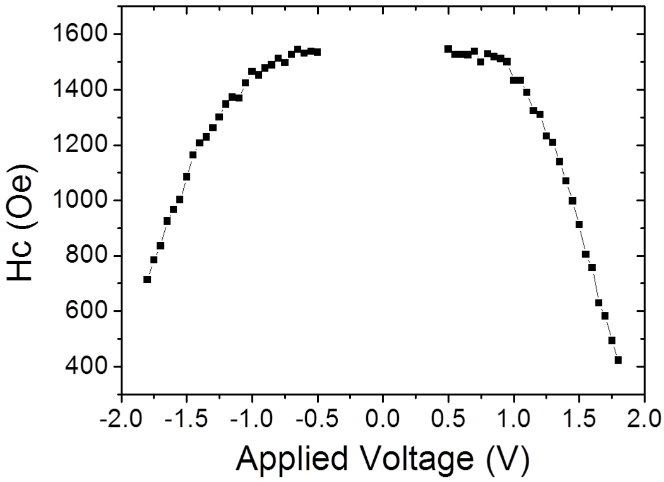

Figure 5.17: Variation of the coercive field with the amplitude of the applied voltage pulses extracted from the RH loops from Fig.5.9 corresponding to asymmetric barriers p-DBMTJ with bottom thick barrier prepared in read mode.

temperature. Since the hysteresis curves keep the same shape with abrupt transitions at all voltages (Fig.5.9), there is no change in the direction of the easy axis. Thus, we may confidently suppose a thermally induced reduction of anisotropy without reorientation. To check this idea, the temperature evolution under Joule heating is supposed to increase as $V^2 : T = T_0 + k_V V^2$. The change in temperature affects the saturation magnetization according to Boch law [192]:

$$M_s\left(T\right) = M_s(0)\left[1 - \left(\frac{T}{T_c}\right)^{1.73}\right] \tag{5.4}$$

where $M_s(0)$ and T_c represent the saturation magnetization at T = 0 K and the Curie temperature, respectively. The effective anisotropy diminishes also when temperature increases. In a coarse approximation, it can be modeled as a function of the saturation magnetization:

$$K(T) = K_0\left(\frac{M_s(T)}{M_s(0)}\right)^{\gamma} \tag{5.5}$$

where γ is an exponent that may vary between 2 and 3 [193].

By using these formulas within macrospin simulations, it is possible to model the phase diagram of single barrier magnetic tunnel junctions with perpendicular anisotropy. Various shapes of phase diagram were obtained (see Fig.5.18) as a function of the value of γ exponent. The comparison between various phase diagrams observed experimentally in single junctions with composite free layer [10] and the macrospin simulations (see Fig.5.19) shows that all shapes can be reproduced by playing on the value of γ. The only difference between experiment and simulation lies in the fact that STT starts at $V = 0$ in the simulation contrary to experiments. It is well-known and can be easily explained: in macrospin simulations, the coercive field is defined by the anisotropy field. On the contrary, due to switching by nucleation and propagation, the coercive field H_c is smaller than the anisotropy field H_K, thus leading to a vertical line cut-off of the phase diagram at $H = \pm H_c$ (dashed lines in left side phase diagrams in Fig.5.19). By applying such a cut-off, the diagrams obtained by simulation would look exactly similar to

---

[10] In section 5.2.2 we have already mentioned that the unexpected curvature of the phase boundaries has not been observed in single barrier p-MTJs with a single free layer.

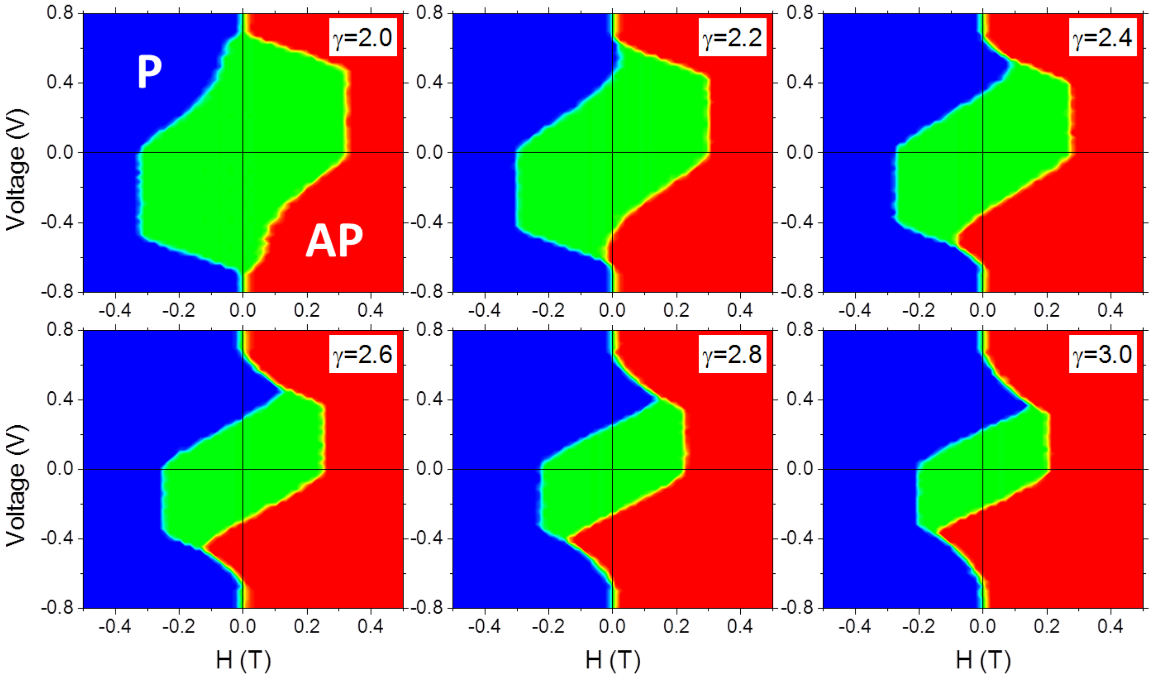

Figure 5.18: Simulated phase diagrams of single barrier p-MTJs obtained for different γ values in Eq.(5.5), from γ = 2 until γ = 3. Courtesy of N. Strelkov.

the measured ones. In particular, the various and unusual curvatures of the phase diagram boundaries at high voltages are reproduced by the calculation by adjusting the exponent γ. It would be interesting to perform similar simulations for double barrier junctions in write and read modes in order to compare with our experiments. Nevertheless, the nearly exact similarity between experiments and simulations for single barrier junctions with composite free layer already supports strongly the hypothesis of a thermally induced reduction of anisotropy. In particular, this effect explains why the bistable region shrinks under positive and negative voltages in read mode.

5.3 Summary

In this chapter, the spin transfer torque was studied in p-DBMTJ junctions with sizes ranging from 30 nm up to 300 nm. The experiments were carried out for the two possible operation modes: write and read.

First, it was demonstrated how to set the write and read modes in patterned devices, by a proper sweep of the magnetic field. Read mode can be set by a full magnetic saturation ($|H| >$10 kOe) followed by a return to zero field. Whereas write mode requires, after full saturation, to sweep the magnetic field into the opposite direction ($|H|$ = 4 kOe) to ensure the sole rotation of the control layer (top reference) and thus, set a magnetic configuration where the two references magnetizations are in antiparallel alignment.

The STT was evaluated first for the double junctions in write mode. Regarding the composite free layer composition, the p-DBMTJ whose free layer spacer was W showed a STT efficiency up to 3x higher than a similar device with a Ta spacer. In addition, p-DBMTJs with symmetric and asymmetric barriers were compared with p-MTJs with single and composite free layers, in terms of writing current, current

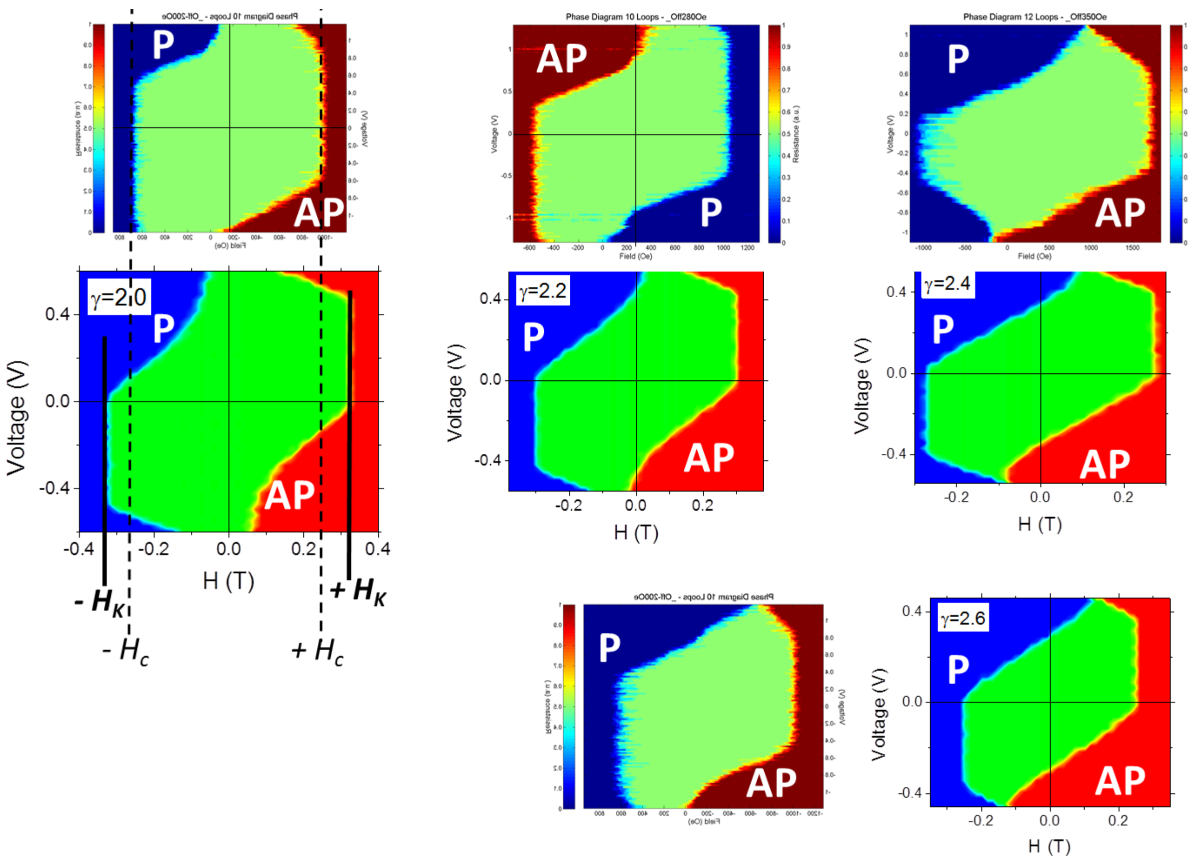

Figure 5.19: Comparison between experimental (P state in dark blue and AP state in dark red) and simulated (P state in light blue and AP state in light red)) phase diagrams for single barrier p-MTJ. The experimental phase diagrams were obtained for measurements performed in single barrier p-MTJs with composite free layer. In the simulated phase diagram at the left, the dashed lines represent H_c and the solid lines represent H_K. Cortesy of N. Strelkov.

density and thermal stability factor. In general, the less current consuming device was the asymmetric barriers p-DBMTJ with a thick bottom barrier which exhibited a reduction of approximately 3x in writing current when compared to a single barrier p-MTJ with single free layer. In terms of STT switching efficiency, which was represented by the figure of merit Δ/I_c, both p-DBMTJs presented better results than the single free layer p-MTJ. In 45 nm devices, $\Delta/I_c = 1.5\,\mu A^{-1}$ for asymmetric barriers p-DBMTJs while for the single free layer p-MTJ, $\Delta/I_c = 0.25\,\mu A^{-1}$ which translates in an efficiency gain of 6x. On the other hand, the efficiency gain was only of 1.5x when compared to a p-MTJ with a composite free layer which usually possesses a higher PMA. Between the symmetric and asymmetric barriers p-DBMTJs, the one with a thicker bottom barrier presented higher STT efficiency probably due to an higher TMR exhibited by the thickest barrier.

In read mode, at H = H$_{off}$, no switching is observed at voltages that produce switching in write mode. Although switching is thus prevented in read mode, we observe that the bistable region significantly shrinks at high voltage, which reduces the stability of the data. Several possible explanations to the unexpected read mode behavior were proposed and studied. The most probable is ascribed to a temperature rise due to Joule effect and heat confinement between the two MgO barriers. This increase of temperature produces a reduction of the saturation magnetization and of the effective anisotropy. Macrospin numerical simulation taking into account this effect reproduce well the distortions of the phase diagram observed in single junctions with composite free layer, identical to the free layer of the p-DBMTJs. Similar distortions observed in the phase diagrams of p-DBMTJ are, therefore, most probably due to the same effect.

Conclusions

This thesis focuses on the optimization and development of double magnetic tunnel junctions, both with planar and perpendicular anisotropy, to be used as alternative improved technology for STT-MRAM. This type of structure has demonstrated to be a reliable alternative to the single barrier magnetic tunnel junction in order to achieve higher data access speeds and to reduce the energy consumption for memory writing. Through the control of the magnetizations directions between the two reference layers of DBMTJ, the amplitude of the spin transfer torque acting on the storage layer can be modulated. Therefore, an antiparallel alignment between the magnetizations of two reference layers allows for a maximization of STT - write mode - while a parallel alignment between them allows for a reduction of STT - read mode. In the write mode, the memory dot can be written using lower currents and the read mode enables a faster and more reliable access to the data.

P.-Y. Clément *et al.* [1] were the first to study spin transfer torque switching in planar DBMTJ patterned pillars, both in write and read modes. While in write mode they have achieved a factor 2 reduction of the current density, in read mode, undesired switchings were observed [80] for DBMTJs with symmetric barriers. In order to complement their results and deepen the comprehension of the interplay between damping-like and field-like torques, in this thesis, we have performed further measurements in planar DBMTJs with symmetric (RA$_{Top}$ = RA$_{Bottom}$) and asymmetric barriers (RA$_{Top}$ $>$ RA$_{Bottom}$ and RA$_{Top}$ $<$ RA$_{Bottom}$). First, measurements were conducted in a similar way as P.-Y. Clément *et al.* using DC current. In write mode, independently of the symmetry or asymmetry of the barriers, the 2x reduction of current density was also observed: $\mathrm{J_{sw}^{DBMTJ}} = 1.9\,\mathrm{MA/cm^2}$ in DBMTJs while $\mathrm{J_{sw}^{SBMTJ}} = 4.1\,\mathrm{MA/cm^2}$ for a comparable single barrier MTJ. Thus proving the efficiency of DBMTJ in write mode in the decrease of power consumption for STT-MRAM. Nevertheless, in read mode, undesired switchings towards both high and low resistance states were observed, also independently of the barriers symmetry or asymmetry. Further measurements using 100 ns voltage pulses were performed in the same samples. In write mode, the DBMTJs presented two types of behaviors: 1) a predominant effect of linear damping-like torque ($T_{\parallel} \propto a\,V$) where each of the voltage polarities stabilizes a different state and 2) a predominant effect of a quadratic perpendicular torque component ($T_{\perp} \propto b\,V^2$) which favors the antiparallel alignment between the storage layer and reference (or control) layer around the thicker barrier. Surprisingly, for the asymmetric barriers DBMTJ with thick bottom barrier, the perpendicular torque favored the antiparallel alignment between the storage and control layers adjacent to the thinner barrier, in opposition to what was observed for the other two DBMTJs and in disagreement with theoretical predictions. In read mode, all the DBMTJs exhibited an unanimous behavior: P-P→AP-AP switching being favored with V^2, in agreement with the findings of P.-Y. Clément *et al.* [80]. Among these experiments, we have also studied an undesired event, which compromises the application of the in-plane anisotropy DBMTJ as an MRAM, the current induced mode switch. While believed to have an origin on Joule heating, the reversal, or not, of the control layer magnetization have shown to depend on the magnetic configuration of the DBMTJ and the applied magnetic field. The macrospin simulations performed allowed to study the individual and combined effects of both damping-like and field-like torques in DBMTJs with in-plane magnetization, prepared in write and read modes. The two damping-like torques proportional to V coming from reference and control layers were shown to add up in write mode and subtract in read mode. While the opposite happens for the V^2 component of the field-like torque. The experimental phase diagrams obtained for the voltage pulse measurements could only be reproduced in the simulations by setting a larger value to the torque prefactors coming from the polarizer adjacent to the thickest barrier. While for the case of the asymmetric DBMTJs with thick bottom barrier, the experimental phase diagrams were only in agreement with simulation if the field-like V^2 prefactor of the reference layer adjacent to the thinner barrier was larger than the prefactor of the reference layer adjacent to the thicker barrier.

Due to the growing interest and development of MTJs with perpendicular anisotropy, we have also directed our efforts towards the realization and study of double barrier magnetic tunnel junctions with perpendicular magnetization. Compared to planar systems, this type of junctions shows improvements regarding storage density, thermal stability and writing current. L. Cuchet *et al.* [81] were the first to develop a double barrier MTJ stack with perpendicular magnetic anisotropy, using [Co/Pt]-based multilayers for the bottom reference and [Co/Pd]-based multilayers for the top reference. Together with J. Chatterjee [132], we developed novel seedless multilayers (NSML) to be used as top reference in perpendicular DBMTJs. We have demonstrated that the use of a W texture breaking layer between the reference FeCoB and the NSML improves the PMA of the ensemble, thus corresponding to a reference in the form of FeCoB/W/NSML. The optimal thickness of the W texture breaking layer was found to be 0.35 nm. Moreover, experiments on perpendicular top pinned single barrier MTJs, revealed that a top SAF reference of the form FeCoB/W/NSML/Ru/[Co/Pt]$_n$ has a larger perpendicular anisotropy than a top SAF of the form FeCoB/W/NSML/Ru/NSML. Analytical calculations of the stray field were performed to obtain the optimal number of repetitions (n) of [Co/Pt] multilayers in the top SAF hard layer to reduce the offset fields in p-DBMTJs. For pillars of diameters between 50 and 100 nm, n = 7 correspond to offset fields below 100 Oe, for both parallel or antiparallel alignments between bottom and top references' magnetizations. We have demonstrated the realization of a new p-DBMTJ stack using a top SAF reference including NSML as soft layer and [Co/Pt]-multilayers as hard layer. Read and write modes have been also shown to be achieved by setting the proper magnetic field sweeps. As a proof of concept, we present the first realization of a perpendicular DBMTJ using a bottom thin SAF of the form [Co/Pt]$_n$/Co/Ru/W/FeCoB, where Ru/W is a new type of RKKY coupling layer developed by J. Chatterjee *et al.* [166].

Finally, the spin transfer torque of p-DBMTJs using the newly developed stack was studied experimentally in patterned junctions with diameters between 30-300 nm. First, the separation between read and write modes, in patterned junctions, was possible through a proper sweep of the magnetic field. In write mode, p-DBMTJs with a composite storage layer of the form FeCoB/W/FeCoB showed a 3x higher STT efficiency than similar p-DBMTJ with FeCoB/Ta/FeCoB storage layer. Similarly to the in-plane DBMTJs, p-DBMTJs with symmetric and asymmetric barriers were studied and compared to single barrier p-MTJs. Among the p-DBMTJs, the one with a thicker bottom barrier present an higher STT efficiency than those with symmetric barriers. That same asymmetric barriers p-DBMTJ showed a gain in STT efficiency up to 6x when compared to a single barrier p-MTJ. In read mode, although switching is prevented at the center of the loop, we observe that the bistable region significantly shrinks at high voltage, which reduces the stability of the data. Among several proposed explanations to this phenomenon, the most probable was ascribed to a temperature rise due to Joule effect and heat confinement between the two MgO barriers. This increase of temperature produces a reduction of the saturation magnetization and of the effective anisotropy. Macrospin numerical simulations accounting for this anisotropy decrease with temperature provided similar results to the experimental phase diagrams obtained.

Although the promising results of DBMTJs, their implementation as a functional STT-MRAM for applications still demands some improvements. The write mode has proven to reduce the switching currents for both in-plane and perpendicular DBMTJs. The read mode has not demonstrated perfect operation. For planar DBMTJs, the field-like torque triggers undesired switching towards an antiparallel alignment between the storage layer and both references. In perpendicular DBMTJs, the reduction of the perpendicular anisotropy due to temperature reduces the thermal stability of the device. Moreover, the current method to switch between write and read modes is not very energetically efficient for all application ranges. However, for memories that are seldom written and often read (*e.g.* data base), an more reliable option has been proposed [194]. In a device, mode selection could be performed at once for all bits of a given word by propagating a domain wall in a control line serving as top polarizing electrode or by using spin-orbit torque switching.

Bibliography

[1] P.-Y. Clement, *Transport electronique dans les jonctions tunnel magnetiques a double barriere*. PhD thesis, Universite de Grenoble, 2014.

[2] W. Thomson, "Xix. on the electro-dynamic qualities of metals:—effects of magnetization on the electric conductivity of nickel and of iron," *Proceedings of the Royal Society of London*, vol. 8, pp. 546–550, 1857.

[3] M. N. Baibich, J. M. Broto, A. Fert, F. N. Van Dau, F. Petroff, P. Etienne, G. Creuzet, A. Friederich, and J. Chazelas, "Giant magnetoresistance of (001) fe/(001) cr magnetic superlattices," *Physical review letters*, vol. 61, no. 21, p. 2472, 1988.

[4] G. Binasch, P. Grünberg, F. Saurenbach, and W. Zinn, "Enhanced magnetoresistance in layered magnetic structures with antiferromagnetic interlayer exchange," *Physical review B*, vol. 39, no. 7, p. 4828, 1989.

[5] S. Wolf, D. Awschalom, R. Buhrman, J. Daughton, S. Von Molnar, M. Roukes, A. Y. Chtchelkanova, and D. Treger, "Spintronics: a spin-based electronics vision for the future," *Science*, vol. 294, no. 5546, pp. 1488–1495, 2001.

[6] B. Dieny, V. S. Speriosu, S. S. Parkin, B. A. Gurney, D. R. Wilhoit, and D. Mauri, "Giant magnetoresistive in soft ferromagnetic multilayers," *Physical Review B*, vol. 43, no. 1, p. 1297, 1991.

[7] H. Fukuzawa, H. Yuasa, S. Hashimoto, K. Koi, H. Iwasaki, M. Takagishi, Y. Tanaka, and M. Sahashi, "Mr ratio enhancement by nol current-confined-path structures in cpp spin valves," *IEEE Transactions on Magnetics*, vol. 40, no. 4, pp. 2236–2238, 2004.

[8] J. S. Moodera, L. R. Kinder, T. M. Wong, and R. Meservey, "Large magnetoresistance at room temperature in ferromagnetic thin film tunnel junctions," *Physical review letters*, vol. 74, no. 16, p. 3273, 1995.

[9] M. B. Stearns, "Simple explanation of tunneling spin-polarization of fe, co, ni and its alloys," *Journal of Magnetism and Magnetic Materials*, vol. 5, no. 2, pp. 167–171, 1977.

[10] E. C. Stoner, "Collective electron ferromagnetism in metals and alloys," *J. phys. radium*, vol. 12, no. 3, pp. 372–388, 1951.

[11] A. Fert and I. Campbell, "Two-current conduction in nickel," *Physical Review Letters*, vol. 21, no. 16, p. 1190, 1968.

[12] P. Tedrow and R. Meservey, “Spin polarization of electrons tunneling from films of fe, co, ni, and gd,” *Physical Review B*, vol. 7, no. 1, p. 318, 1973.

[13] M. Julliere, “Tunneling between ferromagnetic films,” *Physics letters A*, vol. 54, no. 3, pp. 225–226, 1975.

[14] C. A. Elwell, *The development of magnetic tunnel junction fabrication techniques*. PhD thesis, University of Cambridge, 2002.

[15] J. C. Slonczewski, “Conductance and exchange coupling of two ferromagnets separated by a tunneling barrier,” *Physical Review B*, vol. 39, pp. 6995–7002, Apr. 1989.

[16] J. S. Moodera and G. Mathon, “Spin polarized tunneling in ferromagnetic junctions,” *Journal of Magnetism and Magnetic Materials*, vol. 200, pp. 248–273, Oct. 1999.

[17] H. Swagten, P. Paluskar, R. Lavrijsen, J. Kohlhepp, and B. Koopmans, “Tunneling spin polarization and annealing of co72fe20b8,” *Journal of Magnetism and Magnetic Materials*, vol. 310, no. 2, pp. 2012–2014, 2007.

[18] D. Monsma and S. Parkin, “Spin polarization of tunneling current from ferromagnet/al 2 o 3 interfaces using copper-doped aluminum superconducting films,” *Applied Physics Letters*, vol. 77, no. 5, pp. 720–722, 2000.

[19] W. E. Pickett and J. S. Moodera, “Half metallic magnets,” *Physics Today*, vol. 54, no. 5, pp. 39–45, 2001.

[20] M. Bowen, M. Bibes, A. Barthélémy, J.-P. Contour, A. Anane, Y. Lemaıtre, and A. Fert, “Nearly total spin polarization in la 2/3 sr 1/3 mno 3 from tunneling experiments,” *Applied Physics Letters*, vol. 82, no. 2, pp. 233–235, 2003.

[21] Y. Sakuraba, a. M. Hattori, M. Oogane, Y. Ando, H. Kato, A. Sakuma, T. Miyazaki, and H. Kubota, “Giant tunneling magnetoresistance in co 2 mn si/ al–o/ co 2 mn si magnetic tunnel junctions,” *Applied Physics Letters*, vol. 88, no. 19, p. 192508, 2006.

[22] Y. Lee, J. Hayakawa, S. Ikeda, F. Matsukura, and H. Ohno, “Effect of electrode composition on the tunnel magnetoresistance of pseudo-spin-valve magnetic tunnel junction with a mgo tunnel barrier,” *Applied Physics Letters*, vol. 90, no. 21, p. 212507, 2007.

[23] W. Butler, X.-G. Zhang, T. Schulthess, and J. MacLaren, “Spin-dependent tunneling conductance of fe— mgo— fe sandwiches,” *Physical Review B*, vol. 63, no. 5, p. 054416, 2001.

[24] S. Yuasa and D. D. Djayaprawira, “Giant tunnel magnetoresistance in magnetic tunnel junctions with a crystalline MgO(0 0 1) barrier,” *Journal of Physics D: Applied Physics*, vol. 40, no. 21, p. R337, 2007.

[25] W. H. Butler, “Tunneling magnetoresistance from a symmetry filtering effect,” *Science and Technology of Advanced Materials*, vol. 9, no. 1, p. 014106, 2008.

[26] X.-G. Zhang and W. Butler, “Large magnetoresistance in bcc co/ mg o/ co and fe co/ mg o/ fe co tunnel junctions,” *Physical Review B*, vol. 70, no. 17, p. 172407, 2004.

[27] S. Yuasa, A. Fukushima, T. Nagahama, K. Ando, and Y. Suzuki, “High tunnel magnetoresistance at room temperature in fully epitaxial fe/mgo/fe tunnel junctions due to coherent spin-polarized tunneling,” *Japanese Journal of Applied Physics*, vol. 43, no. 4B, p. L588, 2004.

[28] S. S. Parkin, C. Kaiser, A. Panchula, P. M. Rice, B. Hughes, M. Samant, and S.-H. Yang, “Giant tunnelling magnetoresistance at room temperature with mgo (100) tunnel barriers,” *Nature materials*, vol. 3, no. 12, p. 862, 2004.

[29] X. Zhang, B.-Z. Li, G. Sun, and F.-C. Pu, “Spin-polarized tunneling and magnetoresistance in ferromagnet/insulator(semiconductor) single and double tunnel junctions subjected to an electric field,” *Physical Review B*, vol. 56, pp. 5484–5488, Sept. 1997.

[30] M. Watanabe, T. Suemasu, S. Muratake, and M. Asada, “Negative differential resistance of metal (cosi2)/insulator (caf2) triple-barrier resonant tunneling diode,” *Applied physics letters*, vol. 62, no. 3, pp. 300–302, 1993.

[31] F. Montaigne, J. Nassar, A. Vaurès, F. N. Van Dau, F. Petroff, A. Schuhl, and A. Fert, “Enhanced tunnel magnetoresistance at high bias voltage in double-barrier planar junctions,” *Applied Physics Letters*, vol. 73, pp. 2829–2831, Nov. 1998.

[32] M. Wilczynski and J. Barnas, “Tunnel magnetoresistance in ferromagnetic double-barrier planar junctions: coherent tunneling regime,” *Journal of magnetism and magnetic materials*, vol. 221, no. 3, pp. 373–381, 2000.

[33] M. Chshiev, D. Stoeffler, A. Vedyayev, and K. Ounadjela, “Magnetic diode effect in double-barrier tunnel junctions,” *EPL (Europhysics Letters)*, vol. 58, no. 2, p. 257, 2002.

[34] A. Iovan, S. Andersson, Y. G. Naidyuk, A. Vedyaev, B. Dieny, and V. Korenivski, “Spin diode based on fe/mgo double tunnel junction,” *Nano letters*, vol. 8, no. 3, pp. 805–809, 2008.

[35] T. Nozaki, N. Tezuka, and K. Inomata, “Quantum oscillation of the tunneling conductance in fully epitaxial double barrier magnetic tunnel junctions,” *Physical review letters*, vol. 96, no. 2, p. 027208, 2006.

[36] B. Tao, H. Yang, Y. Zuo, X. Devaux, G. Lengaigne, M. Hehn, D. Lacour, S. Andrieu, M. Chshiev, T. Hauet, *et al.*, “Long-range phase coherence in double-barrier magnetic tunnel junctions with a large thick metallic quantum well,” *Physical review letters*, vol. 115, no. 15, p. 157204, 2015.

[37] Z. Diao, A. Panchula, Y. Ding, M. Pakala, S. Wang, Z. Li, D. Apalkov, H. Nagai, A. Driskill-Smith, L.-C. Wang, E. Chen, and Y. Huai, “Spin transfer switching in dual MgO magnetic tunnel junctions,” *Applied Physics Letters*, vol. 90, p. 132508, Mar. 2007.

[38] H. D. Gan, S. Ikeda, W. Shiga, J. Hayakawa, K. Miura, H. Yamamoto, H. Hasegawa, F. Matsukura, T. Ohkubo, K. Hono, and H. Ohno, "Tunnel magnetoresistance properties and film structures of double MgO barrier magnetic tunnel junctions," *Applied Physics Letters*, vol. 96, p. 192507, May 2010.

[39] W. Feng, C. Fowley, K. Bernert, V. Sluka, E. Kowalska, Y. Aleksandrov, J. Lindner, J. Fassbender, H. D. Gan, A. Kunz, R. Hübner, J. M. D. Coey, and A. M. Deac, "Effect of Deposition Conditions and Annealing Temperature on Tunnel Magnetoresistance and the Structure of MgO-Based Double-Barrier Magnetic Tunnel Junctions," *IEEE Transactions on Magnetics*, vol. 51, pp. 1–4, Nov. 2015.

[40] G. Hu, J. H. Lee, J. J. Nowak, J. Z. Sun, J. Harms, A. Annunziata, S. Brown, W. Chen, Y. H. Kim, G. Lauer, L. Liu, N. Marchack, S. Murthy, E. J. O'Sullivan, J. H. Park, M. Reuter, R. P. Robertazzi, P. L. Trouilloud, Y. Zhu, and D. C. Worledge, "STT-MRAM with double magnetic tunnel junctions," in *2015 IEEE International Electron Devices Meeting (IEDM)*, pp. 26.3.1–26.3.4, Dec. 2015.

[41] Z. Duan, S. Schäfer, V. Voznyuk, X. Tang, G. Feng, D. Lee, L. Zheng, D. Apalkov, R. Beach, and V. Nikitin, "High TMR Dual-MTJ STT-MRAM Design with Perpendicular Magnetic Anisotropy," in *2017 Conference on Magnetism and Magnetic Materials (MMM)*, (Pittsburgh), 2017.

[42] C. Baraduc, M. Chshiev, and U. Ebels, "Introduction to spin transfer torque," in *Nanomagnetism And Spintronics: Fabrication, Materials, Characterization and Applications*, pp. 173–192, World Scientific, 2011.

[43] J. C. Slonczewski, "Currents, torques, and polarization factors in magnetic tunnel junctions," *Physical Review B*, vol. 71, p. 024411, Jan. 2005.

[44] J. C. Slonczewski, "Current-driven excitation of magnetic multilayers," *Journal of Magnetism and Magnetic Materials*, vol. 159, pp. L1–L7, June 1996.

[45] X. Waintal, E. B. Myers, P. W. Brouwer, and D. Ralph, "Role of spin-dependent interface scattering in generating current-induced torques in magnetic multilayers," *Physical Review B*, vol. 62, no. 18, p. 12317, 2000.

[46] M. D. Stiles, "Exchange coupling in magnetic heterostructures," *Physical Review B*, vol. 48, no. 10, p. 7238, 1993.

[47] D. C. Ralph and M. D. Stiles, "Spin transfer torques," *Journal of Magnetism and Magnetic Materials*, vol. 320, pp. 1190–1216, Apr. 2008.

[48] J. Xiao, G. E. W. Bauer, and A. Brataas, "Spin-transfer torque in magnetic tunnel junctions: Scattering theory," *Physical Review B*, vol. 77, p. 224419, June 2008.

[49] A. Kalitsov, W. Silvestre, M. Chshiev, and J. P. Velev, "Spin torque in magnetic tunnel junctions with asymmetric barriers," *Physical Review B*, vol. 88, p. 104430, Sept. 2013.

[50] I. Theodonis, N. Kioussis, A. Kalitsov, M. Chshiev, and W. H. Butler, “Anomalous Bias Dependence of Spin Torque in Magnetic Tunnel Junctions,” *Physical Review Letters*, vol. 97, p. 237205, Dec. 2006.

[51] M. Chshiev, I. Theodonis, A. Kalitsov, N. Kioussis, and W. H. Butler, “Voltage Dependence of Spin Transfer Torque In Magnetic Tunnel Junctions,” *IEEE Transactions on Magnetics*, vol. 44, pp. 2543–2546, Nov. 2008.

[52] W. Skowroński, M. Czapkiewicz, M. Frankowski, J. Wrona, T. Stobiecki, G. Reiss, K. Chalapat, G. S. Paraoanu, and S. van Dijken, “Influence of MgO tunnel barrier thickness on spin-transfer ferromagnetic resonance and torque in magnetic tunnel junctions,” *Physical Review B*, vol. 87, p. 094419, Mar. 2013.

[53] J. C. Sankey, Y.-T. Cui, J. Z. Sun, J. C. Slonczewski, R. A. Buhrman, and D. C. Ralph, “Measurement of the spin-transfer-torque vector in magnetic tunnel junctions,” *Nature Physics*, vol. 4, pp. 67–71, Jan. 2008.

[54] C. Wang, Y.-T. Cui, J. Z. Sun, J. A. Katine, R. A. Buhrman, and D. C. Ralph, “Bias and angular dependence of spin-transfer torque in magnetic tunnel junctions,” *Physical Review B*, vol. 79, p. 224416, June 2009.

[55] C. Heiliger and M. D. Stiles, “Ab Initio,” *Physical Review Letters*, vol. 100, p. 186805, May 2008.

[56] S. Petit, C. Baraduc, C. Thirion, U. Ebels, Y. Liu, M. Li, P. Wang, and B. Dieny, “Spin-Torque Influence on the High-Frequency Magnetization Fluctuations in Magnetic Tunnel Junctions,” *Physical Review Letters*, vol. 98, p. 077203, Feb. 2007.

[57] Z. Li, S. Zhang, Z. Diao, Y. Ding, X. Tang, D. M. Apalkov, Z. Yang, K. Kawabata, and Y. Huai, “Perpendicular Spin Torques in Magnetic Tunnel Junctions,” *Physical Review Letters*, vol. 100, p. 246602, June 2008.

[58] O. G. Heinonen, S. W. Stokes, and J. Y. Yi, “Perpendicular Spin Torque in Magnetic Tunnel Junctions,” *Physical Review Letters*, vol. 105, p. 066602, Aug. 2010.

[59] H. Kubota, A. Fukushima, K. Yakushiji, T. Nagahama, S. Yuasa, K. Ando, H. Maehara, Y. Nagamine, K. Tsunekawa, D. D. Djayaprawira, N. Watanabe, and Y. Suzuki, “Quantitative measurement of voltage dependence of spin-transfer torque in MgO-based magnetic tunnel junctions,” *Nature Physics*, vol. 4, pp. 37–41, Jan. 2008.

[60] K. Bernert, V. Sluka, C. Fowley, J. Lindner, J. Fassbender, and A. M. Deac, “Phase diagrams of MgO magnetic tunnel junctions including the perpendicular spin-transfer torque in different geometries,” *Physical Review B*, vol. 89, p. 134415, Apr. 2014.

[61] J. Grollier, V. Cros, H. Jaffrès, A. Hamzic, J. M. George, G. Faini, J. Ben Youssef, H. Le Gall, and A. Fert, “Field dependence of magnetization reversal by spin transfer,” *Physical Review B*, vol. 67, p. 174402, May 2003.

[62] L. Landau and E. Lifshitz, “On the theory of the dispersion of magnetic permeability in ferromagnetic bodies,” *Phys. Z. Sowjetunion*, vol. 8, no. 153, pp. 101–114, 1935.

[63] T. L. Gilbert, “A phenomenological theory of damping in ferromagnetic materials,” *IEEE Transactions on Magnetics*, vol. 40, pp. 3443–3449, Nov. 2004.

[64] J. Z. Sun, “Spin-current interaction with a monodomain magnetic body: A model study,” *Physical Review B*, vol. 62, pp. 570–578, July 2000.

[65] D. Apalkov, B. Dieny, and J. M. Slaughter, “Magnetoresistive Random Access Memory,” *Proceedings of the IEEE*, vol. 104, pp. 1796–1830, Oct. 2016.

[66] W. F. Brown, “Thermal Fluctuations of a Single-Domain Particle,” *Physical Review*, vol. 130, pp. 1677–1686, June 1963.

[67] Z. Diao, Z. Li, S. Wang, Y. Ding, A. Panchula, E. Chen, L.-C. Wang, and Yiming Huai, “Spin-transfer torque switching in magnetic tunnel junctions and spin-transfer torque random access memory,” *Journal of Physics: Condensed Matter*, vol. 19, no. 16, p. 165209, 2007.

[68] R. H. Koch, J. A. Katine, and J. Z. Sun, “Time-Resolved Reversal of Spin-Transfer Switching in a Nanomagnet,” *Physical Review Letters*, vol. 92, p. 088302, Feb. 2004.

[69] D. M. Apalkov and P. B. Visscher, “Spin-torque switching: Fokker-Planck rate calculation,” *Physical Review B*, vol. 72, p. 180405, Nov. 2005.

[70] A. t. Khvalkovskiy, “Switching current in thermally-activated switching regime for perpendicular stt-mram structures,” in *Proc. 58th MMMConf.*, pp. DC–08, 2013.

[71] J. Slaughter, N. Rizzo, *et al.*, “St-mram gets practical,” *ST-MRAM, Technical Brief*, 2013.

[72] L. Savtchenko, B. N. Engel, N. D. Rizzo, M. F. Deherrera, and J. A. Janesky, “Method of writing to scalable magnetoresistance random access memory element,” Apr. 8 2003. US Patent 6,545,906.

[73] S. Bandiera, R. C. Sousa, M. Marins de Castro, C. Ducruet, C. Portemont, S. Auffret, L. Vila, I. L. Prejbeanu, B. Rodmacq, and B. Dieny, “Spin transfer torque switching assisted by thermally induced anisotropy reorientation in perpendicular magnetic tunnel junctions,” *Applied Physics Letters*, vol. 99, p. 202507, Nov. 2011.

[74] B. Dieny, R. Sousa, J. Herault, C. Papusoi, G. Prenat, U. Ebels, D. Houssameddine, B. Rodmacq, S. Auffret, L. Buda-Prejbeanu, *et al.*, “Spin-transfer effect and its use in spintronic components,” *International Journal of Nanotechnology*, vol. 7, no. 4-8, pp. 591–614, 2010.

[75] I. M. Miron, K. Garello, G. Gaudin, P.-J. Zermatten, M. V. Costache, S. Auffret, S. Bandiera, B. Rodmacq, A. Schuhl, and P. Gambardella, “Perpendicular switching of a single ferromagnetic layer induced by in-plane current injection,” *Nature*, vol. 476, no. 7359, p. 189, 2011.

[76] D. Worledge, “Theory of Spin Torque Switching Current for the Double Magnetic Tunnel Junction,” *IEEE Magnetics Letters*, vol. PP, no. 99, pp. 1–1, 2017.

[77] J. C. Slonczewski and J. Z. Sun, “Theory of voltage-driven current and torque in magnetic tunnel junctions,” *Journal of Magnetism and Magnetic Materials*, vol. 310, pp. 169–175, Mar. 2007.

[78] Y. Huai, M. Pakala, Z. Diao, and Y. Ding, “Spin transfer switching current reduction in magnetic tunnel junction based dual spin filter structures,” *Applied Physics Letters*, vol. 87, p. 222510, Nov. 2005.

[79] P. Y. Clément, C. Baraduc, M. Chshiev, B. Diény, L. Vila, and C. Ducruet, “Double barrier magnetic tunnel junctions with write/read mode select layer,” in *2014 IEEE 6th International Memory Workshop (IMW)*, pp. 1–4, May 2014.

[80] P.-Y. Clément, C. Baraduc, C. Ducruet, L. Vila, M. Chshiev, and B. Diény, “Modulation of spin transfer torque amplitude in double barrier magnetic tunnel junctions,” *Applied Physics Letters*, vol. 107, p. 102405, Sept. 2015.

[81] L. Cuchet, B. Rodmacq, S. Auffret, R. C. Sousa, I. L. Prejbeanu, and B. Dieny, “Perpendicular magnetic tunnel junctions with double barrier and single or synthetic antiferromagnetic storage layer,” *Journal of Applied Physics*, vol. 117, p. 233901, June 2015.

[82] M. Gajek, J. Nowak, J. Sun, P. Trouilloud, E. O’sullivan, D. Abraham, M. Gaidis, G. Hu, S. Brown, Y. Zhu, *et al.*, “Spin torque switching of 20 nm magnetic tunnel junctions with perpendicular anisotropy,” *Applied Physics Letters*, vol. 100, no. 13, p. 132408, 2012.

[83] N. Perrissin, S. Lequeux, N. Strelkov, L. Vila, L. Buda-Prejbeanu, S. Auffret, R. Sousa, I. Prejbeanu, and B. Dieny, “Highly thermally stable sub-20nm magnetic random-access memory based on perpendicular shape anisotropy,” *arXiv preprint arXiv:1803.02663*, 2018.

[84] L. Lombard, E. Gapihan, R. C. Sousa, Y. Dahmane, Y. Conraux, C. Portemont, C. Ducruet, C. Papusoi, I. L. Prejbeanu, J. P. Nozières, B. Dieny, and A. Schuhl, “IrMn and FeMn blocking temperature dependence on heating pulse width,” *Journal of Applied Physics*, vol. 107, p. 09D728, May 2010.

[85] P.-Y. Clement, C. Ducruet, C. Baraduc, M. Chshiev, and B. Diény, “Diffusive model of current-in-plane-tunneling in double magnetic tunnel junctions,” *Applied Physics Letters*, vol. 100, p. 262404, June 2012.

[86] S. Lee, T. Bae, and J. Hong, “Modified analytical method for evaluation of unpatterned double-barrier magnetic tunnel junctions,” *Applied Physics Letters*, vol. 104, no. 26, p. 263502, 2014.

[87] T. Nozaki, A. Hirohata, N. Tezuka, S. Sugimoto, and K. Inomata, “Bias voltage effect on tunnel magnetoresistance in fully epitaxial MgO double-barrier magnetic tunnel junctions,” *Applied Physics Letters*, vol. 86, p. 082501, Feb. 2005.

[88] G. Feng, S. van Dijken, and J. M. D. Coey, “Influence of annealing on the bias voltage dependence of tunneling magnetoresistance in MgO double-barrier magnetic tunnel junctions with CoFeB electrodes,” *Applied Physics Letters*, vol. 89, p. 162501, Oct. 2006.

[89] Z. Qian, R. Bai, C. Yang, Q. Li, Y. Sun, D. Huo, L. Li, H. Zhan, Y. Li, and J. Zhu, “Effective anisotropy field in the free layer of patterned spin-valve resistors,” *Journal of Applied Physics*, vol. 109, p. 103904, May 2011.

[90] J. Sun, M. Gaidis, G. Hu, E. O’Sullivan, S. Brown, J. Nowak, P. Trouilloud, and D. Worledge, “High-bias backhopping in nanosecond time-domain spin-torque switches of mgo-based magnetic tunnel junctions,” *Journal of Applied Physics*, vol. 105, no. 7, p. 07D109, 2009.

[91] S.-c. Oh, S.-y. Park, A. Manchon, M. Chshiev, J.-h. Han, H.-w. Lee, J.-e. Lee, K.-t. Nam, Y. Jo, Y.-c. Kong, B. Dieny, and K.-j. Lee, “Bias-voltage dependence of perpendicular spin-transfer torque in asymmetric MgO-based magnetic tunnel junctions,” *Nature Physics*, vol. 5, no. 12, pp. 898–902, 2009.

[92] W. Skowroński, P. Ogrodnik, J. Wrona, T. Stobiecki, R. Świrkowicz, J. Barnaś, G. Reiss, and S. van Dijken, “Backhopping effect in magnetic tunnel junctions: Comparison between theory and experiment,” *Journal of Applied Physics*, vol. 114, p. 233905, Dec. 2013.

[93] T. Min, J. Sun, R. Beach, D. Tang, and P. Wang, “Back-hopping after spin torque transfer induced magnetization switching in magnetic tunneling junction cells,” *Journal of Applied Physics*, vol. 105, no. 7, p. 07D126, 2009.

[94] P. K. Amiri, Z. M. Zeng, P. Upadhyaya, G. Rowlands, H. Zhao, I. N. Krivorotov, J. P. Wang, H. W. Jiang, J. A. Katine, J. Langer, K. Galatsis, and K. L. Wang, “Low Write-Energy Magnetic Tunnel Junctions for High-Speed Spin-Transfer-Torque MRAM,” *IEEE Electron Device Letters*, vol. 32, pp. 57–59, Jan. 2011.

[95] S. Zhang, P. M. Levy, A. C. Marley, and S. S. P. Parkin, “Quenching of Magnetoresistance by Hot Electrons in Magnetic Tunnel Junctions,” *Physical Review Letters*, vol. 79, pp. 3744–3747, Nov. 1997.

[96] E. Y. Tsymbal, A. Sokolov, I. F. Sabirianov, and B. Doudin, “Resonant Inversion of Tunneling Magnetoresistance,” *Physical Review Letters*, vol. 90, p. 186602, May 2003.

[97] C. Heiliger, P. Zahn, B. Y. Yavorsky, and I. Mertig, “Influence of the interface structure on the bias dependence of tunneling magnetoresistance,” *Physical Review B*, vol. 72, p. 180406, Nov. 2005.

[98] S. Yuasa, Y. Suzuki, T. Katayama, and K. Ando, “Characterization of growth and crystallization processes in CoFeB-MgO-CoFeB magnetic tunnel junction structure by reflective high-energy electron diffraction,” *Applied Physics Letters*, vol. 87, no. 24, p. 242503, 2005.

[99] T. Miyajima, T. Ibusuki, S. Umehara, M. Sato, S. Eguchi, M. Tsukada, and Y. Kataoka, “Transmission electron microscopy study on the crystallization and boron distribution of CoFeB-MgO-CoFeB magnetic tunnel junctions with various capping layers,” *Applied Physics Letters*, vol. 94, no. 12, p. 122501, 2009.

[100] S. V. Karthik, Y. K. Takahashi, T. Ohkubo, K. Hono, S. Ikeda, and H. Ohno, “Transmission electron microscopy investigation of CoFeB/MgO/CoFeB pseudospin valves annealed at different temperatures,” *Journal of Applied Physics*, vol. 106, p. 023920, July 2009.

[101] W. Zhu, H. Li, Y. Chen, and X. Wang, “Current Switching in MgO-Based Magnetic Tunneling Junctions,” *IEEE Transactions on Magnetics*, vol. 47, pp. 156–160, Jan. 2011.

[102] Z. Diao, D. Apalkov, M. Pakala, Y. Ding, A. Panchula, and Y. Huai, “Spin transfer switching and spin polarization in magnetic tunnel junctions with MgO and AlOx barriers,” *Applied Physics Letters*, vol. 87, p. 232502, Dec. 2005.

[103] Z. Li and S. Zhang, “Thermally assisted magnetization reversal in the presence of a spin-transfer torque,” *Physical Review B*, vol. 69, p. 134416, Apr. 2004.

[104] S. Iihama, S. Mizukami, H. Naganuma, M. Oogane, Y. Ando, and T. Miyazaki, “Gilbert damping constants of Ta/CoFeB/MgO(Ta) thin films measured by optical detection of precessional magnetization dynamics,” *Physical Review B*, vol. 89, p. 174416, May 2014.

[105] C. L. Platt, B. Dieny, and A. E. Berkowitz, “Spin polarized tunneling in reactively sputtered tunnel junctions,” *Journal of Applied Physics*, vol. 81, pp. 5523–5525, Apr. 1997.

[106] E. L. Wolf, *Principles of electron tunneling spectroscopy*, vol. 152. Oxford University Press, 2012.

[107] Y. Lu, X. W. Li, G. Xiao, R. A. Altman, W. J. Gallagher, A. Marley, K. Roche, and S. Parkin, “Bias voltage and temperature dependence of magnetotunneling effect,” *Journal of Applied Physics*, vol. 83, pp. 6515–6517, June 1998.

[108] J. Zhang and R. M. White, “Voltage dependence of magnetoresistance in spin dependent tunneling junctions,” *Journal of Applied Physics*, vol. 83, pp. 6512–6514, June 1998.

[109] M. Sharma, S. X. Wang, and J. H. Nickel, “Inversion of Spin Polarization and Tunneling Magnetoresistance in Spin-Dependent Tunneling Junctions,” *Physical Review Letters*, vol. 82, pp. 616–619, Jan. 1999.

[110] J. M. D. Teresa, A. Barthélémy, A. Fert, J. P. Contour, F. Montaigne, and P. Seneor, “Role of Metal-Oxide Interface in Determining the Spin Polarization of Magnetic Tunnel Junctions,” *Science*, vol. 286, pp. 507–509, Oct. 1999.

[111] J. G. Simmons, “Generalized Formula for the Electric Tunnel Effect between Similar Electrodes Separated by a Thin Insulating Film,” *Journal of Applied Physics*, vol. 34, pp. 1793–1803, June 1963.

[112] J. Wang and P. Freitas, “Low-current blocking temperature writing of double barrier magnetic random access memory cells,” *Applied physics letters*, vol. 84, no. 6, pp. 945–947, 2004.

[113] A. Chavent, *Réduction du champ d’écriture de mé moires magnétiques à écriture assistée thermiquement à l’aide du couple de transfert de spin*. PhD thesis, Université de Grenoble, 2016.

[114] C. Wang, Y.-T. Cui, J. A. Katine, R. A. Buhrman, and D. C. Ralph, “Time-resolved measurement of spin-transfer-driven ferromagnetic resonance and spin torque in magnetic tunnel junctions,” *Nature Physics*, vol. 7, pp. 496–501, June 2011.

[115] A. A. Timopheev, R. Sousa, M. Chshiev, L. D. Buda-Prejbeanu, and B. Dieny, “Respective influence of in-plane and out-of-plane spin-transfer torques in magnetization switching of perpendicular magnetic tunnel junctions,” *Physical Review B*, vol. 92, p. 104430, Sept. 2015.

[116] L. Néel, “Anisotropie magnétique superficielle et surstructures d’orientation,” *Journal de Physique et le Radium*, vol. 15, pp. 225–239, Apr. 1954.

[117] C. Aron, D. G. Barci, L. F. Cugliandolo, Z. G. Arenas, and G. S. Lozano, “Magnetization dynamics: path-integral formalism for the stochastic Landau–Lifshitz–Gilbert equation,” *Journal of Statistical Mechanics: Theory and Experiment*, vol. 2014, no. 9, p. P09008, 2014.

[118] J. P. Liu, E. Fullerton, O. Gutfleisch, and D. J. Sellmyer, *Nanoscale Magnetic Materials and Applications*. Springer Science & Business Media, Apr. 2010. Google-Books-ID: QLXVW0JRDUMC.

[119] J. Xiao, A. Zangwill, and M. D. Stiles, “Macrospin models of spin transfer dynamics,” *Physical Review B*, vol. 72, p. 014446, July 2005.

[120] M. Beleggia, M. D. Graef, and Y. T. Millev, “The equivalent ellipsoid of a magnetized body,” *Journal of Physics D: Applied Physics*, vol. 39, no. 5, p. 891, 2006.

[121] J. A. Katine, F. J. Albert, R. A. Buhrman, E. B. Myers, and D. C. Ralph, “Current-Driven Magnetization Reversal and Spin-Wave Excitations in Co $/$Cu $/$Co Pillars,” *Physical Review Letters*, vol. 84, pp. 3149–3152, Apr. 2000.

[122] L. Berger, “Emission of spin waves by a magnetic multilayer traversed by a current,” *Phys. Rev. B*, vol. 54, pp. 9353–9358, Oct 1996.

[123] S. Zhang, P. M. Levy, and A. Fert, “Mechanisms of Spin-Polarized Current-Driven Magnetization Switching,” *Physical Review Letters*, vol. 88, p. 236601, May 2002.

[124] A. Kalitsov, M. Chshiev, I. Theodonis, N. Kioussis, and W. H. Butler, “Spin-transfer torque in magnetic tunnel junctions,” *Physical Review B*, vol. 79, p. 174416, May 2009.

[125] P. Chowdhury, P. D. Kulkarni, M. Krishnan, H. C. Barshilia, A. Sagdeo, S. K. Rai, G. S. Lodha, and D. V. Sridhara Rao, “Effect of coherent to incoherent structural transition on magnetic anisotropy in Co/Pt multilayers,” *Journal of Applied Physics*, vol. 112, p. 023912, July 2012.

[126] Z. Kugler, J.-P. Grote, V. Drewello, O. Schebaum, G. Reiss, and A. Thomas, “Co/Pt multilayer-based magnetic tunnel junctions with perpendicular magnetic anisotropy,” *Journal of Applied Physics*, vol. 111, p. 07C703, Feb. 2012.

[127] T. Young Lee, D. Su Son, S. Ho Lim, and S.-R. Lee, “High post-annealing stability in [Pt/Co] multilayers,” *Journal of Applied Physics*, vol. 113, p. 216102, June 2013.

[128] S. Ishikawa, H. Sato, M. Yamanouchi, S. Ikeda, S. Fukami, F. Matsukura, and H. Ohno, “Magnetic properties of MgO-[Co/Pt] multilayers with a CoFeB insertion layer,” *Journal of Applied Physics*, vol. 113, p. 17C721, Apr. 2013.

[129] H. Sato, S. Ikeda, S. Fukami, H. Honjo, S. Ishikawa, M. Yamanouchi, K. Mizunuma, F. Matsukura, and H. Ohno, “Co/Pt multilayer based reference layers in magnetic tunnel junctions for nonvolatile spintronics VLSIs,” *Japanese Journal of Applied Physics*, vol. 53, p. 04EM02, Feb. 2014.

[130] S. T. Lim, M. Tran, J. W. Chenchen, J. F. Ying, and G. Han, “Effect of different seed layers with varying Co and Pt thicknesses on the magnetic properties of Co/Pt multilayers,” *Journal of Applied Physics*, vol. 117, p. 17A731, Mar. 2015.

[131] M. Bersweiler, K. Dumesnil, D. Lacour, and M. Hehn, “Impact of buffer layer and Pt thickness on the interface structure and magnetic properties in (Co/Pt) multilayers,” *Journal of Physics: Condensed Matter*, vol. 28, no. 33, p. 336005, 2016.

[132] J. Chatterjee, *”Engineering of magnetic tunnel junction stacks for improved STT-MRAM performance and development of novel and cost-effective nano-patterning techniques”*. PhD thesis, Université Grenoble-Alpes, 2018.

[133] M. T. Johnson, R. Jungblut, P. J. Kelly, and F. J. A. den Broeder, “Perpendicular magnetic anisotropy of multilayers: recent insights,” *Journal of Magnetism and Magnetic Materials*, vol. 148, pp. 118–124, July 1995.

[134] P. Bruno, “Tight-binding approach to the orbital magnetic moment and magnetocrystalline anisotropy of transition-metal monolayers,” *Physical Review B*, vol. 39, pp. 865–868, Jan. 1989.

[135] G. H. O. Daalderop, P. J. Kelly, and M. F. H. Schuurmans, “First-principles calculation of the magnetic anisotropy energy of (co)$_n$/(x)$_m$ multilayers,” *Phys. Rev. B*, vol. 42, pp. 7270–7273, Oct 1990.

[136] G. H. O. Daalderop, P. J. Kelly, and M. F. H. Schuurmans, “Magnetocrystalline anisotropy and orbital moments in transition-metal compounds,” *Phys. Rev. B*, vol. 44, pp. 12054–12057, Dec 1991.

[137] Y. Yang, J. S. Chen, and G. M. Chow, “Highly chemical ordered L11 CoPt (111) films with perpendicular anisotropy grown on glass substrates,” *Journal of Applied Physics*, vol. 109, p. 07B744, Apr. 2011.

[138] M. Ohtake, S. Ouchi, F. Kirino, and M. Futamoto, “L10 ordered phase formation in FePt, FePd, CoPt, and CoPd alloy thin films epitaxially grown on MgO(001) single-crystal substrates,” *Journal of Applied Physics*, vol. 111, p. 07A708, Feb. 2012.

[139] C. S. Kim, D. Choi, S. Chung, A. Wise, Y. Y. Dang, and M. H. Kryder, “Surface roughness and magnetic properties of l10 fept films on mgo/crru/tin,” *Journal of Applied Physics*, vol. 112, no. 2, p. 023907, 2012.

[140] P. F. Carcia, A. D. Meinhaldt, and A. Suna, “Perpendicular magnetic anisotropy in pd/co thin film layered structures,” *Applied Physics Letters*, vol. 47, no. 2, pp. 178–180, 1985.

[141] P. F. Carcia, “Perpendicular magnetic anisotropy in pd/co and pt/co thin-film layered structures,” *Journal of Applied Physics*, vol. 63, no. 10, pp. 5066–5073, 1988.

[142] F. J. A. den Broeder, D. Kuiper, A. P. van de Mosselaer, and W. Hoving, “Perpendicular magnetic anisotropy of co-au multilayers induced by interface sharpening,” *Phys. Rev. Lett.*, vol. 60, pp. 2769–2772, Jun 1988.

[143] S. Monso, B. Rodmacq, S. Auffret, G. Casali, F. Fettar, B. Gilles, B. Dieny, and P. Boyer, “Crossover from in-plane to perpendicular anisotropy in Pt/CoFe/AlOx sandwiches as a function of Al oxidation: A very accurate control of the oxidation of tunnel barriers,” *Applied Physics Letters*, vol. 80, pp. 4157–4159, May 2002.

[144] B. Rodmacq, S. Auffret, B. Dieny, S. Monso, and P. Boyer, “Crossovers from in-plane to perpendicular anisotropy in magnetic tunnel junctions as a function of the barrier degree of oxidation,” *Journal of Applied Physics*, vol. 93, pp. 7513–7515, May 2003.

[145] A. Manchon, C. Ducruet, L. Lombard, S. Auffret, B. Rodmacq, B. Dieny, S. Pizzini, J. Vogel, V. Uhlíř, M. Hochstrasser, and G. Panaccione, “Analysis of oxygen induced anisotropy crossover in Pt/Co/MOx trilayers,” *Journal of Applied Physics*, vol. 104, p. 043914, Aug. 2008.

[146] H. X. Yang, M. Chshiev, B. Dieny, J. H. Lee, A. Manchon, and K. H. Shin, “First-principles investigation of the very large perpendicular magnetic anisotropy at Fe$|$MgO and Co$|$MgO interfaces,” *Physical Review B*, vol. 84, p. 054401, Aug. 2011.

[147] B. Rodmacq, A. Manchon, C. Ducruet, S. Auffret, and B. Dieny, “Influence of thermal annealing on the perpendicular magnetic anisotropy of Pt/Co/AlOx trilayers,” *Physical Review B*, vol. 79, p. 024423, Jan. 2009.

[148] S. Ikeda, K. Miura, H. Yamamoto, K. Mizunuma, H. D. Gan, M. Endo, S. Kanai, J. Hayakawa, F. Matsukura, and H. Ohno, “A perpendicular-anisotropy CoFeB–MgO magnetic tunnel junction,” *Nature Materials*, vol. 9, p. nmat2804, July 2010.

[149] H. Sato, M. Yamanouchi, S. Ikeda, S. Fukami, F. Matsukura, and H. Ohno, “Perpendicular-anisotropy CoFeB-MgO magnetic tunnel junctions with a MgO/CoFeB/Ta/CoFeB/MgO recording structure,” *Applied Physics Letters*, vol. 101, p. 022414, July 2012.

[150] H. Sato, T. Yamamoto, M. Yamanouchi, S. Ikeda, S. Fukami, K. Kinoshita, F. Matsukura, N. Kasai, and H. Ohno, “Comprehensive study of CoFeB-MgO magnetic tunnel junction characteristics with single- and double-interface scaling down to 1x nm,” in *2013 IEEE International Electron Devices Meeting*, pp. 3.2.1–3.2.4, Dec. 2013.

[151] F. J. A. den Broeder, W. Hoving, and P. J. H. Bloemen, “Magnetic anisotropy of multilayers,” *Journal of Magnetism and Magnetic Materials*, vol. 93, pp. 562–570, Feb. 1991.

[152] E. Liu, J. Swerts, S. Couet, S. Mertens, Y. Tomczak, T. Lin, V. Spampinato, A. Franquet, S. Van Elshocht, G. Kar, A. Furnemont, and J. De Boeck, "[Co/Ni]-CoFeB hybrid free layer stack materials for high density magnetic random access memory applications," *Applied Physics Letters*, vol. 108, p. 132405, Mar. 2016.

[153] L. Cuchet, B. Rodmacq, S. Auffret, R. C. Sousa, C. Ducruet, and B. Dieny, "Influence of a ta spacer on the magnetic and transport properties of perpendicular magnetic tunnel junctions," *Applied Physics Letters*, vol. 103, no. 5, p. 052402, 2013.

[154] S. Bandiera, *"....".* PhD thesis, Université de Grenoble, 2012.

[155] L. Cuchet, *"Magnetic and transport properties of single and double perpendicular magnetic double junctions".* PhD thesis, Université de Grenoble, 2015.

[156] J. Chatterjee, R. C. Sousa, N. Perrissin, S. Auffret, C. Ducruet, and B. Dieny, "Enhanced annealing stability and perpendicular magnetic anisotropy in perpendicular magnetic tunnel junctions using W layer," *Applied Physics Letters*, vol. 110, p. 202401, May 2017.

[157] S. Bandiera, R. C. Sousa, Y. Dahmane, C. Ducruet, C. Portemont, V. Baltz, S. Auffret, I. L. Prejbeanu, and B. Dieny, "Comparison of Synthetic Antiferromagnets and Hard Ferromagnets as Reference Layer in Magnetic Tunnel Junctions With Perpendicular Magnetic Anisotropy," *IEEE Magnetics Letters*, vol. 1, pp. 3000204–3000204, 2010.

[158] S. S. P. Parkin, "Systematic variation of the strength and oscillation period of indirect magnetic exchange coupling through the 3d, 4d, and 5d transition metals," *Phys. Rev. Lett.*, vol. 67, pp. 3598–3601, Dec 1991.

[159] S. V. Halilov, A. Y. Perlov, P. M. Oppeneer, A. N. Yaresko, and V. N. Antonov, "Magnetocrystalline anisotropy energy in cubic Fe, Co, and Ni: Applicability of local-spin-density theory reexamined," *Physical Review B*, vol. 57, pp. 9557–9560, Apr. 1998.

[160] H. Sato, M. Yamanouchi, K. Miura, S. Ikeda, R. Koizumi, F. Matsukura, and H. Ohno, "CoFeB Thickness Dependence of Thermal Stability Factor in CoFeB/MgO Perpendicular Magnetic Tunnel Junctions," *IEEE Magnetics Letters*, vol. 3, pp. 3000204–3000204, 2012.

[161] D.-Y. Lee, S.-H. Hong, S.-E. Lee, and J.-G. Park, "Dependency of Tunneling-Magnetoresistance Ratio on Nanoscale Spacer Thickness and Material for Double MgO Based Perpendicular-Magnetic-Tunneling-Junction," *Scientific Reports*, vol. 6, p. 38125, Dec. 2016.

[162] J.-H. Kim, J.-B. Lee, G.-G. An, S.-M. Yang, W.-S. Chung, H.-S. Park, and J.-P. Hong, "Ultrathin W space layer-enabled thermal stability enhancement in a perpendicular MgO/CoFeB/W/CoFeB/MgO recording frame," *Scientific Reports*, vol. 5, p. 16903, Nov. 2015.

[163] L. Néel, "Magnetisme-sur un nouveau mode de couplage entre les animantations de deux couches minces ferromagnetiques," *Comptes Rendus Hebdomadaires Des Seances De L Academie Des Sciences*, vol. 255, no. 15, p. 1676, 1962.

[164] J. Moritz, F. Garcia, J. Toussaint, B. Dieny, and J. Nozieres, “Orange peel coupling in multilayers with perpendicular magnetic anisotropy: Application to (co/pt)-based exchange-biased spin-valves,” *EPL (Europhysics Letters)*, vol. 65, no. 1, p. 123, 2004.

[165] L. E. Nistor, B. Rodmacq, S. Auffret, A. Schuhl, M. Chshiev, and B. Dieny, “Oscillatory interlayer exchange coupling in mgo tunnel junctions with perpendicular magnetic anisotropy,” *Physical Review B*, vol. 81, no. 22, p. 220407, 2010.

[166] J. Chatterjee, S. Auffret, R. Sousa, P. Coelho, I.-L. Prejbeanu, and B. Dieny, “Novel multifunctional rkky coupling layer for ultrathin perpendicular synthetic antiferromagnet,” *Scientific Reports*, vol. 8, no. 1, p. 11724, 2018.

[167] T. Devolder, J. V. Kim, J. Swerts, S. Couet, S. Rao, W. Kim, S. Mertens, G. Kar, and V. Nikitin, “Material developments and domain wall based nanosecond-scale switching process in perpendicularly magnetized STT-MRAM cells (invited),” *IEEE Transactions on Magnetics*, vol. PP, no. 99, pp. 1–1, 2017.

[168] X. Feng and P. B. Visscher, “Sweep-rate-dependent coercivity simulation of FePt particle arrays,” *Journal of Applied Physics*, vol. 95, pp. 7043–7045, May 2004.

[169] L. Tillie, E. Nowak, R. C. Sousa, M. C. Cyrille, B. Delaet, T. Magis, A. Persico, J. Langer, B. Ocker, I. L. Prejbeanu, and L. Perniola, “Data retention extraction methodology for perpendicular STT-MRAM,” in *2016 IEEE International Electron Devices Meeting (IEDM)*, pp. 27.3.1–27.3.4, Dec. 2016.

[170] J. Z. Sun, S. L. Brown, W. Chen, E. A. Delenia, M. C. Gaidis, J. Harms, G. Hu, X. Jiang, R. Kilaru, W. Kula, G. Lauer, L. Q. Liu, S. Murthy, J. Nowak, E. J. O’Sullivan, S. S. P. Parkin, R. P. Robertazzi, P. M. Rice, G. Sandhu, T. Topuria, and D. C. Worledge, “Spin-torque switching efficiency in CoFeB-MgO based tunnel junctions,” *Physical Review B*, vol. 88, p. 104426, Sept. 2013.

[171] H. Sato, E. C. I. Enobio, M. Yamanouchi, S. Ikeda, S. Fukami, S. Kanai, F. Matsukura, and H. Ohno, “Properties of magnetic tunnel junctions with a MgO/CoFeB/Ta/CoFeB/MgO recording structure down to junction diameter of 11nm,” *Applied Physics Letters*, vol. 105, p. 062403, Aug. 2014.

[172] J. Z. Sun, R. P. Robertazzi, J. Nowak, P. L. Trouilloud, G. Hu, D. W. Abraham, M. C. Gaidis, S. L. Brown, E. J. O’Sullivan, W. J. Gallagher, and D. C. Worledge, “Effect of subvolume excitation and spin-torque efficiency on magnetic switching,” *Physical Review B*, vol. 84, p. 064413, Aug. 2011.

[173] R. Dittrich, A. Thiaville, J. Miltat, and T. Schrefl, “Rigorous micromagnetic computation of configurational anisotropy energies in nanoelements,” *Journal of Applied Physics*, vol. 93, no. 10, pp. 7891–7893, 2003.

[174] D. Apalkov, A. Khvalkovskiy, and V. Nikitin, “Nudged elastic band calculation of switching modes and energy barriers in perpendicular MRAM,” in *Proc. 11th Joint MMM-Intermag Conf.*, 2013.

[175] Y. X. Wang, Z. Wang, H. Gan, and B. K. Yen Hui, “Perpendicular STT-MRAM thermal stability scaling and robust retention design,” in *Proc. MMM Conf., 2014*, 2014.

[176] L. Thomas, G. Jan, S. Le, Y. J. Lee, H. Liu, J. Zhu, S. Serrano-Guisan, R. Y. Tong, K. Pi, D. Shen, R. He, J. Haq, Z. Teng, R. Annapragada, V. Lam, Y. J. Wang, T. Zhong, T. Torng, and P. K. Wang, “Solving the paradox of the inconsistent size dependence of thermal stability at device and chip-level in perpendicular STT-MRAM,” in *2015 IEEE International Electron Devices Meeting (IEDM)*, pp. 26.4.1–26.4.4, Dec. 2015.

[177] L. Thomas, G. Jan, J. Zhu, H. Liu, Y.-J. Lee, S. Le, R.-Y. Tong, K. Pi, Y.-J. Wang, D. Shen, R. He, J. Haq, J. Teng, V. Lam, K. Huang, T. Zhong, T. Torng, and P.-K. Wang, “Perpendicular spin transfer torque magnetic random access memories with high spin torque efficiency and thermal stability for embedded applications (invited),” *Journal of Applied Physics*, vol. 115, no. 17, p. 172615, 2014.

[178] P. J. Jensen and K. H. Bennemann, “Direction of the magnetization of thin films and sandwiches as a function of temperature,” *Physical Review B*, vol. 42, pp. 849–855, July 1990.

[179] J. Wang and P. P. Freitas, “Low-current blocking temperature writing of double barrier magnetic random access memory cells,” *Applied Physics Letters*, vol. 84, pp. 945–947, Feb. 2004.

[180] I. L. Prejbeanu, S. Bandiera, J. Alvarez-Hérault, R. C. Sousa, B. Dieny, and J.-P. Nozières, “Thermally assisted MRAMs: ultimate scalability and logic functionalities,” *Journal of Physics D: Applied Physics*, vol. 46, no. 7, p. 074002, 2013.

[181] L. Thomas, M. Benzaouia, S. Serrano-Guisan, G. Jan, S. Le, Y. Lee, H. Liu, J. Zhu, J. Iwata-Harms, R. Tong, Y. Yang, V. Sundar, S. Patel, J. Haq, D. Shen, R. He, V. Lam, J. Teng, P. Liu, A. Wang, T. Zhong, T. Torng, and P. Wang, “Spin Transfer Torque driven dynamics of the synthetic antiferromagnetic reference layer of perpendicular MRAM devices,” in *2017 IEEE International Magnetics Conference (INTERMAG)*, pp. 1–1, Apr. 2017.

[182] A. D. Kent, B. Özyilmaz, and E. del Barco, “Spin-transfer-induced precessional magnetization reversal,” *Applied Physics Letters*, vol. 84, pp. 3897–3899, Apr. 2004.

[183] O. Redon, B. Dieny, and B. Rodmacq, “Magnetic spin polarization and magnetization rotation device with memory and writing process, using such a device,” Mar. 11 2003. US Patent 6,532,164.

[184] A. A. Timopheev, R. Sousa, M. Chshiev, H. T. Nguyen, and B. Dieny, “Second order anisotropy contribution in perpendicular magnetic tunnel junctions,” *Scientific Reports*, vol. 6, p. srep26877, June 2016.

[185] B. Dieny and A. Vedyayev, “Crossover from easy-plane to perpendicular anisotropy in magnetic thin films: canted anisotropy due to partial coverage or interfacial roughness,” *EPL (Europhysics Letters)*, vol. 25, no. 9, p. 723, 1994.

[186] N. Strelkov, A. Timopheev, R. C. Sousa, M. Chshiev, L. D. Buda-Prejbeanu, and B. Dieny, “Stability phase diagram of a perpendicular magnetic tunnel junction in noncollinear geometry,” *Physical Review B*, vol. 95, p. 184409, May 2017.

[187] J. Zhu, J. Katine, G. E. Rowlands, Y.-J. Chen, Z. Duan, J. G. Alzate, P. Upadhyaya, J. Langer, P. K. Amiri, K. L. Wang, *et al.*, “Voltage-induced ferromagnetic resonance in magnetic tunnel junctions,” *Physical review letters*, vol. 108, no. 19, p. 197203, 2012.

[188] J. Alzate, P. Amiri, S. Cherepov, J. Zhu, P. Upadhyaya, M. Lewis, I. Krivorotov, J. Katine, J. Langer, K. Galatsis, *et al.*, “Voltage-induced switching of cofeb-mgo magnetic tunnel junctions,” in *56th Conference on Magnetism and Magnetic Materials*, pp. EG–11, 2011.

[189] W.-g. Wang, M. Li, S. Hageman, and C. L. Chien, “Electric-field-assisted switching in magnetic tunnel junctions,” *Nature Materials*, vol. 11, no. 1, pp. 64–8, 2012.

[190] M. Endo, S. Kanai, S. Ikeda, F. Matsukura, and H. Ohno, “Electric-field effects on thickness dependent magnetic anisotropy of sputtered MgO/Co40fe40b20/Ta structures,” *Applied Physics Letters*, vol. 96, p. 212503, May 2010.

[191] P. K. Amiri and K. L. Wang, “Voltage-controlled magnetic anisotropy in spintronic devices,” in *Spin*, vol. 2, p. 1240002, World Scientific, 2012.

[192] K.-M. Lee, J. W. Choi, J. Sok, and B.-C. Min, “Temperature dependence of the interfacial magnetic anisotropy in w/cofeb/mgo,” *AIP Advances*, vol. 7, no. 6, p. 065107, 2017.

[193] E. R. Callen and H. Callen, “Anisotropic magnetization,” *Journal of Physics and Chemistry of Solids*, vol. 16, no. 3-4, pp. 310–328, 1960.

[194] B. Dieny, “Magnetic device, and method for reading from and writing to said device,” Aug. 2014. U.S. Classification 365/158, 365/173, 365/148, 977/935, 365/171, 977/933; International Classification H01L27/22, G11C11/00, B82Y25/00, H01L43/08, G11C11/16, H01F10/32; Cooperative Classification G11C11/1659, G11C11/1675, G11C11/1673, H01F10/3272, H01F10/329, H01L43/08, Y10S977/933, Y10S977/935, H01F10/3254, G11C11/161, H01L27/228, B82Y25/00.